UNIVERSITÀ
DI TRENTO

UNIVERSITY OF TRENTO

DOCTORAL THESIS

Agnostic method to detect low energetic signals nearby a gravitational wave transient from a binary black hole system

Author:
Dr. ANDREA MIANI

Supervisor:
Prof. GIOVANNI ANDREA PRODI
Co-supervisor:
Dr. CLAUDIA LAZZARO

A thesis submitted in fulfillment of the requirements for the degree of Doctor of Physics

in the

Department of Physics

October 5, 2022

Declaration of Authorship

I, Dr. ANDREA MIANI, declare that this thesis titled, "Agnostic method to detect low energetic signals nearby a gravitational wave transient from a binary black hole system" and the work presented in it are my own. I confirm that:

- This work was done wholly or mainly while in candidature for a research degree at this University.
- Where any part of this thesis has previously been submitted for a degree or any other qualification at this University or any other institution, this has been clearly stated.
- Where I have consulted the published work of others, this is always clearly attributed.
- Where I have quoted from the work of others, the source is always given. With the exception of such quotations, this thesis is entirely my own work.
- I have acknowledged all main sources of help.
- Where the thesis is based on work done by myself jointly with others, I have made clear exactly what was done by others and what I have contributed myself.

Signed:

Date:

"A luminous star, of the same density as the Earth, and whose diameter should be two hundred and fifty times larger than that of the Sun, would not, in consequence of its attraction, allow any of its rays to arrive at us; it is therefore possible that the largest luminous bodies in the universe may, through this cause, be invisible."

P. S. Laplace (1798)

UNIVERSITY OF TRENTO

Abstract

Science
Department of Physics

Doctor of Physics

Agnostic method to detect low energetic signals nearby a gravitational wave transient from a binary black hole system

by Dr. ANDREA MIANI

The first detection of a gravitational wave (GW) enabled our observation of the Universe through a revolutionary messenger and unveiled phenomena that are occurring in a range of very strong gravitational fields and relativistic velocities. These physical regimes, previously inaccessible to humankind, can now be studied. In particular, the discoveries of an unexpected population of stellar-mass binary black holes (BBH), and unexpected masses for binary neutron star (BNS) components have both pointed to new astrophysics, and to unprecedented tests of the general relativity theory.

This thesis focuses on the development of a new method of gravitational wave data analysis, aiming to investigate weak features in the proximity to well-identified BBH merger signals. The method is based on a dedicated version of coherentWaveBurst (cWB), an unmodelled gravitational waves transient search algorithm, developed in the LIGO Scientific Collaboration (LSC) and Virgo Collaboration and widely used on LIGO-Virgo-KAGRA (LVK) data. CoherentWaveBurst relies on the coherent detection of an excess of energy inside the combined data of all the gravitational waves detectors inside the detectors network. Such excess of energy must pass several internal thresholds of the pipeline to be accepted as a possible gravitational wave candidate and these thresholds evaluate not only the strength of the signal with respect to the background noise but also how balanced is the energy distribution among the detectors of the network, its coherence, as well as other quantities whose purpose is to rule out possible outliers due to the presence of non-stationary noise.

To develop such a method, it was decided to adopt as science case the search for echoes. In literature, it has been proposed that the gravitational radiation generated from a binary compact objects (CBCs) coalescence might display exotic characteristics if compared to the predicted one generated by black hole-black hole (BH-BH), neutron star-neutron star (NS-NS), or neutron star-black hole (NS-BH) binaries which are, for now, the only detected emitters of gravitational waves. Such differences arise from the proposal that the involved compact objects (COs) of the binary are not standard black holes but instead black hole mimickers called exotic compact objects (ECOs). If this is the case the gravitational wave signal generated from such a binary would display repeated gravitational wave pulses, of widely uncertain morphology, after the merger-ringdown phase of the gravitational signal. These repeated gravitational wave pulses are called echoes, one class of low energetic signals whose presence inside gravitational wave data, this new algorithm is searching for.

The proposed data analysis methodology searching for echoes is agnostic over the properties of the predicted gravitational wave pulses emitted by an ECO binary. Indeed, the variety of theoretical alternatives to black holes is not converging over a well-defined post-merger-ringdown signal, each model has its own properties and characteristic features. Therefore, the possibility to investigate the morphological features of possible outliers in the post-merger phase of detected GW signals is fundamental in the process of inferring their nature. Having their morphology recovered without priors makes the proposed search more general than the variety of theoretical models of echoes. This procedure is tested over real data from past LIGO-Virgo observing runs (O1, O2, and O3), and the capability of the search in estimating the main morphological parameters of echoes, such as their arrival time, mean frequency, as well as the amplitude attenuation between subsequent pulses, is investigated. This work concludes that the current state-of-the-art methods and detectors find no evidence for echoes of any morphologies. Such a study extended to lower signal-to-noise ratio (SNR) the detectability of echoes associated with the public gravitational-wave transient catalog of BBH mergers released by the LIGO and Virgo Collaboration. It also sets best quantitative upper limits on the amplitude of low energy signals occurring after the merger-ringdown. To achieve these results, new post-processing tools are developed and optimised to detect and characterize possible energy excess inside a user-defined time window. This required the development of the code and to adapt the cWB infrastructure to the new working requirements which also involves a re-tuning of cWB itself. The optimization of the performances is based on off-source simulations for assessing the detection efficiency and false alarm probability of signal candidates.

In the first chapter (1) of this dissertation, I give a theoretical overview of the gravitational waves' nature, their formation mechanism, as well as the information they carry inside the framework of the general relativity theory.

The second chapter (2) focuses on the dominant sources of gravitational waves in our Universe, giving major attention to black holes and their binary system. Moreover, we delve into the most important physical aspects of this system, which are related to gravitational waves.

In chapter three, (3), overviews the possible subthreshold gravitational wave signals that this search can target, with a deeper insight into echoes and their main morphological parameters.

In chapter four (4), the first part is dedicated to the introduction the gravitational wave detectors and the information they can provide. The second half, briefly reviews the main sources of noise that affect a gravitational wave detector and their impact on the data quality.

Chapter five (5) is dedicated to the coherent WaveBurst pipeline. Firstly, a general overview of the algorithm is given to the reader, then it describes the data analysis procedure, how it works, and the physical motivations behind its fundamental features.

In the following chapter, chapter 6 (6), there is a deep study of the implementation of the search in cWB, its tuning as well as its optimisation. Each choice made to boost the search is commented and physically motivated.

Chapter seven, (7), shows the performance of the search highlighting the information it can provide, and compares the on-source results with reference statistics. The two on-source outliers are further investigated. Through additional statistical analyses and morphological studies, we demonstrate these outliers are originated from noise glitches.

Chapter eight (8) explains the deployed morphological investigation and its potential in providing additional clues to the nature of candidate signals. The capability of a search to reconstruct the main morphological parameters of possible outliers can in fact give their nature.

In chapter nine (9), in the first half, we carry on a comparison of this search with other similar published searches The second half of the chapter highlights the echo's templates proposed in the literature also describing possible future improvements of cWB LES search.

My conclusions and final remarks are presented in chapter ten (10). In particular, I summarize the major achievements and strengths of the cWB LES search algorithm together with the next improvements based on the lessons learned from this work. Finally, I highlight the possibility to extend this method to other science cases.

Acknowledgements

First and foremost I am grateful to the EGO consortium, Trento Institute for Fundamental Physics and Applications (TIFPA), University of Trento, and the people who made it happen Giovanni Andrea Prodi, and Stefano Vitale. Thanks for funding my research and giving me this opportunity to be part of the gravitational waves research.

I would like to thank my professors, colleagues, and the staff at the University of Trento and the University of Padova for providing me with all the support and for educating me in various branches of physics. In particular my supervisor Giovanni Andrea Prodi and my co-supervisor Claudia Lazzaro for the guidance, support, and patience you gave me.

I would also like to thank all the researchers of the coherent WaveBurst group, in particular Marco Drago, Shubhanshu Tiwari, Gabriele Vedovato, Edoardo Milotti, and Francesco Salemi as well as my office mates Michele Valentini and Sophie Bini.

I must mention and sincerely thank my family. To them I own everything.

Of course, I have to thank my girlfriend Matilde to whom I dedicate this thesis. She was there whenever it was needed and even further.

This material is based upon work supported by NSF's LIGO Laboratory which is a major facility fully funded by the National Science Foundation. I also gratefully acknowledge the support of the Science and Technology Facilities Council (STFC) of the United Kingdom, the Max Planck Society (MPS), and the State of Niedersachsen/Germany for support of the construction of Advanced LIGO and the construction and operation of the GEO600 detector. Additional support for Advanced LIGO was provided by the Australian Research Council. I gratefully acknowledge the Italian Istituto Nazionale di Fisica Nucleare (INFN), the French Centre National de la Recherche Scientifique (CNRS) and the Netherlands Organization for Scientific Research (NWO), for the construction and operation of the Virgo detector and the creation and support of the EGO consortium Moreover, I also acknowledge the support of the NSF, STFC, INFN, and CNRS for the provision of computational resources.

Contents

Declaration of Authorship iii

Abstract vii

Acknowledgements xi

1 Gravitational waves in a nutshell 1
1.1 Einstein field equation . . . 1
1.2 Road map to GWs equation . . . 2
1.3 The transverse traceless gauge . . . 4
1.4 Plane and stationary GWs . . . 4
1.5 Generation of GWs . . . 6
1.6 Propagation and energy-momentum tensor of GWs . . . 8
1.7 Energy and momentum flux of GWs . . . 10

2 Sources of gravitational waves 11
2.1 Pudding of GWs sources . . . 11
2.1.1 Gravitational collapse . . . 11
2.1.2 Rotating neutron star . . . 12
2.1.3 Binary system . . . 12
2.1.4 Stochastic GWs background . . . 12
2.2 Black holes . . . 13
2.2.1 Schwarzschild black hole . . . 14
2.2.2 A "strange" potential . . . 15
2.2.3 Kerr black hole . . . 16
2.3 Binary black hole systems . . . 17
2.3.1 Inspiral phase . . . 17
2.3.2 Merger phase . . . 19
2.3.3 Ring-down phase . . . 20
Ring-down: quasi-normal modes . . . 20
2.3.4 Spin effects . . . 21

3 Low-energetic gravitational wave signals 23
3.1 Echoes . . . 23
3.1.1 BH and ECO: boundary conditions . . . 23
3.1.2 Post-merger GW signature for an ECO . . . 24
3.2 Highly eccentric BBH . . . 27
3.3 Memory effects . . . 28
3.4 Other sub-threshold gravitational signals . . . 29

4 Detecting gravitational waves **33**
4.1 GWs detectors: interferometers . . . 33
4.1.1 Detector signal . . . 34
4.1.2 Detectors network . . . 36
4.2 The noise . . . 37
4.2.1 Shot noise . . . 39
4.2.2 Radiation pressure noise . . . 40
4.2.3 Seismic noise . . . 41
4.2.4 Thermal noise . . . 41

5 The search for low energy signals **43**
5.1 Why are GWs' searching algorithms needed? . . . 43
5.2 Coherent WaveBurst (cWB) . . . 44
5.2.1 Maximum likelihood (ML) approach . . . 44
5.2.2 Initialisation stage . . . 46
5.2.3 Event trigger generator (ETG) . . . 48
5.2.4 CWB thresholds . . . 49
5.3 Methodology to detect low energy signals . . . 50
5.3.1 How to get a statistic? . . . 51
Background (BGK) distribution . . . 52
Signal (SIG) distribution. . . . 52
5.3.2 Statistics . . . 52
5.3.3 Post-merger time window . . . 55
5.3.4 Injections . . . 56

6 Tuning cWB pipeline **61**
6.1 Arrival time of the first echo, t_{echo} . . . 62
6.2 Black pixel probability and network coherent coefficient . . . 65
6.3 Post-merger blind time, t_{blind} . . . 66
6.4 Pixel selection rule . . . 67
6.5 Receiver Operating Curve (ROC) . . . 68
6.6 Tuning the cluster's defragmentation time . . . 70
6.7 Post-merger time window (PMW) . . . 72
6.8 Post-merger coherence and trigger preselection thresholds . . . 73
6.9 Whitening . . . 80
6.10 Final configuration . . . 80

7 CWB search for low energy signals: performances **83**
7.1 Configuration of the injected echoes . . . 84
7.2 SGE echoes morphology vs chirp one: LES search performances . . . 84
7.3 Sensitivity of the LES search to echoes . . . 87
7.4 On-Source results . . . 89
7.4.1 On-source p-values . . . 91
7.4.2 Confidence interval on echoe's amplitude . . . 91
7.5 The on-source outliers . . . 92
7.5.1 Case of GW190701 . . . 93
7.5.2 Case of GW200224 . . . 98

8 Morphological characterization of echoes **105**
8.1 Scan of the post-merger window . . . 105
8.2 Results on the signal's amplitude . . . 107
8.3 Results on the arrival time of the signal . . . 109
8.4 Results on the pulses' amplitude damping factor . . . 110
8.5 Frequency of the signal . . . 111

9 Echoes in the literature: searches and models **113**
9.1 Comparison with other echo searches . . . 113
9.2 Echoes templates . . . 117

10 Conclusions **121**
10.1 Lessons learned for further improvements . . . 121
10.2 Remarks on the LIGO-Virgo detector network . . . 122
10.3 Beyond echoes . . . 124

A ECO's models **127**

B CWB LES search parameters **129**

List of Figures

1.1 Illustration of two black holes merging together. In their inspiral motion, they create ripples in spacetime known as gravitational waves. Such ripples can be imagined like waves over the ocean surface. This is a very simplified picture since such waves should be embedded in a three-dimensional space. Credits: [3] 2

1.2 Here the effects of a plane GW are represented. The GW propagates along the z axis with wave vector $\vec{k}$ and hitting a particles ring which lies in the xy-plane (pale blue plane). On the left are shown the effects of a $+$ polarised GW, while on the right are the effects of a $\times$ polarised GW. Each slice is a picture of the particle's ring shape in function of the arrival time t and period P. The solid lines with dark dots represent the motion of the particles ring under the effect of a GW, while the dashed line with white dots shows the initial and static configuration of the system. 6

2.1 The first image of a black hole thanks to Event Horizon Telescope observations of the center of the galaxy M87. The image shows a bright ring formed as light bends in the intense gravity around the black hole. Credits: [20] 13

2.2 The plot on the left (a) shows the effective potential $\tilde{V}^2(\tilde{L}, r)$ for a massive particle coming from infinity toward a BH. Its initial energy is $\tilde{E}^2$, horizontal lines in the plot. The plot on the right (b) displays the same physical scenario for a massless particle where the potential wall is labeled as $B^{-2}(r)$ and the initial energy is replaced with its impact parameter b which can always be represented with a horizontal line in the plane. In both plots on the x-axis is reported the ratio between the radius of the BH and its mass: r/M. Credits to [2], chapter 25. 15

2.3 Here is shown the GW signal emitted during the three phases of a binary system's evolution. On the top of the picture, there is a cartoon that from left to right depicts the evolution stages of a binary system: inspiral, merger, and ring-down, while on the bottom is shown the related GW signal emitted from the binary. This picture refers to the first GW ever detected, GW150914. The red line is the numerical relativity model, while the grey belt the reconstructed template which matches at best the data. Credits from [24] 18

3.1 Wave packet behaviour, generated at the light ring, for both cases of a BH and an ECO as a remnant of a binary coalescence. The black solid line is the system potential $V(x)$ as a function of the tortoise coordinate x, and at x_0 is located the sourface of the ECO. Top panel depicts the BH scenario, where the ingoing radiation is not reflected back. In the bottom panel the remnant is an ECO: the ingoing radiation is reflected towards the potential "wall" creating a cavity. Credits for the figure from [48] 24
3.2 This plot shows the amplitude of a simulated inspiral-merger-ringdown-echoes (IMRE) GW signal as function of time with echoes. In orange and light blue there are the two polarization $h_+, h_\times$ of the wave and the time 0.0 s is the merger time. The following signals (positive times) are the echoes, for whose are enhanched their major parameters $A, \gamma, \Delta t_{echo}$ and t_{echo}. Credits to [56] 26
3.3 Example of a GW signal from a BBH system of $10M_\odot - 10M_\odot$ with eccentricity e equal to 0.0 (black line) and 0.5 (red line). On y-axis there is the amplitude of the signal $h(t)$ while on x-axis the time t in seconds is expressed using as reference time the merger time of the binary. Credits for the figure from [60] 27
3.4 Example of gravitational wave signals with memory. The plot shows the $h(t)_+$ polarization, y-axis, for an equal-mass BBH coalescence with (blue/solid) and without (red/dashed) the nonlinear memory effect as a function of time, x-axis. M is the total mass of the system and R is the distance of the source to the observer. Here geometrized units are used: $G = c = 1$. Credits for the figure from [63] 28
3.5 In the top figure there is a schematic representation of the lensing mechanism. GW radiation emitted from a coalescing COs binary (top left) in its propagation encounter a energy-mass distribution (central point) and undergoes the gravitational lensing effect before reaching the observer (bottom right). Credits to [67] In the bottom plot is plotted as a function of time the GW strain for the original (grey) and lensed (blue) GW signal for a non spinning circular binary with equal masses. Credits to [68] 30
3.6 This figure shows two overlapping signals A and B and the resulting signal (blue). Their merger times are time separated by 1 s. The zero value of the x-axis is set in coincidence with the merger time of the second signal, B. Credits to [71] 32

4.1 Here is represented schematically the set-up of the LIGO interferometers (the picture is not in scale). In the lower left corner there is a small map showing the location of the two detectors **H1** and **L1**. As in Section 1.4 if an incident GW linearly polarised hits the interferometer perpendicularly to the plane defined by the arms then the interferometer's arms are streched by a quantity δL while the other has its length reduced by the same quantity. This picture is taken from [74]. 33

4.2 In this figure are shown the two planes which identify the detector reference frame and the wave reference frame. The detector plane is defined by the two orthogonal arms of the detector, while the wave plane is assumed to be orthogonal to the propagation direction of the wave (for plane waves). The angle θ and ϕ are referred to the detector plane while the Ψ angle defines an arbitrary rotation of the polarization components of the wave inside the wave plane. Credit: [78]. . . . 35
4.3 Ratio between $|F_\times|^2/|F_+|^2$ antenna pattern polarisations. **Top panel**: two aligned detectors' network (L1 and H1). **Bottom panel**: three detector network (L1, H1,and V1). In white are painted and oriented the detectors. Credits [79]. . . . 36
4.4 Amplitude spectral density (y-axis) of the three detectors' strain sensitivity. L1 (5 September 2019 20:53 UTC), H1 (29 April 2019 11:47 UTC), and V1 (10 April 2019 00:34 UTC) as a function of the frequency (x-axis). Credit: [80] . . . 38
4.5 Comparison of the AdV reference sensitivity, $S^{(1/2)}(f)$ (solid black) compared to an AdV noise budget $S_n^{(1/2)}(f)$ (dashed black) as function of the frequency. In the figure are represented the single components of te noise budget such as the quantum noise (violet), radiation pressure noise, seismic noise, and thermal noise. Credit: [82] . . . 39

5.1 GW150914. Comparison between the output time data series from the Livingston (L1) GW detector 5.1a (not whitened), and the same data 5.1a but cleaned. Cleaned data are obtained by the output data that are filtered to remove known noise spectral lines, and whitened. Data are taken from [13]. . . . 44
5.2 Schematic representation of the whitening procedure of the data performed by cWB algorithm. The time-frequency data representation over which the whitening coefficients (RMS) (red line at the bottom) are estimated, is the finest in frequency resolution, so $\Delta f = dF =$ 4 Hz. This holds for this search. . . . 47
5.3 Visual representation of the possible pixels selection rules implemented in cWB algorithm. Each cluster of pixels is a mask, which scans the data evaluating the properties of the pixels and selecting or rejecting the ones which fulfill the thresholds and selection rules. On the y-axis there is the frequency, while on the x-axis the time to mimic a TF map. The single-pixel selection criteria (WP10) is the mask at the bottom left (black), while, immediately on his right in green the chirping-up selection criteria (WP5, in cWB), which is the best suited for CBC burst events detection. . . . 48
5.4 Visual representation of the flowchart of the LES search. Once cWB all-sky burst search detects a CBC event, mainly a BBH signal, then it is possible to run cWB LES search as a follow-up. Once the data set to perform the study is selected, the search runs two parallel studies: the background (BGK) and the signal (SIG) and computes all the statistical estimators described in section 5.3.2. The BBH or primary injections are randomly picked from the PE samples distribution for that event. . . . 51

5.5 Two examples of the injections performed in this analysis. Top: an example of injection for the background (BGK) distribution, only the primary signal (GW150914) is injected. Bottom: an example of injection for the signal (SIG) distribution, the primary (GW150914) plus the echoes mimicker signals are injected. For both scenarios, on the left there is the time representation of the signal, in amplitude, while on the right its TF representation. 53
5.6 Visual representation of the post-merger time-window (PMW), in yellow. The grey area is the blind time t_{blind}. GW event: GW150914. 55

6.1 Here are represented the BGK (left plots) and SIG (right plots) $iSNR$ and $oSNR$ distributions referred to the LES cWB search with standard thresholds, table 6.6. The green distributions are referred to the $iSNR$ while the blue one to $oSNR$. Top row the scenario for $t_{echo} = 0.1\,s$, bottom for $t_{echo} = 0.2\,s$. 62
6.2 In first column shows the reconstructed snr in the inspiral-merger (IM) phase for the primary (blue) and primary + secondary (red) studies. The second column shows the same distributions for but related to the reconstructed snr in the post-merger (PM) phase. The first row is referred to the test with $t_{echo} = 0.1\,s$, while the second row for $t_{echo} = 0.2\,s$. 64
6.3 Here is a comparison of the snr_{rec}^{PM} distribution when no time gap is applied (left plot), and when it is appllyed (right plot) for the cWB configuration: $bpp = 0.001, cc = 0.5, t_{echo} = 0.1\,s$ and $t_{blind} = 40\,ms$. In blue the BGK distribution, while in red the SIG distribution. 67
6.4 Receiver operating curves (ROCs) for the LES cWB search configurations listed in the legend: $WP5$ and $WP10$ with both the bpp values 0.001 and 0.004. On the x-axis, in logarithmic scale the false alarm probability (FAP), while on the y-axis, always in logarithmic scale, the detection efficiency (DE) counterpart. 69
6.5 Comparison between the low energy cWB set-up for $Tgap = 0.2\,s$ (left) and $Tgap = 2\,s$ (right). The thresholds and parameters of the seaches are: $bpp = 0.001$, $netCC = 0.5$, WP10, $t_{gap} = 40\,ms$ and $t_{echo} = 0.1\,s$. Top row: snr_{rec}^{PM} distribution for BGK (blue) and SIG (red) studies. Bottom row: ROC curve with a $cc^{PM} \geq 0.5$ cut, to compare the detection efficiency performances. 70
6.6 Comparison between the low energy cWB set-up for when no post-merger time window (PMW) is applied (left) or when it is applied (right). The thresholds and parameters of the seaches are: $bpp = 0.001$, $cc = 0.5$, WP10, $t_{blind} = 40\,ms$, $Tgap = 2\,s$ and $t_{echo} = 0.1\,s$. Top row: snr_{rec}^{PM} distribution for BGK (blue) and SIG (red) studies. Bottom row: ROC curve with a $cc^{PM} \geq 0.5$ cut, to compare the detection efficiency performances. 71
6.7 Comparison between the low energy search when $t_{echo} = 0.1\,s$ (left column) and 1s (right column) after applying a 1 s time window in the post-merger phase of the signal, with the low threshold configuration developed so far: $bpp = 0.001$, $netCC = 0.5$, $Tgap = 2\,s$, $t_{blind} = 40\,ms$, WP10 as pixels selection rule. Top row the injected (green) and reconstructed (blue) snr inside the time window. Bottom row the BGK (blue)and SIG (red) distributions of snr_{rec}^{PMW}. 72

6.8 Comparison between the low energy search when $t_{echo} = 1$ s without and with the 1 s time window in the post-merger phase of the signal. The window is centred over the injection time of the secondary signal. On the top row the snr_{rec}^{PM} (left) snr_{rec}^{PMW} (right) distributions, while on the bottom row the ROC curves for these two configurations. 74
6.9 Histograms and cumulative distributions (lines and right red y-axis) of the coherent coefficient cc (eq (5.31)) for the full event (green) for the IM phase (blue) and for the PM phase (red). Here the post-merger, PM, is meant as the data segment contained in the post-merger window of 1 s. The left plot is referred to the BGK study, while the right one to the SIG study. 75
6.10 ROC curves for the cWB LES configuration with $bpp = 0.001$, $cc = 0.5$, $Tgap = 2$ s, $t_{blind} = 40$ ms, $WP10$, and the PMW applied. Here are compared the performances of the searching algorithm applying in post-production a cut over the cc^{PM} parameter in order to rule out from the analysis high-confidence noise events. In black the curve without any cut applied, then in the legend the colours' code is explained. 76
6.11 Distribution of ρ^{PM} (y-axis) as a function of cc^{PM} (x-axis) for the BGK (left) and SIG (right) study. We see a bimodal distribution with a clear gap belt between $2 \lesssim \rho^{PM} \lesssim 5$ for the SIG study. 77
6.12 Here are reported the scatter plot of ρ^{PMW} versus cc^{PMW} for the BGK analysis (left) and SIG analysis (right). Top row, the results for the $SUBRHO = 3$. Bottom row, the results for $SUBRHO = 2$ scenario. . . 78
6.13 ROC curves for the cWB LES search for different values of $SUBRHO$ threshold. The top row reports the $SUBRHO = 3$ (left) and $SUBRHO = 2$ (right) curves. On the bottom row the standard case of $SUBRHO = 5$. Studied event: GW150914. 79

7.1 The first row shows the the injected (green) and reconstructed (blue) snr^{PMW} for both the cWB LES search: the high mass BBH signal as echo mimicker (left) and SGE as echo mimicker (right) configuration. The second row shows the cumulative event distribution as function of snr_{rec}^{PMW} for the high mass BBH echo-like signal (left) and SGE one (right). In blue the background distributions (P), in red the signal distribution (P+S). The third row shows the ROC curves for both the previous configurations, high mass BBH echo-like (left) and SGE echo-like (right). Primary event: GW150914. 85
7.2 Detection efficiency as function of snr_{inj}^{PMW}. The study is carried on for two different morphologies of echo's signals: a high mass BBH coalescence (blue), and an elliptically polarised sine-Gaussian train of two pulses (orange). For details see sec. 7.1. 86
7.3 Plot of the detection efficiency as function of the $hrss_{inj}$ of the secondary signal. $hrss_{inj}$ units: $10^{-23} \cdot \sqrt{\text{Hz}}$. We have not reported here all the efficiency curves of the analysed events, but only a small subgroup for each observing run of the LIGO-Virgo-KAGRA collaboration. The $hrss_{inj}$ in the legend corresponds to a detection efficiency of 50% with a FAP of 5%. 87

7.4 Visual display of the ranking statistics of the null hypothesis p-value for the on-source event for each GWs under investigation with their relative uncertainties, blue dots. The **red dashed line** corresponds to a false discovery rate $FDR = 50\%$. The **orange dashed and filled line** highlights the region of the p-value plot in which the false discovery rate (DR) is smaller than 10%. **Violet dots** show the on-source p-value for a complete analysis (BGK, LES, and on-source study) carried on using only the 4096 s around the main BBH event under study. **Green dots** are referred to the on-source p-value for a complete analysis (BGK, LES, and on-source study) carried on over the same standard analysis data but after applying a 32 Hz data mitigation plugin to suppress some noisy data features contaminating the O3a and O3b observational periods. 89
7.5 Confidence belt for the echo's amplitude hrss, $hrss_{inj}$, vs the reconstructed snr snr_{rec}^{PMW} in the PMW for GW150914. The blue region corresponds to 95% coverage. The on-source 95% confidence interval in terms of the $hrss_{inj}$ is set by the intersection between the vertical line at the on source value $snr_{rec}^{ON} \sim 0.37$ (red line) and the blue region. The y-axis are in 10^{-21} per $\sqrt{\text{Hz}}$. 92
7.6 Comparison for the GW event GW190701 between the standard LES search, left column, with the 4096 s LES search on the right column of the figure. In the top row there are reported the snr_{rec}^{PMW} distributions for the P (blue) and P+S (red) studies. The dashed vertical green line marks the on-source snr_{rec}^{PMW} value. In the bottom row there are the ROC curves for the above analysis. 94
7.7 On the left the strain plot of the reconstructed signal strain (units multiplied for 10^{-21}) versus time (in seconds) of GW190701, while the right there is the whitened signal. For each plot the time is given with an offset called GPS OFFSET. 95
7.8 On source reconstruction of the GW190701 event. In the first row are reported the reconstructed TF map for the two detectors of the network, L1 and H1 respectively. The colour legend is on the right of the plots. In the bottom row, from left to right, are reported the network event's likelihood (left plot) and the null energy (right plot). 95
7.9 On source reconstruction of the GW190701 data period (job, in cWB formalism) with the best PE sample of GW190701 subtracted to the data, to cancel the BBH event. In the first row are reported the reconstructed TF map for the two detectors of the network, L1 and H1 respectively. The colour legend is on the right of the plots. In the bottom row, from left to right, are reported the event's network likelihood (left plot) and the null (right plot). 96
7.10 Here on the left is reported the TF map of the reconstructed events in the same cWB job of GW190701 after the subtraction of the GW event. On the right there is the plot showing the likelihood map of the same reconstructed events. 97
7.11 In this figure the snr_{rec}^{PMW} distributions for the P (blue) and P+S (red) studies (plot on the left) and the ROC curves (plot on the right) for the GW event GW190701 mitigated 32 Hz LES search. 98

7.12 Comparison for the GW event GW200224 between the standard LES search, left column, with the 4096 s LES search on the right column of the figure. In the top row there are reported the snr_{rec}^{PMW} distributions for the P (blue) and P+S (red) studies. The dashed vertical green line marks the on-source snr_{rec}^{PMW} value. In the bottom row there are the ROC curves for the above analysis. 99
7.13 On the left the strain plot of the reconstructed signal strain (units multiplied for 10^{-21}) versus time (in seconds) of GW200224, while the right there is the whitened signal. 100
7.14 On source reconstruction of the GW200224 event. In the first row are reported the reconstructed TF map for the two detectors of the network, L1 and H1 respectively. The colour legend is on the right of the plots. In the bottom row, from left to right, are reported the event's likelihood (left plot) and the null (right plot). 101
7.15 On source reconstruction of the GW200224 data period (job, in cWB formalism) with the best PE sample of GW200224 subtracted to the data, to cancel the BBH event. In the first row are reported the reconstructed TF map for the two detectors of the network, L1 and H1 respectively. The colour legend is on the right of the plots. In the bottom row, from left to right, are reported the event's likelihood (left plot) and the null (right plot). 102
7.16 Here on the left the TF map in its best resolution of the reconstructed events in the same cWB job of GW200224 after subtracting the GW event, while on the right there is the plot showing the likelihood map of the same reconstructed events. 103
7.17 In this figure the snr_{rec}^{PMW} distributions for the P (blue) and P+S (red) studies (plot on the left) and the ROC curves (plot on the right) for the GW event GW200224 mitigated 32 Hz LES search. 104

8.1 Examples of the shape of a Blackman-Harris window, in blue. The time width is fixed to 80 ms. On the x-axis there is the time in [ms]. Top row: comparison between the injected amplitude of the Sine-Gaussian pulse (red) and the Blackman-Harris window with different time amplitude τ_W, $\tau_W = 80$ ms(left), and $\tau_W = 20$ ms (right). Bottom row, the same distinction of the top row, but energy an not amplitude is reported on the y-axis. 106
8.2 Here, on the left the injected amplitude A_{inj}^{MW} versus the snr_{inj}^{PMW} for both the BGK (blue) and SIG (red) analysis. On the right the same plot but with the reconstructed amplitude in the MW A_{rec}^{MW} versus snr_{rec}^{PMW}. 107
8.3 On-source instantaneous *snr* profile inside the PMW for GW150914. The red line is referred to L1 detector, while the green to H1. By comparing the amplitude values here to the one in figure 8.2b we can see we are dealing with noise fluctuations, responsible for the oscillatory behavior near times of 0.3 s − 0.6 s. 108
8.4 The plots of the on-source amplitude profile inside the PMW for GW190701 (left) and GW200224 (right). 109

8.5 In this figure, on the left, there is the scatter plot of the A^{MW}_{max1} (red) and A^{MW}_{max2} (blue) reconstructed by the moving windows versus their estimated arrival time t^{MW}_{max1} (red) and t^{MW}_{max2} (blue), respectively. I use as reference time the t_{coa} of the BBH signal. The green star represents the on-source event. The analysis is performed over the LES study to verify if the two clusters around 300 s and 600 s are correctly identified. On the right, the plot is a histogram of the estimated t^{MW}_{max1} (red) and t^{MW}_{max2} (blue). 110
8.6 Both plots report the BGK (blue) and SIG (red) distributions for the γ factor. The line in green is a fit of the SIG distribution in the region $[0.2 - 0.9]$. The values $\gamma \leq 0.2$ are considered not informative for the purpose of the fit. The right plot is obtained by requiring a minimum peak amplitude value, so only the events for which $A^{MW}_{max1} > 0.3$ are selected. 111
8.7 Here there is a histogram of the first energy peak frequency distribution for both the LES study (red) and the BGK one (blue). The vertical green line reports the on-source value. It is possible to see, form the blue distribution that the background does not show any particular shape or trend, while the red one, following the injection. The GW event used as a refernce is: GW150914 112

9.1 Detection efficiency DE (y-axis) versus injected snr (x-axis) for GW150914. The red line is the fit of the data. 114
9.2 Reconstructed amplitude (y-axis) versus injected amplitude (x-axis) for Gaussian noise for single L and H detectors. This figure is taken from [54], FIG. 5. 114
9.3 ROC comparison between cWB LES search (left) and echo template-based search proposed by Rico K. L. Lo, et al. [56] (right). The curves to be "compared" (a fair comparison is not possible since the injections' set is different for the two studies) are the ones referred to O1 data: green for the cWB LES study, orange for Rico K. L. Lo, et al. Moreover, the cWB LES search result is based on GW150914, while Rico K. L. Lo, et al. use templates inspired by GW150914, nevertheless the data sets for both the analysis are from O1 observing run. . . . 115
9.4 In this figure, the y-axis of each plot represents the real part of the GW amplitude of echo signals. The x-axis is the time. Each column of the plots' matrix is referred to a different reflection coefficient value of the final ECO, while each row is related to different δ values. Reference: [49]. 118
9.5 In this figure, the y-axis of each plot represents the real part of the GW amplitude, rind-down + echo, for both the + (blue) and $\times$ (orange) polarisations. The x-axis is the time. Each column of the plots' matrix is referred to different spin values of the final ECO, while each row is related to different R values. Reference: [119]. 119
9.6 The plot shows the energy ratio between the ring-down plus echo signal and ring-down alone as function of the reflectivity of the ECO remnant for different values of spin χ of the final remnant. Reference: [119]. 120

9.7 This plot reports the square of the reflectivity absolute value as a finction of the ring-down snr, $\rho_{ringdown}$. The vertical bands represents the predicted typical values of $\rho_{ringdown}$ for aLIGO/Virgo, 3G detectors, and LISA. The remnant is assumed to possess a spin equal to 0.7. Reference: [119]. 120

10.1 Sensitivity for the best BNS range [120] for the three detectors' network: L1, H1, and V1. The data are taken from [121] and relative to the observing day: 2020, February 10th. 123
10.2 Amplitude spectral density for the three detectors' network: L1, H1, and V1. The data are taken from [121] and relative to the observing day: 2020, February 10th. 123
10.3 Detection efficiency as function of snr_{inj}^{PMW}. The study is carried on for different morphologies of echo's signals: a high mass BBH coalescence (blue), elliptically polarised sine-Gaussian trains of two pulses with different central frequencies $f_0 = 80, 140, 200, 400$Hz (orange, green, red, and violet respectively). 124

A.1 Illustrative example of a wormhole. Reference: [45]. 128

List of Tables

5.1 This table lists from left to right: the observing run, The GW event's name, the waveform model used to generate its CBC PE samples, its coalescence GPS time, the network signal to noise ratio (snr_{net}) of the event, the final mass of the object and its luminosity distance from the observer. These events are the GW signals detected by cWB whose $snr_{net} \geq 10$, and they are analysed in this work. 57

5.2 In this table are listed from left to right: the GW event's name, the expected Δt_{echo}, whose value can be compatible also with the one expected for t_{echo}, for different ECO models n. The Δt_{echo} was performed through equation (3.4). Moreover, the final cWB LES search configuration requires $Tgap = 2\,\mathrm{s}$ and $Fgap = 128\,\mathrm{Hz}$, thus each Δt_{echo} is well contained by $Tgap$, see section 6.6. 59

6.1 In this table are listed the values of the production thresholds (see sec. 5.2.4) for the cWB all-sky O3 search. In the first row are listed the names of the parameters. bpp is the black pixels probability, cc the network coherent coefficient, ρ the effective network coherent snr, $subnet$ the subnetwork energy asymmetry statistic, $Acore$ the pixel average amplitude, $SUBRHO$ and $SUBNET$ are the internal cut-off on ρ and $subnet$, $Tgap$ and $Fgap$ the maximum time and frequency gap between subsequent pixels' clusters respectively. In the second row are reported their values. Fore more details see appendix B. 61

6.2 This table reports the values of the reconstructed snr for the primary (P) (third and sixth column) and primary + secondary (P+S) (fourth and seventh column) analysis while varing the bpp and cc cWB thresholds (first column). These comparison is carried on for two physical conditions, when $t_{echo} = 0.1\,\mathrm{s}$ and $t_{echo} = 0.2\,\mathrm{s}$. 63

6.3 Here there is a comparison between the reconstructed snr in the inspiral-merger phase (IM) and post-merger (PM) one, for both the primary (P) and primary + secondary (P+S) studies. These comparisons are performed over the two values of t_{echo}: $[0.1, 0.2]$s under study here in section 6.1. 63

6.4 In this table are listed the values of the reconstructed snr in the post-merger (PM) phase for each values of the blind time t_{blind} between the coalescence time and the starting time of the PM phase. The studies are performed over the two LES configurations of cWB $bpp = 0.001$ and $bpp = 0.004$, both having $cc = 0.5$. 66

6.5 This table reports the reconstructed *snr* before (IM) and after (PM) the coalescence time for two different pixels selection criteria, single pixel selection (WP10 in cWB) and chirping-up pixel selection (WP5 in cWB). WP10 is used in typical all-sky burst searches beeing the best unmodelled pixels selection criteria, while WP5 is more suitable for CBC searces. These studies are performed for both the t_{echo} configurations studied so far. 68
6.6 In this table are compared the values of cWB production thresholds. In the first column are listed the cWB parameters, in the second and third columns are reported their values for the standard search (O3 all-sky burst search) and the LES search respectively. Only ρ, $Tgap$, and $SUNRHO$ thresholds are different from one search to the other, having their values decreased for the current search in order to allow cWB pipeline to collect more energy without compromising its detection capabilities. The Δt_{PMW} labels the time width of the post-merger window. 82

7.1 The table lists the values of injected hrss needed to have a detection efficiency of 50% requiring a false alarm probability of the 5% for each gravitational wave events analysed in this study. 88
7.2 The table lists for all the analysed GW events their relative on-source p-value, p-value$_{\mathrm{ON}}$ (third column), and on-source reconstructed *snr* inside the post-merger window (PMW), snr_{rec}^{ON} (fourth column). When, for snr_{rec}^{ON} is reported ≥ 0 it means that the reconstructed signal to noise ratio is so small that its estimate is meaningfull, having *snr* values smaller than the per thousands. 90

B.1 In this table are listed the names (first column), the threshold values (second column) of the cWB production parameters as well as their physical meaning (third column). This table is meant as an operative summary of the parameters introduced and defined in chapter ch. 5, section sec. 5.2.4. 129

List of Abbreviations

BBH	Binary black hole
BH	Black hole
BHNS	Black hole - neutron star
BGK	Background
BNS	Binary neutron star
CBC	Compact binary coalescence
CO	Compact object
cWB	coherent WaveBurst
ECO	Exotic compact object
FT	Fourier transform
GR	General relativity
GW	Gravitational wave
IM	Inspiral-merger
IMR	Inspiral-merger-ringdown
IMRE	Inspiral-merger-ringdown-echoes
ISCO	Innermost stable circular orbit
LES	Low energy signal
MW	Moving window
NS	Neutron star
PM	Post-merger
PMW	Post-merger window
PN	Post newtonian
QNM	Quasi-normal mode
ROC	Receiver operating curve
SIG	Signal
SQL	Standard quantum limit
TT	Transverse traceless

List of Symbols

P	power	W ($\mathrm{J\,s^{-1}}$)
c	speed of light in vacuum	$\sim 3 \times 10^8\,\mathrm{m\,s^{-1}}$
G	gravitational constant	$\sim 6.67 \times 10^{-11}\,\mathrm{N\,m^2\,kg^{-2}}$
h_p	Planck length	$\sim 6.63 \times 10^{-34}\,\mathrm{J\,s^{-1}}$
$M_\odot$	Solar mass	$\sim 2 \times 10^3\,\mathrm{kg}$
μ	reduced mass	kg
ω	angular frequency	rad
ν or f	frequency	Hz
λ	wavelength	m
∇	Nabla	
$\Box$	d'Alembertian $\Box = \left(-\frac{1}{c^2}\frac{\partial^2}{\partial t^2} + \nabla^2\right)$	
∂	partial derivative	
$\otimes$	tensor product	
$\Re$	real part	
$\Im$	immaginary part	
$g_{\mu\nu}$	space time metric	
$\eta_{\mu\nu}$	Minkowski metric	
$G_{\mu\nu}$	Einstein tensor	
$R^{\alpha}_{\mu\beta\nu}$	Riemann tensor	
$R_{\mu\nu}$	Ricci tensor	
R_{sh} or r_{sh}	Schwartzshild radius	
$i, j, k, ... \in \{1, 2, 3, ...\}$	latin letters	
$\alpha, \beta, \gamma, ... \in \{0, 1, 2, 3, ...\}$	greek letters	

Dedicated to Matilde.
Half of this "binary black hole system"

Chapter 1

Gravitational waves in a nutshell

The detection of gravitational waves (GWs) is a successful test of one major prediction of Albert Einstein's 1915 general theory of relativity. In sight of this, in this chapter, a little overview of the derivation of gravitational waves from the Einstein field equations will be given, as well as the mathematical description and physical interpretation of such physical phenomena. There will also be a brief overview of the main properties of gravitational waves since currently they are the cornerstone to probe the validity of the general relativity theory.

1.1 Einstein field equation

In order to speak about GWs one cannot avoid passing through the Einstein field equations, [1] one of the greatest achievements of the general relativity (GR) theory, whose equations are [1]:

$$G_{\mu\nu} = \frac{8\pi G}{c^4} T_{\mu\nu}\,, \tag{1.1}$$

where $G_{\mu\nu}$ is the Einstein tensor ($\mu, \nu \in \{0,1,2,3\}$), G is the gravitational constant, c is the speed of light in vacuum, and $T_{\mu\nu}$ is the energy-momentum tensor of matter. It is worth to remember some definitions starting with the Einstein tensor $G_{\mu\nu}$:

$$G_{\mu\nu} = R_{\mu\nu} - \frac{1}{2} g_{\mu\nu} R\,, \tag{1.2}$$

where $R = g^{\mu\nu} R_{\mu\nu}$ is the Ricci scalar, $g_{\mu\nu}$ is the metric tensor of the space-time, and $R_{\mu\nu}$ is the Ricci tensor, which is defined as the trace of the Riemann tensor: $R_{\mu\nu} = R^{\alpha}_{\mu\alpha\nu}$. The Riemann tensor express the curvature of a generic Riemann manifold and it is defined as [2]:

$$R^{\alpha}_{\mu\beta\nu} = \partial_\beta \Gamma^{\alpha}_{\mu\nu} - \partial_\nu \Gamma^{\alpha}_{\mu\beta} + \Gamma^{\alpha}_{\rho\beta} \Gamma^{\rho}_{\mu\nu} - \Gamma^{\alpha}_{\rho\nu} \Gamma^{\rho}_{\mu\beta}\,, \tag{1.3}$$

where $\Gamma^{\rho}_{\mu\nu}$ is the Christoffel symbol which can be written through the metric tensor as

$$\Gamma^{\rho}_{\mu\nu} = \frac{1}{2} g^{\rho\gamma} \left(\partial_\mu g_{\nu\gamma} + \partial_\nu g_{\gamma\mu} - \partial_\gamma g_{\mu\nu} \right)\,. \tag{1.4}$$

After all these definitions if we look at eq.(1.1), we can realise that the Einstein tensor carries the information of the space-time curvature. Indeed, $G_{\mu\nu}$ is related with the Riemann tensor eq.(1.3) through eq.(1.2), and the Riemann tensor expresses the curvature of a manifold, so its geometry. In light of this, eq.(1.1) states that

[1] Section 1.1 is based on [1]. If equations are taken from other textbooks or papers it will be reported, otherwise, it means the formula is taken from [1].

it is possible to know the geometry of the space-time ($g_{\mu\nu}$) knowing the energy-momentum tensor of the system, so its energy and momentum distribution. Furthermore, $G_{\mu\nu}$ involves second derivatives of the metric tensor $g_{\mu\nu}$ and this sounds like something related to the force concept, which in turn defines the motion of an object. Einstein field's equations provide a set of differential equations for the metric tensor components $g_{\mu\nu}$.

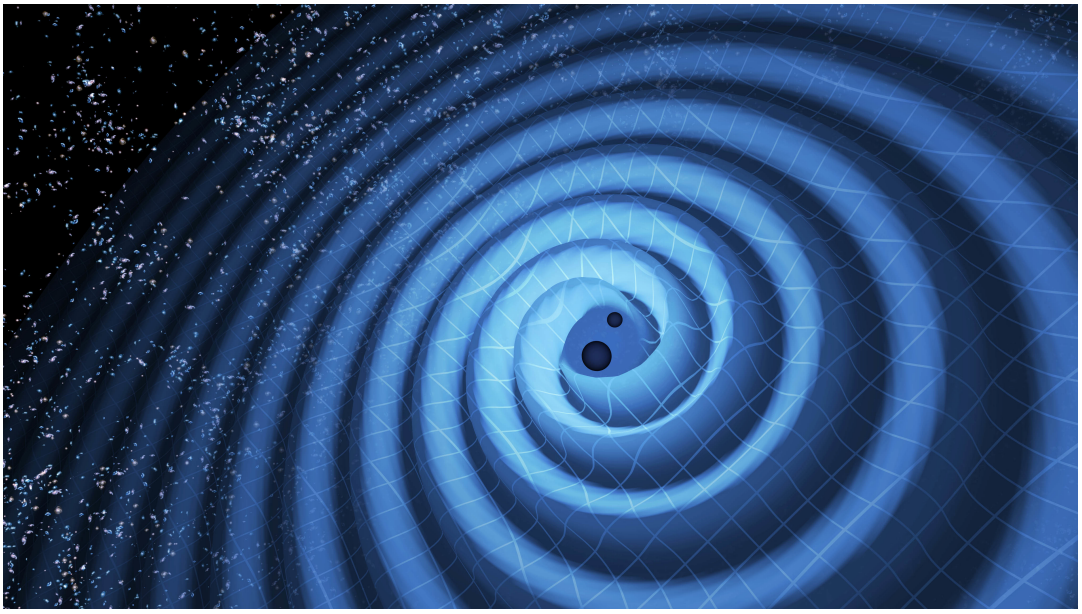

Figure 1.1: Illustration of two black holes merging together. In their inspiral motion, they create ripples in spacetime known as gravitational waves. Such ripples can be imagined like waves over the ocean surface. This is a very simplified picture since such waves should be embedded in a three-dimensional space. Credits: [3]

1.2 Road map to GWs equation

To derive the equation of gravitational waves it is necessary to make some considerations: first of all, what are gravitational waves? They can be thought of as perturbations of space-time. In a naive picture, if the space-time is compared to an ocean, then gravitational waves are water waves, small ripples rolling across the ocean, figure 1.1. This kind of mental representation of GWs carries an assumption that is perfectly suited for this study: it implies that GWs are perturbations propagating through a flat space-time, a Minkowski space-time usually labeled with the metric tensor $\eta_{\mu\nu}$ defined as:

$$\eta_{\mu\nu} = \begin{pmatrix} -1 & 0 & 0 & 0 \\ 0 & 1 & 0 & 0 \\ 0 & 0 & 1 & 0 \\ 0 & 0 & 0 & 1 \end{pmatrix} . \tag{1.5}$$

Such kind of assumption lays at the base of the linearised theory of gravity, which is a weak field approximation of general relativity where Einstein field equation is written and solved assuming a flat space-time. Then, the metric tensor $g_{\mu\nu}$ (the overall ocean) can be written as:

$$g_{\mu\nu} = \eta_{\mu\nu} + h_{\mu\nu} , \quad |h_{\mu\nu}| \ll 1 \tag{1.6}$$

where $h_{\mu\nu}$ is our perturbation of the flat Minkowski metric $\eta_{\mu\nu}$ [4] so, in our example, the water ripples and the static part of the ocean respectively. Here, eq.(1.6), $h_{\mu\nu}$ is a symmetric second rank tensor field where the condition $|h_{\mu\nu}| \ll 1$ represents the weak field request, so one can expand the metric tensor in powers of $h_{\mu\nu}$ using a coordinate frame in which $|h_{\mu\nu}| \ll 1$ holds and keep only the linear terms. An idea of how the linearisation process works can be obtained by looking at the Christoffel symbol which in the weak field approximation has the form:

$$\Gamma^{\rho}_{\mu\nu} = \frac{1}{2}\eta^{\rho\gamma}\left(\partial_{\mu}h_{\nu\gamma} + \partial_{\nu}h_{\gamma\mu} - \partial_{\gamma}h_{\mu\nu}\right) , \tag{1.7}$$

the static part vanishes since the derivative of a constant value is null and the second-order part in $h_{\mu\nu}$ is negligible with respect to first-order effects. Now with some straightforward but endless calculations, starting from Einstein field equations, it is possible to redefine the field metric $h_{\mu\nu}$

$$h_{\mu\nu} \longrightarrow \bar{h}_{\mu\nu} = h_{\mu\nu} - \frac{1}{2}\eta_{\mu\nu}h \quad \text{with} \quad h \equiv \eta^{\mu\nu}h_{\mu\nu} \tag{1.8}$$

similarly to what was done with the Einstein tensor, eq.(1.2). Then, in analogy to the electromagnetic theory, it is possible to choose the *Lorenz gauge* (also called *de Donder gauge* or *harmonic gauge*) in order to reduce the degree of freedom of the system having that $\bar{h}_{\mu\nu}$ must satisfy the condition [2]

$$\partial_{\alpha}\bar{h}^{\mu\nu} = 0 . \tag{1.9}$$

This gauge, or coordinate choice, means that it is possible to recover another solution to Einstein field equations, different from $\bar{h}_{\mu\nu}$ for a given $T_{\mu\nu}$, that describes the same physical situation but changing the reference frame by some ε^{μ} ($x^{\mu} \longrightarrow x^{\mu} + \varepsilon^{\mu}$), an arbitrary small function. This is a consequence of the invariance under infinitesimal and local transformations of coordinates of the linearised theory of general relativity. [3] Now, putting together eq.(1.6) and eq.(1.8), in the weak field approximation the Einstein field equations assume the following form:

$$\Box\bar{h}_{\mu\nu} = -\frac{16\pi G}{c^4}T_{\mu\nu} \tag{1.10}$$

where $\Box$ is the d'Alembert operator or d'Alembertian: $\Box = \left(-\frac{1}{c^2}\frac{\partial^2}{\partial t^2} + \nabla^2\right)$. Eq.(1.10) describes the generation of GWs by a source with an energy-momentum tensor $T_{\mu\nu}$.

The assumption $|h_{\mu\nu}| \ll 1$ means that one is choosing a reference frame in which eq.(1.6) holds on a sufficiently large region of the space-time such that the GWs can be seen as small perturbation. Then, at the same time, the space-time region is small enough to allow to neglect the intrinsic curvature of the space-time. It is like a sailor, standing on a boat, can neglect the effect due to the large curvature of the sea surface and pretend that waves are spreading on a flat surface [1, 2].

[2] Indices are rised or lowered thanks to $\eta_{\mu\nu}$ and because we are working in the weak field approximation [2].

[3] A detailed explanation can be found in [1, chapter 1, section 1.1] and it is not reported here because it goes beyond the purposes of this dissertation.

1.3 The transverse traceless gauge

It is possible to solve eq.(1.10) imposing $T_{\mu\nu} = 0$, having:

$$\Box \bar{h}_{\mu\nu} = 0\,. \tag{1.11}$$

Physically it means that the wave propagation is studied outside the source, in the vacuum. Notice that eq.(1.11) has the same form of the waves equation for electromagnetic radiation in the vacuum, suggesting that gravitational waves should propagate in space-time with the speed of light [5].

Eq.(1.11) has six degrees of freedom out of the initial ten thanks to the *Lorenz gauge* choice, but it is possible to impose another condition on the ε^μ function, requiring that

$$\Box \varepsilon^\mu = 0\,. \tag{1.12}$$

Such coordinate choice is called *transverse traceless gauge*, usually shortened as *TT-gauge*, and allows to further reduce the degrees of freedom of the system, being left with only two independent components for $\bar{h}_{\mu\nu}$. The metric tensor under such gauge is written as $\bar{h}^{TT}_{\mu\nu}$ and *Lorenz gauge* plus *TT-gauge* can be summarized through the following equations [1]:

$$\bar{h}_{0\nu} = 0\,; \qquad \bar{h}^{\,i}{}_{i} = 0\,; \qquad \partial_i \bar{h}^{ij} = 0 \tag{1.13}$$

where indices i and $j \in \{1,2,3\}$.

Physically, in the reference frame in which the TT-gauge holds, free test particles at rest before the GW passage stay at rest even after the arrival of the wave: their position does not change [1] because the coordinates of the reference frame (in which TT-gauge holds) are stretched themselves during the GW passage. As a consequence, the effects of a GW passage cannot be studied by looking at the variation of the coordinates but can be detected by looking at how the system's proper distances vary when the wave passes.

1.4 Plane and stationary GWs

Now that eq.(1.11) is in our hand we can solve it: its solutions are monochromatic plane waves: [2]

$$h^{TT}_{\mu\nu}(x) = \Re\left(A^{TT}_{\mu\nu}\, e^{ik_\alpha x^\alpha}\right) \tag{1.14}$$

where we have used $h^{TT}_{\mu\nu}$ and not $\bar{h}^{TT}_{\mu\nu}$ because in *TT-gauge* $\bar{h}$ and h are the same. $\Re(\dots)$ denotes the real part of the expression, $k^\alpha = (\frac{\omega}{c}, \vec{k})$ is the four-dimensional wave vector, ω is the wave angular frequency and $\vec{k}$ is the usual wave vector. Then $x^\alpha = (ct, \vec{x})$ is the four-dimensional coordinate vector, and $A^{TT}_{\mu\nu}$ is the wave amplitute tensor. $A^{TT}_{\mu\nu}$ and k_α satisfied the conditions [2]:

$$A^{TT}_{\mu\nu} k^\nu = 0 \qquad \text{and} \qquad k_\alpha k^\alpha = 0\,. \tag{1.15}$$

We can set the propagation direction of the wave along the z component such that [1]: [4]

$$h_{\mu\nu}(t,z) = \begin{pmatrix} 0 & 0 & 0 & 0 \\ 0 & A_+ & A_\times & 0 \\ 0 & A_\times & -A_+ & 0 \\ 0 & 0 & 0 & 0 \end{pmatrix}_{\mu\nu} e^{i\omega(t-z/c)} \tag{1.16}$$

where A_+ and $A_\times$ are respectively the so-called amplitude of the "plus" $(+)$ and "cross" $(\times)$ polarization of the wave, the two degrees of freedom of the equations that were left. Thanks to eq.(1.15) and eq.(1.16) we can see that the non zero components of the polarization tensor lies in the plane orthogonal to the direction of propagation of the wave which versor is $\hat{n} = \frac{\vec{k}}{|\vec{k}|}$.

We have seen in Section 1.3 that effects of a GW transit can be detected by looking at the proper distances, i.e. studying the interval ds^2 (the invariant elements under coordinates transformations) between two points P_1 and P_2. [5] To carry on such analysis it is convenient to rewrite the components of a GW like:

$$h_{xx} = -h_{yy} = \Re\left(A_+ e^{i\omega(t-z/c)}\right), \tag{1.17}$$

$$h_{xy} = h_{yx} = \Re\left(A_\times e^{i\omega(t-z/c)}\right) \tag{1.18}$$

which suggests to define two polarization tensor $\hat{e}_+$ and $\hat{e}_\times$ defined as:

$$\hat{e}_+ := \hat{e}_x \otimes \hat{e}_x - \hat{e}_y \otimes \hat{e}_y \tag{1.19}$$

$$\hat{e}_\times := \hat{e}_x \otimes \hat{e}_y + \hat{e}_y \otimes \hat{e}_x \tag{1.20}$$

where $\hat{e}_x$ and $\hat{e}_y$ are the xy-plane versors. In this way it is possible to express eq.(1.16) as

$$h = h_+ \hat{e}_+ + h_\times \hat{e}_\times \,. \tag{1.21}$$

Now, thanks to the simple expression for a polarised GW of eq.(1.21) we know that the proper bistance ds^2 takes the form

$$ds^2 = -c^2dt^2 + [1+h_+]\,dx^2 + [1-h_+]\,dy^2 + 2h_\times dxdy + dz^2 \tag{1.22}$$

for a GW having the same properties as the one in eq.(1.16). Analysing the scenario in which $h_\times = 0$, the ds^2 becomes:

$$ds^2 = -c^2dt^2 + [1+h_+]\,dx^2 + [1-h_+]\,dy^2 \tag{1.23}$$

so, when the wave hits the particles system, if $P_1 = (-ct, x_0, y_0, 0)$ and $P_2 = (-ct, x_0 + dx, y_0, 0)$ (two neighbouring particles) the proper distance between P_1 and P_2 is

$$ds^2 = [1+h_+]\,dx^2\,. \tag{1.24}$$

If, at first, $h_+ > 0$ the proper distance between the two particles increases, on the contrary, when $h_+ < 0$ the proper distance gets smaller. The opposite happens considering the particles with coordinate: $P_1 = (-ct, x_0, y_0, 0)$ and $P_2 = (-ct, x_0, y_0 + dy, 0)$.

[4] From now till the end of this Section 1.4 I omitt the superscript TT when referring to the metric tensor $h_{\mu\nu}(x)$.

[5] From here till the end of Section 1.4 the reference text book is [5].

In this situation the ds^2 will be:

$$ds^2 = [1 - h_+]\, dy^2\,, \tag{1.25}$$

and when $h_+ > 0$ the distance decreases while for $h_+ < 0$ the distance increases. Thanks to this simplified description, when an incident plane GW (lying in the xy-plane and propagating along the z axis) hits a ring of dust particles (in the xy-plane as well), it distorts the particles ring into a pulsating ellipse whose major axis is in turn parallel to the x and y axis, as it is shown in Figure 1.2.

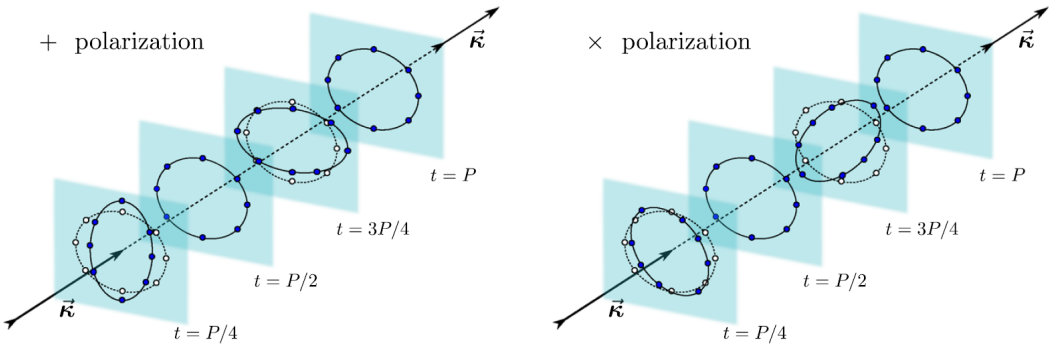

Figure 1.2: Here the effects of a plane GW are represented. The GW propagates along the z axis with wave vector $\vec{k}$ and hitting a particles ring which lies in the xy-plane (pale blue plane). On the left are shown the effects of a $+$ polarised GW, while on the right are the effects of a $\times$ polarised GW. Each slice is a picture of the particle's ring shape in function of the arrival time t and period P. The solid lines with dark dots represent the motion of the particles ring under the effect of a GW, while the dashed line with white dots shows the initial and static configuration of the system.

What we have seen just now are the effects of a $+$ polarised GW. However, it must be clear that an incoming wave possesses, at the same time, both polarizations: the plus and the cross one, and a general wave will be a superposition of these two states [5]. The cross-polarization produces the same effects as the plus one, the only difference is that its axes are rotated by 45 ° with respect to the ones of the plus polarisation, as shown in Figure 1.2. This is a difference with respect to the electromagnetic case. The GW polarisation states are at 45 ° one respect to the other, while electromagnetic ones are at 90 °. This implies that GW's polarizations are invariant under rotations of 180 ° along its direction of propagation while electromagnetic waves's polarizations are invariant under rotations of 360 °.

Plane GWs provide a simplified picture still encoding precious information on the phenomenon.

1.5 Generation of GWs

Now we can go a bit further and try to overview how GWs are generated, so what is the source of the metric perturbation $h_{\mu\nu}$, and how they propagate through the space. Since these two aspects, generation and propagation of GWs, are not easy to deal with, we will treat them separately. [6]

At first, we need to introduce and define the following quantities:

- r, radial distance;

[6] For this section, the reference book is [6].

- r_i, radial coordinate called *inner radius*;
- r_o, radial coordinate called *outer radius*;
- L, the size of the source;
- λ, the GW wavelength;
- $r_{sh} = 2GM/c^2$, is the Schwarzschild radius.

Then, we have to define some of these newly defined lengthscales:

- $r \gg L$;
- $r_i \gg \lambda/2\pi$. This condition defines a distance far enough from the source such that its gravitational field can be considered weak, meaning also $r_i \gg r_{sh}$
- $r_o - r_i \gg \lambda/2\pi$, defining a region of space-time in which there should be lots of GWs ripples [7]. At the same time, the outer radius must not be so far from the source till the point the background curvature of the space-time affects significantly the wave propagation: $r_o - r_i \ll R_B \equiv \mid R^B_{\alpha\beta\gamma\delta} \mid^{-\frac{1}{2}}$ [6].

With these distance references, it is possible to divide the space around the GWs source into three parts, this distinction will allow us to treat separately the problems of generation and propagation of GWs [6]:

1. First region: it is called the *wave generation region* and is the portion of space-time fulfilling the condition $r \lesssim r_i$.
2. Second region: it is called the *local wave zone* and its limits are $r_i \lesssim r \lesssim r_o$.
3. Third region: it is called the *distant wave zone* and is the portion of the space-time fulfilling the condition $r \gtrsim r_o$.

The theory of wave generation can be developed inside the first and second regions while the theory of wave propagation can be developed inside the second and third regions. In this way the two theories have to match up in the overlapping region: the second zone. Moreover, in the local wave zone, this choice allows to ignore the curvature of the space-time and treat it like a Minkowski manifold, thus performing all the analysis concerning GWs using the linearized general relativity theory which is easier than the general relativity one.

Among all the techniques for computing the equation for the GWs generation, the *quadrupole formalism* is especially important since it is highly accurate and reliable in predicting the order of magnitude for the amplitude of the waves for most of the sources [6]. To apply the quadrupole formalism the assumption of slow-motion of the source is needed: more precisely it is required that the source size L has to be small if compared to the GW reduced wavelength $\lambda \equiv \lambda/2\pi$. Then, the GW field in the source local wave zone is [1]:

$$h^{TT}_{ij}(t, \vec{x}) = \frac{1}{r}\frac{2G}{c^4}\frac{\partial^2}{\partial t^2} Q^{TT}_{ij}(t - r/c) \tag{1.26}$$

[7] This concept will be explained in a more detailed way in Section 1.6

where[8] t is the proper time measured by an observer in a reference frame at rest with respect to the source, $t - r/c$ is the retarded time and Q_{ij}^{TT} is the quadrupole moment defined as [1]:

$$Q_{ij}^{TT} = \int \rho(t, \vec{x}) \left(x_i x_j - \frac{1}{3}\delta_{ij} r^2 \right) d^3x \,. \tag{1.27}$$

Here ρ is the source mass density corresponding to $\rho = \frac{T_{00}}{c^2}$. Usually $\frac{T_{00}}{c^2}$ takes into account not only the rest mass density but also the kinetic energy of the particles composing the source as well as potential energy and so on, but in the weak field approximation and non-relativistic sources $\frac{T_{00}}{c^2}$ represents the rest mass density [1].

1.6 Propagation and energy-momentum tensor of GWs

Concerning the problem of GWs propagation, we know that once GWs are completely formed it is not important how massive or energetic their source was [6]. Inside the local wave zone the amplitude of a GW will be negligible with respect to the reference unity, fulfilling the condition $|h_{\mu\nu}| \ll 1$. Under this hypothesis we know that GWs can be described through the linearised theory of general relativity, meaning that eq.(1.6) can be used allowing the derivation of the GW equation (eq.(1.11)) as well as its plane wave solution eq.(1.14). Nevertheless, the weak field approximation leads us to lose one important aspect of GWs: they carry energy and momentum, so they can be described through an energy-momentum tensor which does not stand out from the picture we have done so far.

To derive the energy momentum tensor of a GW we need to leave for a moment the comfortable weak energy approximation and describe the space-time metric as [1]

$$g_{\mu\nu}(x) = \bar{g}_{\mu\nu}^{(B)}(x) + h_{\mu\nu}(x) \,, \qquad |h_{\mu\nu}| \ll 1 \,. \tag{1.28}$$

Such metric has not the form of a flat one ($\eta_{\mu\nu}$) on which we add a perturbation ($h_{\mu\nu}$), but it is composed of a curved background metric $\bar{g}_{\mu\nu}^{(B)}$ plus a perturbation. It is a consequence of the Einstein field equations: they are non-linear differential equations and a GW is itself a distribution of energy and momentum which contributes in varying its own gravitational field [4], which means that we should look at GWs as perturbations over a dynamical and curved background, $\bar{g}_{\mu\nu}^{(B)}$. We can rewrite the Einstein equations eq.(1.1) as [1]:

$$R_{\mu\nu} = \frac{8\pi G}{c^4} \left(T_{\mu\nu} + \frac{1}{2} g_{\mu\nu} T \right) \,, \tag{1.29}$$

where T is the trace of the energy-momentum tensor of matter. Then, expanding in power series of $h_{\mu\nu}$ the Ricci tensor $R_{\mu\nu}$:

$$R_{\mu\nu} = \bar{R}_{\mu\nu}^{(B)} + R_{\mu\nu}^{(1)} + R_{\mu\nu}^{(2)} + \cdots \tag{1.30}$$

where $\bar{R}_{\mu\nu}^{(B)}$ is evaluated for $\bar{g}_{\mu\nu}^{(B)}$ only, $R_{\mu\nu}^{(1)}$ is linear in $h_{\mu\nu}$ and $R_{\mu\nu}^{(2)}$ is quadratic in $h_{\mu\nu}$. Through lots of mathematical passages, [9] it is possible to have the Einstein field

[8] Here $h_{\mu\nu}^{TT}$ has only the spatial indices since in the TT-gauge the time component of the metric are equal to zero.

[9] The full demonstration is carried on in [1, chapter 1, section 1.4]

equations in the form

$$\bar{G}^{(B)}_{\mu\nu} = \bar{R}^{(B)}_{\mu\nu} - \frac{1}{2}\bar{g}^{(B)}_{\mu\nu}\bar{R}^{(B)} = \frac{8\pi G}{c^4}\left(\bar{T}^{(B)}_{\mu\nu} + T^{(GW)}_{\mu\nu}\right) . \tag{1.31}$$

In eq.(1.31) we have defined the following quantities: the GW energy-momentum tensor, $T^{(GW)}_{\mu\nu}$, and the effective energy-momentum tensor of matter $\bar{T}^{(B)}_{\mu\nu}$ [1]:

- energy-momentum of gravitational wave:

$$T^{(GW)}_{\mu\nu} = -\frac{c^4}{8\pi G}\langle R^{(2)}_{\mu\nu} - \frac{1}{2}\bar{g}_{\mu\nu}R^{(2)}\rangle ; \tag{1.32}$$

- energy-momentum of matter $\bar{T}^{(B)}_{\mu\nu}$ for which:

$$\langle T^{(B)}_{\mu\nu} - \frac{1}{2}g_{\mu\nu}T^{(B)}\rangle = \bar{T}^{(B)}_{\mu\nu} - \frac{1}{2}\bar{g}^{(B)}_{\mu\nu}\bar{T}^{(B)} . \tag{1.33}$$

Eq.(1.32) is what we are searching: it strictly depends on $h_{\mu\nu}$ and it is recovered inside the general relativity theory and not in the linearised one. In both eq.(1.31) and eq.(1.32) the $\langle\cdots\rangle$ is the space average over many reduced wavelengths $\lambda\!\!\!^{-} \equiv \lambda/2\pi$ or over several periods $1/f_B$ of the wave. It is worth to notice that inside this picture the geometry of the background ($\bar{g}^{(B)}_{\mu\nu}$) is modelled not only by the energy-momentum distribution of matter but also by the effect of the energy-momentum carried by GWs which, now, are treated as sources of the curvature and do not stand out in the "geometrical" part of Einstein field equations, Eq(1.29).

The fundamental assumption of all this discussion rests on the spatial variation of the $\bar{g}^{(B)}_{\mu\nu}$ metric, L_B, which has to be higher than the wavelength of the gravitational radiation, λ [1]:

$$\frac{\lambda}{2\pi} \ll L_B . \tag{1.34}$$

This conditions, if transposed in the frequency domain as:

$$f \gg f_B \quad \text{where} \quad f \equiv \frac{1}{\lambda} , \, f_B \equiv \frac{1}{L_B} \tag{1.35}$$

means that there is a clear separation in scale between the background and the perturbation. If this separation exists then it is possible to speak about perturbation over a curved space, otherwise, if scales are similar it is impossible to distinguish a GW from the background, having that the concept of wave gets lost [1, 4].

With the equation of the energy-momentum tensor of a GW, eq.(1.32), it is possible to study the energy possessed by a GW under the assumptions of the linearised theory of general relativity, obtaining [1, 2]:

$$T^{(GW)}_{\mu\nu} = \frac{c^4}{32\pi G}\langle \partial_\mu h_{\alpha\beta}\partial_\nu h^{\alpha\beta}\rangle . \tag{1.36}$$

Such passage can be done because we use a general result from the general relativity theory (as long as the condition $\frac{\lambda}{2\pi} \ll L_B$ holds) and we study it inside a specific physical system satisfing the weak field approximation and with a coordinates reference frame in which Lorenz gauge and TT-gauge hold. At this point, from eq.(1.36)

is possible to recover the expression for the energy density carried on by a GW [1]

$$T^{00}_{(GW)} = \frac{c^2}{16\pi G}\langle \dot{h}_+^2 + \dot{h}_\times^2 \rangle \,, \tag{1.37}$$

and we can see that $T^{00}_{(GW)}$ depends on the square of the two time-derivatives of the polarisation amplitudes: $\dot{h}_+$ and $\dot{h}_\times$.

1.7 Energy and momentum flux of GWs

Since we have in our hand the expression for the energy-momentum tensor of GWs we can make the last effort and derive the energy flux and the momentum flux of GWs. The starting point is the conservation law of the energy-momentum tensor [1]:

$$\partial_\mu T^{\mu\nu}_{(GW)} = 0 \tag{1.38}$$

and then, with some straightforward calculations it is possible to recover both the energy flux of a GW (the amount of energy per units of area and time):

$$\frac{dE}{dAdt} = \frac{c^3}{32\pi G}\langle \dot{h}^{TT}_{ij}\dot{h}^{TT}_{ij} \rangle \,, \tag{1.39}$$

as well as the momentum of a GW (the amount of momentum (dP) per units of area and time):

$$\frac{dP^k}{dAdt} = -\frac{c^3}{32\pi G}\langle \dot{h}^{TT}_{ij}\partial^k h^{TT}_{ij} \rangle \,. \tag{1.40}$$

To have an idea about the amount of energy that a GW carries it is useful to analyse eq.(1.39). It is possible to expressed h^{TT}_{ij} as in eq.(1.21) and then we can perform a Fourier transform over h. In this way, it is possible to remove the time derivative and link the amount of energy to the square of the wave amplitude. Now, if we assume as gravitational wave frequency f of the order of $\sim 10^2$ Hz, as it could be the one of a GW generated from a binary black hole merger, we have:

$$\begin{aligned} \frac{dE}{dAdt} = \frac{c^3}{16\pi G}\langle \tilde{h}_+^2 + \tilde{h}_\times^2 \rangle \quad &\rightarrow \quad \sim 10^{45}\,\langle \tilde{h}_+^2 + \tilde{h}_\times^2 \rangle\,\frac{\mathrm{J}}{\mathrm{m^2 s}} \\ &\rightarrow \quad \sim 10^3\,\frac{\langle \tilde{h}_+^2 + \tilde{h}_\times^2 \rangle}{(10^{-21})^2}\,\frac{\mathrm{J}}{\mathrm{m^2 s}} \,. \end{aligned}$$

If we suppose a GW amplitude of around $h \sim 10^{-21}$ (a reasonable value for a binary black hole emission at a frequency of 200Hz and distance from Earth of around $\gtrsim$ 200 Mpc), then the GW energy flux results to be an incredible amount of energy if compared to the amount of energy of the electromagnetic flux of a supernovae in the Virgo cluster $\sim 10^{-12}\,\frac{\mathrm{J}}{\mathrm{m^2 s}}$ (its centre has a distance from Earth of $\sim$ 16 Mpc); even though the energy flux of the GW takes place in fraction of a second while the electromagnetic energy flux for the supernovae can last for days.

Chapter 2

Sources of gravitational waves

In chapter 1 we have introduced the GWs together with their physical and mathematical description and now, in this chapter, it is time to speak about the sources of GWs which could be detected by nowadays technologies. Among all the possible sources of GWs I will focus my attention on binary black hole (BBH) systems since this study is focused on searching low energetic signals nearby the GW transient from BBH coalescence. Moreover, these BBH systems form the majority of observed gravitational events so far.

2.1 Pudding of GWs sources

In principle, GWs are emitted by all sources that possess a quadrupolar momentum of mass varying in time, but looking at the eq.(1.26), since $G/c^4 \sim 10^{-43}$ (in magnitude), it is simple to infer that only extreme astrophysical processes can generate detectable GWs. Therefore, we focus our attention on these extreme astrophysical processes that involve very high energies and masses (recall eq.(1.26)) like: *gravitational collapse*, *fall of matter into a BH*, *supernovae explosion*, *compact binary systems*, and *young pulsars* as well as another less mentioned source of GWs which is the *GW stochastic background* [7]. It clearly stands out that, even inside this not so small set of astrophysical events, there are lots of processes, and some of them share common characteristics like the presence of a BH or being a binary system, or having a similar dynamic. Therefore, we can briefly describe all these scenarios by dividing them into four macro subgroups before focusing on BH and BBH systems [8].

2.1.1 Gravitational collapse

Gravitational collapse can label highly evolved stars that collapse or to the core collapse of an accreting white dwarf. Nevertheless, these processes have as final result the formation of a neutron star (NS) or a BH. In general, these events can lead to *supernovae*. When a massive star is in its last stellar evolutionary stage, its core undergoes an implosion, and this releases a great amount of matter and energy since the outer layers of the star are blown out. A fraction of this released energy can be carried away in the form of GWs [9], because, despite the final result (NS or BH), if the collapse is non-spherical the system will emit GWs losing a small fraction of its binding energy and angular momentum depending on the geometry of the collapse itself [10]. The typical frequencies range for these emitted GWs is around $200\,\text{Hz} - 1000\,\text{Hz}$ and the foreseen signal amplitude is large enough to be detected by ground-based detectors [10].

2.1.2 Rotating neutron star

GWs can be produced via the high rotation of a neutron star which is characterised by some degrees of axial asymmetry. We can think about a neutron star as a highly rotational compact object (CO) having an irregularity in its shape (otherwise would have been axially symmetric), probably on its surface, which is the solid structure of the star [11]. Then, the non axially symmetric distribution of mass leads to an asymmetric quadrupole tensor which is responsible for the GWs generation. Such gravitational radiation has a frequency twice or almost twice the rotational one of the NS. The expected frequencies for the emitted GW signals lie within the interval of $300\,\text{Hz} - 600\,\text{Hz}$ [10].

2.1.3 Binary system

A binary system of compact objects is a physical system where two celestial compact objects will inspiral one around the other till they merge together, and a fraction of the energy of the system is radiated away under the form of GWs [12]. Amongst all the possible compact objects, the detected system so far are formed by two BHs, a BH and a NS, or by two NSs [13, 14, 15, 16, 17]; this, nevertheless, does not change in a first approximation the dynamic of the system. So far these binary coalescences are the main physical events that were observed through GWs since the emitted gravitational radiation is enough energetic to be disentangled from the noise of current ground-based GWs observatories. Furthermore, the merger frequencies of these signals range between 10^{-4}Hz up to the kHz then they are inside the detectable frequency band of GWs detectors [8]. Another possible binary system is the one constituted by two white dwarfs, but the predicted amplitude of its gravitational wave signal is not enough to be detectable by current ground-based detectors.

2.1.4 Stochastic GWs background

The stochastic GWs background is the relic of GWs belonging to the evolution of the Universe: it can be imagined as the analogous of the *Cosmic Microwave Background* (CMB) but for gravitational and not electromagnetic radiation. The GWs constituting the stochastic background are the remnants of a large number of random events of different natures combined together [7]. Thus, depending on the time GWs were produced the stochastic background is classified into two categories: *cosmological* and *astrophysical* [18]. The cosmological background is referred to the overall superposition of all the GWs produced immediately after the Big Bang by different sources, around 10^{-36} to 10^{-32} seconds after the Big Bang (the CMB is dated around $3 \cdot 10^5$ years after it [7]). On the other hand astrophysical background is predicted to be an incoherent superposition of radiation due to astrophysical sources which cannot be individually resolved.

Since the Big Bang is thought to be the generator of all the random processes in the Universe, and these processes act as sources of stochastic background, observations of the cosmological background would bring useful information on the instants immediately after the Big Bang, resulting in an incredible step forward in the study and understanding of early Universe [7]. Astrophysical background, on the other hand, can help in understanding the Universe's evolution in more recent times since for each loud and detected gravitational event there are other many events much weaker that cannot be individually detected. It is probable that the astrophysical background will be predominant over the cosmological one: as a consequence, to study the cosmological background one has to model and study the

astrophysical one in a way through which its predicted astrophysical components can be subtracted from the observed data. In conclusion, a future detection of the stochastic background will provide important information about the astrophysical sources population through the Universe's evolution and on the events which took place during it [19].

Figure 2.1: The first image of a black hole thanks to Event Horizon Telescope observations of the center of the galaxy M87. The image shows a bright ring formed as light bends in the intense gravity around the black hole. Credits: [20]

2.2 Black holes

John Michell, in a paper presented to the Royal Society of London in 1783, noted that, if a star has enough mass (M) for a given radius r, the escape velocity (v_e) from its surface would exceed the speed of light thus light will not be able to escape from it [21]. In Newtonian terms v_e, is defined as:

$$v_e = \sqrt{\frac{2GM}{r}}, \tag{2.1}$$

and if the escape velocity is setted equal to the speed of light, from eq.(2.1), it is possible to recover the value of the radius r_e such star would have:

$$r_e = \frac{2GM}{c^2}, \tag{2.2}$$

where G is the gravitational constant. Moreover, according to general relativity theory, for objects more compact than neutron stars the attractive force of gravity becomes so strong that nothing can prevent the object's collapse into a singularity. Combine these two properties and a black hole has been born: "black" since no radiation can escape from within the radius r_e, and "hole" because the singularity represents a hole in the space-time from which the matter cannot emerge [21, 22].

Then, a BH is simply defined as a region of space-time that cannot communicate with the external universe and the boundary of this space-time region is called the surface of the BH and is commonly referred to as *event horizon* (EH) [2]. Figure fig 2.1 shows a supermassive black hole belonging to the center of the galaxy M87 and its black central hole can clearly be seen.

To study the major properties of BHs and to have a common ground to discuss possible alternative compact objects to BHs and their differences to them, the most powerful tool in our hand is the space-time metric tensor since it is fundamental to describe the dynamic outside a generic compact object. Knowing the space-time metric tensor means to solve Einstein field equations (eq.(1.1)) and remarkably, the most general stationary BH solution is known analytically and it depends only on three parameters (or observables): the BH mass, M, the BH spin, J, and its charge, Q. In the following, I am going to analyse the Einstein field equations solution for two different stationary BHs configurations: the first one is the easiest one (no rotating and not charged BHs) the second one is the more complete one in which all the observables are taken into account [21].

2.2.1 Schwarzschild black hole

The easiest stationary BH one can imagine is spherically symmetric and has $J = Q = 0$ and it is called Schwarzschild black holes (from Karl Schwarzschild that in 1916 derived the exact solution to Einstein field equations for a spherical mass). Its external gravitational field is obtained by solving the Einstein field equations whose solution takes the name of *Schwarzschild metric* in which the line element is [21]

$$ds_{sh}^2 = -\left(1 - \frac{2GM}{c^2 r}\right) c^2 dt^2 + \left(1 - \frac{2GM}{c^2 r}\right)^{-1} dr^2 + r^2 d\theta^2 + r^2 \sin^2\theta d\varphi^2 \,, \tag{2.3}$$

and here (eq.(2.3)) the invariant metric elements ds_{sh}^2 is written in spherical coordinates whose origin coincide with the centre of the BH. Eq.(2.3) possesses two singularities: for $r = 0$ and for $r = (2GM)/c^2$. The first singularity, $r = 0$ is a physical one because it cannot be avoided with any change of coordinates system, on the contrary, the $r = (2GM)/c^2$ singularity is only apparent because it is due to the choice of coordinates. Indeed it is possible to perform a coordinates transformation and pass, for example, from the Schwarzschild metric to the Kruskal[1] coordinates system in which the singularity at $r = (2GM)/c^2$ disappears.

The radius

$$r = r_e = r_{sh} = \frac{2GM}{c^2} \tag{2.4}$$

is called Schwarzschild radius and, for this special class of compact objects, it coincides with the radius of the event horizon. The Schwarzschild metric, eq.(2.3), is significant only for values of $r \geq r_{sh}$ because actually only the space-time region outside the surface with $r = r_{sh}$ is relevant for an external observer whereas what happen inside the event horizon can never influence the exterior [2].

Furthermore, for BH it is possible to define the *innermost stable circular orbit* which is the smallest circular orbit a massive test particle interacting with the BH can have. The radius of such an orbit is indicated with r_{ISCO}, and for a Schwarzschild BH it has the value of [23]

$$r_{ISCO} = 3r_{sh} = \frac{6GM}{c^2} \,. \tag{2.5}$$

[1] Fore more details one can see [23, chapter 12, section 12.6].

It is larger than the Schwarzschild radius, this means that once the radial distance of the particle is smaller than r_{ISCO}, it can only inspiral into the BH. Similarly to the innermost stable circular orbit, it is possible to obtain the radius for the last stable circular orbit, *ligh ring*, for non massive test particles: radiations (such as the light). This radius, r_{LR} is equal to:

$$r_{LR} = \frac{3}{2} r_{sh} = \frac{3GM}{c^2} \tag{2.6}$$

always for a Schwarzschild BH.

2.2.2 A "strange" potential

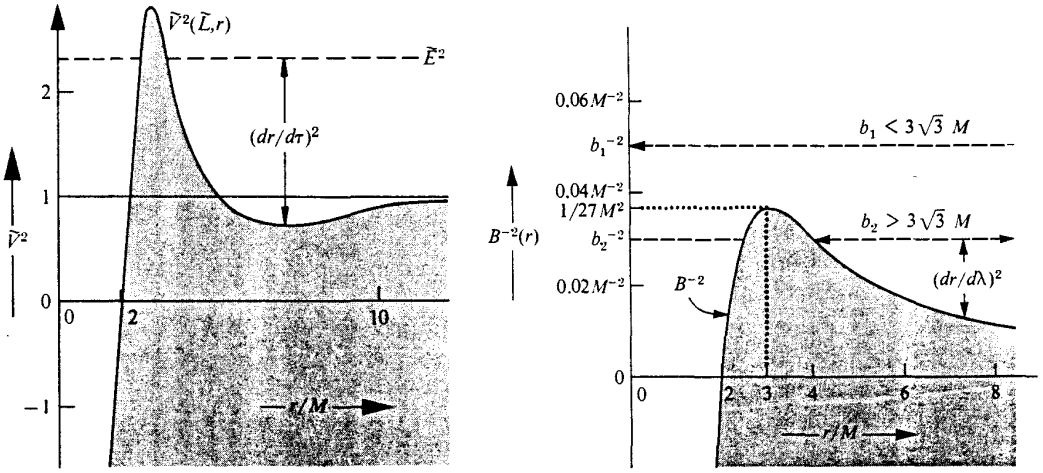

(a) Massive particle

(b) Massless particle

Figure 2.2: The plot on the left (a) shows the effective potential $\tilde{V}^2(\tilde{L},r)$ for a massive particle coming from infinity toward a BH. Its initial energy is $\tilde{E}^2$, horizontal lines in the plot. The plot on the right (b) displays the same physical scenario for a massless particle where the potential wall is labeled as $B^{-2}(r)$ and the initial energy is replaced with its impact parameter b which can always be represented with a horizontal line in the plane. In both plots on the x-axis is reported the ratio between the radius of the BH and its mass: r/M. Credits to [2], chapter 25.

Schwarzschild geometry allows to spot another peculiar aspect of the motion nearby a spherically symmetric BH (or, more in general, nearby a center of attraction). A moving test mass in the proximity of a BH is subject to an "effective potential" possessing not only the Newtonian characteristics (attractive field, $\propto M/r$ for long distances, and repulsive behavior due to the angular momentum for short distances) but also a short distances feature of a "pit" in the potential wall [2]. This pit, which can be seen in Figure 2.2a in the proximity of the vertical double arrow, can trap between its two walls a particle that, coming from infinity, does not possess enough energy, horizontal line 3 in the plot [22]. For a massless particle, such as light, the potential wall assumes a different shape, in Figure 2.2b, where the "pit" in the potential disappears and its trend resembles a little more the Newtonian scenario. Both the plots in Figure 2.2a and Figure 2.2b have on the vertical axis the square of the effective potential $\tilde{V}^2(\tilde{L},r)$, and $B^{-2}(r)$; on the orizontal axis the ratio r/M with the origin coincident with the centre of the BH. The solid black line is $\tilde{V}^2(\tilde{L},r)$ or $B^{-2}(r)$ while horizontal dashed lines are the energy values at infinity for massive particles, and impact parameter for massless particles respectively.

In figure 2.2a can be seen the ISCO orbit (r_{ISCO}) which coincides to the local minimum of the potential in the "pit" while in figure 2.2b the light ring orbit (r_{LR}), eq.(2.6) corresponds to the maximum value of $\tilde{B}^{-2}(r)$. We recall that the expressions for the potential wall for both the masses and massless particles are:

$$\tilde{V}^2(\tilde{L}, r) = \left(1 - \frac{2GM}{c^2 r}\right)\left(1 + \frac{\tilde{L}^2}{r^2}\right), \tag{2.7}$$

$$B^{-2}(r) = \left(1 - \frac{2GM}{c^2 r}\right) r^{-2}, \tag{2.8}$$

[2] where $\tilde{L}$ is the angular momentum of the infalling particle.

2.2.3 Kerr black hole

The *Kerr-Newman metric* is the most general space-time metric to describe space-time metric for a rotating, $J \neq 0$, and charged, $Q \neq 0$ black hole. Nevertheless, *Kerr metric*, which assumes rotating but not charged BHs, is preferred to the *Kerr-Newman one* because in general one has that Q is rapidly neutralized thanks to the surrounding plasma, meaning that BHs do not possess an appreciable electric charge. Then, it is possible to simplify the analysis of a BH assuming it is rotating but not charged, $J \neq 0$ and $Q = 0$ [23]: BHs belonging to these family are called Kerr black holes and can be described through the Kerr metric wich in the Boyer-Lindquist coordinates system has the form [21]:

$$\begin{aligned} ds^2 = &-\left(1 - \frac{2rGM}{c^2\Sigma}\right)c^2dt^2 - \frac{4arGM}{c\Sigma}\sin^2\theta dt d\varphi + \frac{\Sigma}{\Delta}dr^2 \\ &+ \Sigma d\theta^2 + \left(r^2 + a^2 + \frac{2ra^2GM\sin^2\theta}{c^2\Sigma}\right)\sin\theta d\varphi^2 . \end{aligned} \tag{2.9}$$

Here the BH is rotating around the $\hat{\varphi}$ axis and the quantity a, Δ and Σ are defined as [21]

$$a \equiv \frac{J}{cM}; \tag{2.10}$$

$$\Delta \equiv a^2 + r^2 - \frac{2GM}{c^2}r; \tag{2.11}$$

$$\Sigma \equiv r^2 + a^2\cos^2\theta . \tag{2.12}$$

Coefficients of the space-time metric are independent of t and φ, so the metric is stationary and axisymmetric about the rotation axis [23]. Moreover, the Kerr metric, eq.(2.9), reduces to Schwarzschild metric, eq.(2.3), if $a = 0$, so the BH is not rotating, which is consistent with the above symmetries The main properties of a Kerr BH that can be derived from its space-time metric are [3]:

1. For $\Delta = 0$ we obtain the radial distance for which the Kerr metric is singular (same as with Schwarzschild metric):

$$r_+ = \frac{GM}{c^2} + \left[\left(\frac{GM}{c^2}\right)^2 - \left(\frac{J}{cM}\right)^2\right]^{1/2}, \tag{2.13}$$

[2] The derivation of the potential $\tilde{V}^2(\tilde{L}, r)$ and $B^{-2}(r)$ is faced in [2], chapter 25 from page 655 to page 679.

[3] The main reference for this list of BHs properties is [21, chapter 13, section 11].

and can be thought as the radius of the event horizon for a rotating BH.

2. Eq.(2.13) shows that the maximum value for the angular momentum of a BH is $J = \left(GM^2\right)/c$, which means that a BH cannot have an infinite spin, and its upper limit is $\left(GM^2\right)/c$. Since the upper limit of J depends on the mass M of the BH, the matter falling into a BH adds both angular momentum and mass.

3. A rotating BH drags all the physical objects near itself into an orbital motion with the same angular momentum vector: nearer a particle is to the event horizon stronger will be the dragging effect. Nevertheless, it exists a radial distance from the BH for which an observer, at rest with respect to the fixed stars, preserves its status of motion and won't be influenced by the rotation of the BH. This distance, called static radius r_{stat}, is:

$$r_{stat} = \frac{GM}{c^2} + \left[\left(\frac{GM}{c^2}\right)^2 - \left(\frac{J}{cM}\right)^2 \cos^2\theta\right]^{1/2}. \tag{2.14}$$

Notice that in eq.(2.14) r_{stat} depends on θ, so r_{stat} will be equal to r_+ at the pole while it will be greater than r_+ when θ is approaching the equatorial plane.

4. For a maximally rotating Kerr BH the radius of the innermost stable circular orbit can assume two different values, depending on whether a test particle is co-rotating or counter-rotating:

$$\text{co-rotating:} \qquad r_{ISCO} = \frac{GM}{c^2}$$
$$\text{counter-rotating} \qquad r_{ISCO} = \frac{9GM}{c^2}$$

This feature is extremely important: matter, if co-rotating with the BH, can move in stable circular orbits with smaller radii than for a Schwarzschild BH allowing a greater amount of energy to be released from the friction of matter inside the accretion disk since matter falls into the BH through a sequence of almost circular orbits.

2.3 Binary black hole systems

We have seen the main properties and differences between a Schwarzschild and Kerr BH thought as isolated systems, now the time has come to dig into the main sources of GWs in current time: binary black hole systems.

A compact binary system is made of two compact objects which rotate one around the other and are mutually attracted because of the gravity effect: in their motion the two COs emit GWs. These waves carry on energy which is subtracted to the system provoking the two masses to slowly inspiral till they merge, reaching in this way the lowest energetic configuration. It is possible to divide the evolution of the system into three main phases: the *inspiral* phase, the *merger* phase and the *ring-down* phase.

2.3.1 Inspiral phase

This phase of BBH evolution occurs over millennia and it is the time interval during which the two BHs revolve one around the other till they merge, Figure 2.3. In their circular motion they emit GWs which can be described with sufficient accuracy

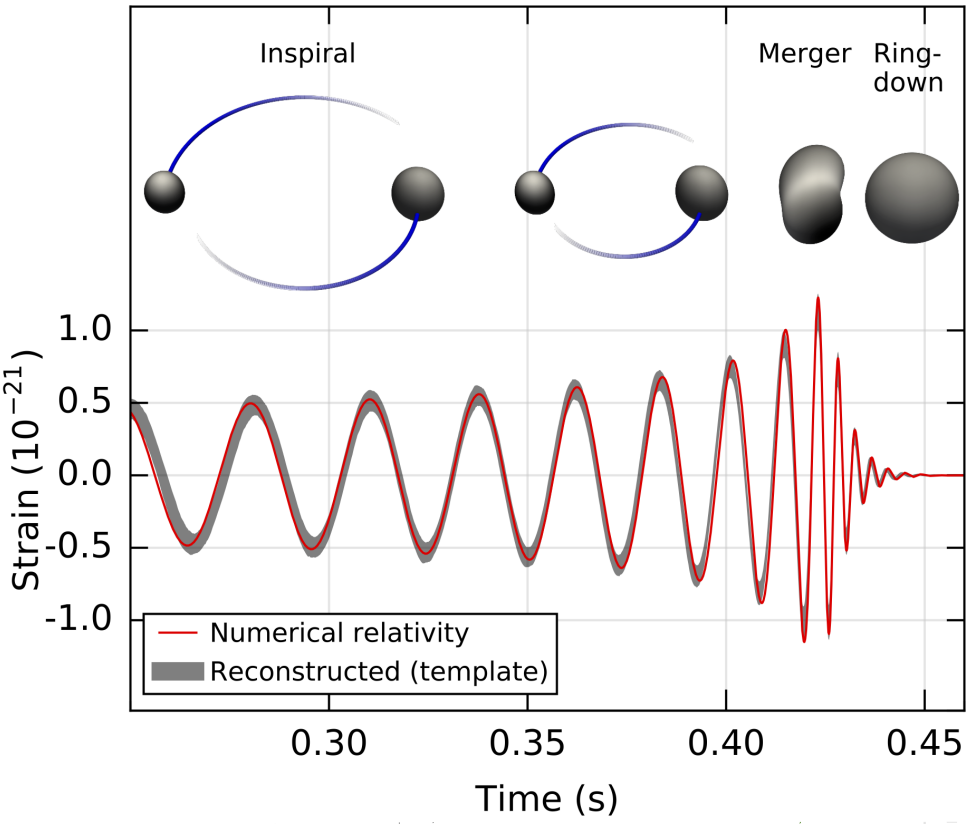

Figure 2.3: Here is shown the GW signal emitted during the three phases of a binary system's evolution. On the top of the picture, there is a cartoon that from left to right depicts the evolution stages of a binary system: inspiral, merger, and ring-down, while on the bottom is shown the related GW signal emitted from the binary. This picture refers to the first GW ever detected, GW150914. The red line is the numerical relativity model, while the grey belt the reconstructed template which matches at best the data. Credits from [24]

through the post Newtonian (shortly PN) formalism which is an approximation of the general relativity theory under suitable conditions [25, 26].

A GW, while it propagates towards the detector in the local wave zone, is entirely described by eq.(1.26) and possesses both the polarization components: h_+ and $h_\times$. Their expressions are evaluated assuming that the source is made of non rotating point masses, moving on a quasi circular orbit centered in the center of mass of the system. Under these hypothesis h_+ and $h_\times$ can be expressed as [27]

$$h_+(t) = \frac{G^{5/4}}{c^{5/2}} \frac{\mu^{3/4} M^{3/4}}{d_L} \left(\frac{c(t_c - t)}{5}\right)^{-\frac{1}{4}} \left(\frac{1 + \cos^2 \iota}{2}\right) \cos\left[\Psi_c + \Psi(t_c, t, m_1, m_2)\right] , \tag{2.15}$$

$$h_\times(t) = \frac{G^{5/4}}{c^{5/2}} \frac{\mu^{3/4} M^{3/4}}{d_L} \left(\frac{c(t_c - t)}{5}\right)^{-\frac{1}{4}} \cos\iota \sin\left[\Psi_c + \Psi(t_c, t, m_1, m_2)\right] , \tag{2.16}$$

where:

- d_L is the luminosity distance of the GW from the source,
- $\mu = (m_1 m_2)/M$ is the reduced mass with m_1, m_2 and M the components masses and the total mass of the binary system,

- t_c is the coalescence time,
- ι is the angle defined by the versor $\hat{n}$, which links the detector to the orbital plane of the binary itself,
- Ψ_c is the phase of the GW at the time $t = t_c$ which is a constant, and finally $\Psi(t_c, t, m_1, m_2)$ is the phase of the wave and depends on the time difference $t_c - t$, and the masses of the sources.

Eq.(2.15)and eq.(2.16) are evaluated at the zero order of post Newtonian formalism [4] and from their expressions we can observe that:

1. when $t = t_c$ there is a divergence in the polarization functions because the two bodies merge and the post-Newtonian approximation cannot describe with sufficient accuracy the metric;
2. for $\iota = \frac{\pi}{2}$, $h_\times = 0$, and the GW is said to be linearly polarized, so the observer is aligned with the orbital plane of the binary;
3. for $\iota = 0$, h_+ and $h_\times$ are equal and the GW is said to be circular polarized, so the observer is perpendicular to the orbital plane of the binary;
4. both the polarizations are monotonically decreasing functions of the luminosity distance d_L;
5. the two polarization amplitudes are monotonically increasing while the rotation frequency of the binary increases. This phenomenon is called "chirping" [28];

Moreover, if the local wave zone description of the radiation holds, it is possible to apply the quadrupole formalism (recall eq.(1.26)) to express the amount of energy radiated away per unit of time by the binary coalescence [22]:

$$L_{GW} \equiv \frac{dE}{dt} = \frac{1}{5}\frac{G}{c^5}\langle \dddot{Q}_{ij} \dddot{Q}^{ij} \rangle \,, \tag{2.17}$$

(the dot expresses the time derivative) and L_{GW} is called gravitation luminosity of the source. From the inspiral signal, through matching filter techniques, informations on the mass of the binary, its components mass and luminosity distance can be inferred.

2.3.2 Merger phase

Once the separation distance between the two BHs becomes comparable to r_{ISCO}, eq.(2.5) for Schwarzschild BHs, then it is time to speak about the merger phase which lasts till the two bodies are unified into one, as shown in Figure 2.3. During the merge phase, the evolution of the system has to be described through numerical relativity because gravity becomes strongly non linear, and so less accessible to approximation techniques as the post Newtonian one used for the inspiral stage. Gravitational waves from the merger could enrich our knowledge of the dynamics of relativistic gravity in a highly nonlinear, and highly dynamic regime over which, nowadays, we have poor theoretical understanding [25, 29].

[4] A more accurate description and expression for the two polarizations can be further explored in [27].

2.3.3 Ring-down phase

The ring-down phase follows the merger one: it starts around the time of formation of a common apparent horizon, corresponding to the peak of the GW amplitude signal [30]. In this phase, the final unstable BH reaches a stable configuration through the emission of GWs. Nevertheless, the final unstable BH can be characterised by only two parameters: its remnant mass M, and its spin S [31]. This is due to the fact that the space-time after the merger closely resembles the one of a stable BH (Kerr one) with little perturbations over it due to its instability. This behaviour can be described via BH perturbation theory [32] and here the dominant part of the GW signal has the form [30]:

$$h_0(t) = \Re\left(A\frac{GM}{c^2}\frac{e^{-i\omega_{22}t}}{r}\right). \tag{2.18}$$

A is the dimensionless amplitude of the $l = m = 2$ vibrational mode (l and m are the spheroidal harmonic angular indices), m is the projection on the z-axis of the angular component l [32], r is the distance of the observer to the source, and M is the total mass of the final BH. Since the ring-down waveform, due to the usage of perturbation theory, results to be a superposition of exponentially damped sinusoidal oscillations (ring-down) or quasi-normal modes (QNMs) [33], the subscript 0 in $h_0(t)$, eq.(2.18), is used to point out the amplitude of the fundamental and dominant vibrational mode of the BH remnant.

Ring-down signal and its detection can play an important role in helping to have an independent estimation, other than the one obtained by the inspiral stage, of the mass and spin of the remnant BH [30], through matching filter techniques of waveforms models for the ring-down phase of a BBH coalescence.

Ring-down: quasi-normal modes

Proper vibrational modes belong to everything around us: in a poetic way they allow us to "hear the shape of a drum" [34], and a more rigorous definition for these vibrational modes is *normal modes*. Now, quasi-normal modes (QNMs), in a general definition, are the eigenmodes for dissipative systems [35] so they are not stationary in time but will change both their amplitude and phase in time.

In 1970 the Indian scientist C. V. Vishveshwara theorised that BHs have a distinct vibrational mode: a set of modes representing the time evolution of some internal displacements of the BH from its equilibrium configuration. For a star it is not unnatural to have perturbations, and usually, they are carried on by the fluids making up the star or, since for BHs we cannot speak about fluids, it has to be the space-time itself that sustains these oscillations. From a purely mathematical point of view, QNM translates in finding the solution to the linear ordinary differential equations, with physical motivated boundary conditions, describing the dynamic of the process (in our case a perturbed BH reaching its stable configuration)[36]: Zerilli and Regge-Wheeler equations [5]. For a BH, the solution has to be described by the metric outside the event horizon, it has to propagate towards infinity since nothing can come out from the BH's EH, and finally, it is also required that no unrelated perturbations to the initial one (i.e. other gravitational waves from other sources) can interfere with the system at later times [37]. Putting all of this togheter, the equation

[5] Zerilli equation (1970) for the even-parity case while the Regge-Wheeler (1975) equation for the odd-parity one.

to be solved is [35]

$$\frac{\partial^2\phi(x)}{\partial x^2} + \left(\frac{\omega^2}{c^2} - V(x)\right)\phi(x) = 0\,, \tag{2.19}$$

where $V(r)$ represents the effective potential (recall 2.2.2) with its polar or axial component, Zerilli or Regge-Wheeler, and $\phi(x)$ is an alternative form for $h_{\mu\nu}$ metric tensor where we have used x and not r since eq.(2.19) is expressed in Fourier domain and for a Eddington–Finkelstein (also tortoise) coordinates reference frame:

$$x = r - 2M\ln\left(\frac{r}{2M} - 1\right)\,. \tag{2.20}$$

In conclusion, there are two one-dimensional wave equations that, if solved, provide the expression for the gravitational radiation emitted from a perturbed BH (es. ringdown phase of a binary coalescence).

For a Kerr BH the emitted GW took the form [35]:

$$h_+ = \frac{M}{r}\,\Re\left(A^+_{lmn}\, e^{i(\omega_{lmn}t+\phi^+_{lmn})}\, e^{-t/\tau_{lmn}}\, S_{lmn}(\theta,\psi)\right) \tag{2.21}$$

$$h_\times = \frac{M}{r}\,\Im\left(A^\times_{lmn}\, e^{i(\omega_{lmn}t+\phi^\times_{lmn})}\, e^{-t/\tau_{lmn}}\, S_{lmn}(\theta,\psi)\right)\,, \tag{2.22}$$

with A^+_{lmn}, $A^\times_{lmn}$ and ϕ^+_{lmn}, $\phi^\times_{lmn}$ the real amplitude and phase of the wave, S_{lmn} is the spin-weighted spheroidal harmonics (with spin weight equal to 2) and (θ,ψ) are the source angles oriented such that the z-axis is indicates the BH spin.

2.3.4 Spin effects

So far we have not taken into account the effects of the BHs' spins on the GW emitted by the binary system, nevertheless, from the literature, we know there are three main effects due to the spin-spin or spin-orbit coupling that modify a binary evolution: spin affects the phase, the amplitude, and the polarization of the emitted gravitational radiation [38]. If spins ($\vec{S}_1$ and $\vec{S}_2$) are misaligned with respect to the orbital angular momentum ($\vec{L}$) the orbital plane of the binary precess around the total angular momentum of the system $\vec{J} = \vec{L} + \vec{S}_1 + \vec{S}_2$ leading to the modulation of the amplitude and the phase of the gravitational signal [39] which is also related with the view angle of the source from the observer. Such precession is due to the projections of the spins on the orbital plane and will lead to a precession of the spins themselves.

Moreover, looking at the projection of the spins along $\vec{J}$ direction, if they are aligned with $\vec{J}$, the number of orbits a binary system would make before merging will increase with respect to a binary system with non-spinning components [39]. On the contrary, if the spins projections are anti-aligned then the system will have fewer orbits before merging if compared to the non-spinning case. Thus, the time the system will take before merging will be higher (lower) if compared to the non-spinning scenario for aligned (anti-aligned) spins components.

The two polarisations of the GW, eq.(2.15) and eq.(2.16), during the inspiral phase of the binary, are obtained at the zero-order PN expansion: the system is treated as a Newtonian one. If we want to take into account also the effects of the spin-orbit and spin-spin interaction the GW functions have to be evaluated till the 1.5 (spin-orbit) or 2 (spin-spin) PN order [40].

Chapter 3

Low-energetic gravitational wave signals

Detecting strong GW signals from compact binary coalescences, whose detection and faithful prediction through the general relativity theory help in corroborating the validity of such a theory, is no more the primarly purpose of current gravitational waves detectors and data analysis algorithms. Now, thanks to continuous studies, thecnological upgrades to the observatories, and novel methodology to analyse the data, it is possible and mandatory to search for other GWs candidates (some of them were already presented in chapter 2) as well as to search for low energetic signals associated to the main detected event. Investigations for low energetic signals aim to find further proofs to validate the GR theory, or possible deviations from the GR theory. In the following we will review some of the most relevant low energetic signals one can search for in GW data, and we majorly focus our attention on echoes since they are the scientific case for this methodology of data analysis.

3.1 Echoes

Echoes are the predicted GWs signature of the post-merger phase of a binary compact object coalescence in which the remnant is theorised to be an exotic compact object (ECO) and not a black hole [41, 42]: possible example are gravastars [43], boson stars [44], wormholes [45], or even fuzzballs [46]. These models may provide a solution to the BH information paradox or the cosmological constant problem [47, 48] and appear in several scenarios such as quantum corrections (Planck-scale modifications [47]) at the horizon scale of the final compact object (CO) [49]. A brief overview of these ECO models is available in appendix A.

3.1.1 BH and ECO: boundary conditions

As we have seen in section 2.3.3, quasi-normal modes (QNMs) are related to the specific boundary conditions of the studied system: for BHs it is required that at the event horizon there should be the absence of outgoing GWs [42] which can be translated thinking to the event horizon as a surface having null reflectivity, $R_{EH} = 0$, and perfect transmittivity, $T_{EH} = 1$ [48]. It is straightforward that any change to the boundary conditions of the system will modify the QNMs structure. Together with QNMs, both BHs and ECOs are charaterised by the presence of an effective potential barrier, section 2.2.2, which possesses its own vibrational modes, called light-ring modes, which are related to the geodesics in the space-time [42].

For black holes it is possible to apply the appoximation such that the light-ring modes describe also the QNMs: this happens because of BHs peculiar boundary

condition where, at the EH, an ingoing wave can no more interact with the outer space and then one can say that the modes of a BH "live" on the external null circular geodesic [50]. However, if the EH is replaced with a surface of different nature, depending on the proposed ECO model, QNMs will be different with respect to the ones of a BH, while the light-ring modes will not be modified [42, 51].

Immediately after the merger, the ring-down waveform is dominated by the light-ring ring-down emission while QNMs dominate in later times [42], which means the ringdown mode of any object which is compact enough will be dominated at early times by a universal ring-down signal [50]. This is a first sight of the importance of being able to study at low energy the post-merger part of the signal for a BBH coalescence: having that QNMs dominates in the later phase of the post-merger GW signal, the capability to detect them will enhance the possibility to discriminate between a BH or an ECO remnant.

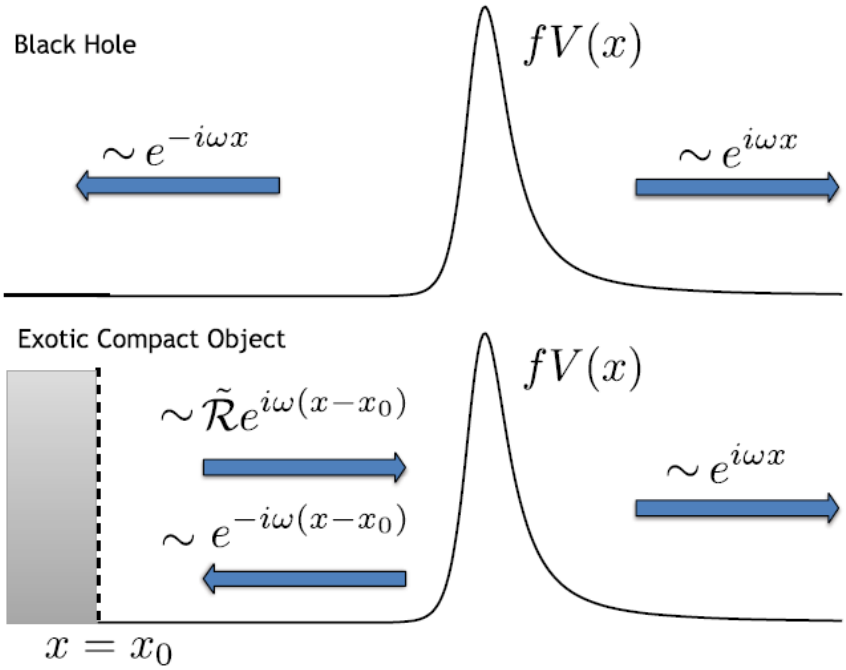

Figure 3.1: Wave packet behaviour, generated at the light ring, for both cases of a BH and an ECO as a remnant of a binary coalescence. The black solid line is the system potential $V(x)$ as a function of the tortoise coordinate x, and at x_0 is located the sourface of the ECO. Top panel depicts the BH scenario, where the ingoing radiation is not reflected back. In the bottom panel the remnant is an ECO: the ingoing radiation is reflected towards the potential "wall" creating a cavity. Credits for the figure from [48]

3.1.2 Post-merger GW signature for an ECO

If the final object is compact enough [42], replacing the EH of the would be BH with a shell or surface whose nature is dependent from the ECO model, will lead to the generation of secondary GW pulses called echoes after the ring-down phase of the binary. Such pulses arise because of the ECO surface, called inner barrier, together with the potential barrier (2.2.2), labeled as outer barrier, would generate a sort of cavity inside which the GW radiation from the ring-down signal is trapped [41]. The ring-down signal undergoes the processes of multiple reflections and transmissions

against the two barriers, and each time the GW radiation hits the potential barrier a fraction of it is transmitted and the rest is reflected inwards. The transmitted radiation takes the name of *echoes*. This process is illustrated in figure 3.1, where the black solid line represents the potential $V(x)$ as a function of the spatial coordinate x (Eq.(2.19) and Eq.(2.20)). In the top pannel is shown the case in which the remnant is a BH, here the ingoing signal will be lost once it passes through the EH, while at the bottom, is shown the scenario in which the remnant is an ECO. Here the ingoing radiation is partially reflected towards the potential barrier to be again partially transmitted to the outer space and partially reflected towards the ECO to repeat again this loop.

Now, in sight of these, a detection of echoes would be a claim of ECOs existence and a starting point to study their nature, which is not well and fully understood yet. Moreover, if the existence of ECOs is proven, a detection of echoes will also provide a unique tools to discriminate between different theoretical models of ECOs. Such possibility can be seen through the predicted time separation between one echo and the following one Δt_{echo} [52]:

$$\Delta t_{echo} \sim 2 \int_{r_{min}}^{r_{LR}} \frac{1}{\sqrt{F(r)B(r)}} dr \,, \tag{3.1}$$

where $F(r)$ and $B(r)$ [1] are the coefficients' functions for the time and radial component of the metric in a spherical symmetric system, and r_{min} is the radius of the minimum of the potential. For the majority of ECO models the radius of their shell, r_{shell}, can be describe as [52]:

$$r_{shell} = r_{EH} + l \,. \tag{3.2}$$

where l is a Planck-scale correction to the radius of the event horizon for the would be BH [53], so Eq.(3.1) can be approximate to:

$$\Delta t_{echo} \sim nM \log\left(\frac{l}{M}\right), \quad \text{if} \quad l << M \quad \text{with} \quad c = G = 1 \tag{3.3}$$

where n is a parameter related to the nature of the exotic compact object, and M is the final mass of the remnant. This time separation between two consecutive echoes, Eq.(3.3), physically can be thought as the time the gravitational radation trapped inside the cavity would take to travel back an forth from the outer barrier (potential barrier) to the inner one [52]. Moreover, since Δt_{echo} depends logarithmically on l, even small correction to r_{EH} can be seen, allowing to derive from Eq.(3.3) a typical time delay

$$\Delta t_{echo} \sim 54 \left(\frac{n}{4}\right) M_{30} \left(1 - 0.001 \log\left(\frac{l/h_p}{M_{30}}\right)\right) \text{ ms} \,, \tag{3.4}$$

where h_p is the Planck length ($\sim 2 \cdot 10^{-35}$m), and $M_{30} \equiv M/30M_\odot$. From Eq.(3.4), for systems like the ones detected during O1, O2 and O3 form LIGO and Virgo collaboration [14, 15, 16, 17], whose masses are of the order of some tens of Solar masses ($M \in [10 - 100]M_\odot$), a typical value of time delay is: $\Delta t_{echo} \in [30 - 400]$ms. So, Eq. (3.4) clearly shows that beeing able to detect the time interval between two consecutive echoes would provide a direct information over the theorised nature of the ECO thanks to the combined parameters n and l.

[1] Here $ds^2 = -F(r)dt^2 + B(r)dr^2 + r^2 d\Omega^2$ is the metric outside a compact object with spherical symmetry and matter localised only in the region $r < r_{shell}$. Following Birkhoff's theorem, in the region $r > r_{shell}$ the Schwarzshild metric holds: $F(r) = B(r) = \left(1 - \frac{2GM}{c^2 r}\right)$.

Other observables of echoes, related with theoretical models of ECOs, that can be studied and constrained, are [54, 55]:

- t_{echo} : the arrival time of the first echo signal with respect to the coalescence time of the binary. It is not setted equal to Δt_{echo} in order to take into consideration possible nonlinear effects close to the merger of the binary;
- γ : the amplitude damping factor between subsequent echoes. Its value can range in $0 < \gamma < 1$ in order to reflect the physical condition of energy loss when the gravitational radiation hits the boundaries of the "cavity";
- A : the relative amplitude of the first echo with respect to the amplitude of the last merger-ringdown part of the GW waveform. like for the γ parameter A lies inside the range $0 < A < 1$ with the reasonable assumption that the first echo should not be louder than the main GW signal.

These observables as well as a possible morphology of a post-merger GW signal emitted by an ECO are shown in figure 3.2, where is plotted the strain of the signal h as a function of time t for both the waveform's polarizations.

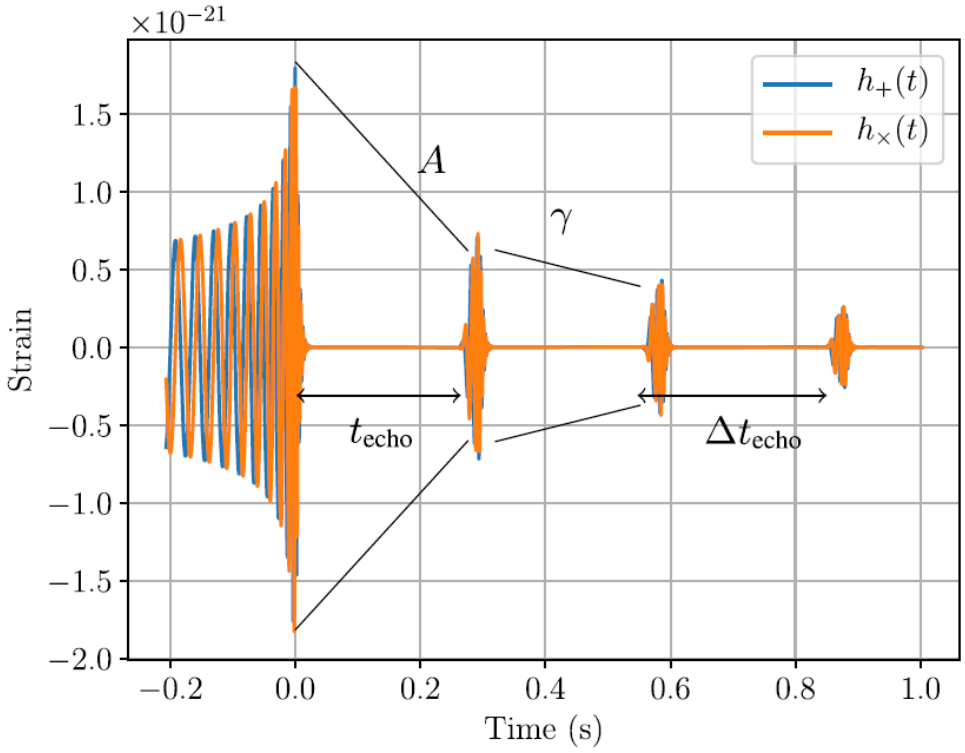

Figure 3.2: This plot shows the amplitude of a simulated inspiral-merger-ringdown-echoes (IMRE) GW signal as function of time with echoes. In orange and light blue there are the two polarization $h_+, h_\times$ of the wave and the time 0.0 s is the merger time. The following signals (positive times) are the echoes, for whose are enhanched their major parameters $A, \gamma, \Delta t_{echo}$ and t_{echo}. Credits to [56]

3.2 Highly eccentric BBH

For current detectors' performances, another subthreshold signal, different to echoes, which can provide useful physical information both over BBHs population and evolution as well as over their formation mechanism, is the modulated part of the inspiral phase of an eccentric BBH signal [57]. For high eccenticity e values, the emitted signal displays pronounced amplitude modulations due to the advance of the periastron [58]; in figure 3.3 is plotted such an effect: the amplitude of the signal $h(t)$ for a non eccentric binary (black line) and for a high eccentric binary $e = 0.5$ (red line, waveform model [59]).

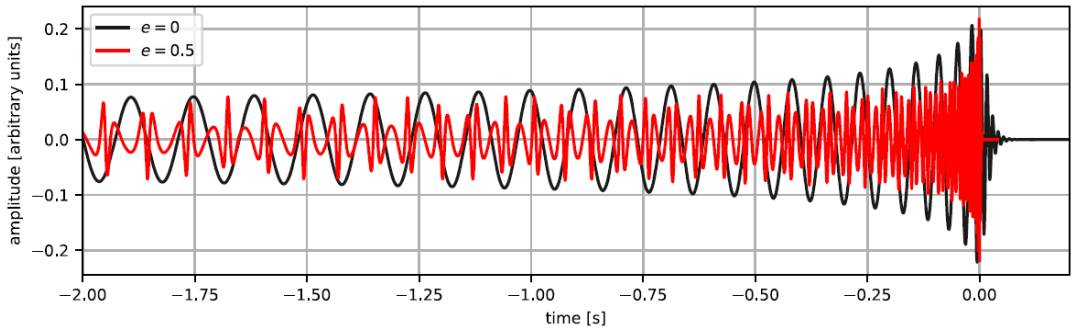

Figure 3.3: Example of a GW signal from a BBH system of $10M_\odot - 10M_\odot$ with eccentricity e equal to 0.0 (black line) and 0.5 (red line). On y-axis there is the amplitude of the signal $h(t)$ while on x-axis the time t in seconds is expressed using as reference time the merger time of the binary. Credits for the figure from [60]

In literature there are many formation mechanism for BBH and among them the two most widely understood are: isolated binary evolution scenario, and binaries formed dynamically in dense stellar environments like globular clusters or active galactic nuclei, AGN [58]. For the isolated binary evolution scenario the BBH system varies its initial eccentricity through the emission of GWs to reach a more stable configuration, leading to a circularization of its orbits by the time the frequency of the emitted GW signal enters the detection band of the interferometers. On the other hand, BBH dynamically formed in dense stellar environments may still retain a significant eccentricity even when their signal resultto be detectable by GW observatories. For these eccentric BBH (eBBH) system a GW burst is theorized to be emitted every time the pair passes at a close encounter (i.e. at periastron) [61], which kindly reminds a wave signature similar to the echoes one. These eBBH are thought to be formed via dynamical capture at very close separations, so without having the time to circularize before the merger, or through a dynamical process that increases the eccentricity of the binary like the Kozai-Lidov oscillations [62]: it consists in a quasi-stable three-body system, one BBH is orbited by another black hole. Here ellipticity can be produced in hierarchal triples through angular momentum exchange from the inner binary and the larger system.

To date, GW observatories have observed gravitational waves from 90 events (84 BBH, 4 (possible) BHNS, and 2 BNS) [17]. The observed signals from BBH coalescences display a constant behaviour: the binaries have quasi-circular orbits, they decrease in radius and increase in frequency as they lose energy through gravitational radiation emission. Nevertheless these observations are biased, in a certain way, since LIGO and Virgo data analysis methodology uses waveform templates that mostly assume a negligible eccentricity, so highly eccentric BBH could go undetected although GR predicts not negligeable effects due to eccentricity. Moreover,

many properties of the detected BBH are currently calculated with the assumption of circular orbits, such as their distance from Earth, and these estimations can be affected from this temporary lack of eBBH templates.

Then, as for echoes, identifying eccentricity could improve the parameters estimation and provide a better understanding the dynamical formation mechanisms for BBHs and the astrophysical environments of their sources [60]. The major observables for such subthreshold signals (the burst of GW radiation during the inspiral phase of the eccentric binary) are represented by their mean frequency, the time separation between each peak (figure 3.3), and amplitude, which are expected to increase pulse after pulse while reaching the merger time. It is straightforward that for the purpose of this study only high eccentric BBH coalescence represent an opportunity, since their morphology is predicted to be different with respect to the one of a quasi circular binary, showing a behaviour which could be compared to a revers echoes scenario. The time separation between each peak can help in constrain theoretical models for eccentric BBH coalescences.

3.3 Memory effects

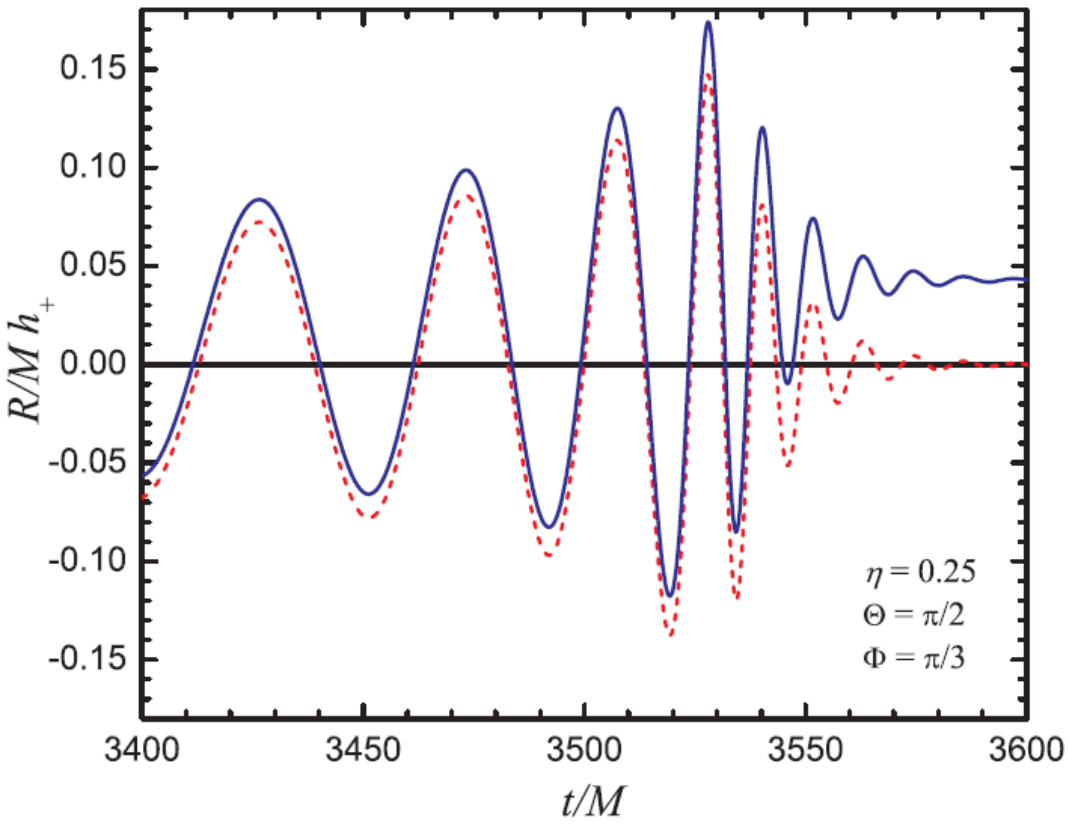

Figure 3.4: Example of gravitational wave signals with memory. The plot shows the $h(t)_+$ polarization, y-axis, for an equal-mass BBH coalescence with (blue/solid) and without (red/dashed) the nonlinear memory effect as a function of time, x-axis. M is the total mass of the system and R is the distance of the source to the observer. Here geometrized units are used: $G = c = 1$. Credits for the figure from [63]

In chapter 1, section 1.4, gravitational waves are described as oscillatory perturbations of the space time whose amplitude starts small at early times, reaches its

maximum at merger time and then decreases to zero during the ring-down phase, all while propagating on the background metric at the speed of light. However such description is incomplete: since 1970s, it is known that sources of gravitational waves possess some kind of gravitational wave memory [63] which prevents the amplitude of the signal to drop to zero. In figure 3.4 is shown such a difference between a GW signal with (solid blue line) and without (dashed red line) the memory effect, where it is possible to see a gravitational DC offset in the post-merger phase of the signal. The signal is obtained form a simulated equal-mass BBH coalescence. For example, taking a detector of gravitational waves, chapter 4, and considering its two free masses with separation L_i, the effect of the passage of the GW can be evaluated by looking at their relative displacement $\delta L_i = \frac{1}{2} h_{ij}^{TT} L^j$. Neglecting the GW memory effect: before the arrival of a GW $h_{ij}^{TT} = 0$ and so $\delta L_i = 0$, then after its transit again $h_{ij}^{TT} = 0$ and so $\delta L_i = 0$. On the other hand, with memory, after the passage of the GW one has that $h_{ij}^{TT} \neq 0$ and so $\delta L_i \neq 0$, which produces a permanent change in the spatial sepatarion of the detector's test masses [64].

To quantify the gravitational memory effect it is possible to idealise the GWs sources as a collection of freely moving systems A (with $A \in [1, ..., N)$ not gravitational bounded between them, either before and after the emission of GWs. Under this perspective the gravitation memory effect can be expressed as [64]:

$$\Delta h_{ij}^{TT} = \Delta \sum_{A=1}^{N} \frac{4GM_A}{rc^4 \sqrt{c^2 - v_A^2}} \left(\frac{v_A^i v_A^j}{1 - v_A \cos\theta_A} \right)^{TT} . \tag{3.5}$$

In Eq.(3.5) Δ is the difference between the final value (after the GW burst) and the initial one (before the GW burst) of the GW amplitude h_{ij}^{TT}. M_A is the mass of the system A, r the distance between the source and the observer, v_A is the velocity of the center of mass for system A, and θ_A is the angle between v_A^j and the direction source-observer. In general, the gravitational memory effect can be recovered both studying the linearised theory of general relativity as well as its complete form. Inside the framework of the linearised theory of general relativity the memory effect arises because the overall change in the linear momenta of the constituent bodies [65] (like binary on a hyperbolic orbit or gamma ray burst jets [63]). The non-linear contribution to the gravitational memory effect arises from the non-linearities inside Einstein field equation [64], and can be interpreted as the component of a gravitational wave that is sourced by the emission of the gravitational wave itself [66]. This contribution were initially thought to be negligeable, since GW sources are at enormous distances from Earth and in the neighborhod of Earth GWs can be studied via the linearised theory of general relativity. Nevertheless, recent studies [64, 65] showed that bound system as BBH can produce a significant amount of gravitational memory to the point its amplitude is estimated can reach the $O(5\%)$ of the peak amplitude of the binary system.

3.4 Other sub-threshold gravitational signals

Other possible sub-threshold gravitational wave signals that could be detected as features linked to the main CBC signal, predicted either form general relativity theory or modified theory, are QNMs, gravitational lensing effects, overlapping signals, and/or signals from the stochastic gravitational waves background.

QNMs have been discussed in chapter 2, section 2.3.3 and for the purpose of this dissertation there is no need to further dig into such a physical properties of gravitational wave signals arising from BBH coalescences.

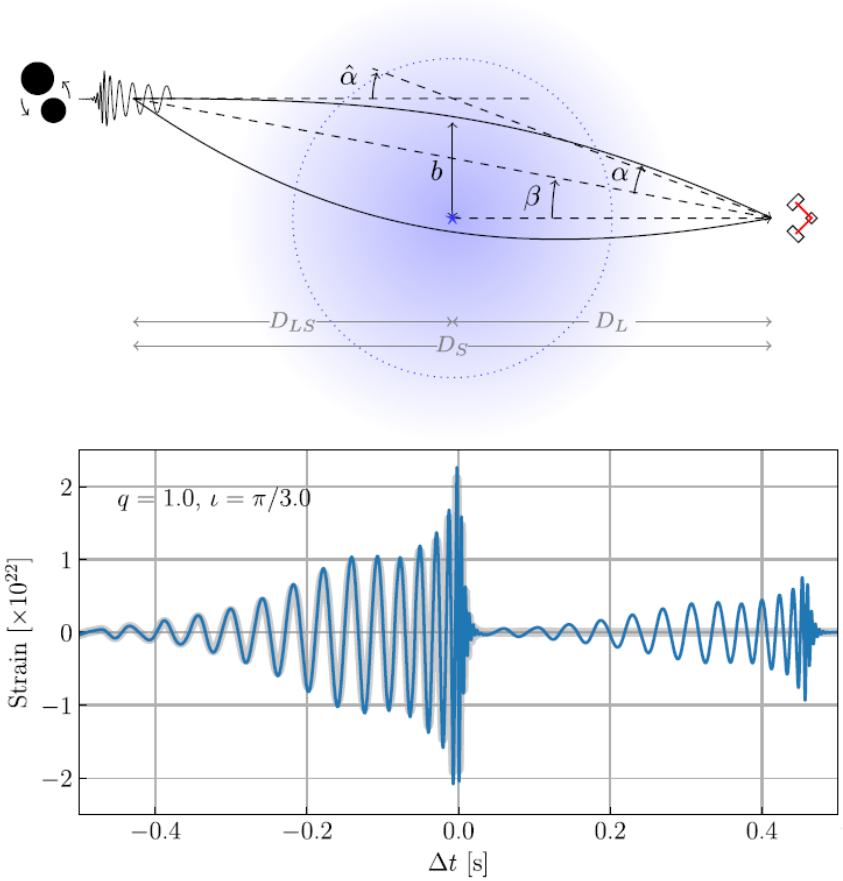

Figure 3.5: In the top figure there is a schematic representation of the lensing mechanism. GW radiation emitted from a coalescing COs binary (top left) in its propagation encounter a energy-mass distribution (central point) and undergoes the gravitational lensing effect before reaching the observer (bottom right). Credits to [67] In the bottom plot is plotted as a function of time the GW strain for the original (grey) and lensed (blue) GW signal for a non spinning circular binary with equal masses. Credits to [68]

Gravitational lensing is the deflection of light rays due to the presence of inhomogeneous matter distributions in the Universe, figure 3.5 top panel. If a gravitational wave pass nearby massive objects such as galaxy, galaxy cluster or even stellar mass celestial bodies or compact objects, gravitational lensing should occur in the same way as it does for light. Furthermore, the gravitational lensing of light can usually be studied through the geometrical optics approximation (which is valid in all observational situations [69]), while for the lensing of gravitational waves the geometrical optic approximation does not hold. This is due to the GWs' wavelengths, which are huge, having comparable dimension with the Schwarzschild radius of many other astronomical objects. Nevertheless, for the fequency band of LIGO and Virgo detectors $f \in [10\,\mathrm{Hz} - 10\,\mathrm{kHz}]$ [69] the geometrical optics approximation can be used as well as the possibility to study the geodesic equations in the weak field approximation, so through the linearised theory of gravity. For this study the most relevant

parameters involved in GW lensing are the arrival time delay Δt_{L-ij} between multiple copies (here i and j) of the original signal [70]:

$$\Delta t_{L-ij} = (1 + z_l)\frac{4G}{c^3} M(< \theta_{Einstein}) \,, \tag{3.6}$$

and the magnification factor $\sqrt{\mu}$ of the images with respect to the original signal. Here, in eq. (3.6), z_l is the redshift of the object acting as a lens, $M(< \theta_{Einstein})$ is the projected mass of the lensing object within the Einstein angle $\theta_{Einstein}$ assuming a spherically symmetric mass distribution for the lensing object. In literature [69, 70] there could be three type of gravitational lensing:

- **strong gravitational lensing**, where the deflecting objects are galaxy or galaxy cluster and a typical time delay between two images is of the order of month-few month;
- **microlensing** is due to lensing objects like the stars inside a galaxy or galaxy cluster, and as example for a Solar mass compact object $\Delta t_{L-ij} \sim 10^{-5}$s;
- **substructure lensing** arises when the lenses are small structure of dark matter (DM). Indeed, in the cold dark matter (CDM) model the DM's distribution inside galaxy and galaxy cluster is predicted to be lumpy.

Sure enough strong gravitational lensing and microlensing can act combined, but for this analysis microlensing is the most interesting gravitational effect that can be studied, since the predicted time delays (which could be greater than 10^{-5}s) foreseen the possibility to have two or more GW signals with different energies close in time, as shown in figure 3.5 bottom panel. Such possibility can fall into the general description of an energetic signal plus one or more signals, lower (probable) in energy, in its neighborhood.

Now, speaking about overlapping signals it is mandatory to differentiate between two possible scenarios: CBCs overlapping signals [71] and stochastic GW background signal overlapping or being nearby a CBC signal. The first case refers to two different CBC signals crossing the detectors simultaneously or with a minimal time delay one with respect to the other. Here, we are not willing to label such signals as sub-thresholds since for our data analysis algorithm it is impossible to discriminate between the presence or not of one or more GW signals inside the data. Such an excess of energy with respect to the detector noise energy level would be labeled as due to only one single GW perturbation. Thus, only further investigations focused on matching filter techniques could discriminate if the best fit of the data is obtained under the hypothesis of one single GW signal, or two overlapping or partially overlapping GW signals. In this picture, the two overlapping signals could both possess competitive energy well above the algorithm thresholds, and this is the reason why we prefer to think and treat such kinds of possible detections as not sub-thresholds signals. So, they are two signals unrelated one to the other which occur at the same times. The probabilities for such detections are well discussed in these papers [72, 73], even if the predicted probabilities for the future O4 observing run are of no overlapping BBH out of a predicted $\sim$ 130 BBH detections, and no overlapping BNS out of the predicted $\sim$ 10 BNS detections [72]. On the contrary, for Einstein telescope, [72] predicts that every detection of BBH or BNS will be an overlapping signals detection. In figure 3.6 there is an example of two CBC overlapping signals.

On the other hand, we could have GW signals from the stochastic gravitational wave background that can be present nearby the main detected CBC signal. These

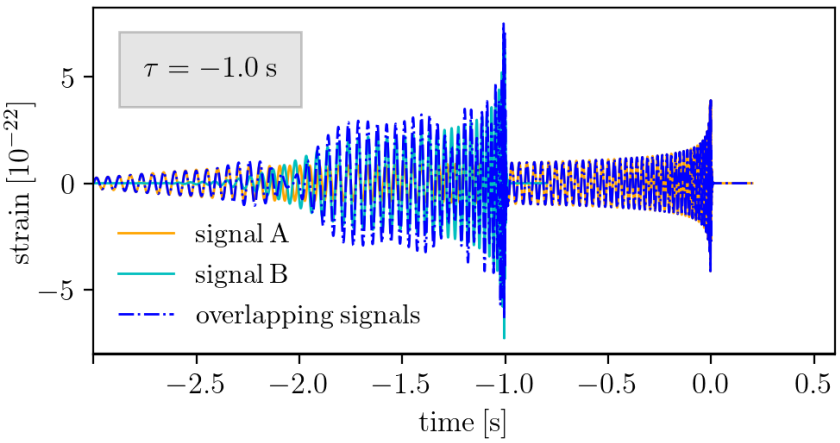

Figure 3.6: This figure shows two overlapping signals A and B and the resulting signal (blue). Their merger times are time separated by 1 s. The zero value of the x-axis is set in coincidence with the merger time of the second signal, B. Credits to [71]

GW signals were already discussed in this dissertation, chapter 2 section 2.1, so here we just recall that for current data analysis algorithm and GW detectors capabilities such signals would be classified as sub-thresholds signals and then they are not detectable with standard GW searches and current GW detectors. This is the reason why we are comfortable in treating these GW signals as possible subthreshold features that could be seen through a follow-up analysis of a CBC detection. Of course, such signals should be searched treating them as impurities contaminating the well-known time evolution of the detected CBC signals if overlapping or partially overlapping with it. The scenario is similar to the one previously described, but the nature and energy of the signals are quite different since they are expected to be weak signals compared to a standard CBC and generated from different physical scenarios.

Chapter 4

Detecting gravitational waves

Reached this point we had a general overview about the theory behind GWs, their sources and the possible low energetic signals associated to specific GW transients. So, how can GWs be detected? Shortly, thanks to interferometers. In this chapter I will try to describe how a gravitational wave detector works, the type of data it can provide, and I will conclude with an outline of the major sources of noise for these instruments and how such noises affect the data.

4.1 GWs detectors: interferometers

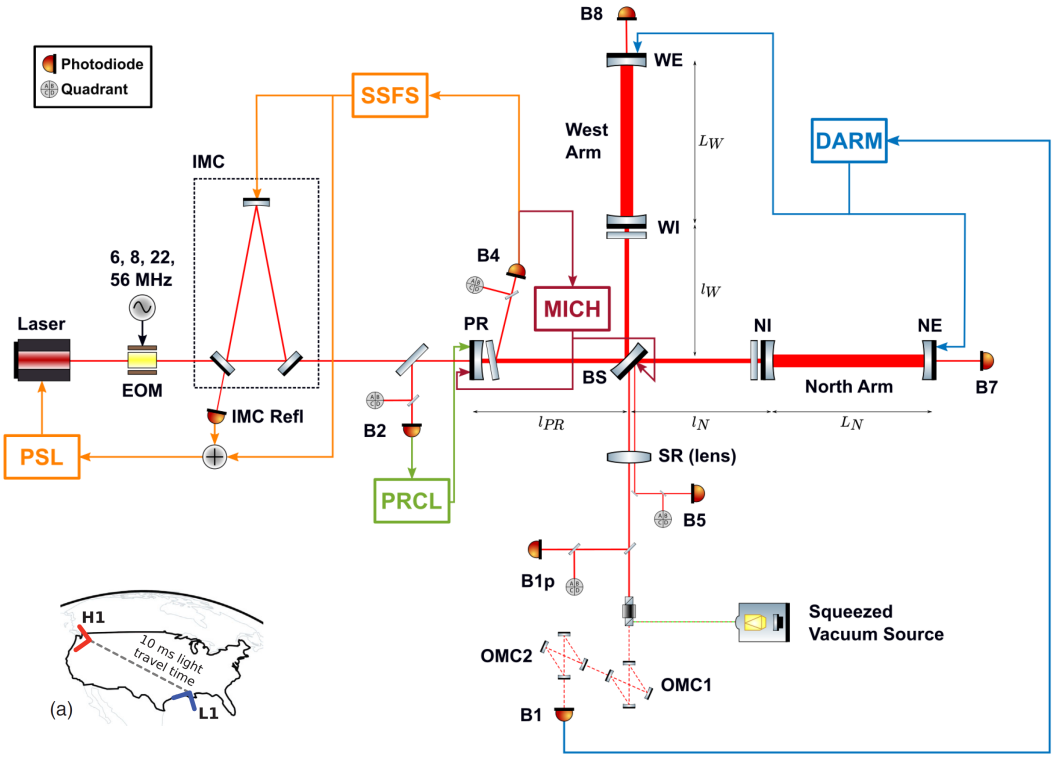

Figure 4.1: Here is represented schematically the set-up of the LIGO interferometers (the picture is not in scale). In the lower left corner there is a small map showing the location of the two detectors **H1** and **L1**. As in Section 1.4 if an incident GW linearly polarised hits the interferometer perpendicularly to the plane defined by the arms then the interferometer's arms are streched by a quantity δL while the other has its length reduced by the same quantity. This picture is taken from [74].

Current operating gravitational wave detectors at zero order approximation are Michelson interferometers (MI), an instrument invented in 1880's by Albert Abraham Michelson, which is designed and operates as follow.

- The starting point of an interferometer is a laser source which emitts a laser beam with gaussian profile (nevertheless, aiming to simplicity, I will approximate the beam as a collection of propagating plane waves). The emitted light hits a beam splitter oriented at 45° with respect to the propagation direction of the laser beam.
- A the beam splitter the light beam is divided into two equal components with a phase difference of $\pi/2$ (being perpendicular between them). The two beams travel through the L-shaped intereferometer arms.
- At the end of each arm there is a nearly perfectly reflective mirror (called *end mirror*) which reflect back the radiation towards the beam splitter. Here the two laser beams recombine and a major fraction of it is transmitted to a photodiode which measures the intensity of the radiation.

These scheme is illustrated in top right corner of figure 4.1. However, current GW detectors are much more complex and larger device if compared to a simple and standard Michelson interferometer [75], indeed we can say that the typical configuration of current GW detectors is a dual-recycled Fabry-Perot Michelson interferometer, figure 4.1. The major difference with respect to a MI is that the arms are Fabry-Perot cavities, which means that a partially reflective mirror (called *input mirrors*) is added at the beginning of each arms, immediately after the beam splitter, figure 4.1. A Fabry-Perot cavities allows the laser beam to be reflected multiple times between the input and end mirror leading to an increase of the beam power and the optical path.

Nowadays GW detectors have arms with a length ($L = L_x = L_y$) of the order of some km [1] which, without fabry-Perot cavities, wont be sufficient to detect GWs signals. Take a GW generated from CBC coalescence with component masses between 1 $M_\odot$ and $10^2 M_\odot$: the signal frequency near the merger time would be in the frequency band between 10Hz and 10^3Hz resulting in a GW wavelengths around 10^4km and 10^2km, far greater than the detector arms length. Fabry-Perot cavities allows to increase the optical path of the laser beam to the order of thousands of km which actually is enough to detect GWs.

4.1.1 Detector signal

The output of any GW detector is a time series, and for interferometers it describes the phase shift of the light after it has travelled inside the detector arms and has recombined. Since we are not in an ideal world, the output $s(t)$ will be a combination of the true GW signal $\xi(t)$ and noise $n(t)$ [76]:

$$s(t) = \xi(t) + n(t)\,.^{2} \tag{4.1}$$

[1] LIGO detectors, L1 and H1, in USA have arms which are 4km length, while VIRGO V1 (Italy) and KAGRA K1 (Japan) have 3km arms.

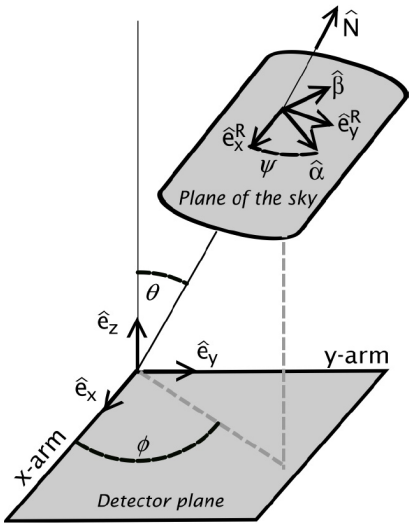

Figure 4.2: In this figure are shown the two planes which identify the detector reference frame and the wave reference frame. The detector plane is defined by the two orthogonal arms of the detector, while the wave plane is assumed to be orthogonal to the propagation direction of the wave (for plane waves). The angle θ and ϕ are referred to the detector plane while the Ψ angle defines an arbitrary rotation of the polarization components of the wave inside the wave plane. Credit: [78].

For an interferometer with equal arms length L, in the xy-plane the value of $\xi(t)$ is given by:

$$\xi(t) = \frac{L_x(t) - L_y(t)}{L} = \frac{(L + \delta L_x(t)) - (L + \delta L_y(t))}{L} = \frac{(\delta L_x(t) - \delta L_y(t))}{L}\,, \quad (4.2)$$

where $\delta L_x(t)$ and $\delta L_y(t)$ are the arms displacement produced by the passage of the GW. It is possible to link the scalar output $\xi(t)$ to the gravitational wave strain $h_{ij}(t)$ (in the TT-gauge formalism) thanks to the *detector tensor* D^{ij} via [76]

$$\xi(t) = D^{ij} h_{ij}(t)\,. \quad (4.3)$$

The response of a detector to a GW has been calculated in the literature (Misner, Thorne & Wheeler 1973) and it is a coordinate transformation which links the wave's direction and polarization from the wave reference frame to the detector one [**det_1988**]. The detector tensor D_{ij} can also be expressed in the TT-gauge fomalism, like for $h_{\mu\nu}$ in section 1.3, such that it results to be a linear superposition of the two GW polarizations [77]:

$$\xi(t) = F_+ h_+(t) + F_\times h_\times(t)\,, \quad (4.4)$$

where the coefficients F_+ and $F_\times$ are known as *antenna patterns*.

Antenna pattern is evaluated through a spherical reference frame centred on the detector and having its x and y axis coinciding with the two interferometer's arms. Such scheme is depicted in figure 4.2, where the angles ϕ (longitude), θ (latitude), and Ψ (a general rotation of the polarization vector in the wave reference frame) define the GW propagation direction. With this convention the antenna pattern tooks

[2]It is possible to treat an interferometer as a linear system, then knowing its transfer function (TF) and working in Fourier domain, one can compute all quantities as if they are at the input or output stage of the device.

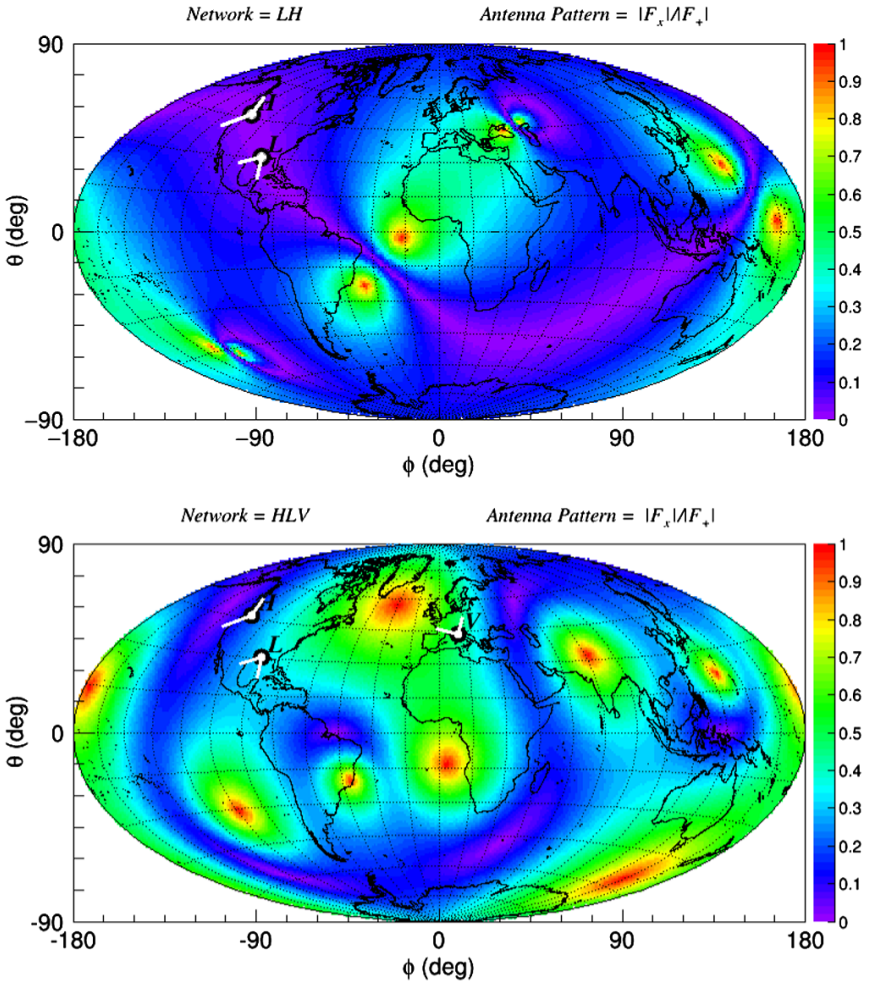

Figure 4.3: Ratio between $|F_\times|^2/|F_+|^2$ antenna pattern polarisations. **Top panel**: two aligned detectors' network (L1 and H1). **Bottom panel**: three detector network (L1, H1,and V1). In white are painted and oriented the detectors. Credits [79].

the following form [78]:

$$
\begin{aligned}
F_+(\theta,\phi,\Psi) &= \frac{1}{2}\left(1+\cos^2\theta\right)\cos 2\phi\cos 2\Psi - \cos\theta\sin 2\phi\sin 2\Psi\,,\\
F_\times(\theta,\phi,\Psi) &= \frac{1}{2}\left(1+\cos^2\theta\right)\cos 2\phi\sin 2\Psi + \cos\theta\sin 2\phi\cos 2\Psi\,,
\end{aligned}
\tag{4.5}
$$

which is valid only when the length scale of the perturbation, i.e. its wavelength, is larger with respect to the detector dimension.

4.1.2 Detectors network

Eq.(4.1) and (4.5) provide a good starting point to discuss why it is neccessary to have a network of ground base detectors to enhance both the detection sensitivity and reconstruction capability of GWs.

Noise, at first, can be thought as a stochastic process. On the contrary, a real astrophysical GW signal is a space-time deformation which affects all the detectors eith time coincidence and coherently; then multiple detectors would help in ruling out false positive signals just by looking at the coherence or uncoherence of the signals

between the detectors of the network. Furthermore, from eq. (4.5) if a cross polarised GW hits the detector orthogonally to the xy-plane, such that both the detector's arms undergo to the same length variation, no signal would be recorded because of the overall null effect of the GW. Because of this, having more than one detector operating around the world would benefit the possibility to cover a more wild sky region, increasing the probability to detect GWs signals. This is shown in figure 4.3 where in the top panel the antenna pattern coverage for the single GW detector scenario and a three detectors network (in the bottom panel) scenario are shown. Moreover, one single detector cannot be sensitive to both the polarizations of an incoming sgnal. The sky localization is not known a priori, then it is not possible to impose any constrain over the angular variables of the antenna pattern tensor D_ij. A single detector will attribute all the signal to only one polarization state, while more non aligned detectors, in particular if oriented 45° one to the other (without taking into account the Earth curvature), would be able to place more severe constraints over the angular parameters of the souce and its polarization states.

Nowadays several GWs detectors are now operating in in the world and further are planned to join the network. The operative GW detectors [3] are **H1** in Hanford (Washington, USA), **L1** in Livingston (Louisiana, USA) and **V1** in Cascina (Pisa, Italy) as well as **K1** in Kagra (Japan) and the resonant mass detectors of the International Gravitational Event Collaboration (IGEC). However, of all these detectors only H1, L1, V1 and K1 (K1 will join in the future observing run O4 of 2023) are sensitive enough to detect GWs.

4.2 The noise

We have seen in section 4.1 that detecting GWs means being able to measure the relative displacement between the two detector's arms due to a GW transient. At the end of chapter 1, section 1.7, we discussed that the expected strain for a GW is of the order of $h \sim 10^{-21}$, then GW detectors should aim at measuring length variation of the order of 10^{-18}m, which is a very demanding task. Nevertheless, nowadays detectors are capable to reach such precision.

To perform such a study the main noise sources are treated as gaussian-like, gaussian and stationary processes, thus the spectral theorem can be applied allowing the possibility to describe both the output signal of the detector $\tilde{s}(f)$ and the noise $\tilde{n}(f)$ in the frequency domain [81]:

$$\tilde{s}(f) = \sqrt{2S_s(f)}\,,^{4} \tag{4.6}$$

$$\tilde{n}(f) = \sqrt{2S_n(f)}\,, \tag{4.7}$$

[3] To the list of interferometers there is **GEO600** in Sarsted near Hanover but it is not as sensitive as the others, so it is not taken into account.

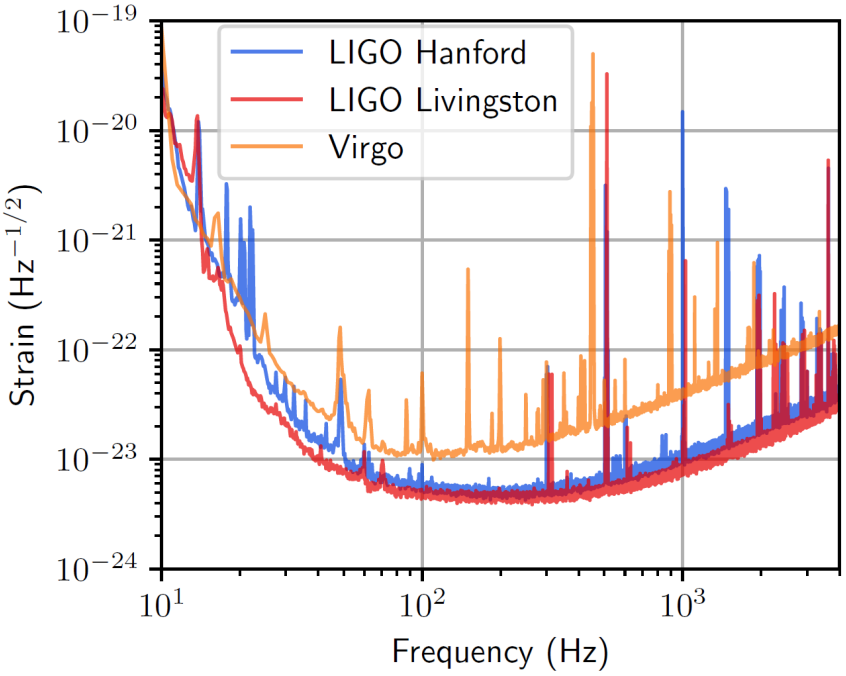

Figure 4.4: Amplitude spectral density (y-axis) of the three detectors' strain sensitivity. L1 (5 September 2019 20:53 UTC), H1 (29 April 2019 11:47 UTC), and V1 (10 April 2019 00:34 UTC) as a function of the frequency (x-axis). Credit: [80]

where $S_s(f)$ and $S_n(f)$ are the signal and noise power spectral densities respectively. They are defined as [81]:

$$S_s(f) = \lim_{T\to\infty} \left| \frac{1}{2T} \int_{-T}^{+T} s(t) e^{-i\omega t} dt \right|^2, \tag{4.8}$$

$$S_n(f) = \lim_{T\to\infty} \left| \frac{1}{2T} \int_{-T}^{+T} n(t) e^{-i\omega t} dt \right|^2. \tag{4.9}$$

with T being the integration time and $\omega = 2\pi f$ (f is the frequency). The amplitude spectral sensity $S^{(1/2)}(f)$ is the square root of the energy spectral density $S(f)$, $S^{(1/2)}(f) = \sqrt{S(f)}$ and it is in units per square root of Hertz, $1/\sqrt{\text{Hz}}$. In figure 4.4 it is reported the noise amplitude spectral density ($S^{1/2}(f)$) as a function of the frequency for the current generation of GW detectors.

For a GW interferometer the noise floor is determined by four main noise contributions: the *shot noise*, the *radiation pressure noise*, the *siesmic noise*, and the *thermal noise*. To have a direct understanding of a detector's performances, in general, it is used to study the amplitude spectral density of the overall noise of the instrument. The theoretical aplitude spectral density for such noise sources and how they contribute in the overall amplitude spectral density for a GW detector is reported in figure 4.5, which shows the noise budget for the Virgo detector in its advanced Virgo plus configuration.

[4]The 2 factor is introduced since only positive frequencies are considered, thus we have a one-sided power spectral density (PSD).

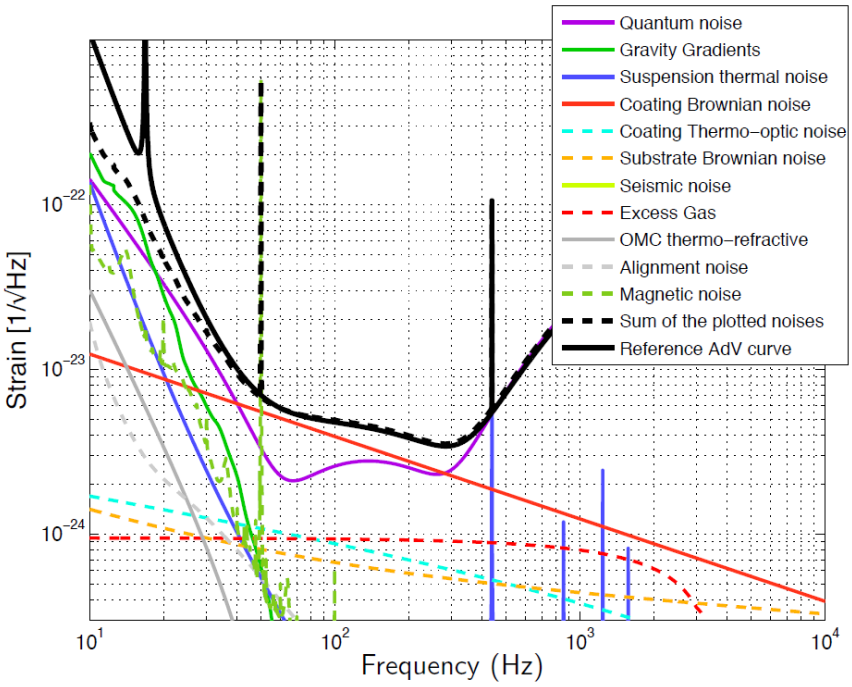

Figure 4.5: Comparison of the AdV reference sensitivity, $S^{(1/2)}(f)$ (solid black) compared to an AdV noise budget $S_n^{(1/2)}(f)$ (dashed black) as function of the frequency. In the figure are represented the single components of te noise budget such as the quantum noise (violet), radiation pressure noise, seismic noise, and thermal noise. Credit: [82]

4.2.1 Shot noise

The shot noise has its origin in the laser source of an interferometer and it arises from the quantistic nature of the light. At the output of a detector there is a photodetector which measures the average power (P) of the laser beam with frequency ω_L hitting its surface. Measuring the power

$$P = \frac{1}{\Delta t} N_\gamma \hbar \omega_L \,, \tag{4.10}$$

practically means to count the number of photon (N_γ) hitting the counter in a time period Δt. Since here photons are discrete and independent, we can say their statistics follows a Poisson distribution. Moreover, when dealing with a high number of photons, a Poisson distribution can be approximate to a Gaussian distribution with a standard deviation equal to $\sqrt{N_\gamma}$, so

$$\Delta N_\gamma = \sqrt{N_\gamma} \,. \tag{4.11}$$

These fluctuations in the photon number are reflected into power fluctuations P_{shot} estimated as:

$$\begin{aligned} P_{shot} &= \frac{1}{\Delta t} \sqrt{N_\gamma} \hbar \omega_L \,, \\ &= \sqrt{\left(\frac{\hbar \omega_L}{\Delta t} \right) P} \,. \end{aligned} \tag{4.12}$$

By looking at the ratio between the signal and noise power, and assuming the shot noise as the only source of noise, we have that:

$$\frac{P_{signal}}{P_{shot}} \propto \sqrt{P_0}\,, \tag{4.13}$$

where P_0 is the input power to the inteferometer. It is possible to express the above results, eq.(4.13) in terms of noise amplitude spectral density $S_n^{(1/2)}(f)|_{shot}$ as:

$$S_n^{(1/2)}(f)|_{shot} \propto \frac{1}{\sqrt{P_0}}\,, \tag{4.14}$$

where f labels the frequency of interest. This means that it is possible to reduce the shot noise (if dealing only with it) increasing the laser power.

4.2.2 Radiation pressure noise

Even if increasing the input power appears to provide a beautiful solution to mitigate the effects of the shot noise, we need to remember that a light beam impinging on a mirror, and then being reflected back, exerts a pressure on the mirror itself. Since the power of the light beam fluctuates also the pressure fluctuates: this leads to an instability, having that the mirror shakes nearby its equilibrium position. The amount of force ($|F|_{rp}$) exerted over the mirror by the light beam is proportional to $\sqrt{P_0}$, then increasing the input power increase also the radiation pressure noise. It is possible to quantify the noise amplitude spectral density of the radiation pressure fluctuations as:

$$S_n^{(1/2)}(f)|_{rp} \propto \frac{1}{f^2}\sqrt{P}\,. \tag{4.15}$$

As expected eq. (4.15) shows that the amplitude spectral density of the radiation pressure noise is proportional to $\sqrt{P}$, this suggests that the optimal noise reduction in order to beat both the shot noise and radiation pressure noise should be obtained by choosing the input power for which the combined amplitude spectral density $S_n^{(1/2)}(f)|_{ql}$ of the two noise's sources:

$$S_n^{(1/2)}(f)|_{ql} = S_n^{(1/2)}(f)|_{shot} + S_n^{(1/2)}(f)|_{rp} \tag{4.16}$$

is the lowest as possible for a fixed frequency f. This leads to a lower limit on the amplitude spectral density of the combined noises which is called the *standard quantum limit* (SQL):

$$S_n^{(1/2)}(f)|_{SQL} = \frac{1}{2\pi L}\sqrt{\frac{8\hbar}{M}}\,, \tag{4.17}$$

where L and M are the intereferometer arms length and mirror mass. It is important to underline that this is the minimum value of the amplitude spectral density of the shot noise and radiation pressure noise combined for a fixed frequency f. At different frequencies, to reach the standard quantum limit, one has to re-evaluate the best input power for that given frequency, so each frequency has its own preferred input power P. Such combined noises will dominate the noise spectrum at frequencies above 200 Hz [83].

4.2.3 Seismic noise

This noise source is due to ground vibrations such as siesmic background (Newtonian noise), natural vibrations as the wind forces coupled with trees or buildings, and man-made sources like traffic on roads or railroads. All of these vibrations are transmitted to the mirrors through their suspensions which are indeed designed to suppress such effects, but at very low frequencies, less than 50 Hz [83, 82], their effectivness drop drastically. Such drop prevents the ground-base GW detectors to be effective below $\sim$ 10Hz which are frequencies typical of human activities [83]. The siesmic noise possesses a strain sensitivity which can be translated into a mirror displacement $x(f)$:

$$x(f) \sim A \left(\frac{1\text{Hz}}{f^n} \right) \frac{\text{m}}{\text{Hz}}, \tag{4.18}$$

where A is an amplitude factor of the order of 10^{-7} in typical quiet places, and the index n is ~ 2 for frequencies greater than 1Hz. While seismic noise can be attenuated "in principle" arbitrarily, the Newtonian noise cannot be suppressed since gravitational forces cannot be screened. The newtonian noise is due to the fluctuations in the gravity gradient arising from the micro-siesmic noise which is responsable for the fluctuations density of Earth and so for its own gravitational field. The siesmic noise is the dominant effect at low frequencies and major contributor to the total noise amplitude spectral density for a GW interferometer.

4.2.4 Thermal noise

This noise source induces vibrations both in mirrors and suspensions and can be studied through the fluctuation and dissipation theorem. The major contribution to the thermal noise in a gravitational wave intereferometer are listed below.

- The suspension thermal noise. Vibrations arising in the suspension of the mirrors lead to perturbations in the equilibrium position of the mirror. Such vibrations can originate from the swinging motion of the suspension, from the vertical motion of the suspension as well as from the so called violin modes, vibrational modes associated to the normal modes of the wires.

- The test-mass thermal noise. Such vibrations arise within the test-masses themselves. One can have noise due to the Brownian motion of the mirrors where the atoms have a Brownian motion and give the mirror thermal noise, thermoelastic fluctuations from the dilatation or compression of the material following temperature variations, and thermo-reflective fluctuations. They are due to the variability of the refraction index of the mirrors which is dependend from the temperature and so temperature oscillations induces variations in the refraction index.

These noise will mostly affect the frequency band between 70 Hz $-$ 200 Hz [83].

Chapter 5

The search for low energy signals

The goal of this novel data analysis method is not the detection of strong (high signal to noise ratio) GW signals, they already have been detected by many GWs' searching algorithms inside LVK collaborations [14, 15, 16, 17]. Conversely, the proposed search aims to investigate the presence or not of low energy signals or features (see chapter 3) nearby a BBH coalescence.

This kind of study can be extremely helpful, or even mandatory, in the current era of GW astronomy; it is not unlikely that when a BBH signal is detected and its waveform is recovered from the data, its purity is contaminated by noise effects (section 4.2). Such noise effects can manifest as excesses of energy over a clean Gaussian noise in the proximity or even partially overlapping with the BBH signal. Therefore, we need methods to discriminate between noise disturbances and possible genuine effects, either consistent or not with GR as we discussed in chapter 3. Then, to develop and test this search I have decided to use the science case study of **echoes signals** which are presented in section 3.1 of this dissertation.

I applied this method to all the GW events detected by the all-sky burst search configuration of coherent WaveBurst (cWB) [84, 85, 86] in the O1, O2 and O3 observing runs which possess a network *snr* greater than ten, $snr_{net} \geq 10$ [1]. What is the meaning of all-sky burst search configuration of cWB (as well as cWB itself) will be clear in the following.

5.1 Why are GWs' searching algorithms needed?

It is well established that the signal extraction from the noise is crucial for any gravitational wave observatory: if we take as an example the first GW ever detected, GW150914 [24, 39] the LIGO-Hanford (H) detector's output signal was the one in figure 5.1a, and the GW signal is buried into the noise. In order to extract information from such data, algorithms of data analysis are needed, and thanks to them it is possible to pass from the signal in figure 5.1a to the one in figure 5.1b: here the GW signal GW150914 can clearly be seen.

One can search for a GW signal or via *matched-filter thecniques* or via *un-modeled searches*. Matching-filter pipelines rely on selected waveform models, compliant or not with GR, to scan the data and use matched-filter techniques to extract the signal candidates [87]. On the contrary, un-modeled searches do not rely over specific signal morphologies, so they result more open to poorly modeled signals.

Moreover, among un-modeled searches, there are two philosophies one can use to study GW data: *coincidence methods* [88] and *coherent methods* [88, 89]. Coincidence methods identify GW candidates in each individual detector using an excess of power statistics and then requiring the time coincidence of the selected triggers

[1] The reason for such a cutoff will be explained in the following.

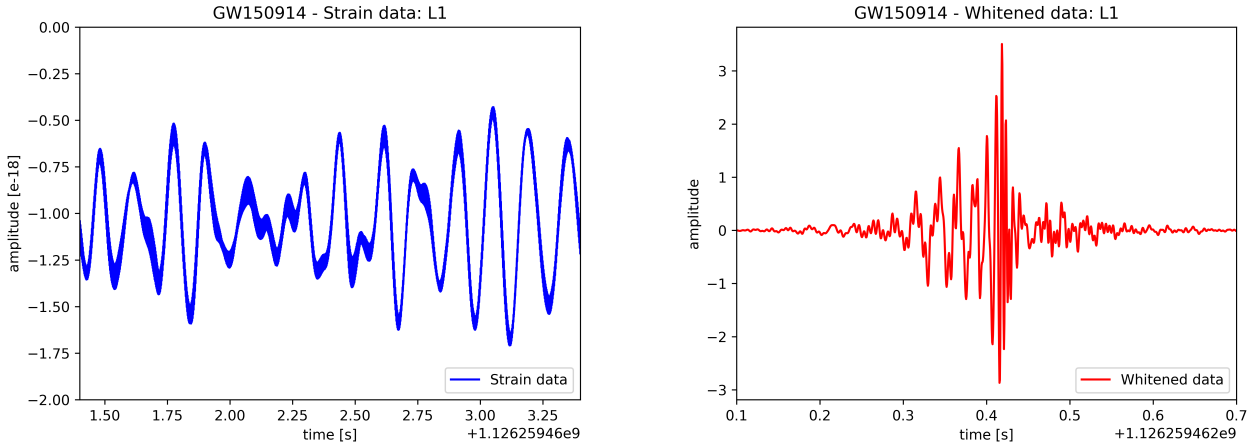

(a) GW150914 data.

(b) GW150914 clean data

Figure 5.1: GW150914. Comparison between the output time data series from the Livingston (L1) GW detector 5.1a (not whitened), and the same data 5.1a but cleaned. Cleaned data are obtained by the output data that are filtered to remove known noise spectral lines, and whitened. Data are taken from [13].

between the interferometers of the network. Coherent methods usually take advantage of an excess power triggering stage and analyse triggers with a coherent statistics over the data streams of the different detectors. Between these two approaches, the coherent ones result to have a better sensitivity for given false alarm probability than coincident methods [2] [89].

That said, the data analysis algorithm used here to develop a search for low energy signals nearby BBH transients is the coherent WaveBurst (cWB) algorithm [90], which was the first algorithm to identify the GW150914 signal, detected by the LIGO interferometers on September 14th, 2015 [24].

5.2 Coherent WaveBurst (cWB)

Coherent WaveBurst (cWB) is a coherent un-modeled data-analysis tool capable to search for a broad range of GW transients. The pipeline identifies coherent events in the GW data from earth-based interferometric detectors and reconstructs the gravitational wave signal by using a *maximum likelihood* approach.

5.2.1 Maximum likelihood (ML) approach

Maximum likelihood (ML) approach allows to extract from the detectors' data $s[i]$ (see eq. (4.1)) both the GW signal $h[i]$, and the sky position (θ, ϕ) of the source (i is the independent data sampling index, since we are working with discrete signals). Such approach, introduced by Flanagan and Hughes [91], defines the likelihood ratio $\Lambda(s, \Omega)$ as [92]:

$$\Lambda(s, \Omega) = \frac{\mathcal{P}(s|h(\Omega))}{\mathcal{P}(s|n)}\,, \tag{5.1}$$

where $\Omega = (h_+, h_\times, \theta, \phi)$ is the general set of parameters which describe the signal, $\mathcal{P}(s|h(\Omega))$ is the probability that data s contain a GW signal ($h(\Omega)$), and $\mathcal{P}(s|n)$ is the

[2] For coherent methods the sensitivity is not limited by the least sensitive detector inside the detectors' network.

probability that in the data is present only instrumental noise n. The explicit form of the likelihood ratio is determined by the signal model $h(\Omega)$ and noise model $\mathcal{P}(s|n)$. The noise of the detectors' network can be approximated to a quasi-stationary Gaussian noise:

$$\mathcal{P}(s|n) = \prod_k \left(\prod_i \frac{1}{\sqrt{2\pi\sigma_k^2}} \exp\left(-\frac{s_k^2[i]}{2\sigma_k^2} \right) \right) , \tag{5.2}$$

with σ_k the standard deviation of the noise and k the detector index, $k \in 1, 2, ..., N$. Then, since CWB makes no assumptions over the signal morphology we have:

$$\mathcal{P}(s|h(\Omega)) = \prod_k \left(\prod_i \frac{1}{\sqrt{2\pi\sigma_k^2}} \exp\left(-\frac{(s_k[i] - \xi_k[i])^2}{2\sigma_k^2} \right) \right) . \tag{5.3}$$

From the likelihood ratio $\Lambda(s, \Omega)$ we can define the likelihood function $\mathcal{L}(s, \Omega)$ as:

$$\mathcal{L}(s, \Omega) = \log\left(\Lambda(s, \Omega)\right) = \sum_{k=1}^{N} \sum_i \left(\frac{s_k^2[i]}{2\sigma_k^2[i]} - \frac{(s_k[i] - \xi_k[i])^2}{2\sigma_k^2[i]} \right) , \tag{5.4}$$

$$\mathcal{L}(s, \Omega) = \sum_{k=1}^{N} \sum_i \left(\frac{s_k[i]\xi_k[i]}{\sigma_k^2[i]} - \frac{1}{2}\frac{\xi_k^2[i]}{\sigma_k^2[i]} \right) \tag{5.5}$$

so, in the maximum likelihood approach, the likelihood $\Lambda(s, \Omega)$ is maximised via numerical variation over the parameter space Ω, obtaining $\mathcal{L}(s, \Omega)_{max}$. This allows to recover the best combinations of $(h_+, h_\times, \theta, \phi)$ from the data [92, 89, 79]. The same procedure and eq. (5.5) can also be interpreted as a more general least square method without requiring the assumption of Gaussian noise [79].

Within our formalism, the detector response to a GW $\xi[i]$ can be expressed as in equation 4.4:

$$\xi_k[i] = F_+[i]_k \, h_+[i] + F_\times[i]_k \, h_\times[i] \, , \tag{5.6}$$

where F_+ and $F_\times$ are the polarisation components of the antenna pattern for detector k. Since $\xi_k[i]$ is invariant for Φ-rotations ($R_{(\Phi)}$) in the wave frame [92], by appling a very specific Φ-rotation to the system, described in [92], one recovers a coordinates system in which the components of the detector's antenna pattern are orthogonal:

$$F_+^k \overset{R_{(\Phi)}}{:\longrightarrow} f_+^k \, , \qquad h^+ \overset{R_{(\Phi)}}{:\longrightarrow} \tilde{h}_+ \tag{5.7}$$

$$F_\times^k \overset{R_{(\Phi)}}{:\longrightarrow} f_\times^k \, , \qquad h^\times \overset{R_{(\Phi)}}{:\longrightarrow} \tilde{h}_\times \, , \tag{5.8}$$

$$f_+^k \cdot f_\times^k = 0 \, . \tag{5.9}$$

Then, having

$$\xi_k[i] \; = \; f_+[i]_k \, \tilde{h}_+[i] + f_\times[i]_k \, \tilde{h}_\times[i] \tag{5.10}$$

also the maximum likeihood ratio can be rewritten as [89]:

$$\mathcal{L}(s,\Omega)_{max} = \mathcal{L}(s,\Omega)_{max,+} + \mathcal{L}(s,\Omega)_{max,\times} \tag{5.11}$$

$$\mathcal{L}(s,\Omega)_{max,+} = \sum_{k=1}^{N} \sum_{i} \left(\frac{(s_k[i] \cdot f_+[i]_k)\, \tilde{h}_+[i]}{\sigma_k^2[i]} - \frac{1}{2} \frac{(f_+[i]_k \tilde{h}_+[i])^2}{\sigma_k^2[i]} \right) \tag{5.12}$$

$$\mathcal{L}(s,\Omega)_{max,\times} = \sum_{k=1}^{N} \sum_{i} \left(\frac{(s_k[i] \cdot f_\times[i]_k)\, \tilde{h}_\times[i]}{\sigma_k^2[i]} - \frac{1}{2} \frac{(f_\times[i]_k \tilde{h}_\times[i])^2}{\sigma_k^2[i]} \right) . \tag{5.13}$$

Now, we can introduce a projector operator $\hat{P}_{nm}$ constructed from the components of $\hat{e}_+$ and $\hat{e}_\times$ (see section 1.20) of each detectors inside the network [79]:

$$P_{nm}[i] = \hat{e}_+[i]_n \hat{e}_+[i]_m + \hat{e}_\times[i]_n \hat{e}_\times[i]_m \,, \tag{5.14}$$

where n and m are the detector indeces. Then, it is possible to combine equations (5.13) and (5.14), such that equation (5.5) of $\mathcal{L}(s,\Omega)_{max}$ assumes the form [79]:

$$\mathcal{L}(s,\Omega)_{max} = \sum_{n,m=1}^{N} \sum_{i} s_n[i]\, \hat{P}_{nm}[i]\, s_m[i] \,. \tag{5.15}$$

Equation (5.15) allows us to define the *coherent* E_c and *incoherent* E_i energy. The coherent energy [79]

$$E_c = \sum_{n,m=1}^{N} \sum_{i} s_n[i]\, P_{nm}[i]\, s_m[i] \quad \text{with} \quad n \neq m \,, \tag{5.16}$$

defines the energy content of the detected signal which results to be coherent between the detectors of the network. We can expect that this energy is proportionally distributed between the detectors depending upon their sensitivity antenna pattern, and the GW signal polarisation. As an example, for the two LIGO, we can expect both the detectors to contribute to the coherent energy half and a half, very roughly. On the contrary, the incoherent energy [79]

$$E_i = \sum_{n,m=1}^{N} \sum_{i} s_n[i]\, P_{nm}[i]\, s_m[i] \quad \text{with} \quad n = m \,, \tag{5.17}$$

is the energy content of the detected signal which is not coherent among the detectors: it is present only in one interferometer and so it is not equally distributed inside the detectors' network. Together, these quantities estimate the overall energy content of the detected signal.

5.2.2 Initialisation stage

For cWB, applying the maximum likelihood approach over all the interferometers' data would be not feasible, so the pipeline needs to select the data segments which are worth to be analysed, it cleans these data in order to remove known noise features, and then the data are whitened. This procedure is performed in steps:

- **the initialisation phase**, where cWB takes in input the customised configuration of the analysis comprehensive of the network over which the analysis has to run and the periods of data that can be analysed (the intervals of time during which the interferometers were operating in science mode).

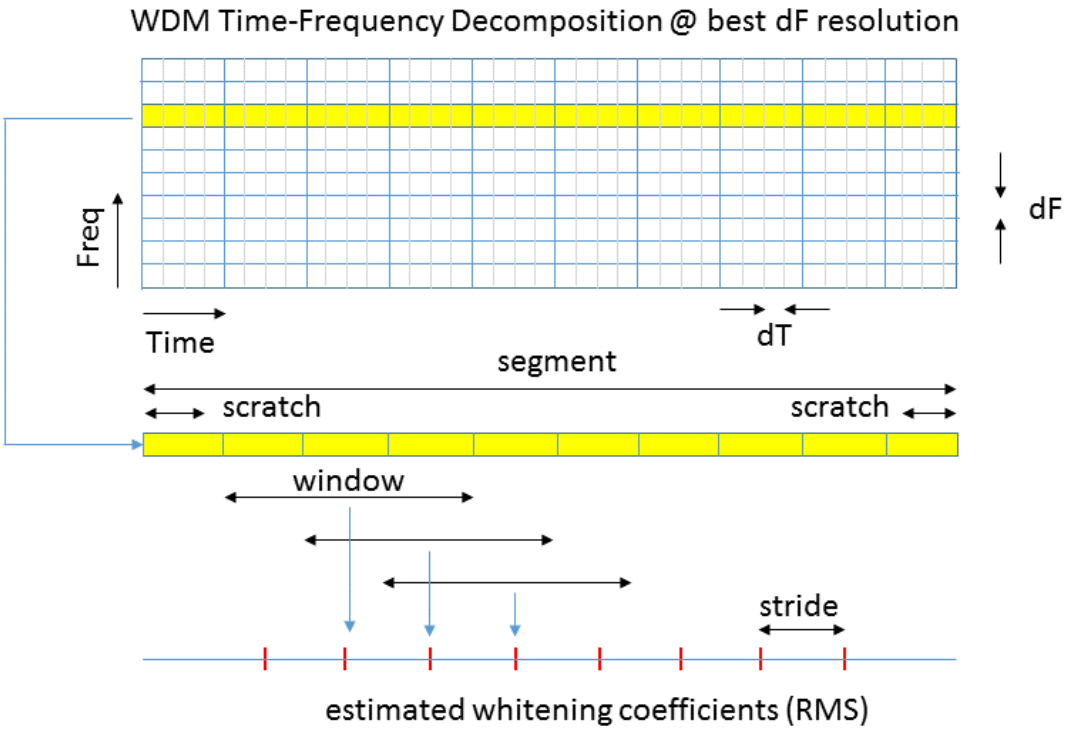

Figure 5.2: Schematic representation of the whitening procedure of the data performed by cWB algorithm. The time-frequency data representation over which the whitening coefficients (RMS) (red line at the bottom) are estimated, is the finest in frequency resolution, so $\Delta f = dF = 4\,\text{Hz}$. This holds for this search.

- **The readout phase**. Here cWB effectively takes in input the data and manipulates them if needed. Some examples of data manipulations are the injections of simulated GW signals, de-synchronising the data between detectors by applying a time shift over one or more data streams, or feeding the pipeline with completely artificial data (to simulate Gaussian noise, as an example).

- **The data conditioning phase**: here spectral lines are removed through data regression. Moreover, if present, noise features correlated to the auxiliary detector's channels are subtracted from the data [90]. Then, the data are transformed from a time domain into a time-frequency (TF) one, usually called time-frequency map or representation, thus in a TF map the data is a pixel. This process is obtained by applying over the time series of the data stream the fast Wilson-Daubechies-Meyer (WDM) transform [93]. For such transformation one needs to provide the desidered time (Δt) and frequency (Δf) resolution of the TF map in which the time series are transformed; such resolution has to fulfill the principle of Heisemberg's uncertainty:

$$\Delta t \cdot \Delta f \geq \frac{1}{2}\,. \tag{5.18}$$

In general cWB decomposes the data in seven TF resolution levels, each one with different time and frequency resolution: $2\,\text{ms} \leq \Delta t \leq 125\,\text{ms}$ and $4\,\text{Hz} \leq \Delta f \leq 256\,\text{Hz}$ [3]. The TF data are whitened: each TF pixel is normalised by the root mean square (RMS) of the noise energy. A sketch of the procedure

[3] These values belong to the used cWB configurations, but they can be modified if needed.

is shown in figure 5.2. The local noise energy RMS is evaluated on the finest frequency resolution between all the TF decomposition levels of the data. For each data segment cWB estimates the energy RMS of the data inside a moving window. In estimating the energy RMS the outliers' energy excess above 3σ are excluded by applying a criterion similar to the Chauvenet's procedure [94]. The estimated energy RMS is the whitening coefficient. It is applied at the center of the whitening window and it affects all the pixels inside the time interval centered on it and width half of the stride. The stride is the name given to the time shift applied to the whitening window. With such a procedure, adjacent whitening coefficients result to be partially time-correlated between them. Such a scheme hold for each frequency's lines (yellow line in figure 5.2) per each TF map.

5.2.3 Event trigger generator (ETG)

Following this initialization phase, cWB proceeds in constructing and selecting the triggers which have to be analysed and reconstructed by the pipeline. This process is called *event trigger generator* (ETG) and is the fundamental brick for whatever analysis one wants to perform with cWB algorithm. This stage is made up of two main phases. they can be summarised as follows:

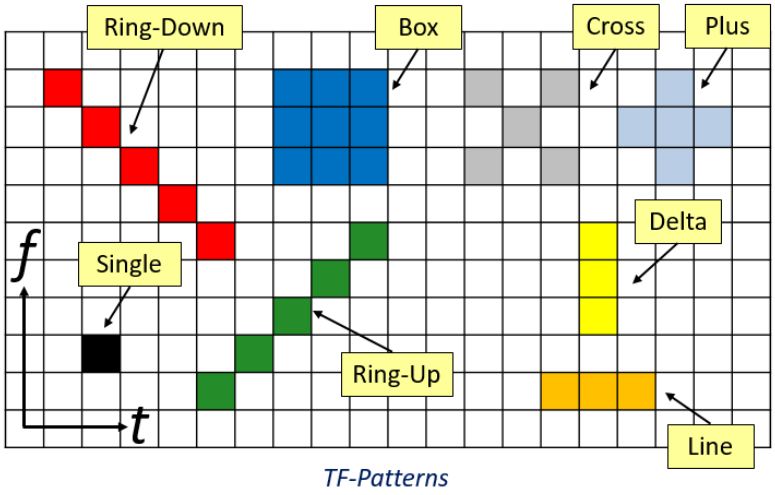

Figure 5.3: Visual representation of the possible pixels selection rules implemented in cWB algorithm. Each cluster of pixels is a mask, which scans the data evaluating the properties of the pixels and selecting or rejecting the ones which fulfill the thresholds and selection rules. On the y-axis there is the frequency, while on the x-axis the time to mimic a TF map. The single-pixel selection criteria (WP10) is the mask at the bottom left (black), while, immediately on his right in green the chirping-up selection criteria (WP5, in cWB), which is the best suited for CBC burst events detection.

- **The time-frequency (TF) pixel selection phase**. Here, for each TF resolution level, the excess power pixels are selected. Such pixels are called core pixels or hot pixels. Over the pixel energy distribution (for the analysed TF map), it is possible to define the core energy threshold. A pixel is selected if its energy is greater than double the core energy threshold [4] (this is the local rule), or if

[4] Here the data are already whitened, so the amplitude is evaluated in units of noise RMS.

its energy is greater than the core one and above twice the core energy when making a geometric mean with some neighboring pixels (this is the nonlocal rule). Once the core pixels are selected for each TF decomposition level, the next step is to identify the burst events. In cWB, burst events are defined as a group of pixels (clusters), and the clustering condition is the proximity of TF pixels in time and frequency. The way to perform such selection can be defined by the user, depending on the analysis that has to be performed, meaning that it is possible to say to cWB which pixels pattern it has to apply when evaluating the single-pixel energy and the surrounding pixels energy content in order to make that pixel pass both the local rule and nonlocal rule. There are multiple ways through which it is possible to scan TF maps and select pixels: they are shown in figure 5.3. To the scope of this dissertation, we can focus our attention on two of them, the *single-pixel selection* rule and the chirping selection one. The chirping selection rule is well suited to searching for chirping events, so signals whose frequencies increase with time, like BBH or BNS signals. In the cWB dictionary, such a selection pattern is labeled with *WP5*. The single-pixel selection rule is the most agnostic type of search available in cWB, and being the more symmetric search it is able to catch wider signals' morphologies if compared to the chirping configuration, which on the opposite has higher performances when signals possess a chirp shape. In cWB dictionary such selection pattern is labeled with *WP10*.

- **The multiresolution phase**, where the coincident clusters in all the different TF maps are grouped in one single trigger obtained by the "union" of the TF decomposition layers: we can call such trigger a multi-resolution clustering. In conclusion, over these triggers are applied some user-defined thresholds to determine if the multi-resolution cluster can undergo the maximum likelihood procedure (see section 5.2.1) or if it has to be rejected.

5.2.4 CWB thresholds

Once cWB selects a trigger and performs the maximisation of its likelihood, it also estimates lots of parameters relative to the event. These parameters can be divided into three categories: *thresholds* (th), *clustering conditions* (clc) and *regulators* (rg) depending upon the usage they are meant to. Threshold parameters are:

- **black pixel probability** (*bpp*). In formula it is defined as:

$$bpp = \frac{\text{n}^\circ \text{ of selected pixels}}{\text{n}^\circ \text{ of total pixels}} . \tag{5.19}$$

  Depending upon its value, cWB pipeline selects only a certain number of core pixels among all, starting from the most energetic one and decreasing: this holds for each TF resolution level.

- **network coherent coefficient** (*cc*). It is a statistical parameter of cWB defined as:

$$cc = \frac{E_c}{(E_c + E_i)} , \tag{5.20}$$

  where E_c and E_i are the coherent and incoherent energy respectively [79], see eg. (5.16) and (5.17) of the detected signal. It provides information about the coherence of a signal among the detectors of the network. It is one of the main

statistical estimators of cWB, and it is used as a threshold to discriminate between noise-like signals and true GW signals, since noise fluctuations, in general, present low *cc* values, while genuine GW signals show high *cc* values.

- **effective network coherent snr** (ρ). It is a parameter defined as:

$$\rho = \sqrt{\frac{E_c \cdot cc}{K}}, \tag{5.21}$$

and represents the coherent *snr* per detector of a trigger. It is an optimal statistical estimator, it is used as a threshold to rule out from the analysis a large portion of noisy events since they are characterized by a very stiff cumulative distribution.

- **subnetwork energy asymmetry statistic** (*subnet*). It is defined as:

$$subnet = \frac{E_s}{E_s + E_i}, \tag{5.22}$$

where $E_s = \min(E_c - E_k)$ with E_k the energy of the detector k. A noise glitch typically will have a significant energy only in one detector, while for others the energy level is defined by the underlying noise. On the contrary, a GW signal should display a more balanced distribution in energy between detectors, so subnet is used to check the symmetry in the energy distribution across detectors.

- **average amplitude** (*Acore*). It is a parameter on the average *snr* amplitude of the data pixel per detector.

CWB also owns other two hard-coded threshold parameters $SUBRHO$ and $SUBNET$ referred to the value of ρ, the detection statistic, and *subnet* respectively. Threshold parameters are mainly used to discriminate between signal and noise, if an event is discarded because its parameter values do not pass the threshold's values it means that the event is quite sure to be due to the noise.

Clustering parameters are used during the clustering stage of cWB pipeline. In a TF map, individual clusters closer to each other in time and frequency with respect to some thresholds are merged together:

- **Maximum time gap** (*Tgap*) and **maximum frequency gap** (*Fgap*): they are the maximum time (Tgap) and frequency (Fgap) gap allowed for two clusters of pixels to be considered part of a single trigger event. For the search presented here, the final configuration is $Tgap = 2\,\mathrm{s}$ and $Fgap = 128\,\mathrm{Hz}$.

Such parameters help in recovering GW signals which can be fragmented in multiple clusters of pixels. A schematic summary of all these parameters, their threshold values, and a brief explanation of their meaning can be found in appendix B.

5.3 Methodology to detect low energy signals

Up to now, we have seen how cWB operates and what are the main user-defined quantities of the cWB pipeline. Now it is time to see how cWB can be used to detect possible low energy GW signals nearby a BBH coalescence: GW echo signals (sec 3.1) are the chosen scientific case of interest to perform such a study. Therefore, I have developed a dedicated follow-up search to be used only after a successful BBH

detection by cWB pipeline. Besides, this requires to optimise the largely used [84, 85, 86, 14, 15, 17] cWB algorithm starting from its O3 all-sky burst search configuration [86]. We call this search the cWB "*low energy signal*" search, or **cWB LES search**.

Now, before digging into the major features of the analysis, here is a bit of terminology:

- **on-source event**: it labels the real detection on real data;
- **on-source search or analysis**: it labels a search performed over the real data;
- **off-source event**: it labels a detection of a simulated signal;
- **off-source search or analysis**: it labels a search run over the real data but with simulated signals added to them or in different conditions from the real ones;
- **template**: it refers to a waveform model (here) estimated from GR theory which is ready to be used;
- **job**: the smallest data period cWB can analyse: the input data segment is divided into smaller subsets with tunable time length, called jobs. CWB performs its analysis separately over single-time data segments contained in the job.

5.3.1 How to get a statistic?

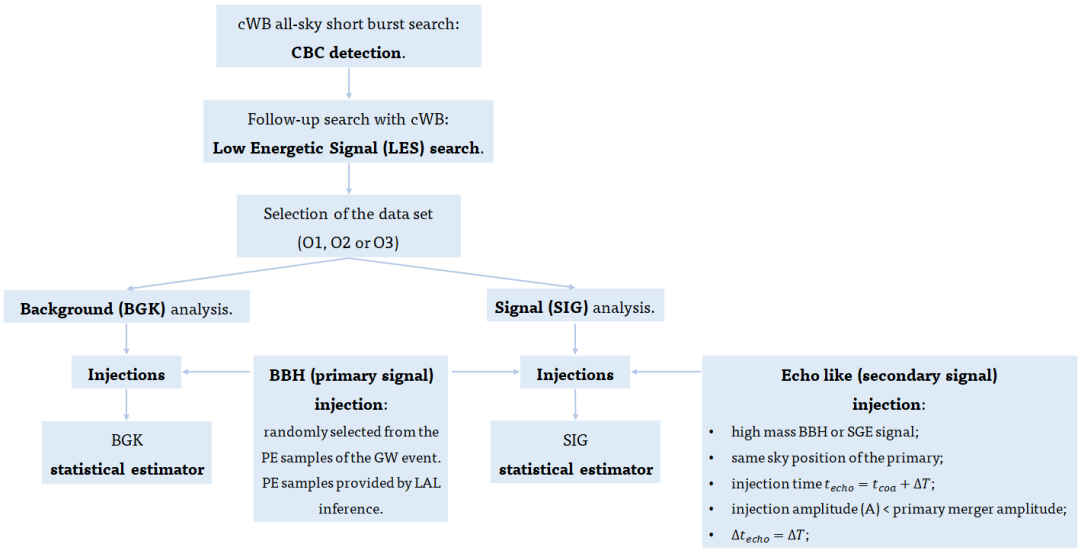

Figure 5.4: Visual representation of the flowchart of the LES search. Once cWB all-sky burst search detects a CBC event, mainly a BBH signal, then it is possible to run cWB LES search as a follow-up. Once the data set to perform the study is selected, the search runs two parallel studies: the background (BGK) and the signal (SIG) and computes all the statistical estimators described in section 5.3.2. The BBH or primary injections are randomly picked from the PE samples distribution for that event.

To understand the statistical significance (false alarm probability, FAP) of any on-source energy excess, its value has to be compared with a background distribution, the null hypothesis $\mathcal{P}(s|n)$. Similarly, to estimate its detection probability (DP), the on-source result has to be compared with a model distribution representative of the

low energy signal hypothesis $\mathcal{P}(s|echo)$ [5]. Aiming to this result, for each GW event under investigation, the analysis builds a background distribution (or null distribution) and the signal distribution. A flowchart of the LES search is reported in figure 5.4.

Background (BGK) distribution

The background distribution is obtained by performing off-source injections of the waveform's models of each specific BBH event over the data stream. These templates are randomly selected from the CBC posterior samples, provided by the Parameter Estimation (PE) methods, of the considered GW event. This simulation is then representative of the null hypothesis since by construction no other astrophysical signals are present inside the data except for the BBH one. We call the BBH signal *primary signal*, an example of these injections is reported in figure 5.5, where is visible the BBH reconstructed signal in its time (left) and TF (right) representations respectively. The primary signals are injected each 600 s such that each cWB job contains only one primary event; this injection rate will then preserve the whitening, avoiding the possibility to introduce systematic errors in the *snr* content of the TF pixels. If many BBH signals are injected very close in time, the whitening procedure, when estimating the mean energy inside the moving average window (see 5.2.3), can be affected by an overestimation of the average energy and so the overall *snr* is reduced because the whitening coefficient is larger than what should have been [6].

Signal (SIG) distribution.

Due to their predicted nature [51] echoes are expected to be emitted after the binary system has merged and the ECO remnant was formed (see section 3.1). The theorised time delay of the first echo signal, t_{echo}, with respect to the coalescence time t_{coa} of the primary signal is around the order of magnitude from some tenths to hundreds of a milli-seconds, accordingly with eq. (3.4). Also the time delay between subsequent echoes Δt_{echo} is predicted to be similar to t_{echo} [95, 96, 56], and both these values where evaluated following eq. (3.4). In table 5.2, from left to right, we have the GW event's name, the expected Δt_{echo}, whose value can be compatible also with the one expected for t_{echo}, for different ECO models n. Thus, the SIG distribution is obtained by performing a simulation that is the perfect copy of the background analysis and injecting, after each simulated BBH signal, a signal template to mimic echoes. We label these "echo" signals as *secondary signals*. Now, this simulation is representative of the GW signature predicted for a binary coalescence with an ECO remnant [42, 50, 51, 56]. Figure 5.5 shows an example of the BBH signal plus the would-be echoes: on the bottom row the time series on the left (figure 5.5c) and the relative TF map on the right (figure 5.5d).

5.3.2 Statistics

Now, over these two distributions, it is time to extract statistical estimators to be compared between them and to the on-source counterpart. Thus, an operative procedure to extract from cWB the most significant and accurate information a GW

[5] Here we have used the same terminology and symbology adopted in section 5.2.1

[6] This injection rate has a negative counterpart: the reduction of the statistics for a fixed data period. Nevertheless, it is possible to mitigate this drawback by running the analysis over a greater data period with a little investment in computational resources.

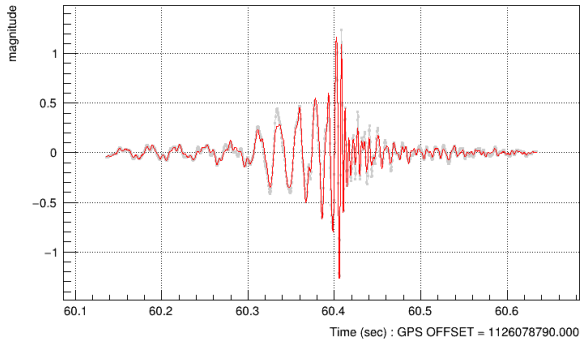

(a) BGK distribution: time series.

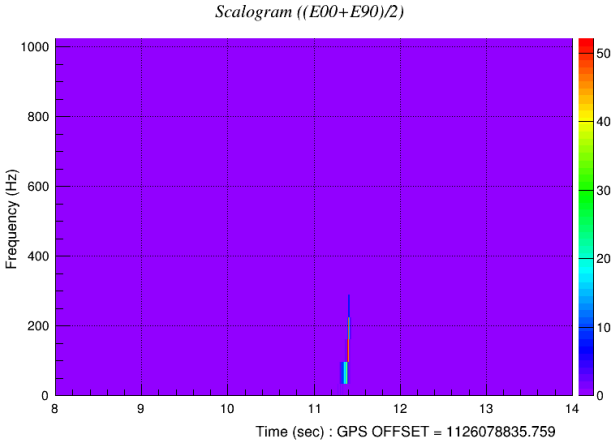

(b) BGK distribution, TF map.

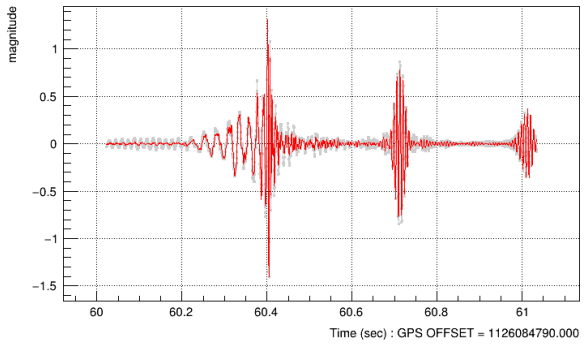

(c) SIG distribution, time series.

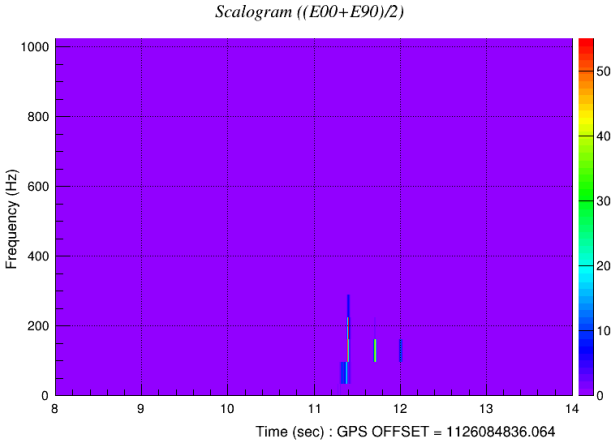

(d) SIG distribution, TF map.

Figure 5.5: Two examples of the injections performed in this analysis. Top: an example of injection for the background (BGK) distribution, only the primary signal (GW150914) is injected. Bottom: an example of injection for the signal (SIG) distribution, the primary (GW150914) plus the echoes mimicker signals are injected. For both scenarios, on the left there is the time representation of the signal, in amplitude, while on the right its TF representation.

unmodeled search can provide about a signal has to be implemented in cWB. Some general informations cWB provide once an injected signal is reconstructed are: the injected signal to noise ratio $iSNR$, and the reconstructed signal to noise ratio $oSNR$ (i - is for input while o - is for output) defined as:

$$iSNR = \sqrt{\sum_{k=1}^{N} \sum_{i \in C} (x_k^{inj}[i])^2} \tag{5.23}$$

$$oSNR = \sqrt{\sum_{k=1}^{N} \sum_{i \in C} (x_k^{rec}[i])^2}\,, \tag{5.24}$$

where k and i are the detector and time indices, C is the time interval analysed, corresponding to the times containing the 99.9% of the signal energy, and $x[i]$ is the

whitened data:

$$x_k[i,j] \equiv \frac{s_k[i,j]}{\sqrt{S_s[i,j]_k}}\,, \tag{5.25}$$

with $S_s(f)[i,j]_k$ the signal power spectral density and $[i,j]$ the convention used to index-link the TF pixels. It is straightforward to see that $iSNR$ and $oSNR$ correspond to the injected and reconstructed signal energy, since $E_{inj} = (iSNR)^2$ and $E_{rec} = (oSNR)^2$:

$$E_{inj} = \sum_{k=1}^{N}\sum_{i\in C}(x_k^{inj}[i])^2 \tag{5.26}$$

$$E_{rec} = \sum_{k=1}^{N}\sum_{i\in C}(x_k^{rec}[i])^2\,, \tag{5.27}$$

Then, it is possible to divide the reconstructed signal into two regions, the inspiral-merger (IM) one, which lasts till the coalescence time of the BBH, $t \leq t_{coa}$, and the post-merger (PM) phase of a binary: $t > t_{coa}$. As before we can define the *injected*, E_{inj}, and *reconstructed*, E_{rec} energy for these data regions:

$$E_{inj}^{IM} = \sum_{k=1}^{N}\sum_{i=i_{inf}}^{i_{coa}}(x_k^{inj}[i])^2, \qquad E_{rec}^{IM} = \sum_{k=1}^{N}\sum_{i=i_{inf}}^{i_{coa}}(x_k^{rec}[i])^2 \tag{5.28}$$

$$E_{inj}^{PM} = \sum_{k=1}^{N}\sum_{i=i_{coa}}^{i_{sup}}(x_k^{inj}[i])^2, \qquad E_{rec}^{PM} = \sum_{k=1}^{N}\sum_{i=i_{coa}}^{i_{sup}}(x_k^{rec}[i])^2\,, \tag{5.29}$$

where i_{inf} and i_{sup} are the indices i corresponding to the starting time and ending time respectively of the 99.9% energy interval for the injection, i_{coa} is the coalscence time index.

Inside these temporal regions it is possible to define other statistical estimators such as:

$$cc^{IM} = \frac{E_{rec}^{IM}}{E_{rec}^{IM} + E_{null}^{IM}} \tag{5.30}$$

$$cc^{PM} = \frac{E_{rec}^{PM}}{E_{rec}^{PM} + E_{null}^{PM}}\,. \tag{5.31}$$

They have the same meaning as the coherent correlation coefficient defined in 5.20, the difference only lies in the limited part of the signal over which they are evaluated. Indeed, the subscripts IM and PM underline that the quantity is evaluated only in the inspiral-merger or post-merger phase respectively. Then:

$$\text{detection probability} = \frac{n^\circ \text{ of events with } snr \geq snr.th.}{N_{tot}}\,|_{\text{for SIG analysis}} \tag{5.32}$$

$$\text{false alarm probability} = \frac{n^\circ \text{ of events with } snr \geq snr.th.}{N_{tot}}\,|_{\text{for BGK analysis}}\,, \tag{5.33}$$

so, the **detection probability** (DE) (or detection efficiency) estimates the probability of detecting an excess of *snr* greater than a certain treshold, if evaluated over the primary plus secondary analysis. The same estimator has the meaning of false alarm probability (FAP) if evaluated on the only primary study. These quantities, DE and FAP, are estimated only in the post-merger part of the signal, comparing the *snr* of

the reconstructed energy with a user-defined grid of values. Here N_{tot} is the number of the recovered events, not the injected one: so these statistical estimators are conditioned to the probability of having an on-source detection. This is the reason why I have studied only the events detected by cWB was able to detect and not all the GW events detected so far by LVK collaboration.

5.3.3 Post-merger time window

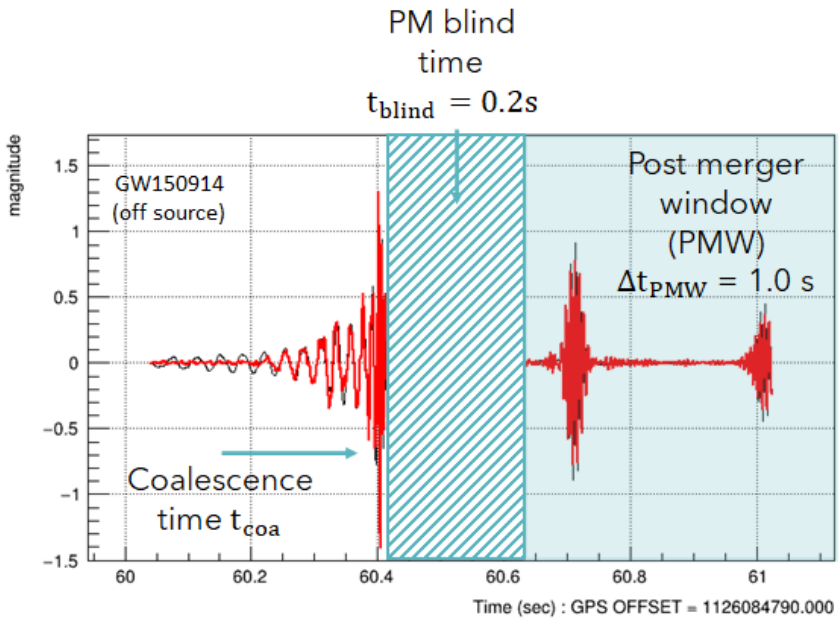

Figure 5.6: Visual representation of the post-merger time-window (PMW), in yellow. The grey area is the blind time t_{blind}. GW event: GW150914.

Looking at table 5.2, we see that [7] the average arrival time of the first echo signal is around ~ 0.2 s, well inside the $Tgap$ upper limit. Moreover, not only the amplitude of the first echo is expected to be a small fraction of the merger phase's amplitude of the binary [54, 55], but echoes' amplitude is expected to decrease at each repetition [49, 95]. This provides a solid ground to limit the post-merger analysis to a well-defined time region, which I call *post-merger time-window* (PMW), smaller than the usual post-merger phase of the signal.

To define the PMW we need to introduce the *blind time*, t_{blind}, (the grey area in figure 5.6). It is a time interval, from the coalescence time of the primary event (t_{coa}) to the starting time of the PMW (t^{PMW}_{start}), inside which the LES search is blind. The reasons for using it, is mainly to mitigate or completely rule out the effects of the primary's ring-down energy over the post-merger statistics. Its time duration, Δt_{blind}, can be tuned and will be discussed in the following chapter 6.

Then, starting from $t_{coa} + t_{blind}$, I set over the data a window of time duration equal to 1 s, and it is only inside this window that the statistical estimators previously defined are evaluated. So we have that:

$$\text{PMW starting time:} \quad t^{PMW}_{start} = t_{coa} + t_{blind} \tag{5.34}$$

$$\text{PMW ending time:} \quad t^{PMW}_{end} = t^{W}_{start} + 1\,\text{s} \tag{5.35}$$

[7] For very peculiar and unusual BBH events, if compared with the average detections, this could not be true. Then a retuning of the $Tgap$ and PMW would be necessary.

This time window will be enough to detect two or three echoes signals, if any, with an average time separation of $\sim 0.2 - 0.3$ ms. Likely they will be the most energetic ones: so, if they cannot be detected then, it will be useless to try to detect something even less energetic, further away from the coalescence time of the binary.

This implies that all the statistical estimators explained in section 5.2.4 evaluated in the post-merger (PM) region of the waveform can be used in the same way, but their evaluations have to be performed inside the PMW and no more over the entire PM time region (so: from PM to PMW subscript).

5.3.4 Injections

Each primary injection is randomly selected between the distribution of CBC PE samples [14, 15, 17] provided by the LIGO-Virgo-KAGRA collaboration, so each GW event detected so far has its own CBC PE samples distribution. These samples possess their own theoretical models of reference, which are described by an approximant. The approximants used in this work follow the ones utilized or suggested by the LVK collaboration to perform their studies and deliver results. Mainly, they are the IMRPhenonPV2 [97, 98, 99], SEBNRv4PHM [100], and the NRSur7dq4 [101] approximants. These informations can be accessed from the gravitational wave open science catalog (GWOSC) [13], an open-access tool provided by the LVK collaboration.

The studied events belong to all three observational runs of LIGO and Virgo's detectors, O1, O2, and O3 [14, 15, 17, 13], and they are listed in table 5.1. These GW events must have been detected by cWB all-sky burst search configuration [84, 85, 86] in the O1, O2 and O3 observing runs which possess a network snr greater than ten, $snr_{net} \geq 10$. The reason is simple: this search needs an on-source detection. The lower threshold in snr_{net} was chosen a priori. Echoes are mostly expected [55] to possess smaller snr if compared to the primary GW emission, then trying to investigate their presence or not after a GW signal whose $snr_{net} \leq 10$ is not informative. The primary snr is already very low and the expectations in detecting some snr excess in the post-merger are even smaller.

In table 5.1, from the left column to the right one are reported: the observing run in which the GW event was detected, its name, the waveform model used to generate its CBC PE samples, its coalescence GPS time, the network signal to noise ratio (snr_{net}) of the event, the final mass of the object and its luminosity distance from the observer.

Echoes mimicker: the waveform models I have used to mimic echoes are:

- single low energy BBH coalescence of an equal mass $80 - 80 M_{\odot}$ binary. The amplitude of these signals ranges in the interval which goes from the merger amplitude of the primary to around a hundredth of it. Their sky location is the same as the primary one while their injection time, t_{echo} was selected to be 0.1 s or 0.2 s after the coalescence time of the primary, accordingly to table 5.2.

- train of two low energy elliptical polarised sine-gaussian (SGE) pulses $f(t)$ [102]. An SGE is descrribed by the following expression:

$$f(t) = Ae^{\left(-\frac{(t-t_0)^2}{\tau^2}\right)} \cos(2\pi f_0 t + \phi_0)\,, \tag{5.36}$$

  where A is the amplitude, t_0 the central time of the SGE, τ the half time duration of the pulse, f_0 and ϕ_0 its central frequency and phase respectively.

List of analysed BBH events						
Run	GW name	Approximant	GPS time	snr_{net}	M_{tot} in $M_\odot$	D_L [Mpc]
O1	GW150914	IMRPhenomPv2	1126259462.421	24.4	$63.1^{+3.4}_{-3.0}$	440^{+150}_{-170}
O1	GW151012	IMRPhenomPv2	1128678900.467	10.0	$35.6^{+10.8}_{-3.8}$	1080^{+550}_{-490}
O1	GW151226	IMRPhenomPv2	1135136350.668	13.1	$20.5^{+6.4}_{-1.5}$	450^{+180}_{-190}
O2	GW170104	IMRPhenomPv2	1167559936.619	13.0	$48.9^{+5.1}_{-4.0}$	990^{+440}_{-430}
O2	GW170608	IMRPhenomPv2	1180922494.501	14.9	$17.8^{+3.4}_{-0.7}$	320^{+120}_{-110}
O2	GW170729	IMRPhenomPv2	1185389807.346	10.2	$79.5^{+14.7}_{-10.2}$	2840^{+1400}_{-1360}
O2	GW170809	IMRPhenomPv2	1186302519.758	12.4	$56.3^{+5.2}_{-3.8}$	1030^{+320}_{-390}
O2	GW170814	IMRPhenomPv2	1186741861.533	15.9	$53.2^{+3.2}_{-2.4}$	600^{+150}_{-220}
O2	GW170823	IMRPhenomPv2	1187529256.501	11.5	$65.4^{+10.1}_{-7.4}$	1940^{+970}_{-900}
O3a	GW190408_181802	SEBNRv4PHM	1238782700.279	14.7	$41.1^{+3.9}_{-2.8}$	1550^{+400}_{-600}
O3a	GW190412	SEBNRv4PHM	1239082262.165	18.9	$37.3^{+3.9}_{-3.8}$	740^{+140}_{-170}
O3a	GW190512_180714	SEBNRv4PHM	1241719652.435	12.3	$34.5^{+3.8}_{-3.5}$	1430^{+550}_{-550}
O3a	GW190513_205428	SEBNRv4PHM	1241816086.800	12.3	$51.6^{+8.2}_{-5.8}$	2060^{+880}_{-800}
O3a	GW190517_055101	SEBNRv4PHM	1242107479.848	10.2	$59.3^{+9.1}_{-8.9}$	1860^{+1620}_{-840}
O3a	GW190519_153544	SEBNRv4PHM	1242315362.418	12.0	$101.0^{+12.4}_{-13.8}$	2530^{+1830}_{-920}
O3a	GW190521	SEBNRv4PHM	1242442967.471	14.4	$156.3^{+36.8}_{-22.4}$	3920^{+2190}_{-1950}
O3a	GW190521_074359	SEBNRv4PHM	1242459857.456	24.4	$71.0^{+6.5}_{-4.4}$	1240^{+400}_{-570}
O3a	GW190602_175927	SEBNRv4PHM	1243533585.093	12.1	$110.9^{+17.7}_{-14.9}$	2690^{+1790}_{-1120}
O3a	GW190701_203306	SEBNRv4PHM	1246048404.578	11.6	$90.2^{+11.3}_{-8.9}$	2060^{+760}_{-730}
O3a	GW190706_222641	SEBNRv4PHM	1246487219.361	12.3	$99.0^{+18.3}_{-13.5}$	4420^{+2590}_{-1930}
O3a	GW190828_063405	SEBNRv4PHM	1251009263.781	16.0	$54.9^{+7.2}_{-4.3}$	2130^{+660}_{-930}
O3a	GW190915_235702	IMRPhenomPv2	1252627040.693	13.1	$57.2^{+7.1}_{-6.0}$	1620^{+710}_{-610}
O3a	GW190929_012149	IMRPhenomPv2	1253755327.505	9.9	$101.5^{+33.6}_{-25.3}$	2130^{+3650}_{-1050}
O3a	GW190814	SEBNRv4PHM	1249852257.009	22.2	$25.6^{+1.1}_{-0.9}$	240^{+40}_{-50}
O3b	GW191109_010717	SEBNRv4PHM	1257296855.783	17.3	107^{+18}_{-15}	1920^{+1130}_{-650}
O3b	GW191204_171526	SEBNRv4PHM	1259514944.087	17.5	$19.2^{+1.8}_{-1.0}$	650^{+190}_{-250}
O3b	GW191215_223052	SEBNRv4PHM	1260484270.995	11.2	$41.4^{+5.1}_{-4.1}$	1930^{+890}_{-860}
O3b	GW191222_033537	SEBNRv4PHM	1261020955.347	12.5	$75.5^{+15.3}_{-9.9}$	3000^{+1700}_{-1700}
O3b	GW191230_180458	SEBNRv4PHM	1261764316.898	14.4	82^{+17}_{-11}	4300^{+2100}_{-1800}
O3b	GW200219_094415	SEBNRv4PHM	1266140673.095	10.7	$62.2^{+11.7}_{-7.8}$	3400^{+1700}_{-1500}
O3b	GW200224_222234	SEBNRv4PHM	1266618172.4	20.0	$68.6^{+6.6}_{-4.7}$	1710^{+490}_{-640}
O3b	GW200225_060421	SEBNRv4PHM	1266645879.3	12.5	$32.1^{+3.5}_{-2.8}$	1150^{+510}_{-530}
O3b	GW200311_115853	SEBNRv4PHM	1267963151.3	17.8	$59.0^{+4.8}_{-3.9}$	1170^{+280}_{-400}

TABLE 5.1: This table lists from left to right: the observing run, The GW event's name, the waveform model used to generate its CBC PE samples, its coalescence GPS time, the network signal to noise ratio (snr_{net}) of the event, the final mass of the object and its luminosity distance from the observer. These events are the GW signals detected by cWB whose $snr_{net} \geq 10$, and they are analysed in this work.

The parameters of the SGE are choosen to have an individual time duration $\tau_{SGE} = 2\tau = 20\,\text{ms}$ and central frequency $f_0 = 140\,\text{Hz}$, with a quality factor $Q = 8.8$. These parameters are chosen as a good compromise since a single echo is expected to have a time duration comparable to the ring-down phase of the primary signal, and a frequency similar or higher than the merger one. The echoes' damping factor is $\gamma = 0.5$, so each sine-gaussian pulse has a maximum amplitude that is half the amplitude of the previous one. The same conditions hold for the amplitude A of the first echo pulse, which is set to be half the merger one, and its minimum value is set to be a hundredth of the merger amplitude. The injected secondary signal has the same sky position as its companion primary signal, since physically both the GW emission should come from the same astrophysical source. Their sky location is the same as the primary one and their injection time, $t_{echo} = 0.3\,\text{s}$ and $\Delta t_{echo} = 300\,\text{ms}$ to mimic the first two pulses of a train of echoes.

To test and tune the LES search and cWB I have used as echo-mimicker the BBH coalescence signal. This will allow checking for possible relevant differences in performances by LES search when using the single-pixel selection rule (WP10) or the chirping-up one (WP5). This is possible because, the high masses of the binary make the waveform enough similar to the one of a SGE pulse, but retain its chirping nature and so a fraction of its *snr* lies in the inspiral phase of the signal.

On the contrary, once the LES search is ready and tuned, to estimate its performances I have used as echo-mimickers the SGE signals. In many specialised papers [96, 103, 104], echoes are treated either like sine-gaussian pulses or like rescaled and delayed in time repetitions of the truncated ring-down signal of the main BBH event. Since echoes are predicted for non-BBH systems I prefer to use an elliptical polarised sine-gaussian (SGE) signal to mimick echoes rather than the adjusted ring-down signal of the BBH.

List of Δt_{echo} for the analysed BBH events		
Run	GW name	Δt_{echo} in [ms]
O1	GW150914	227^{+12}_{-11}
O1	GW151012	127^{+39}_{-14}
O1	GW151226	73^{+23}_{-5}
O2	GW170104	176^{+18}_{-14}
O2	GW170608	63^{+12}_{-2}
O2	GW170729	287^{+53}_{-37}
O2	GW170809	203^{+19}_{-14}
O2	GW170814	191^{+12}_{-9}
O2	GW170823	236^{+36}_{-27}
O3a	GW190408_181802	147^{+14}_{-10}
O3a	GW190412	134^{+14}_{-14}
O3a	GW190512_180714	123^{+14}_{-12}
O3a	GW190513_205428	185^{+29}_{-21}
O3a	GW190517_055101	213^{+33}_{-32}
O3a	GW190519_153544	365^{+45}_{-50}
O3a	GW190521	568^{+133}_{-81}
O3a	GW190521_074359	256^{+23}_{-16}
O3a	GW190602_175927	402^{+64}_{-54}
O3a	GW190701_203306	326^{+41}_{-32}
O3a	GW190706_222641	358^{+66}_{-49}
O3a	GW190828_063405	197^{+26}_{-15}
O3a	GW190915_235702	205^{+26}_{-22}
O3a	GW190929_012149	367^{+122}_{-92}
O3a	GW190814	91^{+4}_{-3}
O3b	GW191109_010717	387^{+65}_{-54}
O3b	GW191204_171526	68^{+6}_{-4}
O3b	GW191215_223052	148^{+18}_{-15}
O3b	GW191222_033537	272^{+55}_{-36}
O3b	GW191230_180458	296^{+61}_{-40}
O3b	GW200219_094415	224^{+42}_{-28}
O3b	GW200224_222234	247^{+24}_{-17}
O3b	GW200225_060421	115^{+13}_{-10}
O3b	GW200311_115853	212^{+17}_{-14}

TABLE 5.2: In this table are listed from left to right: the GW event's name, the expected Δt_{echo}, whose value can be compatible also with the one expected for t_{echo}, for different ECO models n. The Δt_{echo} was performed through equation (3.4). Moreover, the final cWB LES search configuration requires $Tgap = 2\,\mathrm{s}$ and $Fgap = 128\,\mathrm{Hz}$, thus each Δt_{echo} is well contained by $Tgap$, see section 6.6.

Chapter 6

Tuning cWB pipeline

The cWB all-sky burst search [86] (I will refer to it as *standard cWB search*) is the most agnostic search of cWB, so it should be exactly what is needed to investigate the presence or not of possible low energy signals nearby a BBH coalescence. Nevertheless, the aim of the cWB all-sky burst search is to detect the GWs' signals, which requires certain confidence over the selected triggers: it means the algorithm has rather conservative threshold values. So, the standard configuration of cWB prevents us from selecting low-energy signals as possible GWs candidates. For this reason, at first, the LES search (described in section 5.3) was implemented over the cWB O3 all-sky configuration: a new cWB search, working as a follow-up study, and sensitive to low energy signals, was obtained.

Once the LES search was implemented, it was necessary to perform sanity tests and to define the new optimization criteria: task accomplished by comparing the cWB LES configuration with the cWB standard one. Once the LES search is implemented and tuned it is possible to deploy it and to find out its performances in low energy signals detection while carrying out investigations over possible outstanding on-source energy excess not matching with the background predictions.

cWB all-sky O3 search								
Configuration parameters								
bpp	cc	ρ	subnet	Acore	Tgap	Fgap	SUBRHO	SUBNET
0.001	0.5	5.0	0.5	1.7	0.2	128.0	5.5	0.1

TABLE 6.1: In this table are listed the values of the production thresholds (see sec. 5.2.4) for the cWB all-sky O3 search. In the first row are listed the names of the parameters. *bpp* is the black pixels probability, *cc* the network coherent coefficient, ρ the effective network coherent *snr*, *subnet* the subnetwork energy asymmetry statistic, *Acore* the pixel average amplitude, *SUBRHO* and *SUBNET* are the internal cut-off on ρ and *subnet*, *Tgap* and *Fgap* the maximum time and frequency gap between subsequent pixels' clusters respectively. In the second row are reported their values. Fore more details see appendix B.

Here I will report the main steps and results of the optimisation process of the cWB LES search, while in the next chapter the performances and results of the LES search will be given.

Therefore, starting from the standard cWB configuration, whose production thresholds over cWB parameters are listed in table 6.1, I used as research subject GW150914 [24], and studied the performances of cWB LES search when the production thresholds are released, so all the one listed in table 6.1. Together, their interaction with the variables of the LES search is investigated as well as the best configuration for such parameters: the arrival time of an echo signal (t_{echo}, see 5.3.4), the definition of

the PMW and the blind time of the analysis (t_{blind}), see 5.3.3, the morphology of secondary signals (see 5.3.4) as well as the way through which cWB select the cluster's pixels of the events which then will be analysed (section 5.2.3).

I recall that the SIG and BGK analysis are carried on with the configuration exposed in section 5.3, so the injection of only the primary signal for the BGK analysis, while primary plus secondary (single high mass BBH coalescence signal) for the SIG analysis (section 5.3.1). The following notation can be used:

- *background* (BGK) or *primary* (P) study;
- *signal* (SIG) or *primary plus secondary* (P+S) study.

6.1 Arrival time of the first echo, t_{echo}

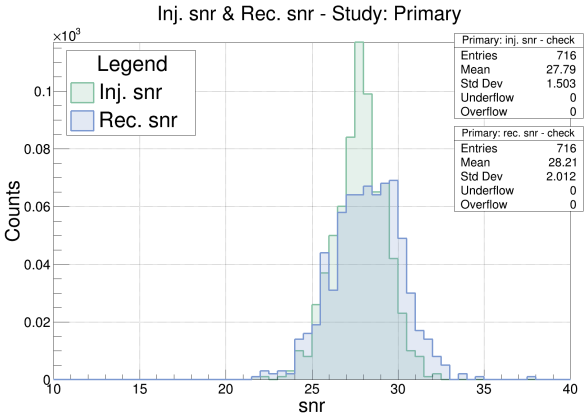

(a) Background distribution. $t_{echo} = 0.1$ s.

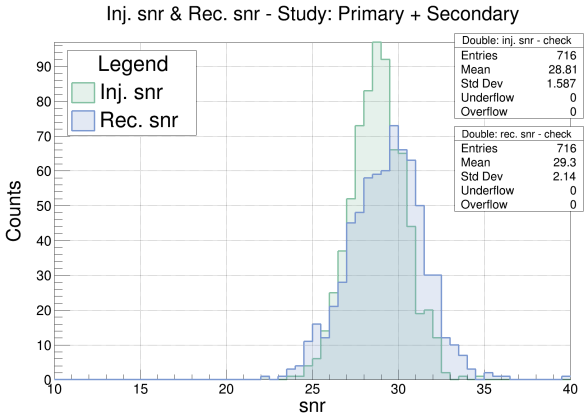

(b) SIG distribution. $t_{echo} = 0.1$ s.

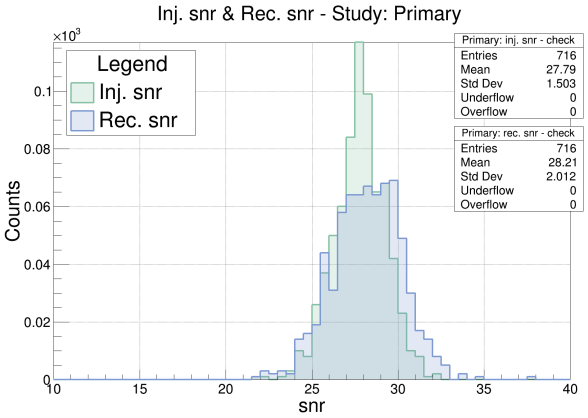

(c) Background distribution. $t_{echo} = 0.2$ s.

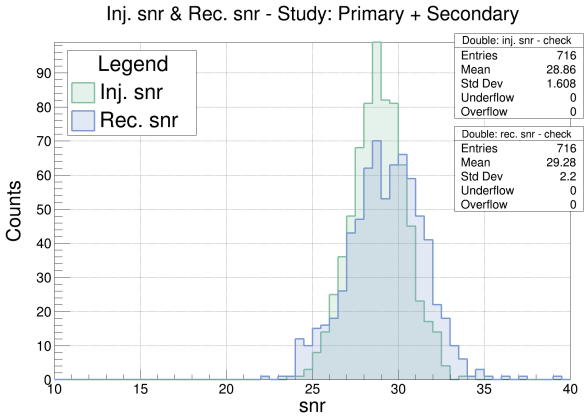

(d) SIG distribution. $t_{echo} = 0.2$ s.

Figure 6.1: Here are represented the BGK (left plots) and SIG (right plots) $iSNR$ and $oSNR$ distributions referred to the LES cWB search with standard thresholds, table 6.6. The green distributions are referred to the $iSNR$ while the blue one to $oSNR$. Top row the scenario for $t_{echo} = 0.1$ s, bottom for $t_{echo} = 0.2$ s.

Thanks to results in table 5.2 we know that the expected values for t_{echo} are around some tens of a second, so the tuning of cWB LES search is performed assuming t_{echo} equal to 0.1 s and 0.2 s. Then, 0.1 s and 0.2 s values are selected to inject the first signal not too close to the ringdown of the BBH, since in that region the

Study of *bpp* and *cc* cWB thresholds						
		P search	P + S search		P search	P + S search
Search set-up	t_{echo}[s]	$\langle oSNR \rangle$	$\langle oSNR \rangle$	t_{echo}[s]	$\langle oSNR \rangle$	$\langle oSNR \rangle$
$bpp = 0.001$, $cc = 0.5$	0.1	28 ± 2	29 ± 2	0.2	28 ± 2	29 ± 2
$bpp = 0.004$, $cc = 0.5$	0.1	29 ± 2	30 ± 2	0.2	29 ± 2	30 ± 2
$bpp = 0.001$, $cc = 0.0$	0.1	28 ± 2	29 ± 2	0.2	28 ± 2	29 ± 2
$bpp = 0.004$, $cc = 0.0$	0.1	29 ± 2	30 ± 2	0.2	29 ± 2	30 ± 2

TABLE 6.2: This table reports the values of the reconstructed *snr* for the primary (P) (third and sixth column) and primary + secondary (P+S) (fourth and seventh column) analysis while varing the *bpp* and *cc* cWB thresholds (first column). These comparison is carried on for two physical conditions, when $t_{echo} = 0.1$ s and $t_{echo} = 0.2$ s.

LES search: t_{echo} studies					
		Primary		Primary + Secondary	
Search set-up	t_{echo}[s]	snr_{rec}^{IM}	snr_{rec}^{PM}	snr_{rec}^{IM}	snr_{rec}^{PM}
$bpp = 0.001$, $netCC = 0.5$	0.1	27 ± 2	9 ± 2	27 ± 2	11 ± 2
$bpp = 0.004$, $netCC = 0.5$	0.1	28 ± 2	9 ± 2	28 ± 2	12 ± 2
$bpp = 0.001$, $netCC = 0.5$	0.2	27 ± 2	9 ± 2	27 ± 2	11 ± 3
$bpp = 0.004$, $netCC = 0.5$	0.2	28 ± 2	9 ± 2	28 ± 2	12 ± 3

TABLE 6.3: Here there is a comparison between the reconstructed *snr* in the inspiral-merger phase (IM) and post-merger (PM) one, for both the primary (P) and primary + secondary (P+S) studies. These comparisons are performed over the two values of t_{echo}: $[0.1, 0.2]$s under study here in section 6.1.

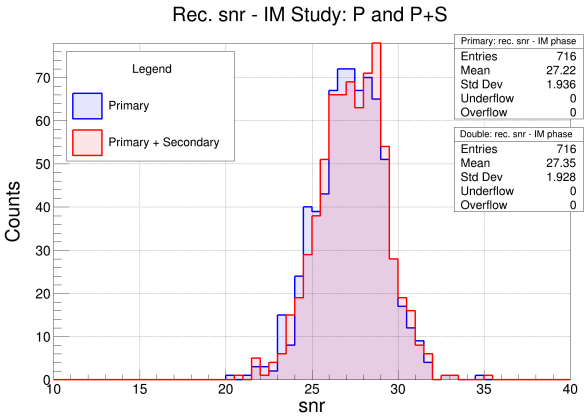

(a) $t_{echo} = 0.1\,\text{s}$. Before t_{coa}

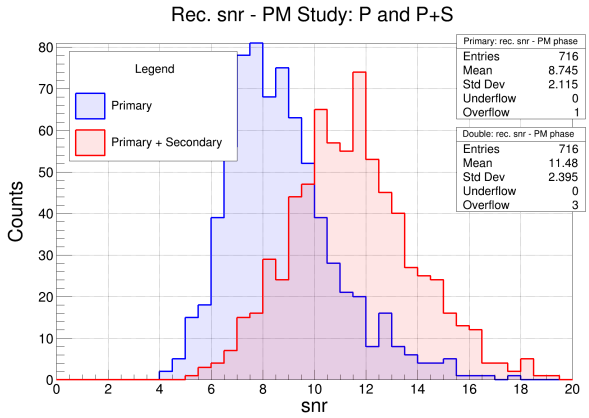

(b) $t_{echo} = 0.1\,\text{s}$. After t_{coa}

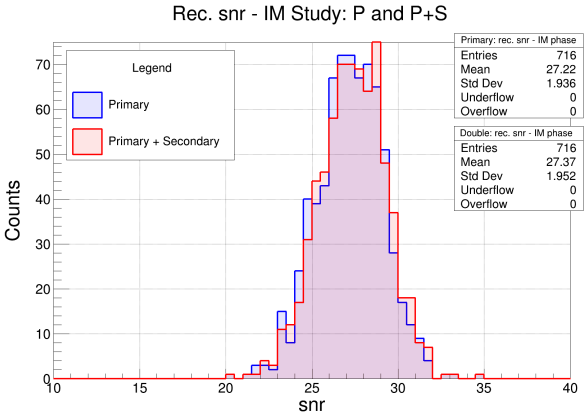

(c) $t_{echo} = 0.2\,\text{s}$. Before t_{coa}

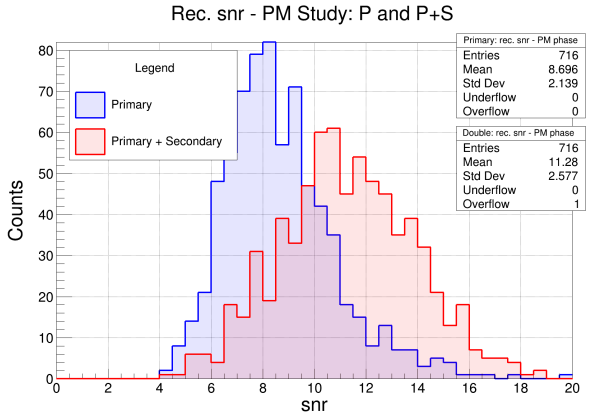

(d) $t_{echo} = 0.2\,\text{s}$. After t_{coa}

Figure 6.2: In first column shows the reconstructed *snr* in the inspiral-merger (IM) phase for the primary (blue) and primary + secondary (red) studies. The second column shows the same distributions for but related to the reconstructed *snr* in the post-merger (PM) phase. The first row is referred to the test with $t_{echo} = 0.1\,\text{s}$, while the second row for $t_{echo} = 0.2\,\text{s}$.

ringdown energy and its fluctuations will contaminate a possible reconstruction of the secondary signal and prevent a clean energy estimation. Moreover, $t_{echo} = 0.1\,\text{s}$ is a good compromise between being neither too close nor too far away from the coalescence time of the BBH signal. The marginal case of $t_{echo} = 0.2\,\text{s}$ allows to test LES search near the maximum time separation of pixels' clusters permitted by the standard cWB search, so $Tgap$ threshold [1]. In this way, one can study if cWB reconstruction capabilities differ when the secondary signal is injected in proximity to the T_{gap} threshold. Moreover, one can also check if having two signals more or less time separated can lead to differences in the signal reconstruction, influencing, for example, the pixels' selections of the algorithm. These effects would be seen by looking either at the energy content of the primary, the IM phase, or at the post-merger one.

The injected *snr* for both the t_{echo} configurations analysis are the same and their distribution is reported in figure 6.1. In blue are shown the injected *snr* while in green the reconstructed ones for both the P and P+S analysis. It is possible to appreciate that the contribution to the overall *snr* due to the presence of a secondary signal is around one or two units in *snr*, having that $\langle snr \rangle_{inj}^{P} \sim 28$ and $\langle snr \rangle_{inj}^{P+S} \sim 29$.

[1] This threshold will be investigated. In this study, it cannot be modified since I want to compare the results under the same analysis's configuration apart from t_{echo}

Then, looking at table 6.2, it is possible to see that no relevant differences between the two configurations of t_{echo} can be seen. We are limiting our discussion to the results labeled with $bpp = 0.001$ and $cc = 0.5$, since they refer to the cWB LES search with standard threshold values.

Then, in table 6.3 I have listed the recovered values of snr (eq (5.29)) for the inspiral-merger (IM) phase and the post-merger (PM) phase [2]. An example of the above results, for both the t_{echo} options, referred to the LES cWB configuration with $bpp = 0.001, cc = 0.5$, is shown in figure 6.2: here, the top histograms are obtained for $t_{echo} = 0.1\,\text{s}$, while the second row for $t_{echo} = 0.2\,\text{s}$. For each row, the first histogram shows the reconstructed snr before the coalescence time t_{coa} (IM phase), for the BGK study (blue distribution) and the SIG study (red distribution). The second histogram, for each row, displays the reconstructed snr in the post-merger phase, so after the coalescence time t_{coa}. From table 6.3 and 6.2 we can confirm that the reconstructed snr for the BGK study in both the time periods (IM and PM) and for both t_{echo} configurations remains the same. Also the BGK-IM results and the SIG-IM results are compatible between them. We are looking only at their IM phase, then it is expected to recover the same snr since both the primary injections and the data over which they are injected are the same. Then, it is possible to see a difference in snr distribution, between the BGK and SIG analysis by looking at the PM results. Here the SIG analysis shows an increase in snr of some units with respect to the BGK one, which is compatible to the results of figure 6.1 and table 6.2.

So, using the LES search with standard cWB threshold values we have seen that even if the secondary signal is injected nearby the $Tgap$ limit, $t_{echo} = 0.2\,\text{s}$, the pipeline does not lose performances and follows the results of $t_{echo} = 0.1\,\text{s}$. This show us that cWB performances are not affected by the arrival time of the first echo t_{echo}, and so there are no losses in tuning cWB by limiting our study to one t_{echo} value or another. Moreover, even if the errors over the distribution mean values are huge, it is still possible to appreciate an overall increase in the reconstructed snr for the SIG study if compared to the BGK one.

6.2 Black pixel probability and network coherent coefficient

The bpp and the cc thresholds are the first to be tested because they are the cWB thresholds that mostly influence the energy content of clusters of pixels. Therefore, aiming to detect poorly energetic clusters of pixels, they have been released to check if the performances of the LES search can improve even if releasing the thresholds will increase the amount of energy in the background. The best compromise between an increase in the noise energy content, so higher false alarm rate (FAR), and an increase in the detection efficiency (DE) for low energy excess in the post-merger phase of a BBH coalescence has to be found.

Looking at table 6.3 and figure 6.2 it is possible to see the effects when releasing the thresholds values of bpp and cc. Even if snr^{PM} in the SIG analysis seems to slightly increase when $bpp = 0.004$, which is an expected result, its value results to be compatible within its uncertainties to the one for the $bpp = 0.001$ study. It is possible that the overall increase of snr_{rec}, both in the IM and PM phase, of one unit, is due to the primary signal rather than to the secondary one. Otherwise, the increase in snr would have been expected only for snr^{PM}_{rec}. Nevertheless, since all the quantities obtained with a release over the bpp threshold are compatible with their

[2] These analyses were limited to the different bpp cWB configurations since we will see in section 6.2 that cc threshold has no impact in this analysis.

Low energy search: t_{blind} studies									
		t_{blind}							
		0 ms	10 ms	20 ms	30 ms	40 ms	50 ms	60 ms	70 ms
$bpp = 0.001$ $t_{echo} = 0.1$ s	$P : snr_{rec}^{PM}$	9 ± 2	5 ± 1	5 ± 1	4 ± 1	4 ± 1	4 ± 1	3 ± 1	3 ± 1
	$P + S : snr_{rec}^{PM}$	11 ± 2	9 ± 2	9 ± 2	8 ± 2	8 ± 2	8 ± 2	8 ± 2	7 ± 2
$bpp = 0.004$ $t_{echo} = 0.1$ s	$P : snr_{rec}^{PM}$	9 ± 2	5 ± 1	5 ± 1	4 ± 1	4 ± 1	4 ± 1	3 ± 1	3 ± 1
	$P + S : snr_{rec}^{PM}$	11 ± 2	9 ± 2	9 ± 2	8 ± 2	8 ± 2	8 ± 2	8 ± 2	7 ± 2

TABLE 6.4: In this table are listed the values of the reconstructed *snr* in the post-merger (PM) phase for each values of the blind time t_{blind} between the coalescence time and the starting time of the PM phase. The studies are performed over the two LES configurations of cWB $bpp = 0.001$ and $bpp = 0.004$, both having $cc = 0.5$.

counterpart of $bpp = 0.001$, we can say that there is not a significant gain in releasing the bpp threshold in the LES cWB configuration. Similarly, also cc threshold does not affect the performance of the analysis. This can happen because contrary to bpp, which acts straightforward to the energy content of the events, cc imposes a lower limit on the energy ratio (see eq. (5.31)) of the total coherent energy of the event. Thus, each event contains the BBH signal, which possesses a high energy content and overcomes any effects of the presence or not of a secondary low energy excess in the post-merger.

In conclusion we have seen an overall agreement between the LES search with cWB standard threshold and released. Then, it is possible to leave bpp and cc thresholds equal to the one of the cWB standard search, so $bpp = 0.001$ and $cc = 0.5$: this will maintain as many similarities as possible with that search.

6.3 Post-merger blind time, t_{blind}

From figure 6.2 it is possible to notice that the post-merger phase the reconstructed *snr* for the background retains very high values $snr_{rec}^{PM} \geq 7$ for all the cWB configurations. This is a problem: aiming to be sensitive to low energy signals means that the interesting *snr* values are around *snr* of $[3 - 5]$. Since a non-negligible amount of energy in the post-merger phase is due to the presence of the ring-down energy of the BBH signal a time gap t_{blind}, see section 5.3.3, between the end of the inspiral-merger phase and the post-merger phase, is introduced. This implies that the IM data period lasts till the coalescence time t_{coa}, then there is a small blind time t_{blind} and at the time:

$$t_{PM} = t_{coa} + t_{blind} \tag{6.1}$$

starts the PM data period. Since a BBH ring-down is expected to last some tens of milliseconds $\sim$ 10 ms I have performed the same studies we had so far for some possible values of t_{blind}: $t_{blind} \in [10, 20, 30, 40, 50, 70, 100]$ ms, and the reconstructed signal to noise ratio in the new post-merger phase snr_{rec}^{PM} is reported in table 6.4. These studies were done over the two cWB LES search configurations $bpp = 0.001$ and $bpp = 0.004$ having $cc = 0.5$, moreover I have analysed both the scenarios of $t_{echo} = 0.1$ s, 0.2 second.

From table 6.4 one can see that, thanks to the introduction of this time gap between the IM phase and the PM one, we have passed from an average $snr_{rec}^{PM} \gtrsim 7$ to

an average $snr_{rec}^{PM} \sim 3.5$ for the background study. Then, we also have that the snr_{rec}^{PM} ratio between the BGK and SIG study, becomes more favorable for larger values of t_{blind}, providing they do not start to cut also the secondary signal, which is centered at 100 ms from the t_{coa}, and has a time duration of around ~ 80 ms.

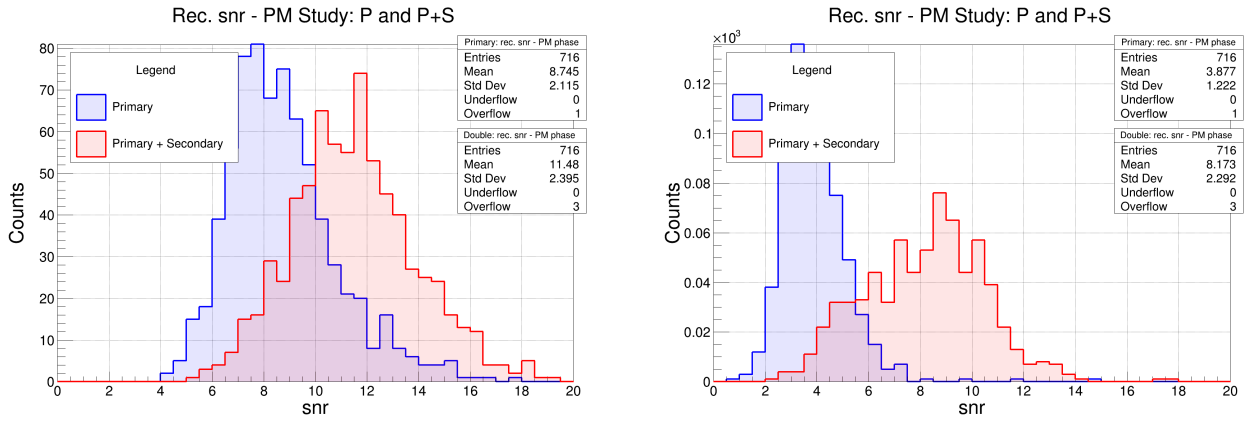

(a) No t_{blind} applied.

(b) A $t_{blind} = 40$ ms is applyed.

Figure 6.3: Here is a comparison of the snr_{rec}^{PM} distribution when no time gap is applied (left plot), and when it is appllyed (right plot) for the cWB configuration: $bpp = 0.001, cc = 0.5, t_{echo} = 0.1$ s and $t_{blind} = 40$ ms. In blue the BGK distribution, while in red the SIG distribution.

These results confirm that a non negligible fraction of snr in the post-merger phase is due to the reconstructed ring-down signal of the BBH event. Following the results in table 6.4, it is possible to say that a $t_{blind} = 40$ ms is sufficient in order to reduce the noise due to the ring-down and prevent a possible cut in the secondary signal energy. Figure 6.3 shows the difference in snr_{rec}^{PM} distribution, for the cWB configuration $bpp = 0.001, cc = 0.5, t_{echo} = 0.1$ s, with $t_{blind} = 40$ ms (right) and without t_{blind} (left).

6.4 Pixel selection rule

During the time-frequency pixels selection phase of the ETG procedure cWB selects the core pixels and the related cluster of pixels, section 5.2.3.

The test performed so far were done starting from the standard cWB search configuration, which uses the single-pixel selection rule (WP10), so now I have repeated these tests with the chirping pattern selection criteria (WP5) aiming to understand if cWB performances are affected by such variation, and if that is the case, to which extent. This is one of the motivations to use as echoes model an equal high masses BBH signal. Such model, at zero-order approximation, resembles a sine Gaussian signal, which is a very common model used to mimic echoes [96, 103, 104] but it retains in its TF representation a small hint of its chirping nature, since it is a BBH signal, which means its detection should be easier when cWB runs in WP5 configuration. Of course, this is true for high snr values, indicatively we can say for $snr \geq 8 - 10$, but here we are dealing with low injected snr, so it is a good opportunity to understand if, even for such low snr values, it is possible to appreciate the difference in performances between the WP5 or WP10 configuration. Since the cc does not influence the pipeline performances i have tested cWB with WP5 pixels selection rule for the $bpp = 0.001$ and $bpp = 0.004$ configurations and for both the t_{echo} tested so far.

Pixels selection rule studies						
			$t_{echo} = 0.1\,s$		$t_{echo} = 0.2\,s$	
Sel. Rule	cWB conf.	Study	snr_{rec}^{IM}	snr_{rec}^{PM}	snr_{rec}^{IM}	snr_{rec}^{PM}
WP10	$bpp = 0.001$	P	27 ± 2	4 ± 1	27 ± 2	4 ± 1
		P+S	27 ± 2	8 ± 2	27 ± 2	8 ± 3
WP10	$bpp = 0.004$	P	28 ± 2	5 ± 1	28 ± 2	5 ± 1
		P+S	28 ± 2	9 ± 2	28 ± 2	9 ± 3
WP5	$bpp = 0.001$	P	28 ± 2	5 ± 1	28 ± 2	5 ± 2
		P+S	28 ± 2	9 ± 2	28 ± 2	9 ± 2
WP5	$bpp = 0.004$	P	28 ± 2	6 ± 1	28 ± 2	6 ± 2
		P+S	28 ± 2	10 ± 2	28 ± 2	10 ± 2

TABLE 6.5: This table reports the reconstructed *snr* before (IM) and after (PM) the coalescence time for two different pixels selection criteria, single pixel selection (WP10 in cWB) and chirping-up pixel selection (WP5 in cWB). WP10 is used in typical all-sky burst searches beeing the best unmodelled pixels selection criteria, while WP5 is more suitable for CBC searces. These studies are performed for both the t_{echo} configurations studied so far.

Table 6.5 reports the comparison between the reconstructed *snr* before (third column) and after (fourth column) the coalescence time of the BBH signal. From table 6.5 it is possible to see that the two pixels selection criteria have similar performances: overall the chirping-up rule, in the post-merger phase, is capable of recovering slightly more energy with respect to the single pixels selection rule, just one unit in *snr* more. So, in conclusion, we can say that both the pixels selection criteria can be used, but since our goal is to detect un-modeled low energy signals which could not possess a chirping-up TF representation then the single pixels selection rule is more suited for such a search, since we want to be as agnostic as possible.

6.5 Receiver Operating Curve (ROC)

A study that can result decisive, since it provides a direct estimate of the pipeline performance is related to the receiver operating characteristic (ROC) [105]. Such a curve, for this analysis, is obtained by plotting the pairs of detection efficiency (DE), and the related false alarm probability (FAP) of the search, as in 5.3.2. [3].

These curves are evaluated for the following cWB LES search configurations:

- $bpp = 0.001, WP10$ and $bpp = 0.004, WP10$;
- $bpp = 0.001, WP5$ and $bpp = 0.004, WP5$.

Moreover, these studies are performed for both the injection times of the echoes: $t_{echo} = 0.1\,s$ and $0.2\,s$. What I have obtained is shown in figure 6.4, for the $t_{echo} = 0.1\,s$ scenario. In the plot, figure 6.4, it is possible to see that for low FAP (x-axis), say lower than 2%, the best configuration is $WP10$ and $bpp = 0.001$, and for such a FAP

[3] Remember that the detection efficiency is obtained from the SIG study, while the false alarm probability is recovered from the BGK study.

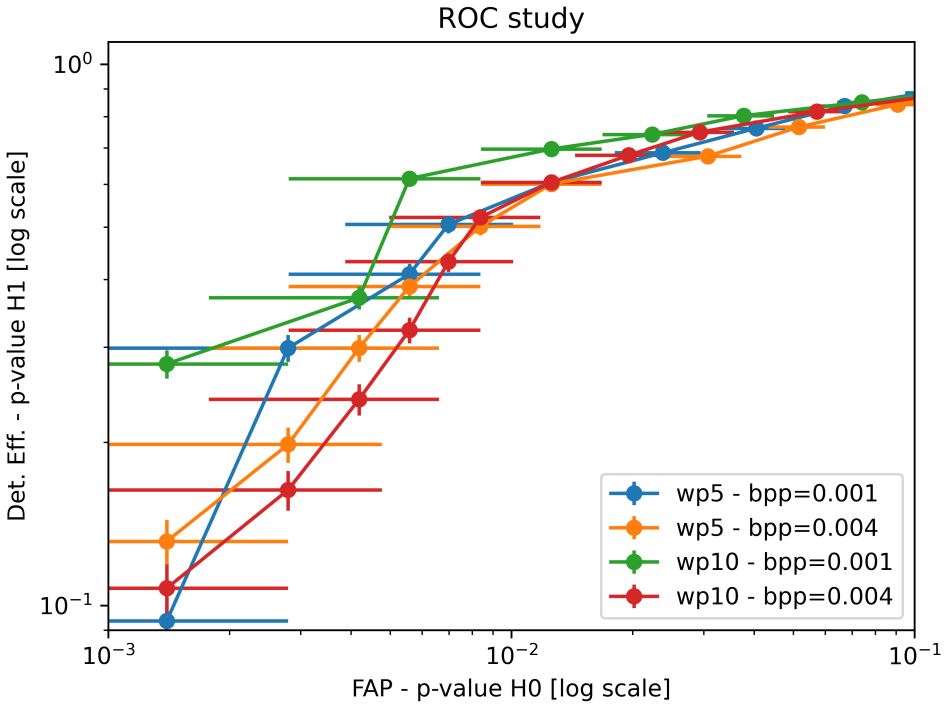

Figure 6.4: Receiver operating curves (ROCs) for the LES cWB search configurations listed in the legend: $WP5$ and $WP10$ with both the bpp values 0.001 and 0.004. On the x-axis, in logarithmic scale the false alarm probability (FAP), while on the y-axis, always in logarithmic scale, the detection efficiency (DE) counterpart.

the corresponding DE is around 70-80%. Such behaviour is common to both the $t_{echo} = 0.1\,\text{s}$ and $0.2\,\text{s}$ studies. Then, the configurations $WP10$ and $bpp = 0.004$ and $WP5$ and $bpp = 0.001$ seems to have similar performances: the DE is between 60% and 70% when the FAP is ∼1-2% respectively, and also here these trends are valid for both the t_{echo} scenarios. The worst configuration for very low FAP is $WP5$ and $bpp = 0.004$: when FAP is around 1-2% then the DE is between 50-65%.

In this study, very few secondary signals are injected with a high snr value, since they are not physically motivated. Reconstructing a $snr_{rec}^{PM} \gtrsim 9$ means we are very close to snr_{rec} values similar to a GW detection one [13]. Therefore, having poor statistics in the low FAP region of the ROC plot, around some per thousand, is of no concern, and it is reflected in the large error bars inside the low FAP region. Since high snr values, for the LES search, are not as interesting as low ones, the interesting FAP interval to be studied in the plot of figure 6.4 is the one around the percent to some tenth of percent. So, low FAP values which nevertheless, still retain a reasonable snr_{rec}^{PM} values, say around ∼5. Moreover, with the current infrastructure trying to reach $snr_{rec}^{PM} \lesssim 2$, so with high FAP values, is not reasonable. All of this leads to utilise the single-pixel ($WP10$) selection rule as preferred configuration of the cWB LES search the one, together with $bpp = 0.001$, $cc = 0.5$, $t_{blind} = 40\,\text{ms}$.

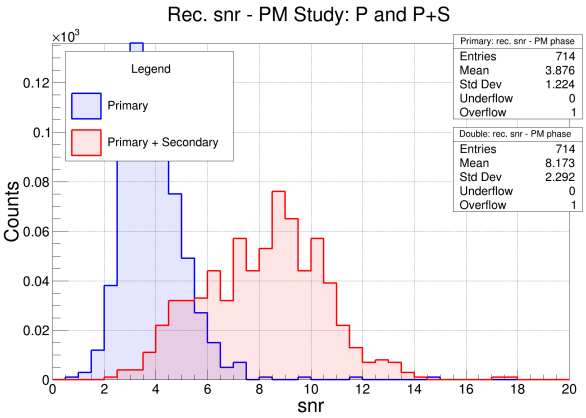

(a) $Tgap = 0.2\,\mathrm{s}$.

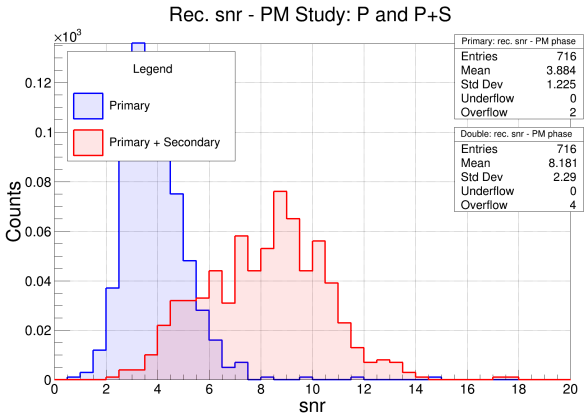

(b) $Tgap = 2\,\mathrm{s}$.

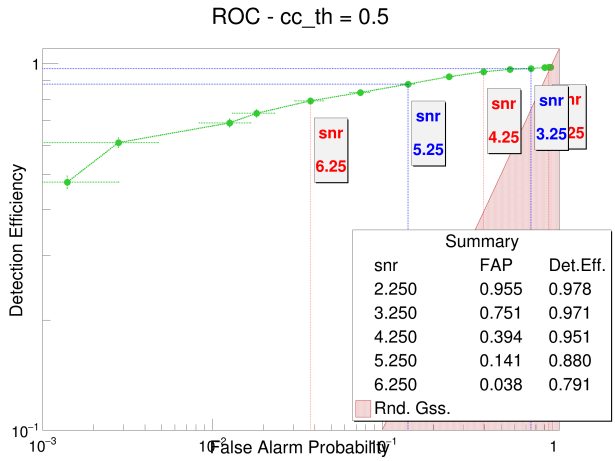

(c) ROC - $Tgap = 0.2\,\mathrm{s}$

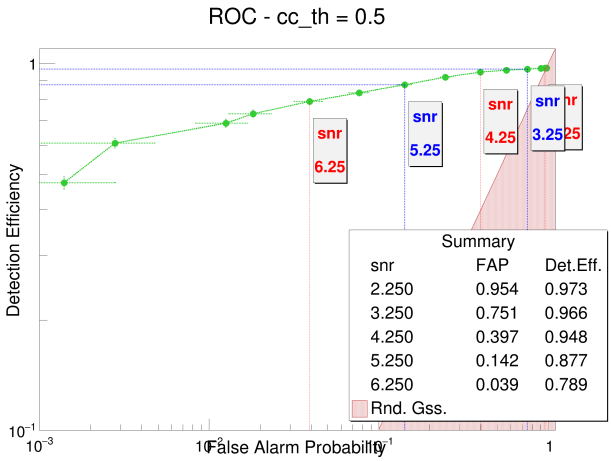

(d) ROC - $Tgap = 2\,\mathrm{s}$

Figure 6.5: Comparison between the low energy cWB set-up for $Tgap = 0.2\,\mathrm{s}$ (left) and $Tgap = 2\,\mathrm{s}$ (right). The thresholds and parameters of the seaches are: $bpp = 0.001$, $netCC = 0.5$, WP10, $t_{gap} = 40\,\mathrm{ms}$ and $t_{echo} = 0.1\,\mathrm{s}$. Top row: snr_{rec}^{PM} distribution for BGK (blue) and SIG (red) studies. Bottom row: ROC curve with a $cc^{PM} \geq 0.5$ cut, to compare the detection efficiency performances.

6.6 Tuning the cluster's defragmentation time

From table 5.2 we can see that the predicted values of the arrival time of the first echo signal can range from 10 ms up to 1 s for GW190521 (due to its high components' masses). This is a hint of the possibility for the $Tgap$ threshold (see section 5.2.3) to be a limiting constraint of the cWB LES search: when two clusters of pixels have a time separation between them that is larger than $Tgap$ (standard is $Tgap = 0.2\,\mathrm{s}$), cWB considers them as two different events. Then, with cWB standard configuration, if two clusters of pixels are time separated between them more than 0.2 s they are not reconstructed in the same event, they are considered different events unrelated between them. This is not what the LES search is aiming for: possible post-merger signals should be reconstructed within the same cWB event. So, adjusting the $Tgap$ threshold value will make the LES search more comfortable in detecting and reconstructing energy excesses located more than 0.2 s away from the primary event, so able to cover extreme scenarios such as GW190521. Then, using table 5.2 as reference, a good value for $Tgap$ could be: $Tgap = 2\,\mathrm{s}$. In figure 6.5, in the first row

are reported the snr_{rec}^{PM} distributions for the analysis with $Tgap = 0.2\,\mathrm{s}$ and $2\,\mathrm{s}$ respectively. The second row shows the ROC curve for the two configurations above.

Figure 6.5 shows that the snr_{rec}^{PM} distributions, the BGK (blue) and SIG (red) ones, possess a similar behaviour: the mean reconstructed snr values are a bit higher when $Tgap = 2\,\mathrm{s}$ than for $Tgap = 0.2\,\mathrm{s}$, but still compatible between them. This is an expected effect: the release of $Tgap$ threshold allows cWB to collect more noisy excess energy because the PM window is wider. Nevertheless, such an increase in energy is limited, so there are no unfavorable effects in setting $Tgap = 2\,\mathrm{s}$. The ROC curves (second row of figure 6.5, confirms this picture. They display similar performances even though with a little deficit for the $Tgap = 2\,\mathrm{s}$ set-up since, with a wider post-merger window the noise floor is expected to increase worsening the performances. Then in the LES search it is indicated to adopt a $Tgap = 2\,\mathrm{s}$ threshold to be sensitive to all the possible predicted astrophysical scenario, t_{echo}, which follow from the study of the BBH signals detected so far.

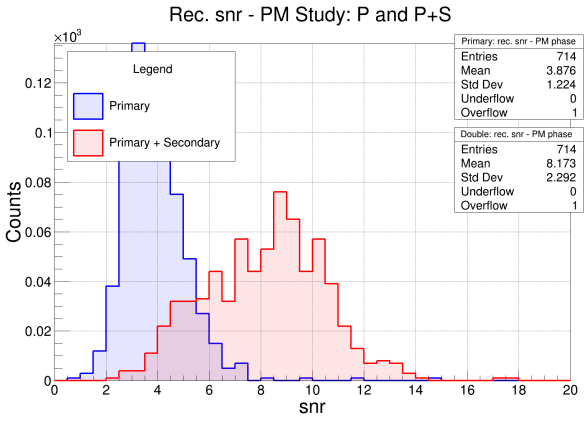

(a) No PMW.

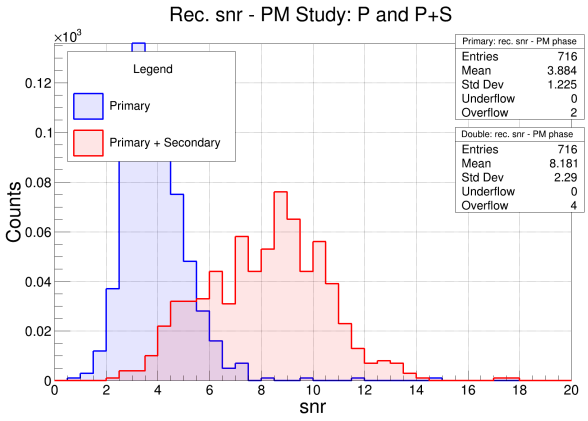

(b) Yes PMW.

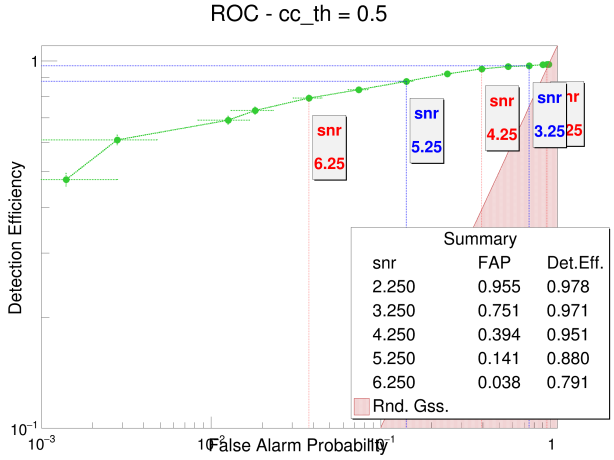

(c) ROC - no PMW.

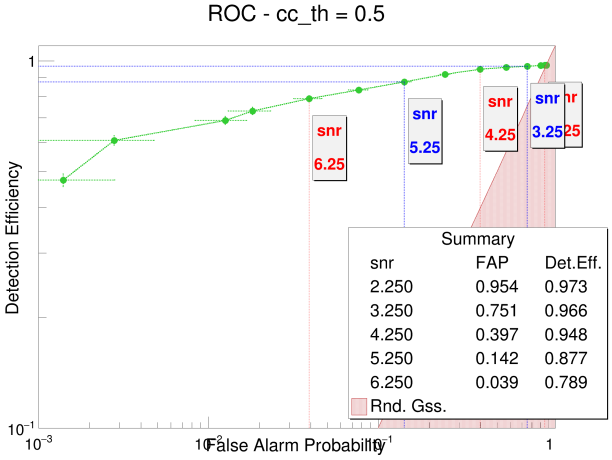

(d) ROC - yes PMW.

Figure 6.6: Comparison between the low energy cWB set-up for when no post-merger time window (PMW) is applied (left) or when it is applied (right). The thresholds and parameters of the seaches are: $bpp = 0.001$, $cc = 0.5$, WP10, $t_{blind} = 40\,\mathrm{ms}$, $Tgap = 2\,\mathrm{s}$ and $t_{echo} = 0.1\,\mathrm{s}$. Top row: snr_{rec}^{PM} distribution for BGK (blue) and SIG (red) studies. Bottom row: ROC curve with a $cc^{PM} \geq 0.5$ cut, to compare the detection efficiency performances.

6.7 Post-merger time window (PMW)

We have seen in section 5.3.3, that table 5.2 [4], suggests that it is possible to introduce in the LES search analysis a post-merger time window PMW. The reason is the will to reduce the energy content of the noise coming from times that are out of interest for current theoretical predictions of t_{echo}, detectors' sensitivity, and pipeline detection capabilities. We recall that when this PMW is used, the statistics of the analysis are estimated only inside this time region. Then, the LES search was performed with its best configuration obtained so far: $bpp = 0.001$, $cc = 0.5$, $Tgap = 2\,\text{s}$, $t_{blind} = 40\,\text{ms}$, and $WP10$ (single pixels selection rule), and the snr_{rec}^{PM} distributions are recovered, figure 6.6. We can compare these distributions with the ones obtained from the same analysis set-up but without the post-merger time window (PMW).

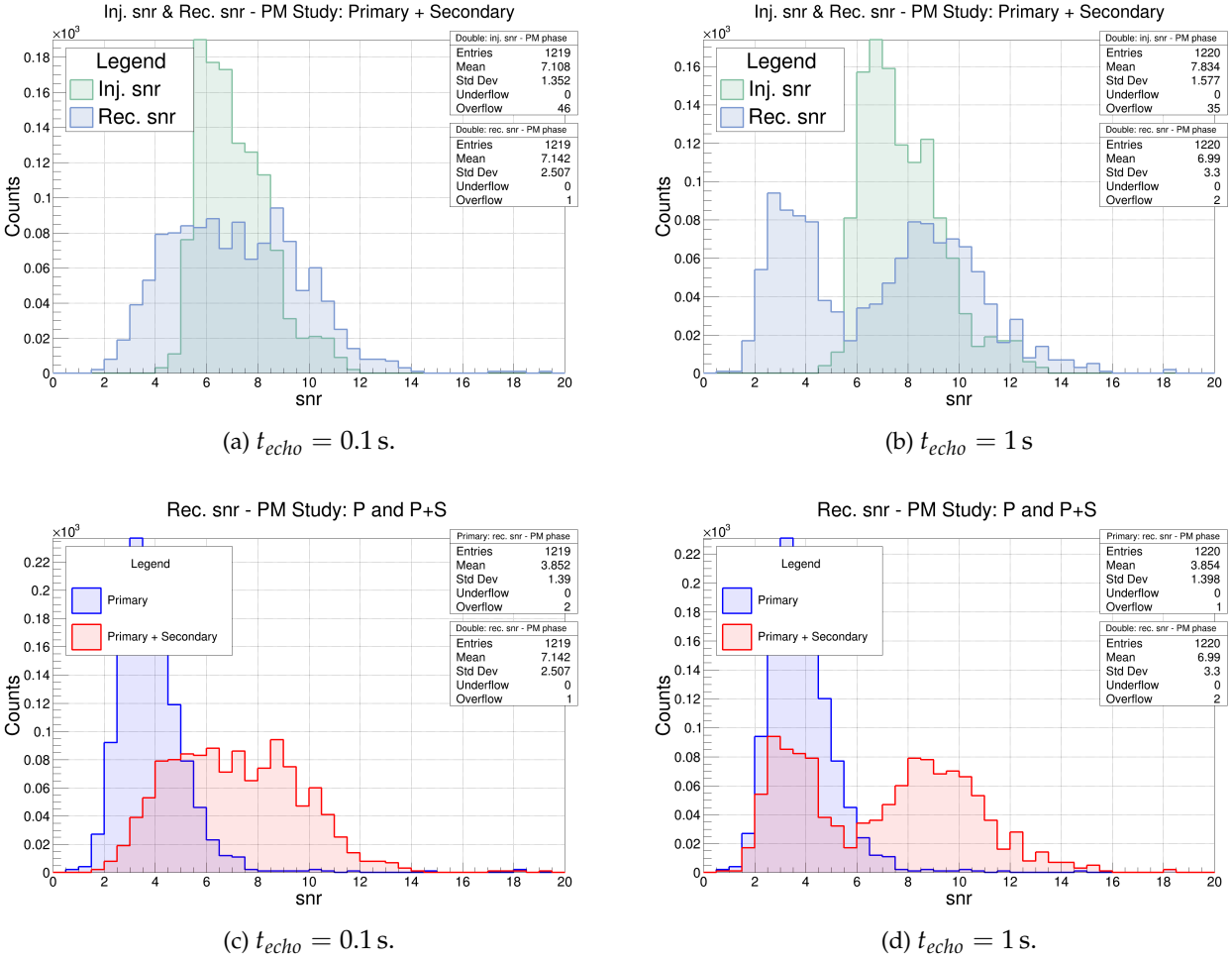

(a) $t_{echo} = 0.1\,\text{s}$.

(b) $t_{echo} = 1\,\text{s}$

(c) $t_{echo} = 0.1\,\text{s}$.

(d) $t_{echo} = 1\,\text{s}$.

Figure 6.7: Comparison between the low energy search when $t_{echo} = 0.1\,\text{s}$ (left column) and 1s (right column) after applying a 1 s time window in the post-merger phase of the signal, with the low threshold configuration developed so far: $bpp = 0.001$, $netCC = 0.5$, $Tgap = 2\,\text{s}$, $t_{blind} = 40\,\text{ms}$, WP10 as pixels selection rule. Top row the injected (green) and reconstructed (blue) snr inside the time window. Bottom row the BGK (blue)and SIG (red) distributions of snr_{rec}^{PMW}.

In figure 6.6 on the first row, left side, there is the snr_{rec}^{PM} distribution for the analysis carried on without the PMW for both the BGK (blue) and SIG (red) studies. On the right is the same plot for the same analysis configuration but introducing the

[4] For very peculiar and unusual BBH events, if compared with the average detections, this could not be true. Then a retuning of the $Tgap$ and PMW would be necessary.

PMW. The results are, within their uncertainties, identical, which is a bit of a surprise at first. The explanation for this unexpected result is that: the highly noisy part of the data is ruled out once t_{blind} is introduced. As anticipated in section 5.3.3 and overviewed in section 2.3 and 6.3, immediately after the merger the primary signal does not vanish, the ring-down signal is still present. Then, unless some noisy and partially coherent glitch is present in the PM, it is the ring-down energy to dominate the snr_{rec}^{PM} content. Moreover, even without a post-merger time window, the analysis is referred to 2 s of data after the coalescence time. This means that the PMW is cutting the least significant part of the data, and its influence over the final results is marginal.

To understand if a PMW could provide benefit, not only for echoes' studies, I have tried to perform the two studies above by injecting the secondary signal with a $t_{echo} = 1$ s and not 0.1 s. We start comparing the cWB LES search with $t_{echo} = 0.1$ s and $t_{echo} = 1$ s, when no PMW is applied. The two scenarios, compared in figure 6.7, display a difference in the reconstructed snr_{rec}^{PM} distribution. Here, figure 6.7, on the top row the snr^{PM} distribution for the $t_{echo} = 0.1$ s (left column) and $t_{echo} = 1$ s (right column): for $t_{echo} = 1$ s the SIG snr^{PM} distribution shows a bimodal behaviour which is due to the detection and null detection of the injected secondary signals. If the secondary signal is not detected the snr^{PM} follow the background distribution (blue one) as in figure 6.7. This behavior is not visible for the $t_{echo} = 0.1$ s scenario and this is due to the proximity of the secondary to the primary signal.

Figure 6.8 shows: in the top row, the difference in the snr_{rec}^{PM} distributions between the two scenarios of using (right) and not using (left) a post-merger window (PMW), while in the bottom row the ROC studies are shown. It is possible to appreciate a clearer distinction between the snr_{rec}^{PM} of BGK and SIG studies when using the PMW ($snr_{rec}^{PM} \rightarrow snr_{rec}^{PMW}$) than when studying the overall postmerger. Moreover, the PMW study allows to introduce another attenuation of the reconstructed snr in the post-merger, and even if it affects both the BGK and SIG analysis, the ratio between snr for both the configurations proves that the PMW provides better results than the only PM analysis. Looking at the ROC plots of figure 6.8, second row, it is possible to appreciate a gain the p-value signal when using the time window: focusing our attention over low p-values noise (i.e lower than < 0.02) we got that

- **no PMW:** the p-value signal, so the related detection efficiency is around $\sim 50\% - 60\%$ and rapidly decreasing, such that for p-value noise ~ 0.004 the detection efficiency drops to values $< 30\%$;
- **yes PMW:** the p-value signal, and so the detection efficiency, is around $\sim 50 - \% - 60\%$, but now it remains constant till p-value noise ~ 0.004, which is a big improvement with respect to the analysis configuration without the time window in the post-merger.

All of this suggests that introducing in the analysis this restriction over the time one has to study in the post-merger phase of a binary provides a relevant improvement in reducing the background noise and so in increasing the detection efficiency.

6.8 Post-merger coherence and trigger preselection thresholds

A common goal of all the analyses is the background noise suppression, and this analysis makes no exception. With this aim, one can estimate the coherent coefficients, cc^{IM} and cc^{PMW} [5] ,eq. (5.31), to understand if these values have different

[5] Here, the sup-script is PMW and not PM since the PMW is applied.

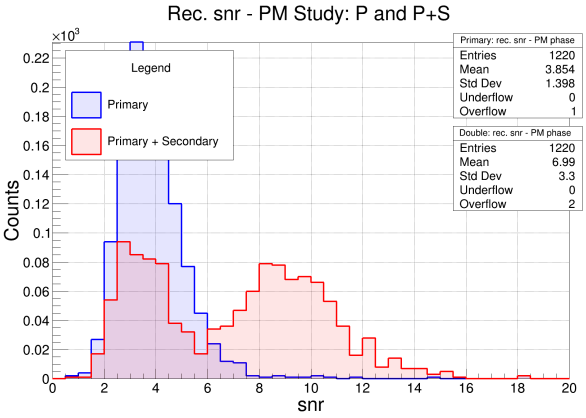

(a) $t_{echo} = 1\,\mathrm{s}$, no PMW.

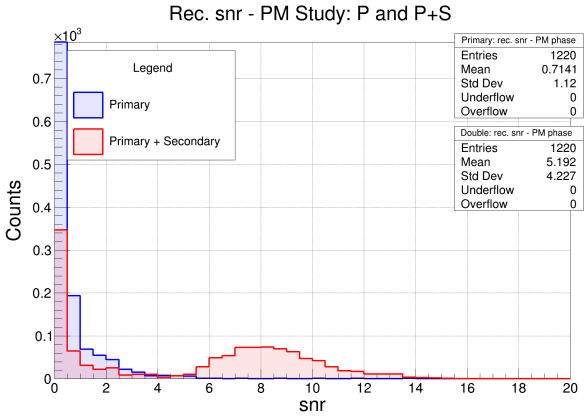

(b) $t_{echo} = 1\,\mathrm{s}$, yes PMW

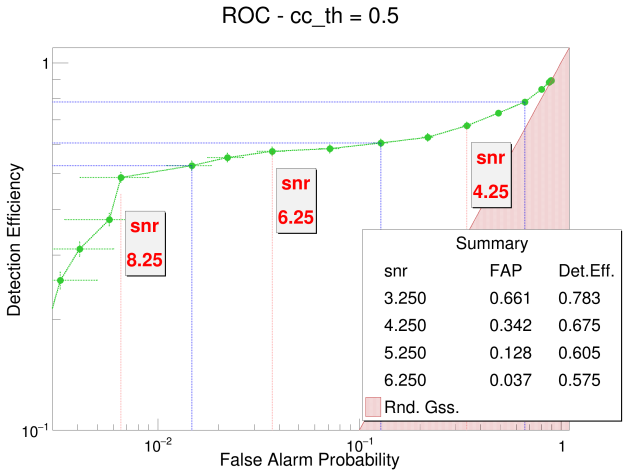

(c) ROC: $t_{echo} = 1\,\mathrm{s}$, no PMW.

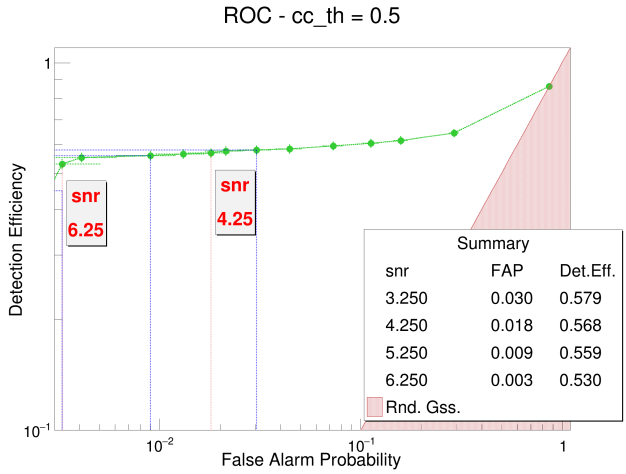

(d) ROC: $t_{echo} = 1\,\mathrm{s}$, yes PMW.

Figure 6.8: Comparison between the low energy search when $t_{echo} = 1\,\mathrm{s}$ without and with the 1 s time window in the post-merger phase of the signal. The window is centred over the injection time of the secondary signal. On the top row the snr_{rec}^{PM} (left) snr_{rec}^{PMW} (right) distributions, while on the bottom row the ROC curves for these two configurations.

distributions between the BGK and the SIG search. If so, they could provide another parameter to suppress the noise and improve the overall performance. The distributions of cc (green), cc^{IM} (blue), cc^{PMW} (red) are shown in figure 6.9. In the left plot 6.9a there are the cc distributions for the BGK analysis (cc_{BGK}), while on the right plot 6.9b the same distributions but for the SIG study (cc_{SIG}) [6].

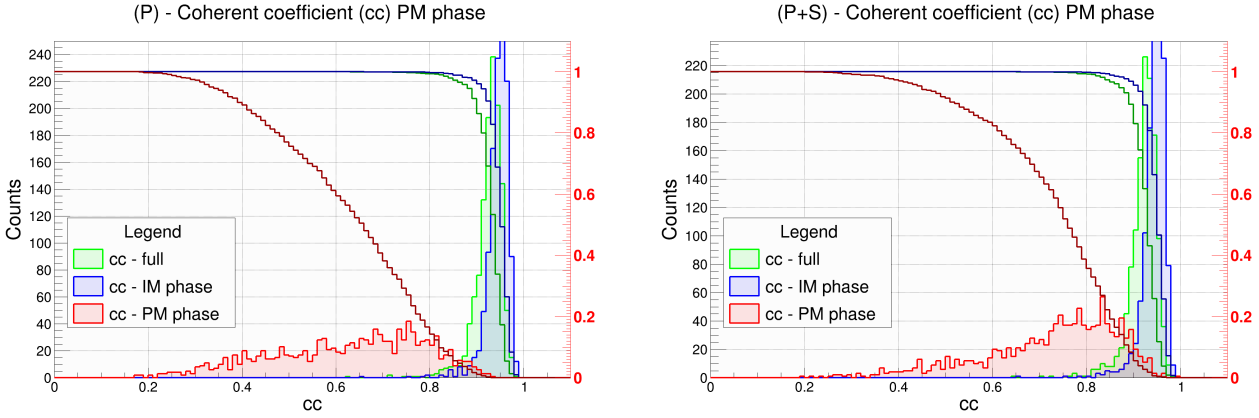

(a) Background study with PMW.

(b) Low energy signal study with PMW.

Figure 6.9: Histograms and cumulative distributions (lines and right red y-axis) of the coherent coefficient cc (eq (5.31)) for the full event (green) for the IM phase (blue) and for the PM phase (red). Here the post-merger, PM, is meant as the data segment contained in the post-merger window of 1 s. The left plot is referred to the BGK study, while the right one to the SIG study.

We can see that selecting only the events with $cc^{PM}_{SIG} \geq 0.5$ or 0.6 one can mitigate the background without significantly affecting the SIG study. The SIG distribution peak is near $cc^{PM}_{SIG} \sim 0.9$, and for values around 0.5 and 0.6, we are already in the tails of the distribution.

As said in 5.3.1, the cc^{PM} estimates the coherence of a trigger in the network of detectors, so the study of ROC curves for different cc^{PM}_{SIG} threshold values will help in understanding if a cut can improve the LES search performance.

Figure 6.10 shows that imposing a threshold on cc^{PM}_{SIG}, so selecting only the events for which $cc^{PM}_{SIG} \geq cc^{PM}_{th}$, penalises the detection efficiency only at high FAR. It is a positive result since we are interested in the low FAR region of the plot (following the discussion in section 6.7). For low FAR values ($FAR \leq 0.5\%$), there is a gain in the detection efficiency if one impose such a threshold; moreover, between $0.5 \leq cc^{PM}_{th} \leq 0.7$ the detection efficiency does not show remarkable difference. The drawback in introducing a cut over cc^{PM}_{SIG} is that imposing $cc^{PM}_{SIG} \geq 0.5$ and 0.6 reduces the starting ensemble of 1220 reconstructed events by a $\sim 8\%$ and $\sim 16\%$ respectively, so it cut upstream the number of follow-ups. Such a decrease is taken into consideration when estimating the ROC curves. Figure 6.10 shows when a cut in cc^{PM}_{SIG} is imposed, the maximum detection efficiency and false alarm probability are lower than the corresponding value for the not-cut analysis. Despite this loss, we still have enough statistics for this tuning phase. The cc^{PM}_{SIG} cut worthes the gain in detection efficiency of figure 6.10 when considering per thousand in FAP. Then, it is possible to choose $cc^{PM}_{SIG} = 0.5$ as the threshold value to be a little more conservative.

Physically this means that by cutting the events with low cc^{PM}_{SIG} one is mainly ruling out from the analysis some of the detections for which the echoes mimicker are very poorly detected or undetected. Any detectable energy excess in the PM of

[6] These analysis are performed with the last cWB LES search set-up: $bpp = 0.001, cc = 0.5, Tgap = 2\,\text{s}, t_{blind} = 40\,\text{ms}$ and $WP10$, with the PMW applied.

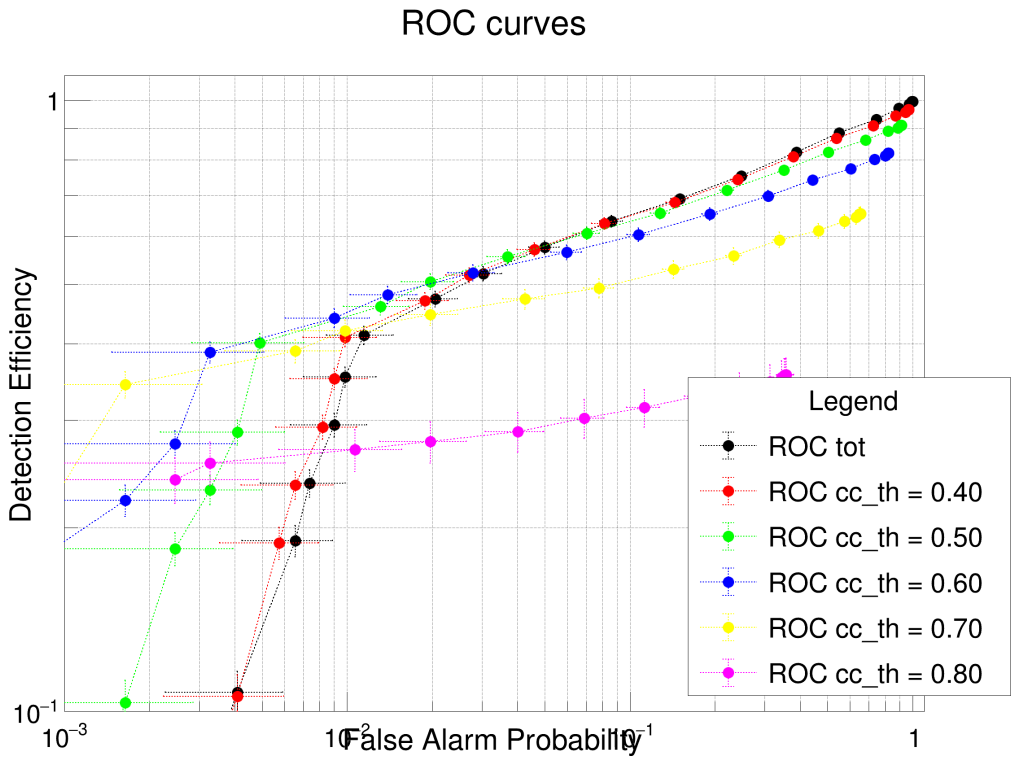

Figure 6.10: ROC curves for the cWB LES configuration with $bpp = 0.001$, $cc = 0.5$, $Tgap = 2\,\mathrm{s}$, $t_{blind} = 40\,\mathrm{ms}$, $WP10$, and the PMW applied. Here are compared the performances of the searching algorithm applying in post-production a cut over the cc^{PM} parameter in order to rule out from the analysis high-confidence noise events. In black the curve without any cut applied, then in the legend the colours' code is explained.

astrophysical origin should possess a relatively high cc^{PM} value because not only it should be present in all the detectors but it also satisfies the sky localisation of the primary event which helps in maximising its reconstruction. So, having an energy content in the PMW that is not highly coherent is a feature common for the noise rather than for astrophysical signals.

Following this analysis, it is possible to study the distributions of ρ^{PM} as a function of cc^{PM}, as shown in figure 6.11. The reason is that there is a link between the coherence of our data and their energy. Recall (section 5.3.2) that ρ^{PM} is defined as:

$$\rho^{PM} = \sqrt{\frac{E_c^{PM} \cdot cc^{PM}}{K}}\,. \tag{6.2}$$

Figure 6.11 shows on the left the ρ^{PM} vs cc^{PM} scatter plot for the BGK study. On the right is the same plot for the SIG study. The BGK analysis highlights that the ρ^{PM} distribution shows a breaking point for values higher than 2, where very few energy excesses were found by the analysis. In the SIG analysis, we can observe a peculiar behavior of the ρ^{PM} parameter: one can notice a belt in the ρ^{PM} distribution between $2 \lesssim \rho^{PM} \lesssim 5$: here very few events are present, and this behavior is unexpected. The reason is the hard-coded $SUBRHO$ threshold of cWB, whose value is set equal to 5 in the standard cWB search. Such a threshold prevents cWB to select clusters of pixels for which

$$\rho_{cluster} \leq SUBRHO\,, \tag{6.3}$$

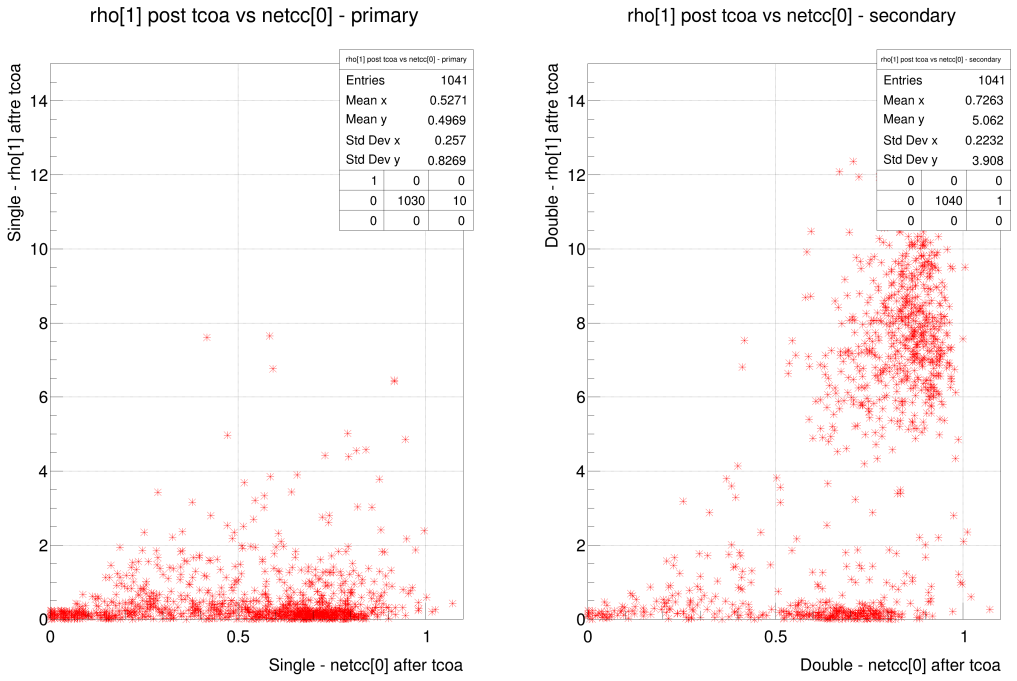

Figure 6.11: Distribution of ρ^{PM} (y-axis) as a function of cc^{PM} (x-axis) for the BGK (left) and SIG (right) study. We see a bimodal distribution with a clear gap belt between $2 \lesssim \rho^{PM} \lesssim 5$ for the SIG study.

where $\rho_{cluster}$ has the same definition of ρ (equation (5.21), but it is estimated for each cluster of pixels [7] (an event can be the collection of one or more clusters, like the primary plus secondary scenario).

To enhance the possibility for cWB LES search to recover these clusters of pixels, the $SUBRHO$ was lowered, testing the values: $SUBRHO = 3$ and 2. The scatter plot of figure 6.12 shows that lowering $SUBRHO$ allows cWB to populate the upper part of the belt in the SIG study. The $SUBRHO = 1$ value was not tested since such threshold is used to reduce the computational load of cWB, and going lower than 1 would have been not optimal. So, as it was always done so far, it is necessary to find a compromise in performances and reconstruction capability. The $SUBRHO = 3$ threshold values results to be the best options since the belt of ρ^{PM} when $SUBRHO = 5$ now is partially filled, meaning that the LES search collects more energy. Also, the ROC curves of figure 6.13 provide a hint over the goodness of using $SUBRHO = 3$. For fixed snr^{PM} values, the detection efficiency for the analysis carried on with $SUBRHO = 3$ increases together with an increase of the false alarm probability with respect to the $SUBRHO = 5$ result. Setting $SUBRHO = 3$ allows to collect more energy in the PMW, having that the LES search performances remain competitive against $SUBRHO = 5$ analysis, even though a small loss in FAR for fixed snr^{PM} values occurs. Nevertheless, between $0.0005 \leq FAP \leq 0.1$, for $SUBRHO = 3$ one has $50\% \leq DE \leq 75\%$, while for $SUBRHO = 5$ for the same FAR range one has: $48\% \leq DE \leq 60\%$. Thus, in conclusion, $SUBRHO = 3$ results to be the best compromise possible for this search.

[7] $SUBRHO$ acts over each cluster of pixels during the clustering phase of the cWB ETG phase, while the usual ρ parameter is a quantity evaluated over the final event, which is the sum of all the clusters of pixels within a time interval defined by the user.

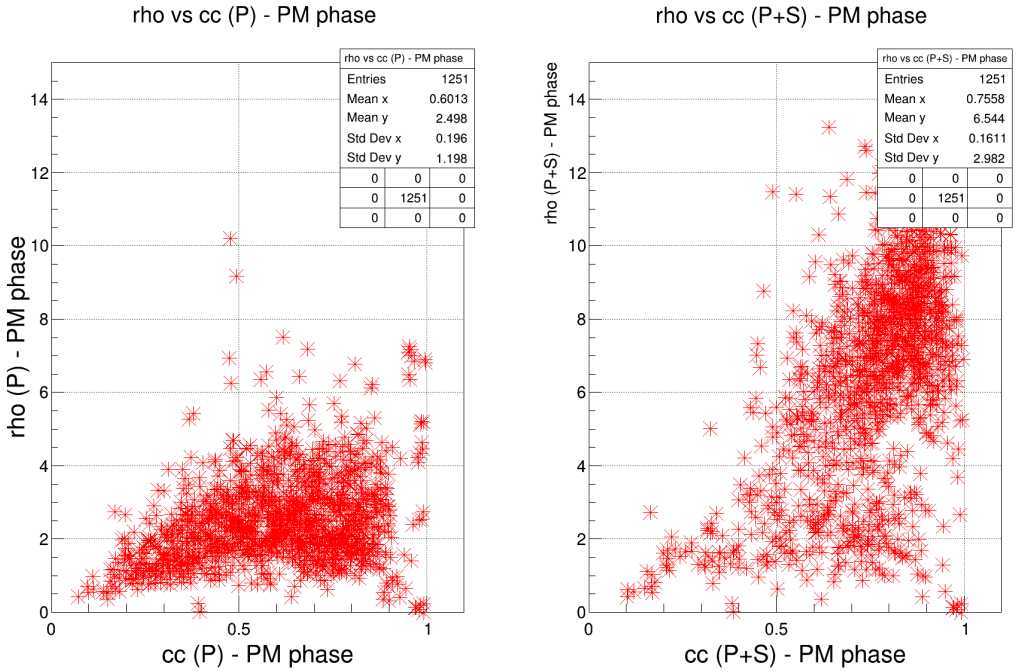

(a) SUBRHO = 3.

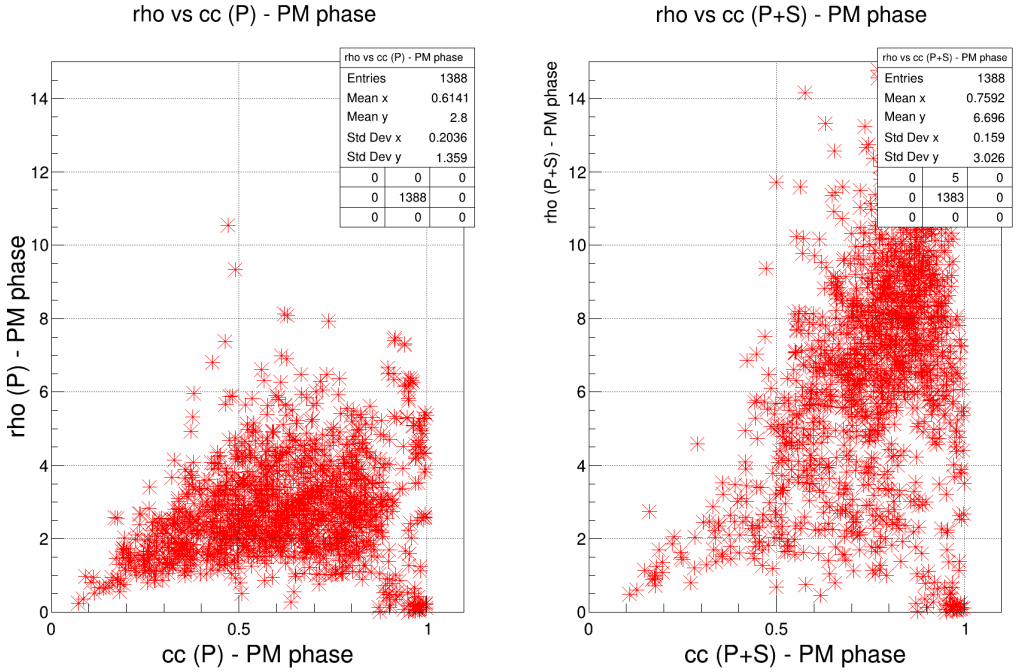

(b) SUBRHO = 2.

Figure 6.12: Here are reported the scatter plot of ρ^{PMW} versus cc^{PMW} for the BGK analysis (left) and SIG analysis (right). Top row, the results for the $SUBRHO = 3$. Bottom row, the results for $SUBRHO = 2$ scenario.

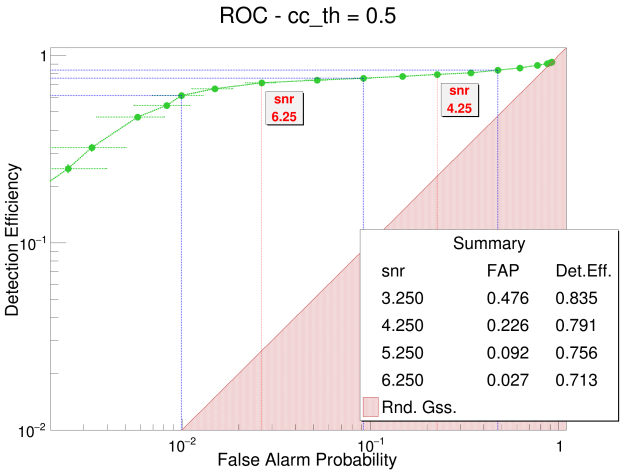

(a) SUBRHO = 3.

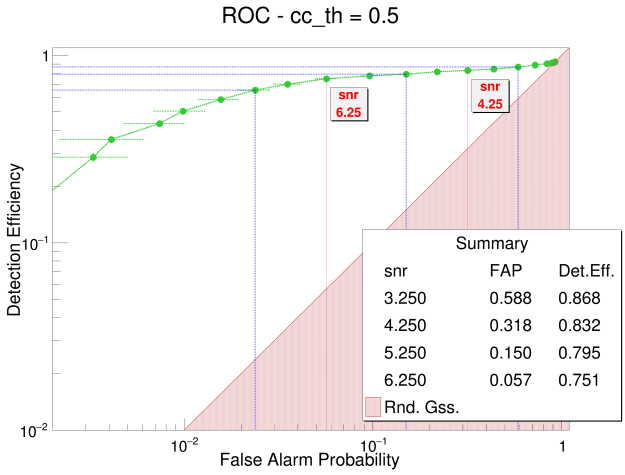

(b) SUBRHO = 2.

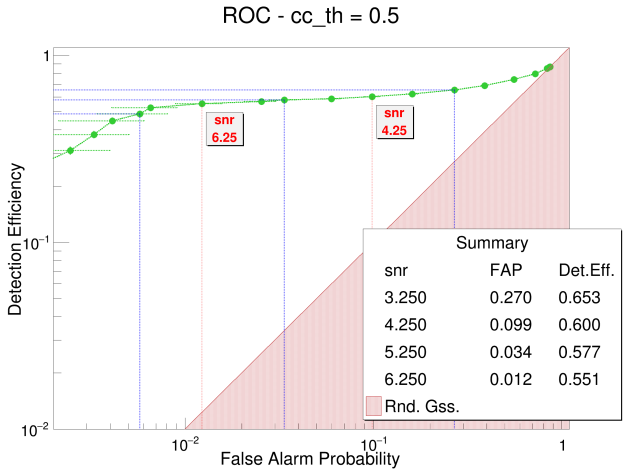

(c) SUBRHO = 5.

Figure 6.13: ROC curves for the cWB LES search for different values of $SUBRHO$ threshold. The top row reports the $SUBRHO = 3$ (left) and $SUBRHO = 2$ (right) curves. On the bottom row the standard case of $SUBRHO = 5$. Studied event: GW150914.

6.9 Whitening

In section 5.2.3 we have seen that the data are whitened in order to mitigate the noise contributions. Normally, the standard cWB configuration whitens the data by evaluating the local noise energy RMS using a TF map with maximum resolution in frequency, which is of 1 Hz and a time resolution of 0.5 s. This configuration is not suitable for the goal of this analysis. In the whitening process the estimated whitening coefficient (see figure 5.2) divides the energy content of pixels whose time duration is 0.5 s. A single whitening coefficient covers 40 pixels since it is estimated each 20 s. Once the TF map is whitened, then the whitened time series is recovered by having the inverse WDM transform. In the multi-resolution stage (5.2.3) when facing finer time resolutions, pixels whose times are contained inside the big interval of 0.5 s, but not containing the CBC signal, have been whitened based on the energy content of the wide-in-time- pixel and not based on their effective energy content. This leads to a leakage of energy inside these pixels.

This disturbance can be attenuated by acting over the TF resolution of the data in the whitening stage: the TF whitening resolution in frequency can be decreased in order to increase the time resolution, and the best compromise results to be:

$$\Delta t = 0.15\,\mathrm{s}, \quad \Delta f = 4\,\mathrm{Hz}\,. \tag{6.4}$$

which has the effect of improving the performances of cWB LES search configuration, meaning that for the same snr_{rec}^{PM} the FAP results to be a little smaller with similar detection efficiencies.

6.10 Final configuration

In conclusion, we have seen (section 6.2) that the threshold over the cc parameter can be left untouched with respect to the cWB standard search: it has no effects due to the presence of the primary signal. Concerning bpp values (section 6.2), although $bpp = 0.004$ allows collecting a little more energy with respect to $bpp = 0.001$, this energy is mostly due to the background noise. This is evident (section 6.5) from the ROC curves that slightly prefer the cWB standard search value, so $bpp = 0.001$, rather than a higher one. We have also seen in section 6.6 that, depending upon the kind of search one wants to perform, there is the necessity to increase the $Tgap$ constraint from 0.2 s up to 2 s to enhance the reconstruction, within the same event using the primary signal as a smoking gun, of possible excess of energy in the post-merger phase of a binary. Another result related to the analysis time is the introduction of a post-merger time window (PMW), lasting 1 s (section 6.7). Such a time window is extremely useful in sensibly reducing the noise as well as preserving cWB performances. Together with the PMW we have seen that to get rid of the spurious energy content due to the BBH ringdown, it is suggested to introduce a blind time t_{blind} (6.7) between the coalescence time of the BBH signal, t_{coa}, and the starting time of the post-merger window. From the analysis of section 6.3 we can say that $t_{blind} = 40$ ms is a good compromise to exclude most of the ring-down energy due to the primary signal without losing too much of the post-merger phase nearby the primary signal, where echoes are predicted by theoretical models. Such value as to be intended as a lower limit: one can set t_{blind} even larger to rule out almost completely the ring-down effects slightly improving cWB LES search performances. It is a choice mostly related to the search and its aim. What is discouraged is to apply the

PMW immediately after the coalescence time. We have also seen that a single pixels' selection rule (WP10) has better performances for low FAP values with respect to the chirping-up one (WP5). This is again a good outcome since the analysis can maintain another similarity with the cWB standard search. Moreover, a fundamental difference between the standard search and the LES one is the decrease of the SUBRHO threshold from 5.0 to 3.0 in order to avoid a hard cut over $\rho_{cluster}$ values. This decrease, studied in section 6.8, does not affect significantly the pipeline performances, even though it contributes a little to reducing the detection capability of the method.

So, to summarize, the final cWB configuration for the LES search is:

- the pixels'selecion rule being $WP10$;
- the user defined threshold are bpp=0.001, cc=0.5, ρ=3.5, $SUBRHO$=3.0, $Tgap$=2 s;
- it is possible to require a cut, in the post-production stage of the analysis, over the **coherent coefficient of the post-merger phase**, cc^{PM}, such that only the events with $cc^{PM} \geq 0.5$ are studied;
- the introduction of the **post-merger time window (PMW)** with a time duration of 1 s as well as the introduction of the **blind time** whose value was set equal to $t_{blind} = 40$ ms;
- an ad hoc TF resolution map for the whitening: $\Delta t = 0.15$ s and $\Delta f = 4$ Hz.

These variations in the cWB analysis' thresholds are summarised in table 6.6.

Sub.Th. search configuration parameters		
Parameters	All-Sky O3 search	LES search
bpp	0.001	0.001
$subnet$	0.5	0.5
cc	0.5	0.5
ρ	5.0	3.5
$Acore$	1.7	1.7
$Tgap$	0.2	2.0
$Fgap$	128.0	128.0
$SUBRHO$	5.5	3.5
$SUBNET$	0.1	0.1
PMW	none	yes, $\Delta t_{PMW} = 1\,\mathrm{s}$
t_{blind}	none	yes, $t_{blind} \geq 40\,\mathrm{ms}$

TABLE 6.6: In this table are compared the values of cWB production thresholds. In the first column are listed the cWB parameters, in the second and third columns are reported their values for the standard search (O3 all-sky burst search) and the LES search respectively. Only ρ, $Tgap$, and $SUNRHO$ thresholds are different from one search to the other, having their values decreased for the current search in order to allow cWB pipeline to collect more energy without compromising its detection capabilities. The Δt_{PMW} labels the time width of the post-merger window.

Chapter 7

CWB search for low energy signals: performances

So far, we have developed an algorithm to be integrated into the coherent WaveBurst pipeline to detect low energy signals (echoes 3.1) in the post-merger phase of a binary black hole coalescence, chapter 5. The name of this new cWB search is: low energy signal (LES) search. The integration of the LES search over the cWB pipeline initially required a phase of code development where different statistical estimators (section 5.3.1) for the post-merger analysis were implemented in cWB. Then, a debugging stage followed. Consequently, we studied the impact of the cWB thresholds (5.2.4) over the LES search (chapter 6), so, when necessary, cWB was tuned to maximise the LES search performances. Together, the response of the LES search for different astrophysical scenarios was investigated. Therefore, it was studied, in chapter 6, inside which range of echo parameters the LES search retains constant performances and results. Moreover, post-production cuts based on the LES search results were implemented (section 6.8) increasing the noise rejection of the LES search.

Now, we have in our hand a performant and working algorithm of the cWB LES search, then, here, it is time to use it and search for the presence of echoes in the PM phase of all the GW events listed in table 5.1. For all of these events the off-source experiments (see chapter 5, figure 5.4), provide the estimates for the distribution of background (BGK) events. Moreover, they also provide, with the signal (SIG) analysis the fraction of detectable echo candidates as a function of their amplitude. Through the detection efficiency (DE) curves in function of the injected *hrss* (eq. (7.1)) [106]

$$hrss = \sqrt{\int_{-\infty}^{+\infty} (\mid h_+(t) \mid^2 + \mid h_\times(t) \mid^2) dt} \tag{7.1}$$

at a fixed false alarm probability (FAP), we estimate the performances of the cWB LES search. Then, we can use the ROC plots to summarise the performances in terms of detection efficiency vs false alarm probability per each GW event. The on-source results are then disclosed, and I provide the estimated p-values as well as confidence intervals on the maximum value of the injected echoes' *hrss* compatible with a null hypothesis.

To fulfill these objectives, the statistic for each GW event under study is increased, trying to recover between 4000 and 8000 events with respect to the $\sim$ 700 - 1000 of the tuning phase.

7.1 Configuration of the injected echoes

In the developing phase of this project, we have used a signal from a BBH coalescence with high component masses $80 - 80 M_{\odot}$ as an echo mimicker (see section 5.3.4). Now, many specialised papers about echoes [96, 103, 104], model these signals with sine-gaussian pulses. Then, we use a sequence of two elliptically polarized sine-gaussian (SGE) signal (section 5.3.4, equation (5.36)), as echo mimickers to evaluate the cWB LES search performances.

Such SGE signals were introduced in chapter 5, section 5.3.4, here I just want to recall their morphological characteristics. These SGE have a frequency $f_0 = 140\,\text{Hz}$, and a quality factor $Q = 8.8$, such that their time duration is $\tau_{SGE} \sim 20\,\text{ms}$. They are injected as a train of two signals. The first SGE is injected 300 ms after the coalescence time (t_{coa}) of the BBH signal, so: $t_{echo} = 300\,\text{ms}$ (section 3.1). Its amplitude ranges between $[0.1 - 4.0] \cdot 10^{-23}$ and is uniformly distributed inside this interval. The second SGE is injected again 300 ms after t_{echo}, so it has a time distance to the first echo mimicker of: $\Delta t_{echo} = 300\,\text{ms}$, (section 3.1, equation (3.1)). Its amplitude is proportional to the one of the first SGE, since the selected damping factor $\gamma = 0.5$ (section 3.1).

The reasons in having $t_{echo} = 300\,\text{ms}$ can be summarised in the following two points:

- the same echoes configuration for each GW event under study will allow understanding if different primary signal morphologies with different *snr* can affect the detection of the echo. Moreover, having the same echoes' configuration after each BBH signal, will allow a fair comparison between results;

- the results of section 6.1 and 6.3 show that, unless t_{eco} is really small, say $t_{echo} < 60\,\text{ms}$, then there is not a real difference for cWB in having a signal injected at 200 ms or 300 ms. The value $t_{echo} = 300\,\text{ms}$, looking at table 5.2, seems a bit higher with respect to the average, but for us, it could be a good compromise. Many tests were performed with $t_{echo} = 100$, 200ms without detecting any significant differences in performances between the two configurations. Nevertheless, in section 6.7, we have seen that the secondary signal results to be slightly less detectable when t_{echo} increases. Then, $t_{echo} = 300\,\text{ms}$ can well represent the performances and results expected for all the events for which $t_{echo} \in [200 - 400]\,\text{ms}$ which are the majority in my analysis.

7.2 SGE echoes morphology vs chirp one: LES search performances

In section 7.1, we have seen that the search for echoes is going to be performed by modeling such signals through a train of two SGE pulses. To check that the results are robust against the choice of the echo proxy, I compared the performances achieved with the SGE echo model to those obtained using a high mass BBH waveform.

In figure 7.1, first row, is reported the injected and reconstructed snr^{PMW} for both the echoes' configurations: HMBBH (left side) and SGE (right side) one. This is a sanity check since the two studies are performed over different data sets and the SGE study has a number of injections that is more than double the one of the HMBBH study.

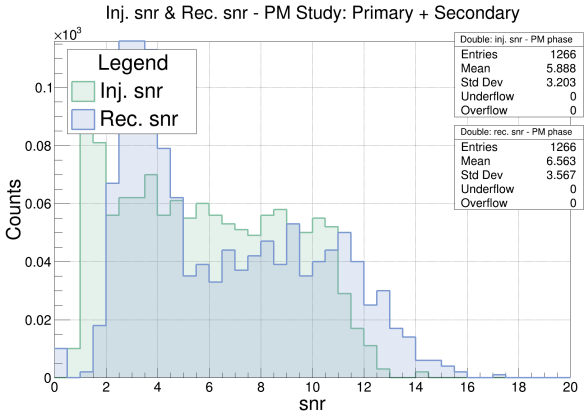

(a) Echo: BBH model.

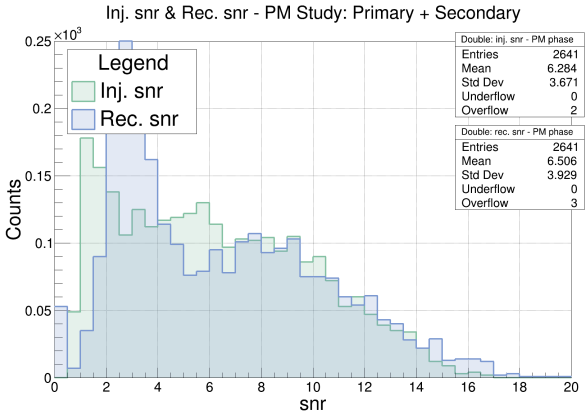

(b) Echo: SGE model.

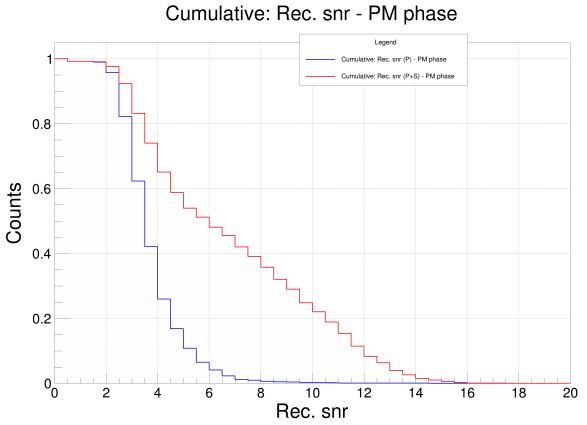

(c) Echo: BBH model.

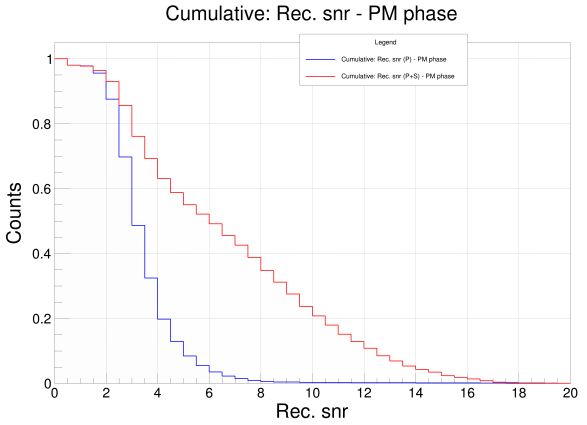

(d) Echo: SGE model.

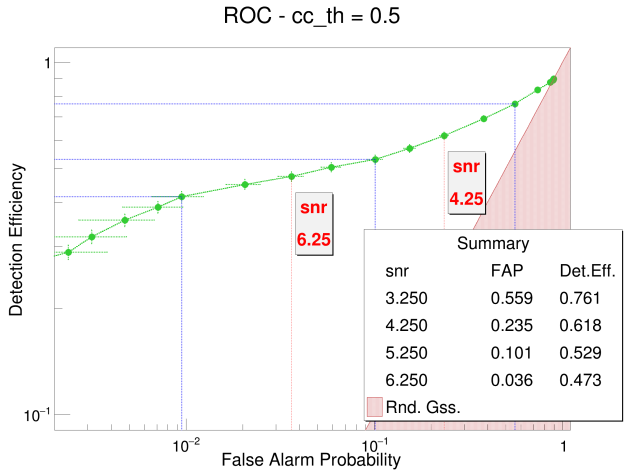

(e) Echo: BBH model.

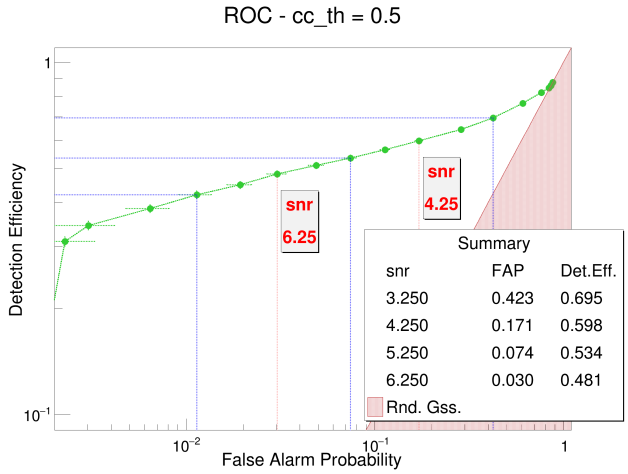

(f) Echo: SGE model.

Figure 7.1: The first row shows the the injected (green) and reconstructed (blue) snr^{PMW} for both the cWB LES search: the high mass BBH signal as echo mimicker (left) and SGE as echo mimicker (right) configuration. The second row shows the cumulative event distribution as function of snr^{PMW}_{rec} for the high mass BBH echo-like signal (left) and SGE one (right). In blue the background distributions (P), in red the signal distribution (P+S). The third row shows the ROC curves for both the previous configurations, high mass BBH echo-like (left) and SGE echo-like (right). Primary event: GW150914.

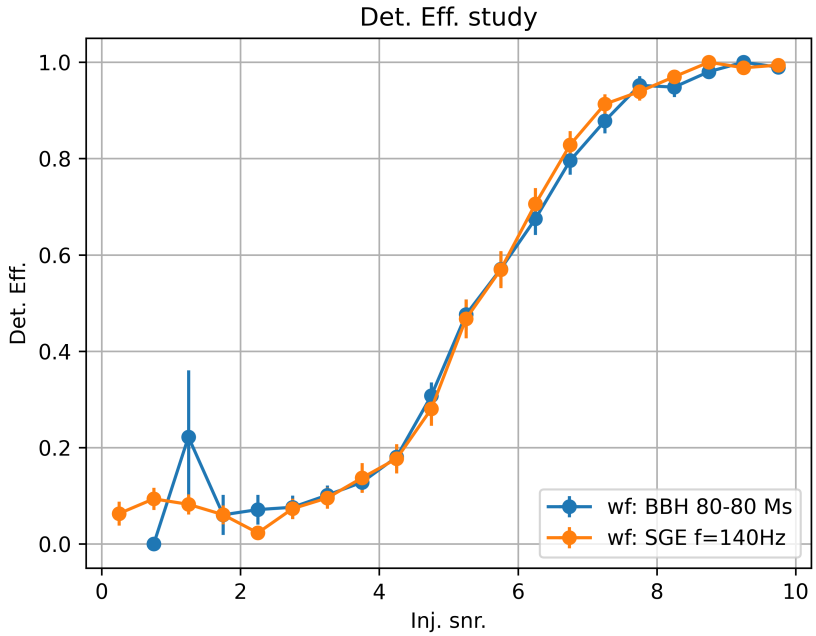

Figure 7.2: Detection efficiency as function of snr_{inj}^{PMW}. The study is carried on for two different morphologies of echo's signals: a high mass BBH coalescence (blue), and an elliptically polarised sine-Gaussian train of two pulses (orange). For details see sec. 7.1.

Now, figures 7.1, second and third rows, and 7.2 compare the performances of the two echoes' configurations. In figure 7.1, by inspecting the background (blue line) cumulative distributions (second row) for both the echoes' configurations it is possible to see there are no relevant differences in behavior or performances between the two echo configurations. This is visible as well in figure 7.2, having that the detection efficiency for both the echo's morphologies shows a compatible trend with respect to the injected snr, snr_{inj}^{PMW}. Then, the ROC plots show similar trends, having comparable FAP and DE for the same snr_{rec}^{PM}, even if the SGE configuration has, for fixed snr_{rec}^{PMW}, lower FAP and DE. This minimal difference between the two echo configurations can be due to a combination of multiple choices. The single-pixel selection rule is more suitable to detect and reconstruct SGE-like signals than chirping-up signals (reference to section 5.2.3, 5.3.4). The BBH signals have their energy content wider spread in their inspiral and ring-down phase which are difficult to be detected by cWB. Then, for the same injected energies, the overall detected energy in the SGE configuration is greater than the BBH ones. This helps in explaining why, for relatively high snr_{rec}^{PMW} ($\sim 5-6$), the DE and FAP are better for SGE configuration than the HMBBH one, and why the trend is inverted for relatively low snr_{rec}^{PMW} ($\sim 2-3$). Some HMBBH, if detected, are not entirely reconstructed and they will increase the statistics in the low snr_{rec}^{PMW} region.

For these reasons, and since the two configurations have shown comparable performances, the general study of the cWB LES search will be done using SGE signals as echoes-mimicker.

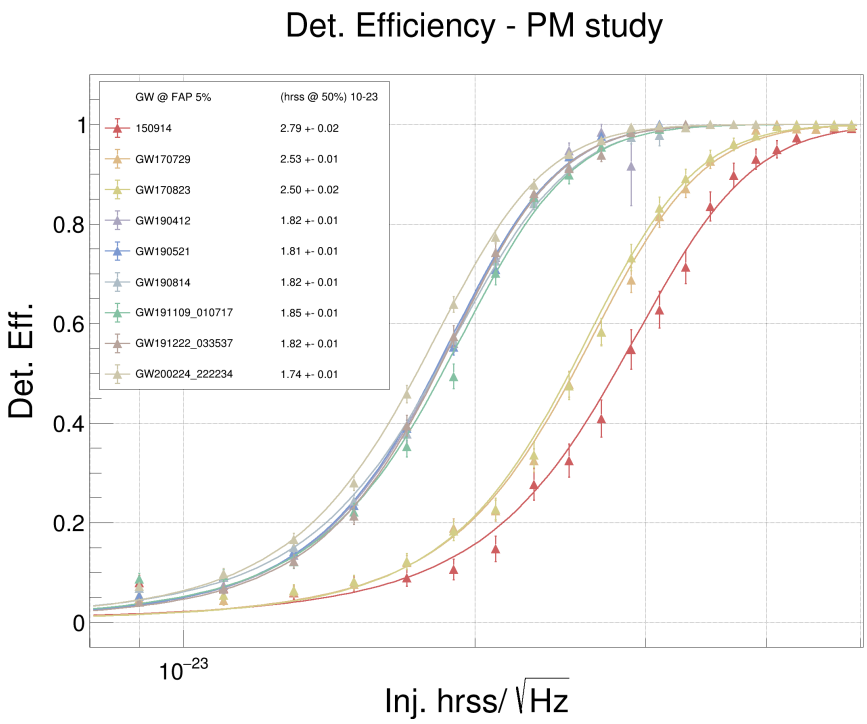

Figure 7.3: Plot of the detection efficiency as function of the $hrss_{inj}$ of the secondary signal. $hrss_{inj}$ units: $10^{-23} \cdot \sqrt{\text{Hz}}$. We have not reported here all the efficiency curves of the analysed events, but only a small subgroup for each observing run of the LIGO-Virgo-KAGRA collaboration. The $hrss_{inj}$ in the legend corresponds to a detection efficiency of 50% with a FAP of 5%.

7.3 Sensitivity of the LES search to echoes

Table 7.1 lists the typical amplitudes sensitivity for echoes, namely the *hrss* at 50% of detection efficiency and 5% of false alarm probability for all the events in table 5.1. From this table 7.1 it seems to be a very small improvement between O1 and O2 observing run in the detection efficiency capabilities, reducing the average detectable *hrss* from $\sim 2.7 \cdot 10^{-23}/\sqrt{\text{Hz}}$ to $\sim 2.5 \cdot 10^{-23}/\sqrt{\text{Hz}}$. Such reduction in *hrss* is more accentuated passing from O2 to O3, where from an average value of $\sim 2.5 \cdot 10^{-23}/\sqrt{\text{Hz}}$ we have passed to an average of $\sim 1.8 \cdot 10^{-23}/\sqrt{\text{Hz}}$, which is an improvement of around the 28%. Such improvement in the *hrss* is mainly due to an improvement in the detectors' sensitivity since the pipeline running over the analysed data has not changed its basic configurations. Figure 7.3 reports the detection efficiency as a function of the injected echoes' strength for selected BBH events from different observing runs. The figure 7.3 clearly shows the systematic improvement of sensitivity in subsequent runs discussed above.

We can also perform a comparison with the results of [86] for the injected *hrss* needed to reach a 50% of detection efficiency. We need to keep in mind that the injected signals are not the same: the most sensitive one out of the set injected in [86] (SGE, Q=100, $f_0 = 235\,\text{Hz}$) reaches a 50% of detection efficiency for an injected $hrss = 8 \cdot 10^{-23}/\sqrt{\text{Hz}}$ requiring a false alarm rate (FAR) of one per 100 years. Here instead, for these injected SGE ($Q = 8.8$, $f_0 = 140\,\text{Hz}$), the 50% detection efficiency is $hrss \sim 1.9 \cdot 10^{-23}/\sqrt{\text{Hz}}$ but corresponding to a much higher FAR of 2 per year during O3. Such value is estimated as the 5%-FAP times the rate of considered BBH mergers, taking into account the observation times of the detectors' network. A tentative to compare our results with other searches dedicated to echo signals is

carried on in chapter 9, section 9.1, nevertheless, we are not aware of any study similar to the one presented here, in the literature relative to echoes.

List of hrss @ det. eff of 50% with 5% of FAP		
Run	GW name	hrss $\cdot \left[10^{-23}\right] / \sqrt{\text{Hz}}$
O1	GW150914	2.79 ± 0.02
O1	GW151012	2.57 ± 0.03
O1	GW151226	2.70 ± 0.03
O2	GW170104	2.52 ± 0.01
O2	GW170608	2.63 ± 0.01
O2	GW170729	2.53 ± 0.01
O2	GW170809	2.40 ± 0.02
O2	GW170814	2.51 ± 0.02
O2	GW170823	2.50 ± 0.02
O3a	GW190408_181802	1.82 ± 0.01
O3a	GW190412	1.82 ± 0.01
O3a	GW190503_185404	1.96 ± 0.03
O3a	GW190512_180714	1.69 ± 0.02
O3a	GW190513_205428	1.83 ± 0.01
O3a	GW190517_055101	1.80 ± 0.02
O3a	GW190519_153544	1.84 ± 0.01
O3a	GW190521	1.74 ± 0.01
O3a	GW190521_074359	1.73 ± 0.01
O3a	GW190602_175927	1.98 ± 0.04
O3a	GW190701_203306	1.84 ± 0.01
O3a	GW190706_222641	1.82 ± 0.01
O3a	GW190828_063405	1.82 ± 0.01
O3a	GW190915_235702	1.88 ± 0.02
O3a	GW190929_012149	1.86 ± 0.02
O3a	GW190814	1.82 ± 0.01
O3b	GW191109_010717	1.85 ± 0.01
O3b	GW191204_171526	2.05 ± 0.05
O3b	GW191215_223052	1.69 ± 0.02
O3b	GW191222_033537	1.82 ± 0.01
O3b	GW191230_180458	1.77 ± 0.08
O3b	GW200219_094415	1.75 ± 0.07
O3b	GW200224_222234	1.74 ± 0.01
O3b	GW200225_060421	1.89 ± 0.04
O3b	GW200311_115853	1.80 ± 0.01

TABLE 7.1: The table lists the values of injected hrss needed to have a detection efficiency of 50% requiring a false alarm probability of the 5% for each gravitational wave events analysed in this study.

7.4 On-Source results

All the studies so far, for both the setting and the performances' estimation of the cWB LES search, are performed off-source through simulations, see section 5.3.1.

The on-source analysis, (section 5.3), allows the comparison of the real detection result with its related background (BGK) distribution and signal (SIG) distribution. Such comparison provides the probability that what is detected on-source is compatible or not with the background. I decided a priori to set a threshold on the false discovery rate [107], namely $FDR \leq 0.1$ to select the cases deserving deeper studies. This follow-up study has to probe the consistency with BGK and SIG results (an example will be given in the following of this chapter) and also perform a morphological study (described in chapter 8) of the PM event. These investigations aim to assess whether the nature of the PM energy excess is a noise instance or a genuine astrophysical event, or an unclear event.

The on-source (OS) analysis follows the same configuration of the cWB LES analysis and estimates in its PMW the same characteristics (section 5.3.2). The coalescence time for each on-source detection is taken with suitable time resolution down to the millisecond, from the PE waveform posterior information available through GWOSC [13] public data.

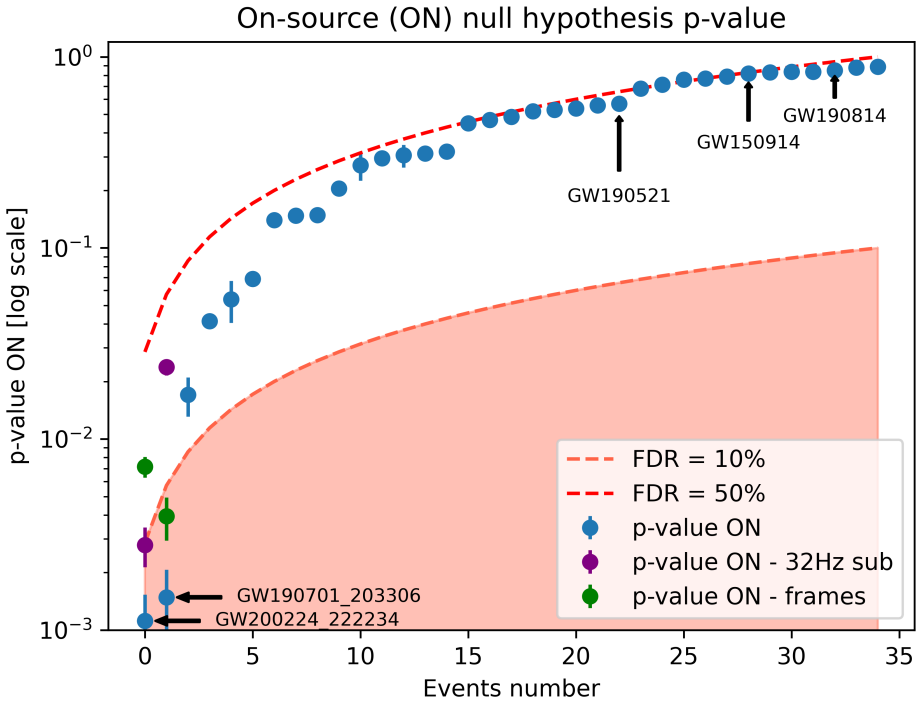

Figure 7.4: Visual display of the ranking statistics of the null hypothesis p-value for the on-source event for each GWs under investigation with their relative uncertainties, blue dots. The **red dashed line** corresponds to a false discovery rate $FDR = 50\%$. The **orange dashed and filled line** highlights the region of the p-value plot in which the false discovery rate (DR) is smaller than 10%. **Violet dots** show the on-source p-value for a complete analysis (BGK, LES, and on-source study) carried on using only the 4096 s around the main BBH event under study. **Green dots** are referred to the on-source p-value for a complete analysis (BGK, LES, and on-source study) carried on over the same standard analysis data but after applying a 32 Hz data mitigation plugin to suppress some noisy data features contaminating the O3a and O3b observational periods.

On source p-values and PMW *snr*			
Run	GW name	p-value$_{\mathrm{ON}}$	snr_{rec}^{ON}
O1	GW150914	0.819 ± 0.006	0.37
O1	GW151012	0.53 ± 0.01	0.02
O1	GW151226	0.79 ± 0.01	0.01
O2	GW170104	0.888 ± 0.004	0.04
O2	GW170608	0.069 ± 0.004	0.47
O2	GW170729	0.041 ± 0.003	2.49
O2	GW170809	0.56 ± 0.02	0.03
O2	GW170814	0.450 ± 0.007	0.25
O2	GW170823	0.835 ± 0.006	0.01
O3a	GW190408_181802	0.320 ± 0.007	0.17
O3a	GW190412	0.295 ± 0.007	0.22
O3a	GW190503_185404	0.836 ± 0.006	0.008
O3a	GW190512_180714	0.54 ± 0.02	≥ 0
O3a	GW190513_205428	0.879 ± 0.004	0.01
O3a	GW190517_055101	0.52 ± 0.01	0.01
O3a	GW190519_153544	0.140 ± 0.004	0.45
O3a	GW190521	0.569 ± 0.006	0.22
O3a	GW190521_074359	0.760 ± 0.006	4.42
O3a	GW190602_175927	0.468 ± 0.007	0.15
O3a	GW190701_203306	0.0015 ± 0.0006	6.44
O3a	GW190706_222641	0.149 ± 0.005	0.27
O3a	GW190828_063405	0.205 ± 0.008	0.14
O3a	GW190915_235702	0.017 ± 0.004	0.21
O3a	GW190929_012149	0.147 ± 0.008	0.11
O3a	GW190814	0.850 ± 0.004	0.13
O3b	GW191109_010717	0.714 ± 0.008	≥ 0
O3b	GW191204_171526	0.31 ± 0.02	0.11
O3b	GW191215_223052	0.48 ± 0.02	≥ 0
O3b	GW191222_033537	0.771 ± 0.007	0.03
O3b	GW191230_180458	0.31 ± 0.04	0.01
O3b	GW200219_094415	0.27 ± 0.05	≥ 0
O3b	GW200224_222234	0.0011 ± 0.0004	7.40
O3b	GW200225_060421	0.05 ± 0.01	5.45
O3b	GW200311_115853	0.683 ± 0.006	0.26

TABLE 7.2: The table lists for all the analysed GW events their relative on-source p-value, p-value$_{\mathrm{ON}}$ (third column), and on-source reconstructed *snr* inside the post-merger window (PMW), snr_{rec}^{ON} (fourth column). When, for snr_{rec}^{ON} is reported ≥ 0 it means that the reconstructed signal to noise ratio is so small that its estimate is meaningfull, having *snr* values smaller than the per thousands.

7.4.1 On-source p-values

From the on-source results, one can extract the *p-value of the null hypothesis*, defined as:

$$\text{p-value}_{\text{ON}} = \frac{n^{\circ} \text{ of events with } snr_{rec}^{PMW} \geq snr_{rec}^{ON}}{N_{tot}} \Big|_{\text{BGK dist.}} . \tag{7.2}$$

Here, equation (7.2), snr_{rec}^{ON} is the on-source reconstructed *snr* inside the PMW. Then, N_{tot} is the total number of BKG instances, while snr_{rec}^{PMW} is the usual reconstructed *snr* inside the PMW referred to the BGK search (equation 5.29). The p-value of the null hypothesis, in our case, is informative about how much the energy excess in the PMW is in agreement with the BGK results. A high p-value means that snr_{rec}^{ON} value falls comfortably inside the BGK distribution of snr_{rec}^{PMW}. Opposite, a low p-value means that snr_{rec}^{ON} lies on the high energetic tail of the snr_{rec}^{PMW} BGK distribution.

Figure 7.4, reports the p-value for each GWs under investigation ranked from the lowest to the highest.

Two gravitational wave events show an interesting snr_{rec}^{ON} and pass the a priori FDR threshold of 0.1, $FDR \leq 10\%$. They are GW190701 and GW200224. All the other studied GW's events are well outside the warning region of a $FDR \leq 10\%$, then their post-merger behavior is well described by the BGK distribution. Thus, there is, leaving aside GW190701, and GW200224 [1], an overall agreement with the null expectations of general relativity [108, 103, 104] predictions. A summary of $\text{p-value}_{\text{ON}}$, and snr_{rec}^{ON} is given in table 7.2.

7.4.2 Confidence interval on echoe's amplitude

The cWB LES search can set confidence intervals on the *hrss* of post-merger signals consistent with the on-source results. Such study is performed by studying the bivariate distribution of $hrss_{inj}$ of the post-merger signals and the snr_{rec}^{PMW} from SIG and BKG simulations, figure 7.5 (based on GW150914 event).

We build the confidence belt by measuring the distribution of snr_{rec}^{PMW} as a function of $hrss_{inj}$, [109]. This is approximately achieved by introducing a binning in $hrss_{inj}$ in order to preserve a minimum number of samples of hundreds per bin from the SIG analysis. This allows us to target the coverage of 95%, the blue area of the plot (figure 7.5). For the special case of $hrss_{inj} = 0$, the null, we exploit the full statistics of the BKG simulation. This belt is then used to set the confidence interval on $hrss_{inj}$ as a function of the snr_{rec}^{PMW} at 95% confidence. The on-source result for snr_{rec}^{ON} then selects the 95% confidence interval on $hrss_{inj}$, the red line in figure 7.5.

This study provides for the first time a quantitative and robust upper limit on the possible amplitude of echo signals. This can be used to set observational constraints on echoes' models. In addition, this method allows to project expected sensitivity to echoes as the detectors improve.

At present, we do not have available this study for all the events. This follows from the choice of the $hrss_{inj}$ range for the SGE pulses and the limited statistics now available for high values of $hrss_{inj}$. Other simulations with an increase in both the statistics and $hrss_{inj}$ values are planned in order to provide such upper limits on $hrss_{inj}$ for the entire set of GW events analysed in this dissertation. In addition, we will need to explore different central frequencies for the injected SGE, to give a sense of the variability of the confidence belt within the plausible spectral range for echoes.

[1] They will be investigated in the following, section 7.5.

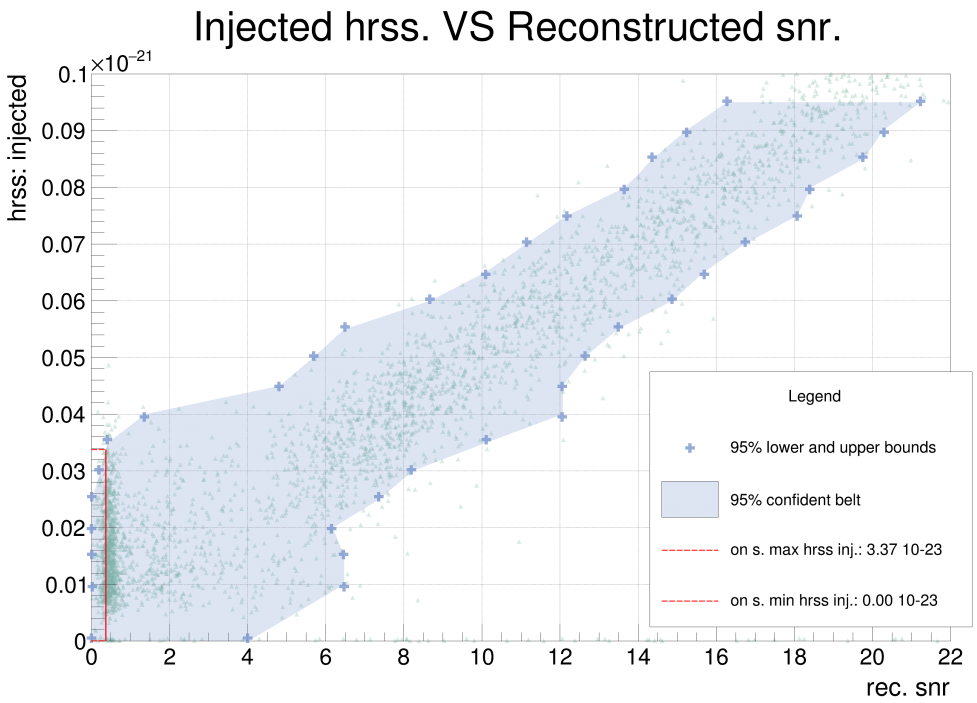

Figure 7.5: Confidence belt for the echo's amplitude hrss, $hrss_{inj}$, vs the reconstructed snr snr_{rec}^{PMW} in the PMW for GW150914. The blue region corresponds to 95% coverage. The on-source 95% confidence interval in terms of the $hrss_{inj}$ is set by the intersection between the vertical line at the on source value $snr_{rec}^{ON} \sim 0.37$ (red line) and the blue region. The y-axis are in 10^{-21} per $\sqrt{\text{Hz}}$.

7.5 The on-source outliers

Figure 7.4 reports two GW events that require a deeper investigation: GW190701 and GW200224. They have been selected according to the FDR threshold of 0.1 and possess a null hypothesis p-value that is lower than 1%, (0.0011 ± 0.0004) (GW190701) and (0.0015 ± 0.0006) (GW200224).

The first test to be performed is focused on understanding if the data around the event possess different features with respect to the overall time period used for the off-source analysis. For this reason, the same off-source study (see section 5.3), but using only the 4096 s of time around the event is performed. These data are used as circular buffer over which the injections are performed. The implementation of this analysis sets a stricter limit on the number of independent realizations of the off-source, in our case they are 1763, due to the combined effects of more technical implementation choices. Additional realizations in the SIG simulation have independently drawn primary signal as well as secondary signal but they are performed over an already analysed background. This means that null hypothesis p-values and their uncertainty, evaluated from the BKG analysis, have partially correlated data. To take into account the effect of the correlation on the uncertainties, the Binomial estimates are multiplied by a factor $\sqrt{\text{n}^\circ \text{ repetitions}}$ [] which takes into account the number of repetitions that the 1763 jobs have done to cover all the total analysed time. We can label this investigation as the **4096s-LES search**, to highlight that the only difference to the standard LES search is in the used data period.

A second followup investigation consists in a morphological study of the PM on-source event. Such a study provides information about the arrival time of the event, its reconstructed *snr*, its frequency as well as its reconstructed strain waveform and

whitened one. This information on the PM event can be compared to those of the primary event to check if they are plausible within the theoretical framework for echoes, which is presented in 3.1. Being able to perform a morphological study is fundamental to fully analyse an event that the LES search marks as worth to be investigated, as for GW190701 and GW200224.

Additional tests have been deployed as well, such performing a single detector analysis of the on source morphology and implementing more stringent data quality mitigation strategies into the LES search. In particular, the on-source morphologies hint to a possible pollution by a glitch family identified in the frequency range $[16-40]$ Hz [110, 111]. Therefore, we repeated the analysis including a specific single detector data filter [112, 113] that estimates the power oscillations for the frequencies in the range $[16-40]$ Hz and attenuates them. We can label such analysis as 32 Hz-LES search, to differentiate it from the standard LES search and the 4096-LES one. The scope is to estimate the on-source null hypothesis p-value when the noise around 32 Hz frequencies is mitigated, expecting to measure a higher value for p-value$_{\rm ON}$.

7.5.1 Case of GW190701

4096s-LES search. Figure 7.6 shows a comparison between the snr_{rec}^{PMW} distributions and ROC curves for the standard LES search on the left and the 4096s-LES search on the right. The two analyses produce compatible results: their on-source null hypothesis p-value are:

$$\text{standard LES search: p-value}_{\rm ON} = 0.0015 \pm 0.0006\,, \tag{7.3}$$

$$\text{4096s-LES search: p-value}_{\rm ON} = 0.004 \pm 0.002\,. \tag{7.4}$$

These results confirm that the BGK distribution of the standard LES search is well estimated, the 4096 s of data around the GW event does not possess irregular noisy features compared to the data period used in the standard search.

On-source morphological study. Analysing the on-source event one finds that the overall *snr* content of the on-source event is around $snr \sim 12.9$ with a $\rho \sim 4.8$, and $cc \sim 0.57$ which is an unusually low value for an event with such an *snr*. Figure 7.7, referred to L1 detector, reports on the left the plot of the reconstructed strain signal. It is possible to notice that the BBH signal is the smallest bump on the left while the two energy excesses are the post-merger signals. The most interesting one is the second (right one) since it falls inside the PMW. No echo models are consistent with these features: in fact the post-merger candidate here shows a larger strain, and longer time duration, around ≥ 100 ms, with respect to the BBH event. On the right of figure 7.7 is shown the whitened signal, it is possible to appreciate the whitening effects on the data as well as the final morphology present in the LES search.

In figure 7.8 are shown the time-frequency (TF) representation of the on-source event for each detector of the network. Moreover, in the bottom row, the network likelihood, and the null TF maps are reported. It is possible to see at ~ 168.55 s the chirping cluster of pixels representing the GW190701 event, going from frequencies around ~ 40 Hz up to ~ 150 Hz. In the post-merger at times ~ 168.65 second and ~ 168.85 s are clearly visible the two energy excesses. Both of them have a central frequency around $f_0 \sim [30-40]$ Hz which is not a frequency range expected for echoes: they should possess similar frequencies or higher than the BBH merger one.

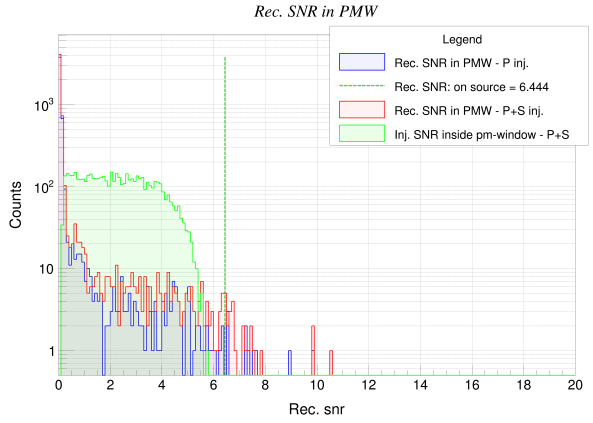

(a) Standard LES search.

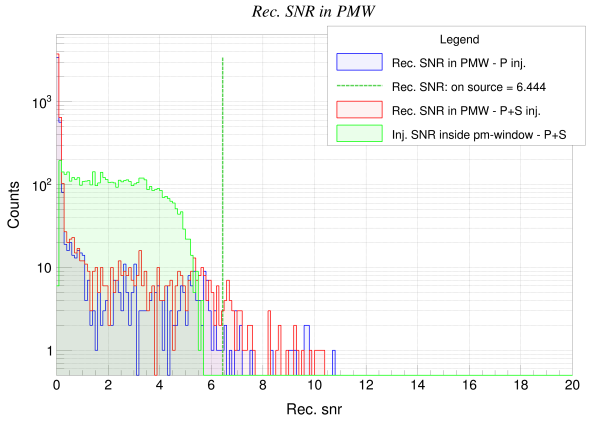

(b) 4096 s LES search.

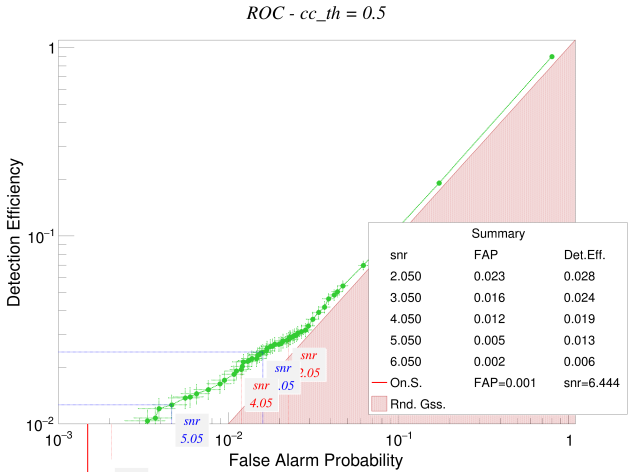

(c) Standard LES search.

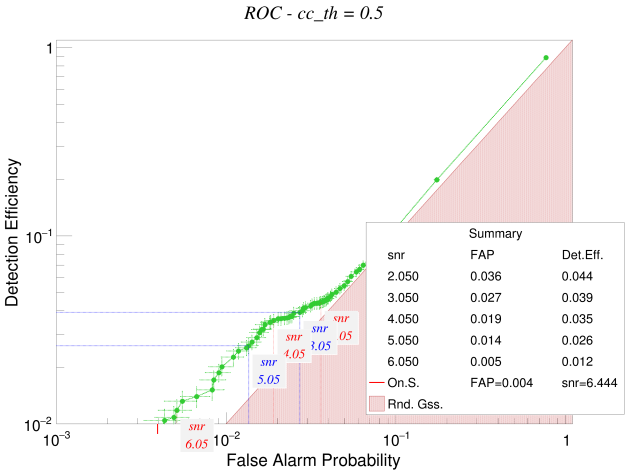

(d) 4096 s LES search.

Figure 7.6: Comparison for the GW event GW190701 between the standard LES search, left column, with the 4096 s LES search on the right column of the figure. In the top row there are reported the snr_{rec}^{PMW} distributions for the P (blue) and P+S (red) studies. The dashed vertical green line marks the on-source snr_{rec}^{PMW} value. In the bottom row there are the ROC curves for the above analysis.

Noteworthy, the first of these energy excesses is extremely energetic in L1 detector, even more than the BBH signal itself, but completely absent in H1 detector. This is not the case for the second energy excess which is present in both the detectors. Subtracting the best PE sample of GW190701 to the on-source data, one can perform the on-source analysis (with cWB LES configuration), figure 7.9. We end up with an *snr* for the reconstructed event around ~ 8.6, a $\rho \sim 3.6$ and a $cc \sim 0.64$. These values seem reasonable since the *snr* has decreased with respect to the on-source scenario ($snr \sim 12.9$), as the ρ values, while cc increased. This increase is due to the maximization of the likelihood by the cWB algorithm in respect to a more suitable sky position in the absence of the BBH signal. Moreover, such a test helps in checking if both the energy excess are detectable or if one or both of them are missed by the algorithm because they do not pass cWB thresholds of coherence. From figure 7.9, we can notice that all the post-merger energy excesses are reconstructed. Nevertheless, the first post-merger signal at ~ 168.75 s is barely detected, losing lots of coherent energy with respect to the scenario with the primary signal. Consistently, figure 7.9d shows that a non-negligible fraction of energy ends in the null data stream. On the

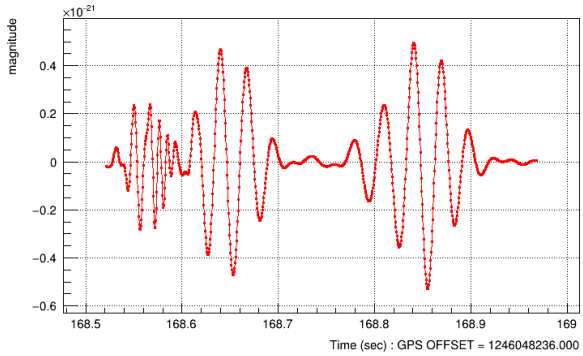

(a) L1 LES search - strain.

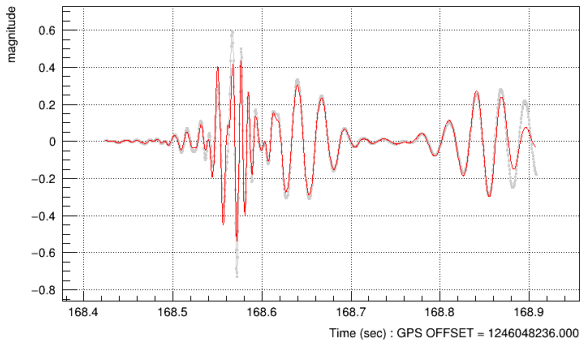

(b) L1 LES search - Whithened WF.

Figure 7.7: On the left the strain plot of the reconstructed signal strain (units multiplied for 10^{-21}) versus time (in seconds) of GW190701, while the right there is the whitened signal. For each plot the time is given with an offset called GPS OFFSET.

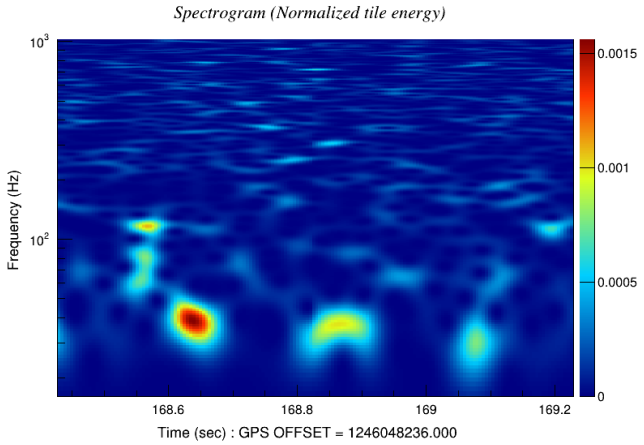

(a) L1 TF map.

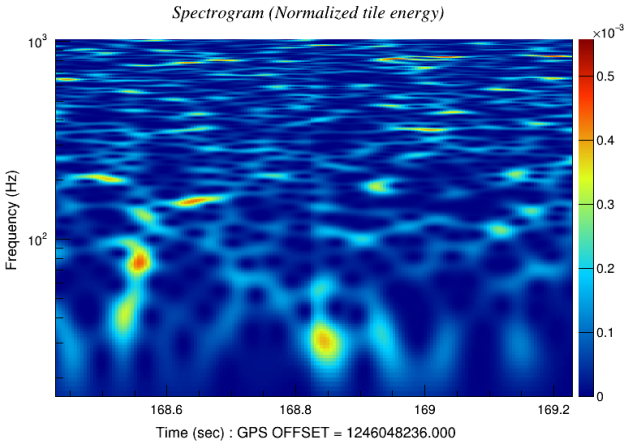

(b) H1 TF map.

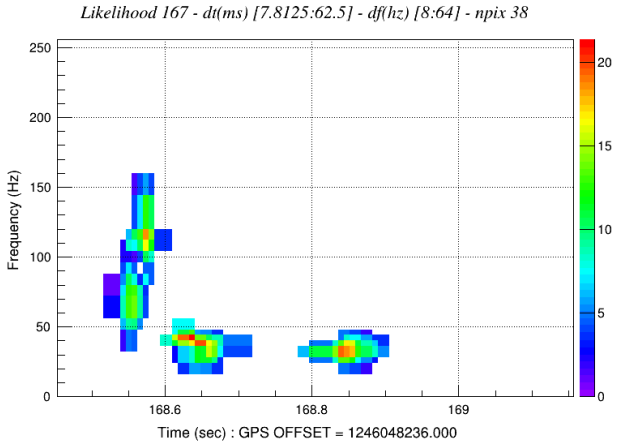

(c) Likelihood TF map.

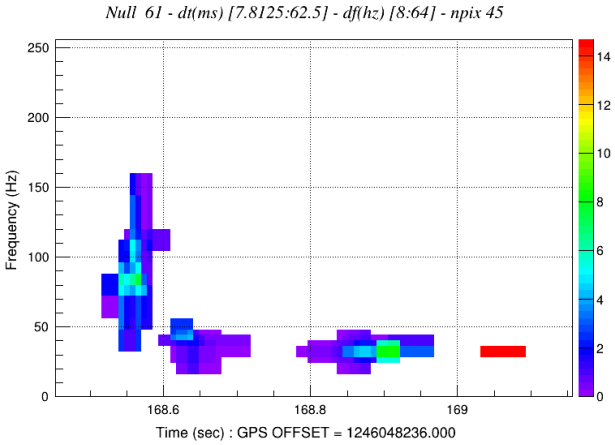

(d) Null TF map.

Figure 7.8: On source reconstruction of the GW190701 event. In the first row are reported the reconstructed TF map for the two detectors of the network, L1 and H1 respectively. The colour legend is on the right of the plots. In the bottom row, from left to right, are reported the network event's likelihood (left plot) and the null energy (right plot).

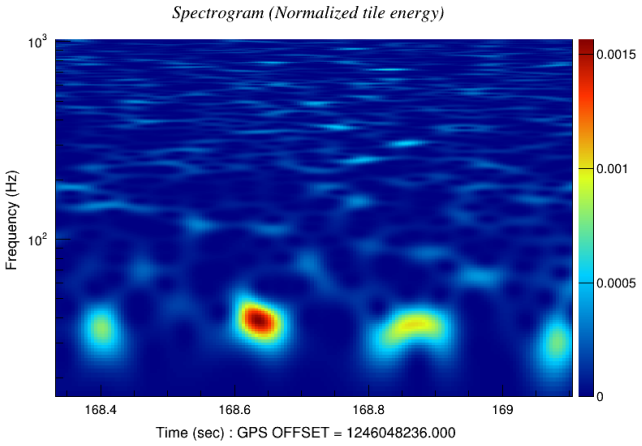

(a) L1 TF map.

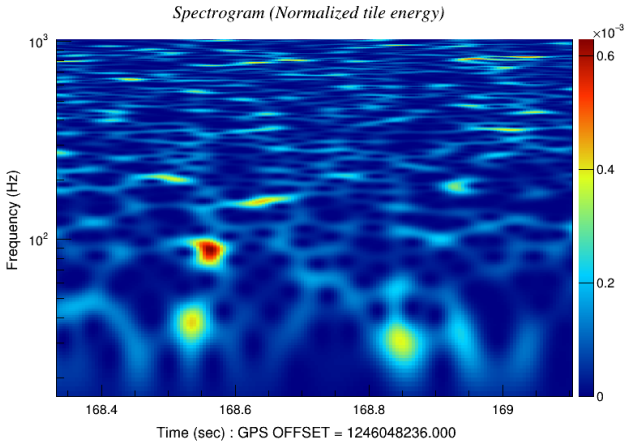

(b) H1 TF map.

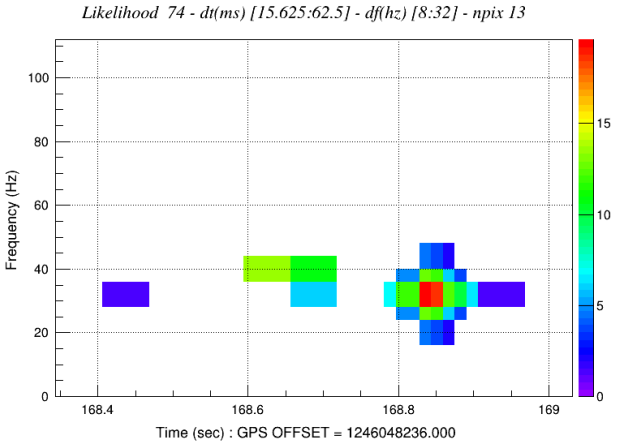

(c) Likelihood TF map.

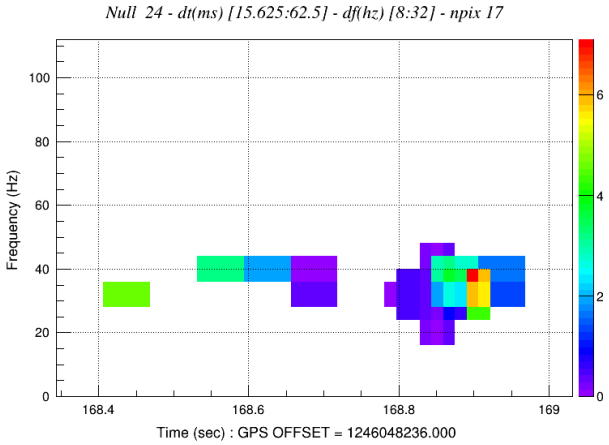

(d) Null TF map.

Figure 7.9: On source reconstruction of the GW190701 data period (job, in cWB formalism) with the best PE sample of GW190701 subtracted to the data, to cancel the BBH event. In the first row are reported the reconstructed TF map for the two detectors of the network, L1 and H1 respectively. The colour legend is on the right of the plots. In the bottom row, from left to right, are reported the event's network likelihood (left plot) and the null (right plot).

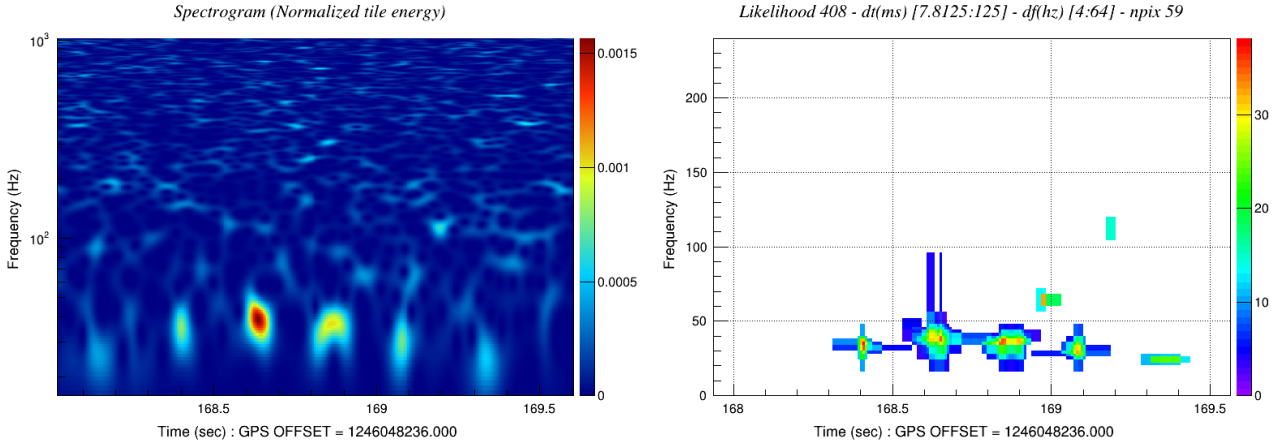

(a) L1 LES search - TF map.

(b) L1 LES search - likelihood TF map.

Figure 7.10: Here on the left is reported the TF map of the reconstructed events in the same cWB job of GW190701 after the subtraction of the GW event. On the right there is the plot showing the likelihood map of the same reconstructed events.

contrary, the second post-merger energy excess ($\sim 168.85\,$s), is better reconstructed in the likelihood. This the opposite to the theoretical predictions for echoes, they want each subsequent echo pulse to be attenuated in amplitude with respect to the previous signal.

On-source single detector morphological study. As a further check, it is possible to perform the on-source LES analysis with the BBH subtraction in a single detector configuration. It is useful both as sanity checks as well as to highlight possible noisy features polluting the data of the single detector. Focusing on L1 detector, which contains both the post-merger signals, the reconstructed event is shown in figure 7.10. It is possible to notice the repetitions of energy excesses either before and after GW190701 event, at time $\sim 168.55\,$s, and all these signals have similar frequencies and morphologies. The overall *snr* of the reconstructed events is around ~ 14.3, definitely not a negligible energy even if it is distributed between the seven clusters of pixels. Furthermore, if we consider that with the presence of the BBH signal the overall *snr* increases up to ~ 17.1 it means that the energies of some of these secondary bumps are comparable to the BBH one. This is a further evidence that the energy excesses recovered in the post-merger time window in the on-source reconstruction of GW190701 are more likely to be glitches other than real echo signals.

32 Hz**-LES search.** It is important to observe that O3 data-taking displays a class of glitches with a mean frequency around $\sim 32\,$Hz [114, 111], and a repetition which shows some periodicity in time. Then, as anticipated at the beginning of section 7.5, one can perform the LES search (usual two detector network configuration) by applying over the data a power reduction filter that acts over clusters of events at frequencies around 32 Hz ($[16-40]$ Hz). The scope is to estimate the on-source null hypothesis p-value when the noise around 32 Hz frequencies is mitigated, expecting to measure a higher value for p-value$_{ON}$.

Figure 7.11 shows both the snr_{rec}^{PMW} distributions and the ROC curve for this study. We can see that the 32 Hz frequency noise reduction suppress by a considerable percentage the overall energy content of the PMW of GW190701 event. Its

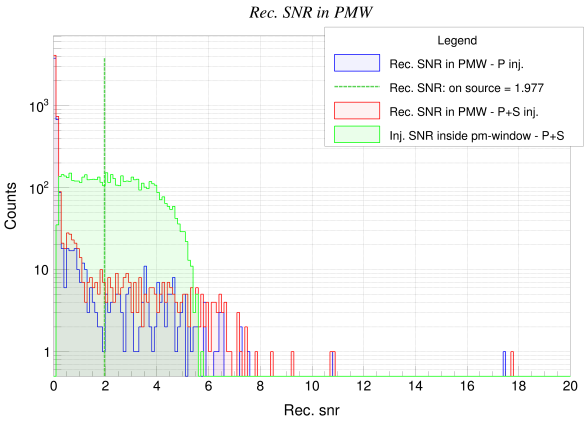

(a) 32 Hz LES search.

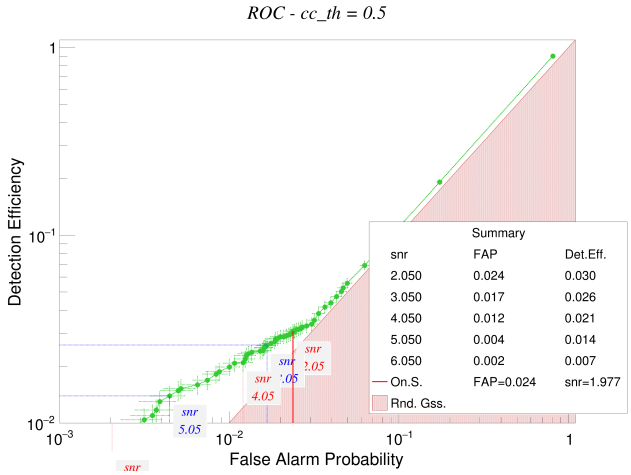

(b) 32 Hz LES search.

Figure 7.11: In this figure the snr_{rec}^{PMW} distributions for the P (blue) and P+S (red) studies (plot on the left) and the ROC curves (plot on the right) for the GW event GW190701 mitigated 32 Hz LES search.

reconstructed *snr* passes from 6.4 down to 2.0 which gives back an on-source null hypothesis p-value:

$$32\,\text{Hz-LES search: p-value}_{\text{ON}} = 0.024 \pm 0.002\,. \tag{7.5}$$

This result makes the on-source p-value of the null-hypothesis for GW190701 well above our a priori interesting threshold of FDR $\leq$ 10% in figure 7.4. Then, this is a further test pointing to the glitch nature of the energy excesses found in the on-source PMW of GW190701.

Remarkable points. We have seen that the 4096s-LES search p-value$_{\text{ON}}$ is compatible within $2\,\sigma$ to the standard LES search p-value$_{\text{ON}}$, equation (7.4). This confirms the goodness of the BGK estimation of the cWB LES search and no strange behaviors are found. The morphological study of GW190701 shows that the amplitude of the PM energy excess does not match the theoretical predictions, resulting to be higher than the merger amplitude of the BBH signal. Neither the time duration, around $\sim$ 100 ms of the PM signals as their frequencies, near 32 Hz, are in agreement with theoretical predictions. Moreover, the single detector analysis, figure 7.10, highlights the presence of multiple signals like the PM ones before and after the BBH event, in the same job. Then, the 32 Hz-LES search, proves that by suppressing the energy content of glitches having mean frequencies inside the band $[16 - 40]$ Hz the on-source null hypothesis p-value$_{\text{ON}}$ for GW190701 improves to such an extent that the event is classified from the search as not worthy to be investigated, figure 7.4 violet dot. Then, the energy excess found in the PMW by cWB LES search can be classified as a glitch, confirming as well the conclusions made by the LVK collaboration [103].

7.5.2 Case of GW200224

4096s-LES search. Following the analysis of GW190701, the 4096s-LES search is performed for GW event GW200224. Its major results are compared with the standard LES search and are highlighted in figure 7.12. Different from the GW190701

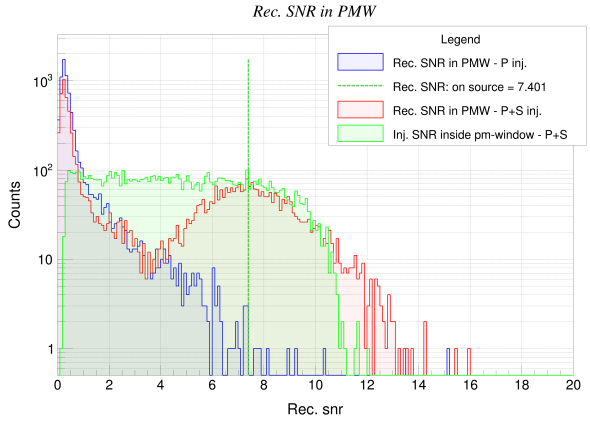

(a) Standard LES search.

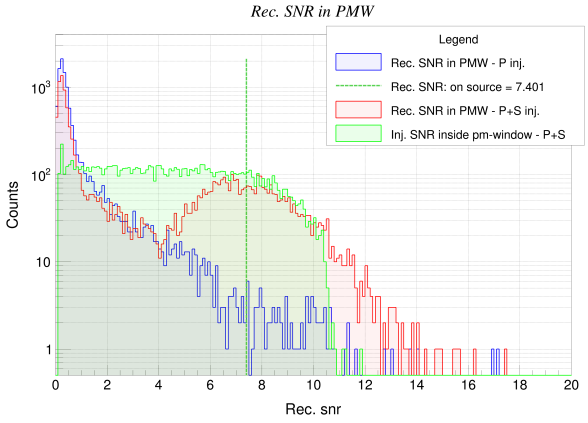

(b) 4096 s LES search.

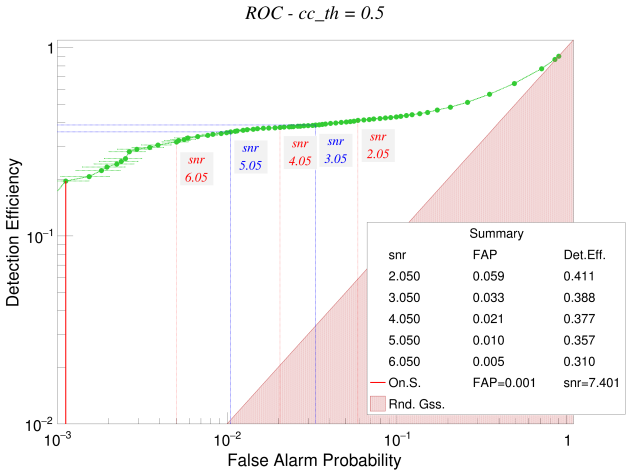

(c) Standard LES search.

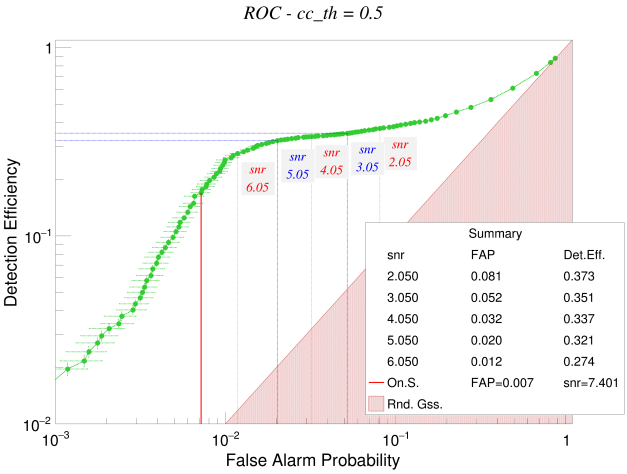

(d) 4096 s LES search.

Figure 7.12: Comparison for the GW event GW200224 between the standard LES search, left column, with the 4096 s LES search on the right column of the figure. In the top row there are reported the snr_{rec}^{PMW} distributions for the P (blue) and P+S (red) studies. The dashed vertical green line marks the on-source snr_{rec}^{PMW} value. In the bottom row there are the ROC curves for the above analysis.

scenario, the on-source p-value of the null-hypothesis significantly increases having:

$$\text{standard LES search: p-value}_{\text{ON}} = 0.0011 \pm 0.0004\,, \tag{7.6}$$

$$\text{4096s-LES search: p-value}_{\text{ON}} = 0.007 \pm 0.002\,. \tag{7.7}$$

The two null hypothesis p-value are not compatible within 2σ. This suggests that the data around the GW event are not well represented by the analysed data period in the standard LES search.

On-source morphological study. The morphological study of the on-source event is summarized in figures figure 7.13 and 7.14 where the PMW energy excess responsible for such a low null hypothesis p-value is clearly visible at the time $\sim$ 183.4 s. Thanks to figure 7.13 we can notice that its time duration is around $\gtrsim$ 400 ms and that its amplitude is far higher than the merger amplitude of the BBH event. Figure 7.14 shows that the mean frequency of this PM excess of energy is around 40 Hz

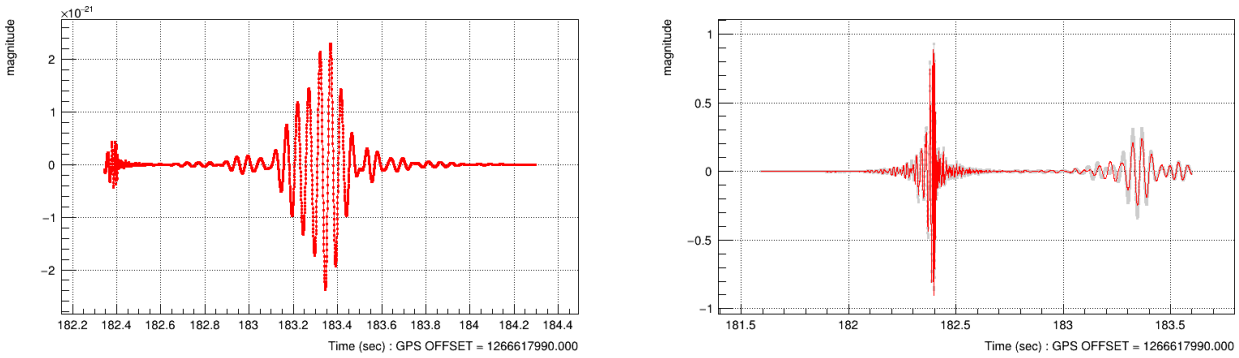

(a) L1 LES search - strain.

(b) L1 LES search - Whithened WF.

Figure 7.13: On the left the strain plot of the reconstructed signal strain (units multiplied for 10^{-21}) versus time (in seconds) of GW200224, while the right there is the whitened signal.

well below the expected frequency values for echoes. These results do not match the theoretical expectations for echoes: the time duration is way too long as its strain amplitude is too high, while its frequency is too low since it is predicted to be around the one of the BBH merger and ring-down, so $\gtrsim 130$ Hz. The overall *snr* is around 20.3 with $\rho = 12.8$ and $cc = 0.89$, and these values suggest we are facing a different scenario to GW190701.

Figure 7.14 also shows that the PM signal is present only in L1 detector, while in H1 such high energy excess is not reconstructed. Here, the null plot (figure 7.14) shows that the null energy of the post-merger energy excess is quite high, meaning that the post-merger cluster of pixels would have failed to pass the coherency checks if analyzed separately. As predicted, subtracting the best PE sample of GW200224 BBH event to the on-source data and then re-running the on-source cWB LES search configuration (as for GW190701) no PM event is reconstructed. This means that the energy excess alone cannot pass the cWB LES search threshold and its cluster of pixels is classified as noise by the pipeline. This is not due to a lack in signal-to-noise ratio from the post-merger energy excess but rather it is due to signal energy disbalance in the two detectors of the network. Since the two LIGO detectors are "aligned", their $\frac{|F_\times|}{|F_+|} \sim 0.25$ (see 4.1), having them sensitive to the same GW's polarisation, for real astrophysical events such energy disbalance in the detectors is suspicious.

An event is reconstructed only by further releasing the LES search production thresholds, but it is not in coincidence with the post-merger feature of the on-source analysis, figure 7.15. This noise glitch is reconstructed at the time ~ 182.9 s and it has a frequency around 900 Hz which is too high to have any relation with GW200224. These outcomes are evidence that the reconstructed post-merger on-source energy excess is likely to be a noise glitch rather than a genuine signal related to the BBH event. The PM event passes the standard LES search only because of the presence of GW200224.

On-source single detector morphological study. To further understand the L1 glitch in the PM phase of GW200224 the single L1 detector on-source study after GW200224 BBH event subtraction is performed. The result is shown in figure 7.16. Here, no undetected energy excess other than the investigated one appears, suggesting that we are not in a scenario similar to the single detector analysis of GW190701. The single

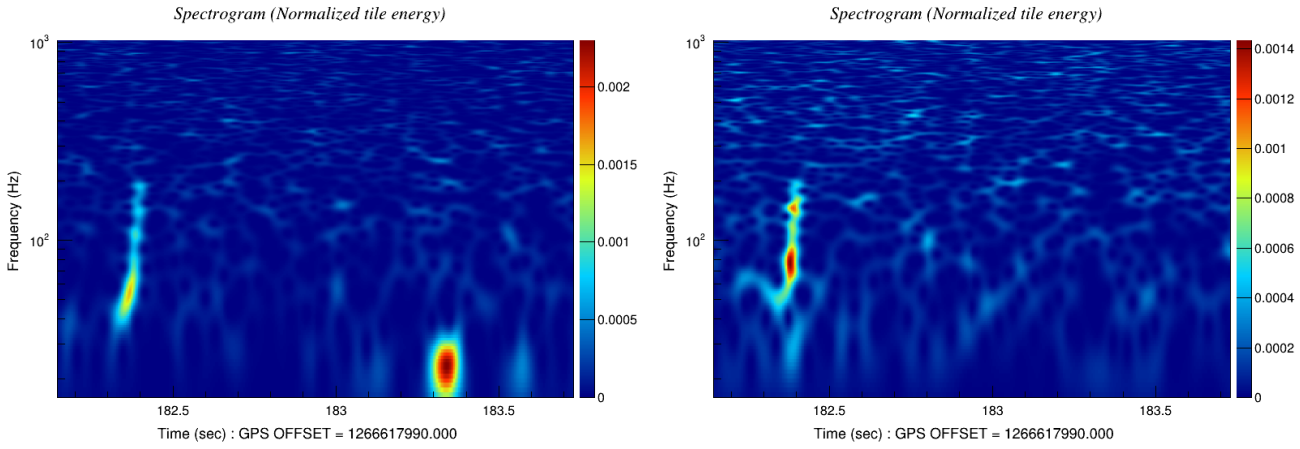

(a) L1 TF map.

(b) H1 TF map.

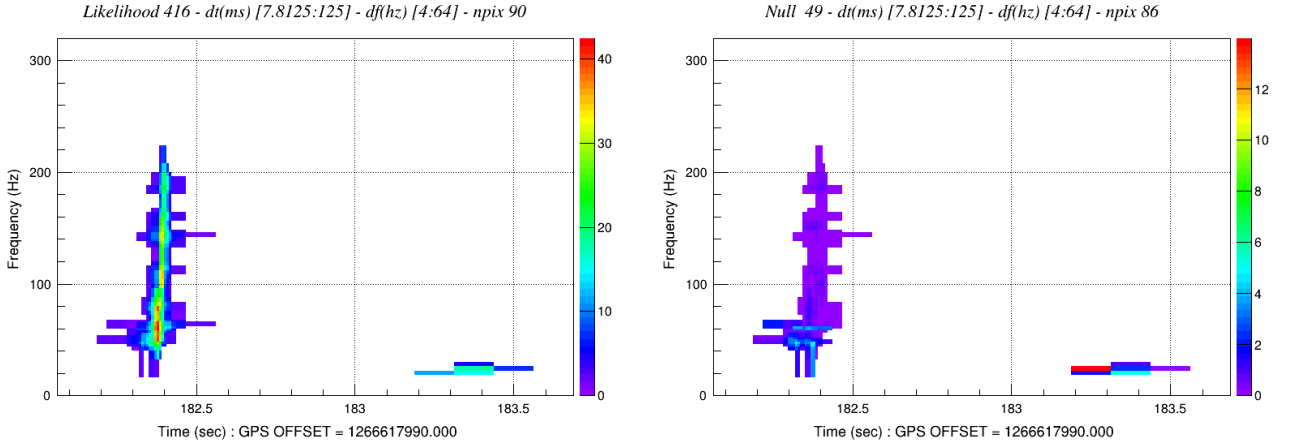

(c) Likelihood TF map.

(d) Null TF map.

Figure 7.14: On source reconstruction of the GW200224 event. In the first row are reported the reconstructed TF map for the two detectors of the network, L1 and H1 respectively. The colour legend is on the right of the plots. In the bottom row, from left to right, are reported the event's likelihood (left plot) and the null (right plot).

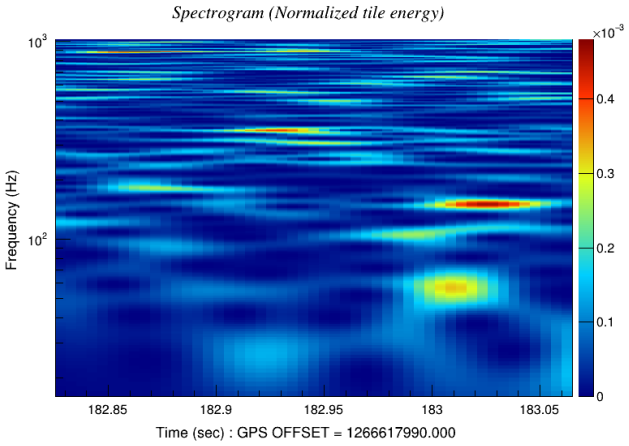

(a) L1 TF map.

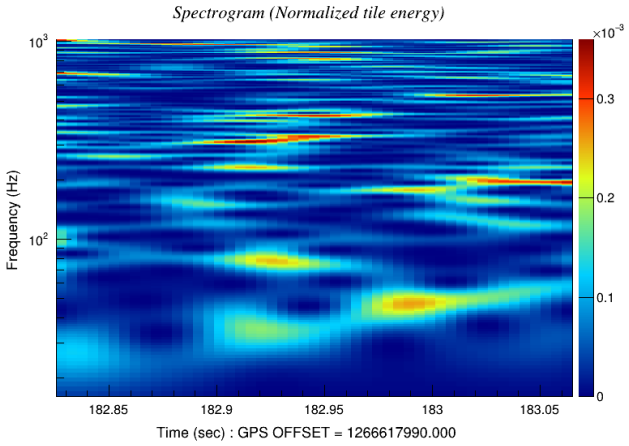

(b) H1 TF map.

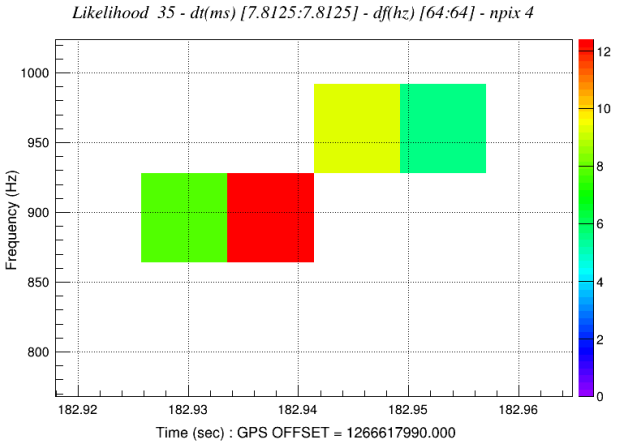

(c) Likelihood TF map.

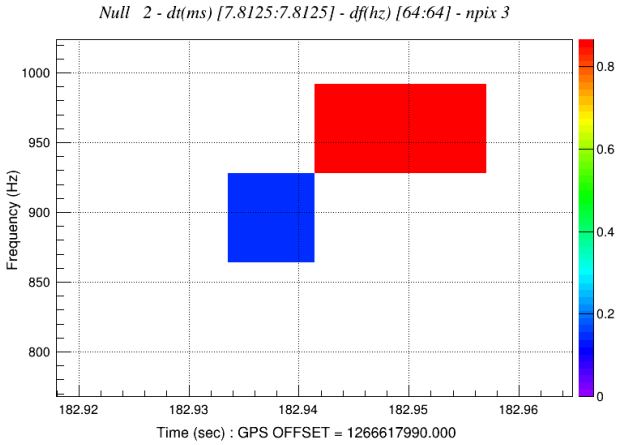

(d) Null TF map.

Figure 7.15: On source reconstruction of the GW200224 data period (job, in cWB formalism) with the best PE sample of GW200224 subtracted to the data, to cancel the BBH event. In the first row are reported the reconstructed TF map for the two detectors of the network, L1 and H1 respectively. The colour legend is on the right of the plots. In the bottom row, from left to right, are reported the event's likelihood (left plot) and the null (right plot).

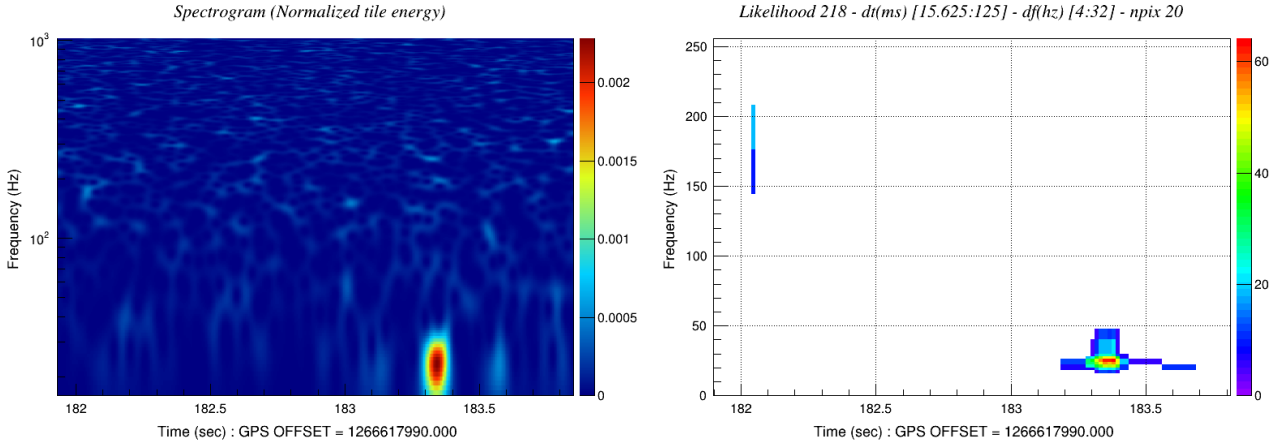

(a) L1 LES search - TF map.

(b) L1 LES search - likelihood TF map.

Figure 7.16: Here on the left the TF map in its best resolution of the reconstructed events in the same cWB job of GW200224 after subtracting the GW event, while on the right there is the plot showing the likelihood map of the same reconstructed events.

energy outlier with $snr \sim 10.4$ against the overall snr of the BBH signal plus post-merger excess of energy equal to ~ 16.8 (in single detector mode). This evidences that in L1 the post-merger signal possesses more energy than the BBH one, which again is the opposite of theoretical predictions for echoes.

32 Hz-LES search. Having that the frequency of the post-merger signal around 40 Hz, the 32 Hz-LES search is carried on. The results of this study are reported in figure 7.17: here it is possible to see that there is an attenuation of the energy content of the post-merger, passing from $snr_{rec}^{PMW} = 7.4$ to 6.2. The related on-source null hypothesis p-value is:

$$\text{32 Hz-LES search: p-value}_{\text{ON}} = 0.003 \pm 0.001\,. \tag{7.8}$$

The p-value still remains in the interesting region with FDR $\leq 10\%$ in the p-value plot of figure 7.4. This suggests that the 32 Hz mitigation has not cleaned the energy excess. A possible reason lies in the working procedure of the power mitigation at 32 Hz: it works well when it faces data periods polluted with multiple glitches around the interested frequencies ($[16 - 40]$ Hz). Here we only have one single isolated glitch.

Remarkable points. We have seen that the 4096s-LES search p-value$_{\text{ON}}$ is not compatible within $2\,\sigma$ to the standard LES search p-value$_{\text{ON}}$, equation (7.7). This indicates that the BGK estimation of the cWB LES search is not fully representative of the 4096 s of data around GW200224. Nevertheless, the morphological study shows that the amplitude of the PM energy excess does not match the theoretical predictions, resulting to be higher than the merger amplitude of the BBH signal. Neither the time duration, around $\gtrsim 400$ ms of the PM signals as its frequency, near 40 Hz, are in agreement with theoretical predictions. This on-source analysis clearly shows the presence of such a glitch only in L1 detector, an evidence supported by the cWB standard LES on-source analysis when the best PE sample of the BBH signal is subtracted to the data. No PM signals are reconstructed compatible with the noise glitch under investigation.

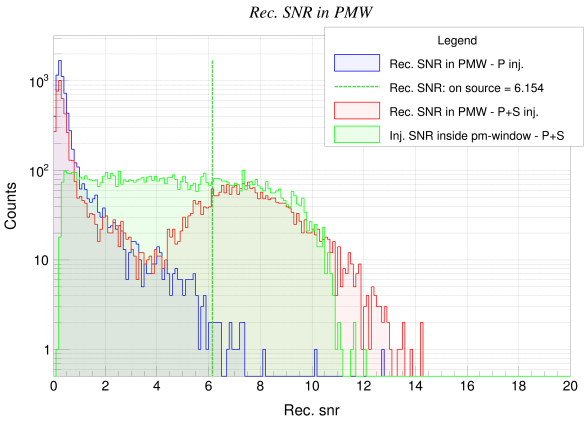

(a) 32 Hz LES search.

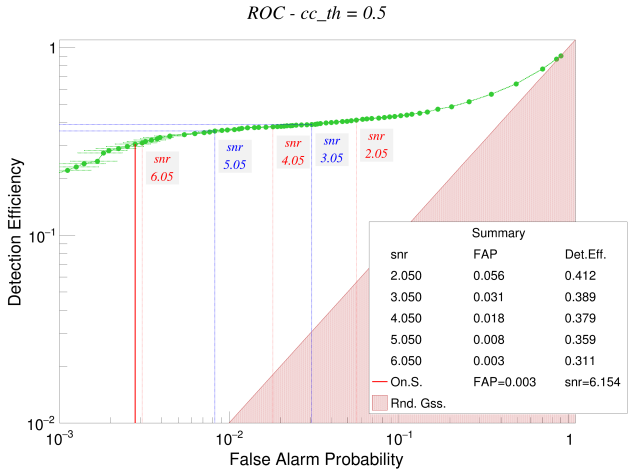

(b) 32 Hz LES search.

Figure 7.17: In this figure the snr_{rec}^{PMW} distributions for the P (blue) and P+S (red) studies (plot on the left) and the ROC curves (plot on the right) for the GW event GW200224 mitigated 32 Hz LES search.

Even if the 32 Hz-LES search does not suppress enough the energy content of the PM glitch the on-source single detector analysis performed after the best GW200224 PE sample subtraction shows that its morphological characteristics are incompatible with the ones theorised for echoes. Furthermore, due to its high energy content, in the single-detector on-source analysis, one would have expected to see a train of damped energy excess as echoes should be, but none of them is detected.

Then, this post-merger signal reconstructed in the PMW by cWB LES search can be classified as a glitch, confirming the discoveries made by the LVK collaboration [103], where no evidence of echoes are found for the common studied events.

Chapter 8

Morphological characterization of echoes

The discussion in section 7.5 shows that the morphological reconstruction of detected energy excess in the post-merger phase of a BBH signal plays a fundamental role in the interpretation of the candidate detection. With these motivations, I implemented some estimators of basic morphological properties of candidate events in the LES search post-processing stage (section 5.3, figure 5.4). In particular, I developed estimators for the signal power, its arrival time and repetition rate, as well as its mean frequency. To enable the interpretation of these observables for any on-source results, the same observables are estimated in the BKG and SIG (section 5.3.1) off-source simulations.

8.1 Scan of the post-merger window

The LES search includes also some estimators to describe the time evolution of candidate signals within the post-merger window. In particular, I monitor the signal power vs time, from which I build estimators of the first pulse arrival time, the repetition rate, and the amplitude decay of subsequent pulses. The implemented procedure is based on a *moving window* (MW) that scans the data inside the PMW.

While scanning the data one can evaluate both the power (P^{MW}) of the data searching for possible peaks as well as their energy-weighted meantimes (t^{MW}):

$$\begin{aligned} P^{MW} &= \frac{\sum_{k=0}^{N}\sum_{i=0}^{\Delta_{MW}}\left(W[i]\cdot x_k[i]^2\right)}{\sum_{i=0}^{\Delta_{MW}} W[i]}\,, \\ t^{MW} &= \frac{\sum_{k=0}^{N}\sum_{i=0}^{\Delta_{MW}}\left(t_k[i]\cdot W[i]\cdot x_k[i]^2\right)}{\sum_{k=0}^{N}\sum_{i=0}^{\Delta_{MW}}\left(W[i]\cdot x_k[i]^2\right)}\,. \end{aligned} \tag{8.1}$$

Here k is the detector index, $x[i]$ the whitened single detector data stream, $W[i]$ the amplitude profile of the moving window, and Δ_{MW} its width. The search is set to select the highest estimated P^{MW} and its corresponding meantime:

$$\begin{aligned} P^{MW}_{max1} &= \max\left(\{P^{MW}\}\right)\,, \\ t^{MW}_{max1} &= t^{MW} \in P^{MW}_{max1}\,, \end{aligned} \tag{8.2}$$

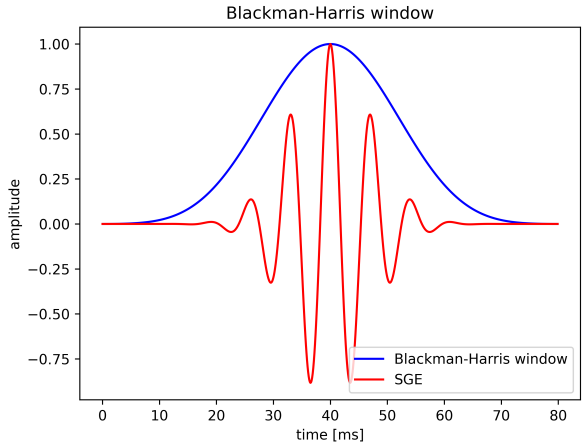

(a) Blackman-Harris window width: 80 ms.

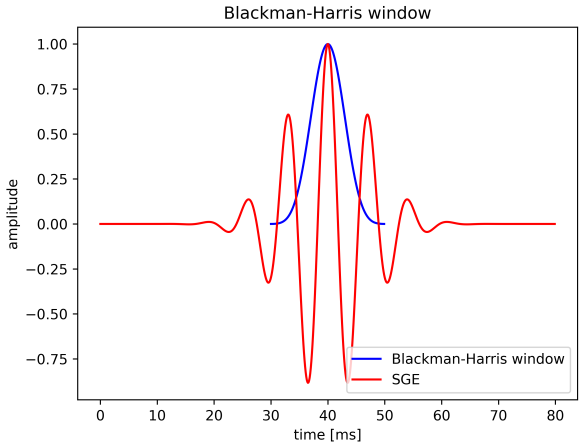

(b) Blackman-Harris window width: 20 ms.

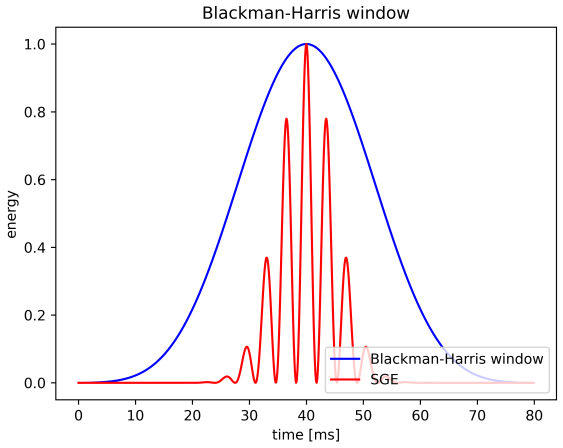

(c) Blackman-Harris window width: 80 ms.

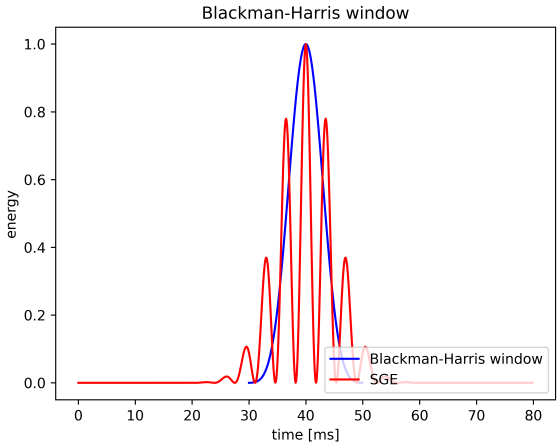

(d) Blackman-Harris window width: 20 ms.

Figure 8.1: Examples of the shape of a Blackman-Harris window, in blue. The time width is fixed to 80 ms. On the x-axis there is the time in [ms]. Top row: comparison between the injected amplitude of the Sine-Gaussian pulse (red) and the Blackman-Harris window with different time amplitude τ_W, $\tau_W = 80$ ms(left), and $\tau_W = 20$ ms (right). Bottom row, the same distinction of the top row, but energy an not amplitude is reported on the y-axis.

[1] as well as the second most energetic peak and its related meantime:

$$\begin{aligned} P^{MW}_{max2} &= \max\left(\{P^{MW}\} \setminus P^{MW}_{max1}\right), \\ t^{MW}_{max2} &= t^{MW} \in P^{MW}_{max2}. \end{aligned} \tag{8.3}$$

Here $\{P^{MW}\} \setminus P^{MW}_{max1}$ represent the ensemble of all the P^{MW} values without P^{MW}_{max1}.

A Blackman-Harris window is chosen as moving window [115]. It is a common window function used in data analysis, it is well suited to attenuate border effects [115]. A Blackman–Harris window has the following form:

$$W^{BH}[i] = a_0 - a_1 \cos\left(\frac{2\pi i}{\tau_W}\right) + a_2 \cos\left(\frac{4\pi i}{\tau_W}\right) - a_3 \cos\left(\frac{6\pi i}{\tau_W}\right), \tag{8.4}$$

[1] The $\{\bullet\}$ labels an ensemble, while $\setminus$ is for the difference between two ensembles.

with

$$a_0 = 0.35875, \quad a_1 = 0.48829 \quad a_2 = 0.14128 \quad a_3 = 0.01168 \tag{8.5}$$

and its visual representation is in figure 8.1. Here, eq .(8.4), τ_W is the time width of the Blackman-Harris window: $\tau_W = 80\,\text{ms}$. The width of 80 ms is chosen because the injected SGE, our echo-like signals, have a time duration of 20 ms. This means that to be reasonable well detected and described by the MW the SGE have to be centred and entirely contained inside the MW, as figure 8.1a and 8.1c show. This is a compromise. The upper limit on the width of the MW is set by the need to resolve adjacent pulses. The lower limit is instead set by noise fluctuations, and to avoid underestimating the power of the SGE pulse 8.1b, and 8.1d. Figure 8.1 shows that the width at half high of the Blakman-Harris window is about $\sim 30\,\text{ms}$, matching the optimal condition to contain the majority of the SGE signal energy, figure 8.1c.

Since we are searching for echoes not only the condition that $P^{MW}_{max1} \geq P^{MW}_{max2}$ is imposed, but also that $t^{MW}_{max2} \geq t^{MW}_{max1}$. Moreover, to avoid that the estimate of the second highest power peak inside the PMW follows from an off-centered MW respect to the first power peak meantime, we impose the condition:

$$t^{MW}_{max2} - t^{MW}_{max1} \geq 2 \cdot \Delta t^{MW}_{\frac{1}{2}\text{height}}, \tag{8.6}$$

where $\Delta t^{MW}_{\frac{1}{2}\text{height}}$ is the time width of the MW at half height.

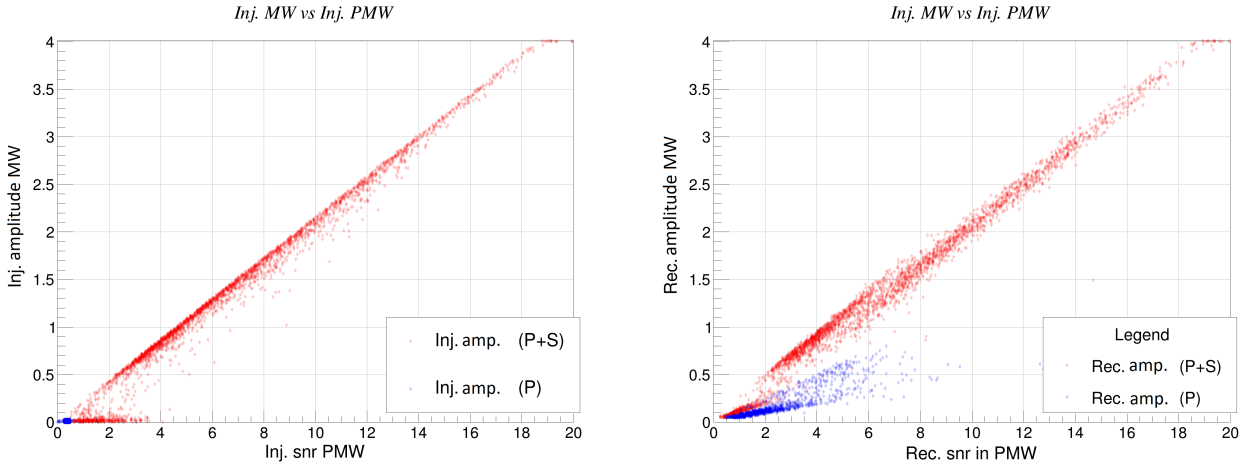

(a) Injected power.

(b) Reconstructed power.

Figure 8.2: Here, on the left the injected amplitude A^{MW}_{inj} versus the snr^{PMW}_{inj} for both the BGK (blue) and SIG (red) analysis. On the right the same plot but with the reconstructed amplitude in the MW A^{MW}_{rec} versus snr^{PMW}_{rec}.

8.2 Results on the signal's amplitude

With this procedure, section 8.1, is now possible to estimate the power P^{MW} inside the PMW. Till now we have studied and compared quantities through the *snr*, then, to have an easier interpretation and comparison of the following results I define the amplitude of the signal as $A^{MW} = \sqrt{P^{MW}}$ [2]. For each GW event studied in

[2] So far, all the quantities related to the energy content and amplitude of a signal are in units of *snr*. Thus, also this amplitude has to be interpreted as an instantaneous *snr*.

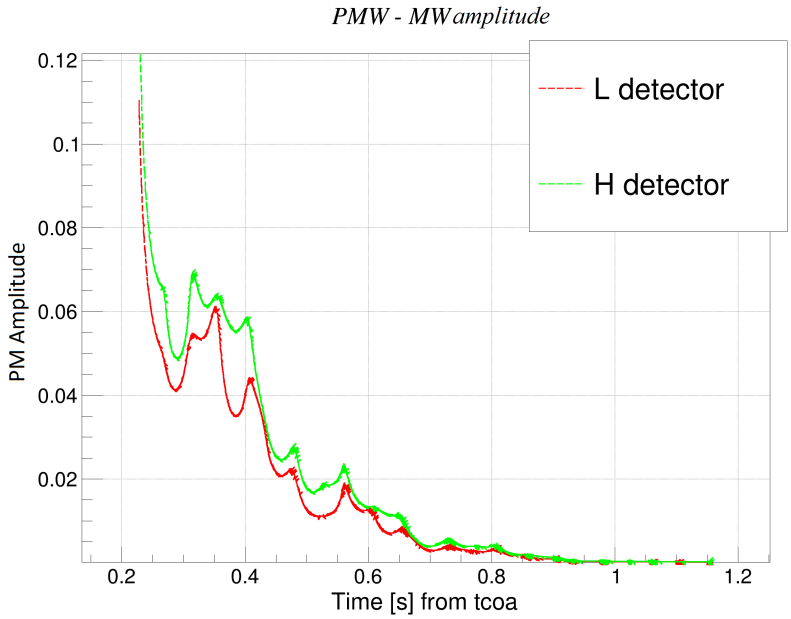

Figure 8.3: On-source instantaneous *snr* profile inside the PMW for GW150914. The red line is referred to L1 detector, while the green to H1. By comparing the amplitude values here to the one in figure 8.2b we can see we are dealing with noise fluctuations, responsible for the oscillatory behavior near times of 0.3 s − 0.6 s.

this dissertation, table 5.1, we compare the injected and reconstructed A^{MW}_{max1} to the related $snr^{PMW}_{inj,rec}$, and the typical result is shown in figure 8.2, based on GW150914.

From the plots in figure 8.2 it is possible to see that A^{MW}_{max1} increase linearly with snr^{PMW}_{inj} and snr^{PMW}_{rec} for the SIG analysis. This confirms the amplitude estimator behaves as it should. Inspecting the results for the BGK analysis, we can spot an increase in reconstructed A^{MW}_{max1} for higher snr^{PMW}_{rec} values, but without a clear pattern, which is expected since here we are dealing with pure noise. The different trend of reconstructed A^{MW}_{max1} in figure 8.2b for very low snr^{PMW}_{rec} ($\lesssim 2$) in the SIG study follows from the non detection or poorly detected injected SGE. In fact, in the low *snr* regime where the noise dominates, the SIG distribution follows the BGK distribution for very low snr^{PMW}_{rec} values. Moreover, in figure 8.2a the SIG distribution shows how the cWB LES search does not reconstruct most of the signals which are injected with an *snr* lower than 2.

We can also draw the amplitude profile inside the PMW for both the on-source as well as the off-source analysis. In figure 8.3 we can see a typical A^{MW} profile for a BGK event. Both the detectors L1 and H1 show a similar amplitude trend and both the amplitude peaks are at the start of the PMW. This is a consequence of the whitening, see section 6.9, so the highest amplitude is estimated as near as possible to the merger time and the ring-down of the BBH coalescence.

The two amplitude profiles in figure 8.4 are referred to GW190701 and GW200224. Here, is possible to see the amplitude peak coincident with the arrival time of the second noise glitch in GW190701 and the first noise glitch in GW200224. It is also possible to appreciate the amplitude disbalance between L1 and H1 detectors. All of these features are consistent with the results of section 7.5. Moreover, it is possible to compare the on-source amplitude for these two events with the one of GW150914; when a noise outlier is present inside the PMW there the amplitude shows orders of magnitude of difference with respect to a null hypothesis scenario.

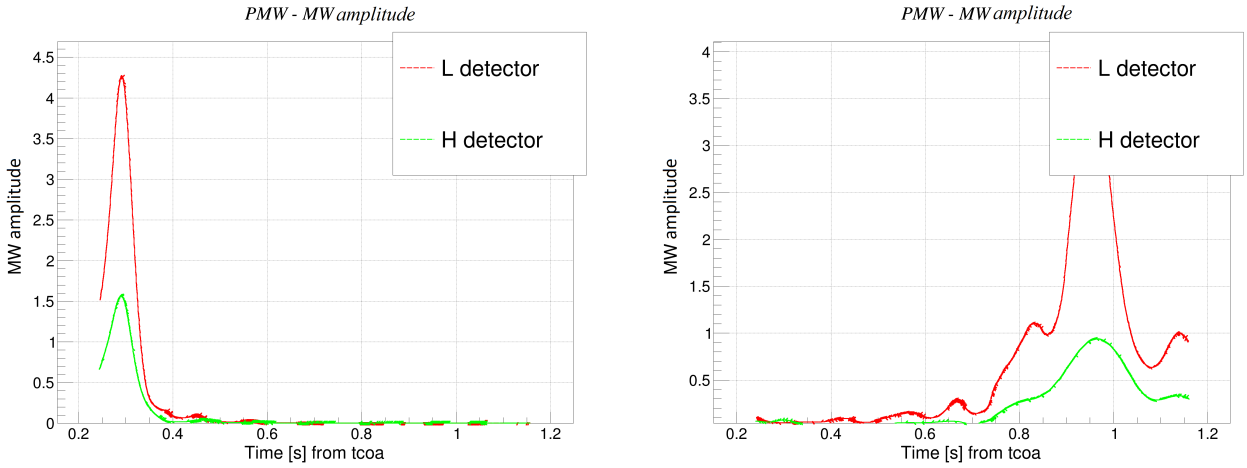

(a) PMW on-source GW190701.

(b) PMW on-source GW200224.

Figure 8.4: The plots of the on-source amplitude profile inside the PMW for GW190701 (left) and GW200224 (right).

8.3 Results on the arrival time of the signal

Figure 8.5 (referred to GW150914) shows the typical scenario the cWB LES search off-source encounters when estimating the energy weighted mean times for the two higher amplitude peaks inside the PMW. These times values are estimated as explained in section 8.1, equation (8.1). Here I just recall the conditions:

$$A^{MW}_{max1} \geq A^{MW}_{max2}\,, \quad \text{and} \quad t^{MW}_{max2} \geq t^{MW}_{max1}\,. \tag{8.7}$$

The plots in figure 8.5 show on the left the $A^{MW}_{max1/2}$ versus its arrival time $t^{MW}_{max1/2}$, while on the right the $t^{MW}_{max1/2}$ distributions. The two SGE signals mimicking echoes are injected at the time of 300 ms and 600 ms respectively. It is possible to see that the arrival time of the two pulses is correctly estimated. The blue cluster of events with low A^{MW}_{max2} is not centered around 600 ms, as should be, since it labels the events in which the second SGE pulse is not detected. In this occurrence, the second most energetic event detected by the MW is detected immediately after the condition $t^{MW}_{max2} - t^{MW}_{max1} \geq 2 \cdot \Delta t^{MW}_{\frac{1}{2}\text{height}}$ (section 8.1). Concerning the $t^{MW}_{max1/2}$ distribution (figure 8.5b) the double peak appearing in both the distributions follows from the uncertainties in the reconstructed sky position. In a multiple detector network, the reconstructed source location relies largely on the time delays between sites, i.e. triangulation. Thus, there is generally a degeneracy in the reconstructed source position. For a two-detector network, this degeneracy is a conical surface of constant time delay around the line connecting the two detectors, whose projection onto the sky plane yields a ring [116].

Now, the two GW events GW190701 and GW200224, the on-source results provide:

$$\begin{aligned} &\text{GW190701 - on-source} \quad 1st \quad t_{echo} = (0.30 \pm 0.02)\text{s}\,, \\ &\qquad\qquad\qquad\qquad\quad 2nd \quad t_{echo} = (0.37 \pm 0.02)\text{s}\,, \\ &\text{GW200224 - on-source} \quad 1st \quad t_{echo} = (0.95 \pm 0.03)\text{s}\,, \\ &\qquad\qquad\qquad\qquad\quad 2nd \quad t_{echo} = (1.07 \pm 0.03)\text{s}\,. \end{aligned} \tag{8.8}$$

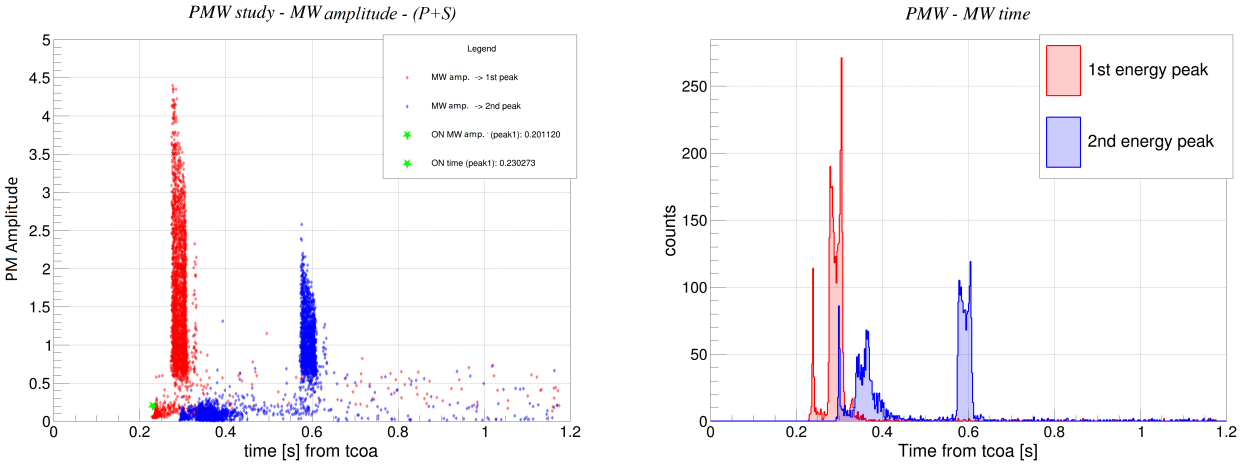

(a) t_{echo} scatter plot.

(b) t_{echo} histogram

Figure 8.5: In this figure, on the left, there is the scatter plot of the A^{MW}_{max1} (red) and A^{MW}_{max2} (blue) reconstructed by the moving windows versus their estimated arrival time t^{MW}_{max1} (red) and t^{MW}_{max2} (blue), respectively. I use as reference time the t_{coa} of the BBH signal. The green star represents the on-source event. The analysis is performed over the LES study to verify if the two clusters around 300 s and 600 s are correctly identified. On the right, the plot is a histogram of the estimated t^{MW}_{max1} (red) and t^{MW}_{max2} (blue).

With these values and the studies of section 7.5 it is possible to understand that the width of the window is too small to fully contain the noise glitch, like in figure 8.5. The two $t^{MW}_{max1/2}$ are correlated since they follow from two different time positions of the MW while scanning the same energy excess. In order to have uncorrelated estimations of $t^{MW}_{max1/2}$, it is sufficient to enlarge the time duration of the Blackman-Harris window, from 80 ms up to 400 ms for GW190701 and up to 800 ms for GW200224. These values follow from the results of chapter 7 and the discussion of section 8.1. With these corrections the new arrival time estimations are:

$$\begin{aligned} \text{GW190701} \quad & 1st \quad t^{ON}_{echo} = (0.30 \pm 0.09)\text{s}\,, \\ & 2nd \quad t^{ON}_{echo} = \text{no second signal found}\,, \\ \text{GW200224} \quad & 1st \quad t^{ON}_{echo} = (0.96 \pm 0.01)\text{s}\,, \\ & 2nd \quad t^{ON}_{echo} = \text{no second signal found}\,. \end{aligned} \tag{8.9}$$

Such values are in agreement with the results of chapter (7), section 7.5, and show that inside the PMW there is only one energy excess that has a relevant *snr*. Furthermore, it is worth noticing that even with an un-tuned MW ($\tau_W = 80$ ms), the estimates of t^{MW}_{max1} for both the GW events, equation (8.8), results to be compatible with the results of the tuned MW, equation (8.9). This highlights that the MW is a valid tool that provides reasonable results even when operating with a non-optimal configuration.

8.4 Results on the pulses' amplitude damping factor

Starting from the $A^{MW}_{max1,2}$ values, it is possible to estimate the damping factor γ between the two main energy peaks within the PMW. Clearly, the estimate of γ if performed on the LES study is expected to result in a distribution of values that are

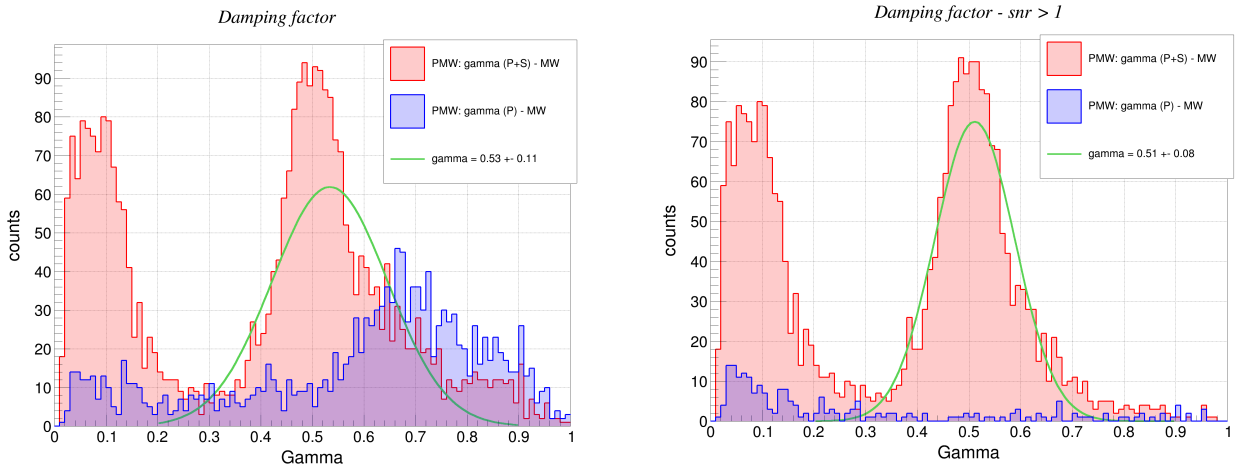

(a) γ, no amplitude cut.

(b) γ, amplitude cut $A^{MW}_{max1} > 0.3$.

Figure 8.6: Both plots report the BGK (blue) and SIG (red) distributions for the γ factor. The line in green is a fit of the SIG distribution in the region $[0.2 - 0.9]$. The values $\gamma \leq 0.2$ are considered not informative for the purpose of the fit. The right plot is obtained by requiring a minimum peak amplitude value, so only the events for which $A^{MW}_{max1} > 0.3$ are selected.

centered around 0.5, the user-defined values. On the contrary, the on-source estimation has no reference and is strictly dependent on the under-window properties. The estimation of γ is obtained as the ratio between the second to the first amplitude peak inside the PMW.

For an average LES study, figure 8.6a is representative of all the results obtained from the GW events studies. We can notice the expected peak of the SIG distribution around $\gamma = 0.5$, but also a peak at $\gamma = 0.1$. This second peak is due to the event in which the second injected SGE pulse is not reconstructed, so its estimated amplitude is very poor, nearby the noise amplitude floor. Opposite, the first injected SGE pulse is reconstructed making its amplitude peak not negligible. Thus, their ratio sees the first amplitude peak dominant and so γ tends to zero.

The BGK distribution shows a trend pointing to a preference for high γ values. These values are due to the events whose amplitude fluctuates within the bulk of the PMW noise, so the ratio between A^{MW}_{max2} and A^{MW}_{max1} is close to 1. Indeed, by looking at figure 8.5, we can see a bulk of events that possess low amplitude, $A^{MW}_{max1} \lesssim 0.3$ in the SIG simulation. These events are the ones for which the SGE pulses were not detected, then the amplitude, $A^{MW}_{max1} \lesssim 0.3$ are not informative and contribute to the statistics by adding noise. If we introduce a cut, and select only the events whose amplitude is $A^{MW}_{max1} > 0.3$ for both SIG and BGK studies, we mitigate the BGK γ distribution, which then shows a uniform distribution for $\gamma > 0.2$, as in figure 8.6b. This cut will clean also the other noise features of plots in figure 8.2a.

8.5 Frequency of the signal

The estimation of the energy weighted mean frequency of the energy peaks is performed over a single TF map with a tuned time-frequency resolution that provides a reasonable compromise in time localisation of the energy excess and frequency resolution to correctly perform an energy-weighted frequency estimation. The TF map resolution I have chosen is: $\Delta t = 12\,\text{ms}$ and $\Delta f = 42\,\text{Hz}$. As for all the other quantities, the frequency is evaluated inside the PMW, an example of the LES search

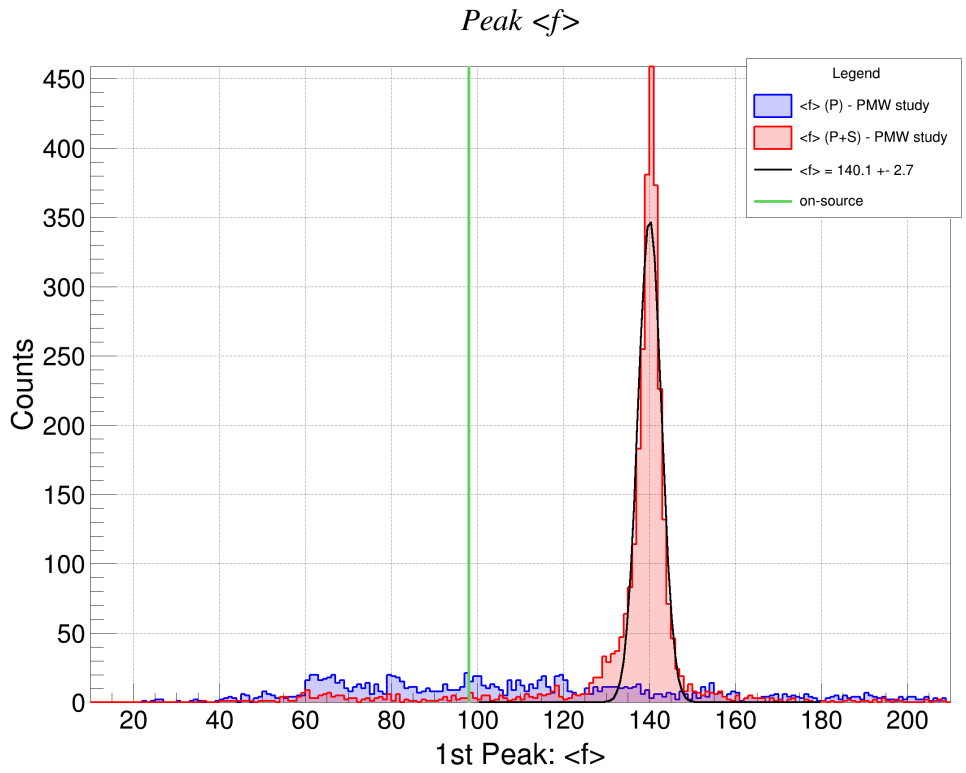

Figure 8.7: Here there is a histogram of the first energy peak frequency distribution for both the LES study (red) and the BGK one (blue). The vertical green line reports the on-source value. It is possible to see, form the blue distribution that the background does not show any particular shape or trend, while the red one, following the injection. The GW event used as a refernce is: GW150914

capabilities can be seen in figure 8.7, where there is a histogram of the first energy peak frequency distribution for both the LES study (red) and the BGK one (blue). The vertical green line reports the on-source value. It is possible to see, from the blue distribution that the background does not show any particular shape or trend, while the red one, follows the morphologies of the injected SGE signals. The injected elliptical Sine-Gaussian has a constant frequency of 140 Hz and from figure 8.7 we can see that its frequency value is estimated correctly, having a mean value of (140 ± 3)Hz which is compatible within its uncertainty with the injected one. This value is obtained through a Gaussian fit over the red distribution (LES study) and the error over the measure corresponds to its standard deviation.

For the usual events GW190701 and GW200224, I have found the following energy-weighted values for the noise glitch frequency:

$$\text{GW190701 - on-source} \quad f = (34.3 \pm 0.1)\text{Hz}\,, \tag{8.10}$$

$$\text{GW200224 - on-source} \quad f = (30.1 \pm 0.1)\text{Hz}\,, \tag{8.11}$$

which seems to be in agreement with the observations in section 7.5. Their values are near the frequency of 32 Hz which is in agreement with the observation of the effectiveness of the 32 Hz mitigation plugin, which acts over the frequency band between 16 Hz - 40 Hz.

Chapter 9

Echoes in the literature: searches and models

In the literature, there are many reports of template-based echo searches [95, 54, 56, 55] but very few try to investigate the nature of current detected BBH signals with an un-modeled approach [96]. One advantage of an echo search independent of the echoes morphology is its capability to detect a large family of possible echo signals at the same time, and since there are no certain models for echoes this leads to a higher detection possibility compared to template-based searches. This already occurred in the case of the detection of a BBH merger with extreme characteristics, GW190521 [114, 117], by the LVK collaboration. On the other hand, template-based searches (also looking at the discoveries of [14, 15, 16, 17]) usually provide a more selective sieve and may allow to detect weaker post-merger signals. The cWB LES search is the last entry of un-modeled echo searches, aiming to fill the gap in performance for low signal-to-noise ratios, and to provide independent results to be compared with the ones from similar studies.

By accepting a compromise that requires decreasing the possible detection efficiency for template-based echo searches, a winning strategy could involve the usage of un-modeled searches to spot possible post-merger energy outliers. With such information, and a preliminary morphological characterisation of the post-merger signal, a template-based search could be tuned, and then deployed to analyse the data, if physically motivated morphological information is retrieved by the un-modeled studies.

The purpose of this chapter is to provide a comparison of search results between cWB LES search and other methods described in the literature and discuss how the cWB LES search morphological reconstruction could impact echoes' emission models.

9.1 Comparison with other echo searches

Since the majority of published searches for echoes have analysed O1 data [95, 54, 56, 55, 96] and some focused their attention on GW150914 event [56, 55] the following comparisons between cWB LES search and the literature results are carried on using as a reference the results obtained for GW150914.

The un-modeled search proposed by Ka Wa Tsang, et al. [96] shows that echo's signals above $snr = 12$ it is possible to have a confident detection. This result is obtained by studying the two LIGO detectors' network at their designed sensitivity [118], and it holds for both the studied noise: stationary Gaussian noise, and glitch-contaminated noise. The cWB LES search for an $snr = 12$, see figure 9.1, provides with a false alarm probability of 5% ($FAP = 5\%$) a detection efficiency of 100%

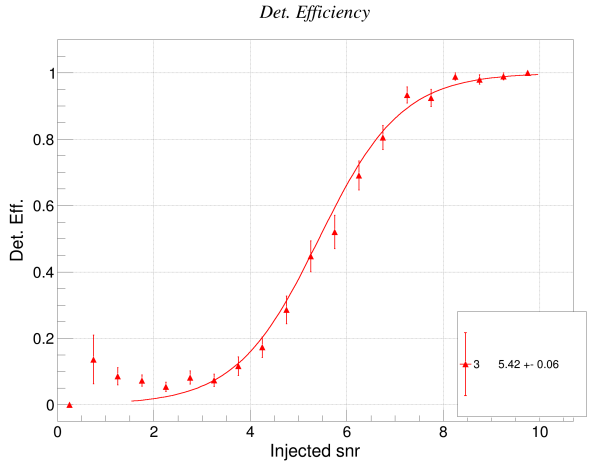

Figure 9.1: Detection efficiency DE (y-axis) versus injected snr (x-axis) for GW150914. The red line is the fit of the data.

($DE = 100\%$) of possible echo's signals in the post-merger. Moreover, the cWB LES search results are estimated over the real O1 detector noise. Then, Ka Wa Tsang, et al. show that for echoes with $snr = 8$, the FAP is between $6 - 30\%$ depending upon the assumptions on the noise properties of the data. For a stationary Gaussian noise assumption $FAP \sim 6\%$, while for a glitch contaminated noise $FAP \sim 30\%$. For such an snr value ($snr = 8$) the cWB LES search with $FAP = 5\%$ reaches a $DE \sim 95\%$, as it is possible to see from figure 9.1. Such comparison hints at better performances of the cWB LES search.

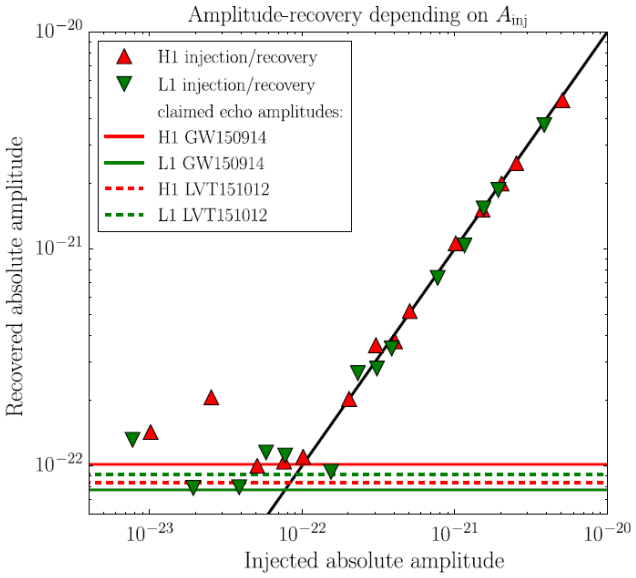

Figure 9.2: Reconstructed amplitude (y-axis) versus injected amplitude (x-axis) for Gaussian noise for single L and H detectors. This figure is taken from [54], FIG. 5.

The template search proposed by Julian Westerweck, et al. [54] provides an on-source null hypothesis p-value for GW150914 around 20% using O1 data, while the cWB LES search finds an on-source null hypothesis p-value of $\sim$ 82%. Both the searches label the energy excess of GW150914 post-merger as a noise fluctuation. Always Julian Westerweck, et al. provide a characteristic reconstructed amplitude

in presence of only Gaussian noise around $h \sim 10^{-22}$, represented by the horizontal lines of figure 9.2 (figure 5 in their paper [54]). The cWB LES search has a 50% detection efficiency with FAP of 5% for $h \sim (2.35 \pm 0.02) \cdot 10^{-22}$ over real O1 data, showing competitive results.

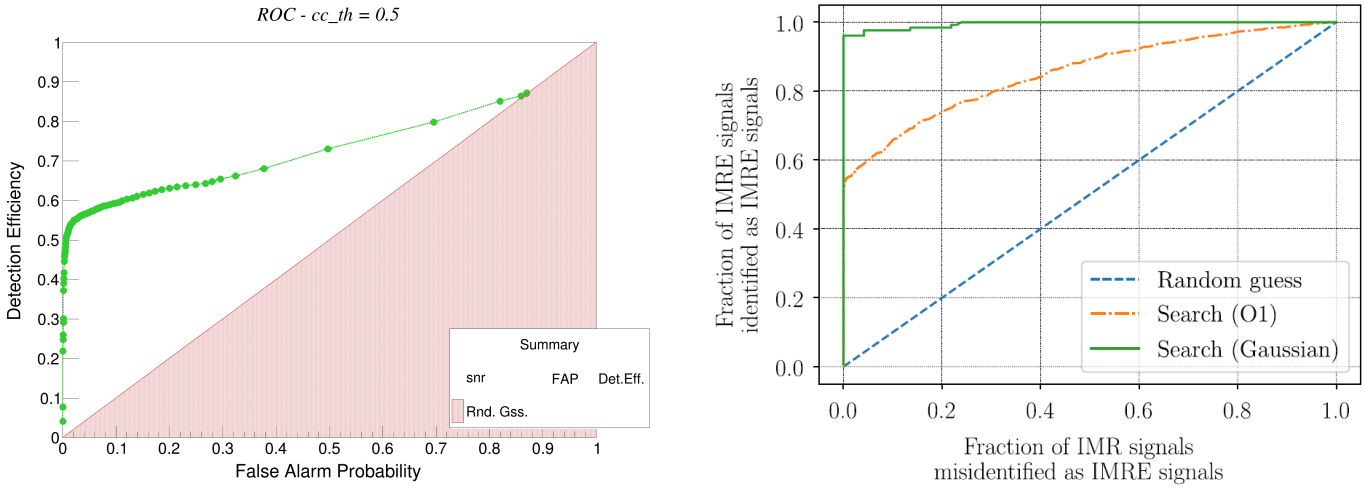

Figure 9.3: ROC comparison between cWB LES search (left) and echo template-based search proposed by Rico K. L. Lo, et al. [56] (right). The curves to be "compared" (a fair comparison is not possible since the injections' set is different for the two studies) are the ones referred to O1 data: green for the cWB LES study, orange for Rico K. L. Lo, et al. Moreover, the cWB LES search result is based on GW150914, while Rico K. L. Lo, et al. use templates inspired by GW150914, nevertheless the data sets for both the analysis are from O1 observing run.

We can compare the detection capability of cWB LES search with the template search proposed by Rico K. L. Lo, et al. [56] by inspecting their respective ROC plot results (introduced in section 6.5): figure 9.3. The SIG distribution (which they label as IMRE, inspiral merger ring-down echoes) between the two searches is different. Rico K. L. Lo, et al. simulate echoes randomly selecting their main morphological parameters (see section 3.1) from uniform distributions of the parameters' values. Parameters $A, \gamma \in [0.0, 1.0]$, and t_{echo}, $\Delta t_{echo} \in [0.05, 0.5]$ s. In figure, 9.3, they have the 10% of their injections with $A \lesssim 0.1$, so for the $hrss \sim 1.6 \cdot 10^{-22}/\sqrt{\text{Hz}}$ of GW150914 ($hrss_{GW150914}$), $hrss \lesssim 1.6 \cdot 10^{-23}/\sqrt{\text{Hz}}$. Our echo parameters distributions have fixed $t_{echo} = \Delta t_{echo} = 300$ ms and $\gamma = 0.5$, while $A \in [0.04, 1.0]$, with the SGE are randomly injected from a uniform logarithmic amplitude distribtion. So we injected many SGE with low *snr*, while very few with high *snr*, indeed the $\sim 34\%$ of our injections have $A \lesssim 0.1$. This higher richness of the low amplitude injections leads to a less performing ROC curve for the cWB LES search. This can be seen if we focus our attention on the FAP region between $1\% - 10\%$ of the ROC plots. We see that for Rico K. L. Lo, et al. the corresponding DE is $\sim 55\% - 65\%$, while for cWB it is $\sim 52\% - 60\%$, so roughly a 5% lower to Rico K. L. Lo, et al. result. Now, since Rico K. L. Lo, et al. have a uniform distribution in the amplitude of the injections, we can think, at zero-order approximation, that the DE decreases linearly in amplitude. So, a $DE = 55\%$ corresponds a waveform amplitude of $(1 - DE) \cdot hrss_{GW150914} \sim 0.7 \cdot 10^{-22}/\sqrt{\text{Hz}}$, while for a $DE = 65\%$ we have that $(1 - DE) \cdot hrss_{GW150914} \sim 0.7 \cdot 10^{-22}/\sqrt{\text{Hz}}$. Then, one has the following relationship

for the Rico K. L. Lo, et al. analysis:

$$\begin{cases} FAP = 1\% \\ DE \sim 55\% \\ snr \sim 13 \end{cases} \qquad \begin{cases} FAP = 10\% \\ DE \sim 65\% \\ snr \sim 11 \end{cases}$$

With our cWB LES search, for the same snr values, we have the following results (eq. (9.1))

$$\begin{cases} FAP = 0.13\% \\ DE \sim 29\% \\ snr \sim 13 \end{cases} \qquad \begin{cases} FAP = 0.17\% \\ DE \sim 34\% \\ snr \sim 11 \end{cases}$$

and it is possible to see that our search has a significantly lower FAP for a given snr. Notice that for such high snr values cWB LES search possesses a detection efficiency around 100%. Such an estimate can be obtained by looking at the injected echo's signals with $snr_{inj} \geq 11$ or 13 and checking how many signals are recovered with $snr_{rec} \geq 11$ or 13 respectively. Moreover, to cWB the FAP values of 1% and 10%, corresponds to the following snr_{rec} (eq. (9.1)):

$$\begin{cases} FAP = 1\% \\ DE \sim 52\% \\ snr \sim 6 \end{cases} \qquad \begin{cases} FAP = 10\% \\ DE \sim 60\% \\ snr \sim 2 \end{cases}$$

In their paper, Rico K. L. Lo, et al. ([56]) present a method to combine evidence from multiple gravitational wave echo events. Such a study follows from the Bayesian analysis they adopted. It does not require to assume that the GW events have to be described by the same set of echo parameters. They consider a set of GW events, N_{GW}, each of those with its respective background distribution of Bayes factor ${}^{i}\mathcal{B}$ for the null hypothesis (i labels the GW event). They do not merge all the background distributions of ${}^{i}\mathcal{B}$ into one unique statistic since it implies that each echo parameter for each event has to be the same. Instead, they select one background event for each N_{GW}, and estimate the "catalog" Bayes factor ${}^{cat}\mathcal{B}$:

$${}^{cat}\mathcal{B} = \sum_{i=1}^{N_{GW}} {}^{i}\mathcal{B}\,. \tag{9.1}$$

The null hypothesis "catalog" Bayes factor distribution is obtained by estimating n times ${}^{cat}\mathcal{B}$ by using different events from different background distributions of the N_{GW} events. In this way it is possible to construct a single statistics of ${}^{cat}\mathcal{B}$ that summarises all the N_{GW} independent statistics. This approach assumes that each GW event is independent and all the related echo parameters are not required to be correlated between them.

Such a study is extremely interesting: it lowers the statistical mean of the Bayes factor, in case of a null hypothesis, allowing to increase the significance of one ${}^{cat}\mathcal{B}$ outliers. It is possible to catch an overall evidence for echoes also in case the single candidates are too weak to stand out singularly

Inside the framework of the cWB LES search, this combined analysis of single null hypothesis p-values could bring similar advantages. We have set, in section 7.4, a first tentative to spot possible outliers from the null hypothesis p-value distribution by ranking their values and imposing a threshold below which an event is marked as an outlier, see figure 7.4. Nevertheless, such threshold's value is arbitrary and the whole search is a frequentist analysis and not a Bayesian one.

9.2 Echoes templates

In section 3.1 we have introduced some of the major echoes' observables mainly used in papers focused on the development of a modeled or unmodeled search for echoes signals. In section 5.3.4 we have overviewed the echo waveforms we used in this dissertation. Till now we did not focus on a specific waveform template for echoes because our search does not need that and because in literature there are no safe templates for echoes. Therefore, different waveform choices for echoes are used in recent papers:

- train of SGE signals;
- train with Gaussian envelope of the ring-down signal;
- reprocessing the BH ring-down signal with an analytical transfer function $\mathcal{K}$.

Nevertheless, the mechanism to generate echoes has not changed, it always involves the two barriers scheme (section 3.1), figure 3.1.

The usage of a train of SGE signals to model echoes has already been discussed in this dissertation (see 5.3.4), so here we can focus our attention on the last two models in the list above.

The ring-down plus echo-like gaussian pulses is a phenomenological approach used in literature **[maselli]** to model the possible post-merger signal of an ECO. In general, the waveform $h(t)_{PM}$ is obtained analytically and has the form:

$$h(t)_{PM} = h(t)_{RD} + h(t)_{echo}\,. \tag{9.2}$$

Here $h(t)_{RD}$ is the ring-down waveform, which usually is modeled with an exponentially decaying sinusoidal signal:

$$h(t)_{RD} = Ae^{-\frac{t}{\tau}}\cos\left(2\pi f t + \phi\right), \tag{9.3}$$

so characterised by an amplitude A, central frequency f, a phase term ϕ, and a damping time τ. The $h(t)_{echo}$ is the waveform that models the echo signals, with the possibility to use different gaussian pulses morphologies. As $h(t)_{echo}$ one can have either a simple train of cos-Gaussian pulses

$$h(t)_{echo} = \sum_{n=0}^{N-1}(-1)^{n+1}A_{n+1}e^{-\frac{(t-t_{echo-n})^2}{2\tau^2}}\cos\left(2\pi f_1(t-t_{echo-n})\right), \tag{9.4}$$

or more sophisticated templates [1]. They can add either multiple components at different frequencies to the oscillatory part ($+\cos\left(2\pi f_2(t-t_{echo-n})\right)$), or add different Gaussian functions ($+e^{-\frac{(t-t_{echo-n})^2}{2\tau_2^2}}\cos\left(2\pi f_2(t-t_{echo-n})\right)$) in order to increase the oscillating modes of the signal. Nevertheless, such phenomenological description is still characterised by the same parameters discussed in section 3.1, then our search is already capable of estimating the main morphological characteristics (see chapter 8) of such echo observables.

Concerning the last listed echo model, the ring-down signal is not simply repeated with damped amplitudes, time delayed, and eventually adjusted with a

[1] Here N refers to the number of echo pulses after the ring-down signal, A is the echo pulse amplitude, τ the Gaussian pulse time duration, f_1 the frequency of the first mode, and $t_{echo-n} = t_{echo} + n\Delta t$ is the mean-time of n^{th}-gaussian pulse, with t_{echo} the mean arrival time of the first echo and Δt the time delay between subsequent echoes.

phase factor (as for [54]), but it is filtered according to an analytical evaluation of the *transmission* and *reflession* coefficient at the two barriers. The emitted gravitational radiation of the final CO, after the merger, can be expressed as [119]:

$$\tilde{\Psi}(\omega, \chi \to \text{inf}) \sim \tilde{Z}^{+}(\omega) e^{i\omega\chi}\,, \tag{9.5}$$

where $\tilde{\Psi}$ is the Fourier transform (FT) of the solution of Teukololsky's master equation. It represents the outgoing radiation ($+$ symbol) emitted from the perturbed source. $\tilde{Z}^{+}(\omega)$ is the FT of the system response to a perturbation, and χ is the radial coordinate in a tortoise coordinate system. The system response $\tilde{Z}^{+}(\omega)$ has the form:

$$\tilde{Z}^{+}(\omega) = \tilde{Z}^{+}_{BH}(\omega) + \mathcal{K}(\omega)\tilde{Z}^{-}_{BH}(\omega)\,, \tag{9.6}$$

where $\tilde{Z}^{+}_{BH}$ and $\tilde{Z}^{-}_{BH}$ are the responses of a Kerr BH (at infinity and near the horizon $+$ and $-$ sign respectively) to a perturbation, and $\mathcal{K}(\omega)$ is the final CO transfer function:

$$\mathcal{K}(\omega) = \frac{T_{BH} R(\omega) e^{-2ik\chi_0}}{1 - R_{BH} R(\omega) e^{-2ik\chi_0}}\,. \tag{9.7}$$

For the outer barrier (or potential barrier, see section 2.2.2) it is possible to define the transmission, T_{BH}, and reflection, R_{BH}, coefficients. Their equations do not change if the final CO is a BH or an ECO. For the inner barrier, the reflection coefficient $R(\omega)$ is defined, and its expression depends upon the nature of the final object; if it is a BH then $R(\omega) = 0$ otherwise $R(\omega) \neq 0$.

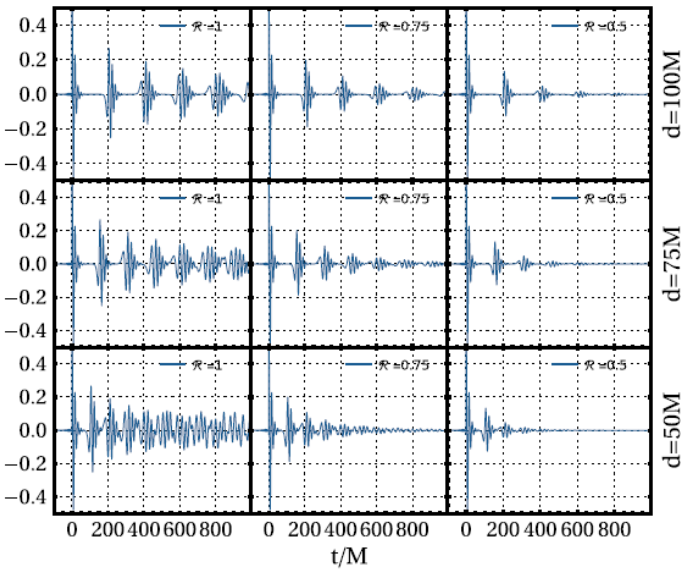

Figure 9.4: In this figure, the y-axis of each plot represents the real part of the GW amplitude of echo signals. The x-axis is the time. Each column of the plots' matrix is referred to a different reflection coefficient value of the final ECO, while each row is related to different δ values. Reference: [49].

The source properties related to the ring-down are the final mass of the CO, its spin, the amplitude and phase of the two ring-down polarisation waveforms, and the starting time of this star's evolutionary phase. The parameters strictly related to the echoes' morphology are the reflectivity coefficient of the ECO, and the proper distance δ of the ECO surface from the horizon radius r_+ (see, 2.2).

From figure 6 of [49], here figure 9.4, it is possible to see that the time separation between two subsequent echoes depends only by δ, for a non-spinning remnant. If

the radial distance of the inner barrier with respect to the would-be event horizon's radius increases then also t_{echo} increases, as seen also in section 3.1, so measuring t_{echo} would provide an indirect estimate of δ.

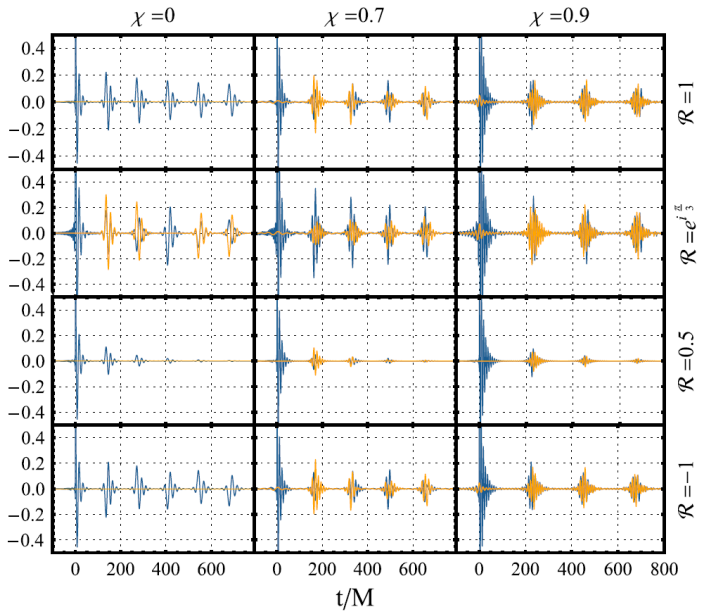

Figure 9.5: In this figure, the y-axis of each plot represents the real part of the GW amplitude, rind-down + echo, for both the + (blue) and × (orange) polarisations. The x-axis is the time. Each column of the plots' matrix is referred to different spin values of the final ECO, while each row is related to different R values. Reference: [119].

From the results of [119], this analytical approach (already introduced in [49]) to generate echo templates highlights possible non-trivial behaviors of the amplitude of the two echoes' polarisations. They show that even if the ring-down waveform is pure +-polarised, echoes can be generated with both polarisations. Moreover, the amplitude of subsequent echo pulses, for both the polarisations, is not necessarily damped as described by the γ factor, but it can grow and decrease at each repetition. Nevertheless, accordingly to other echo models, the overall energy content of each echo pulse is damped with respect to the previous one, if the final ECO is outside the superradiance condition [119].

The new features of this model hint to the need to measure both GW polarization components, which is feasible by analysing a network of detectors larger than the LIGO observatory alone, as performed in this dissertation. This will unlock the capability to recover both the waveform polarisations and enhance the possibility to set upper limits over the possible ECO spin and reflectivity parameter. This follows since we know [119] that this mixing of polarisations for echo signals is related either to the complex nature of R, or to the combination of a non-zero R and a non-null spin of the source. Such behavior is well depicted in figure 2 of the paper [119], which I copy here for clarity, figure 9.5.

Another quantity that [119] examines to infer the possible nature of an ECO is the ratio between the ring-down energy E_{RD} and the overall ring-down and echoes energy $E_{RD+echo}$. This ratio is highly dependent upon the ECO reflectivity R and only marginally on the spin of the remnant, as one can see from figure 9.6, taken from [119].

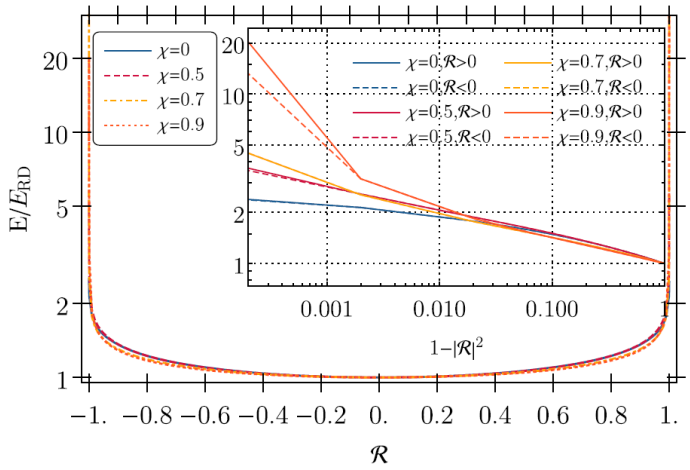

Figure 9.6: The plot shows the energy ratio between the ring-down plus echo signal and ring-down alone as function of the reflectivity of the ECO remnant for different values of spin χ of the final remnant. Reference: [119].

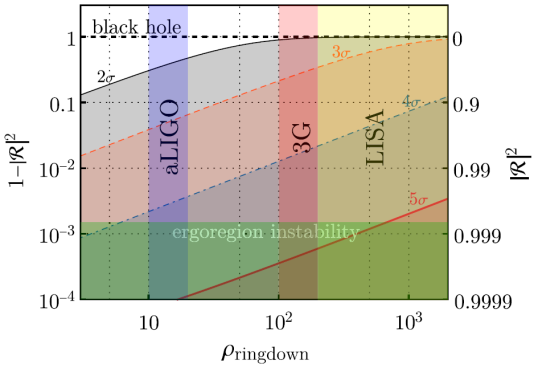

Figure 9.7: This plot reports the square of the reflectivity absolute value as a finction of the ring-down *snr*, $\rho_{ringdown}$. The vertical bands represents the predicted typical values of $\rho_{ringdown}$ for aLIGO/Virgo, 3G detectors, and LISA. The remnant is assumed to possess a spin equal to 0.7. Reference: [119].

In their paper [119], Maggio, et al. highlight as the $R = 1$ condition was already ruled out due to the ergoregion instability and the absence of stochastic GW background in O1 LIGO run. Upper limits from our cWB LES search on LIGO-Virgo observing runs could help in ruling out additional $R(\omega)$ values, therefore excluding a part of the ECOs' models related to the discarded $R(\omega)$ values, if any.

Moreover, with the current layout of the search, it would be possible to provide an estimate of the ring-down energy of the detected events from LVK collaboration. Such an estimation can be compared with the study of [119]: they predicted the possible excluded range of $R(\omega)$ values as a function of the ring-down *snr* with different confidence levels, as shown in figure 9.7.

Chapter 10

Conclusions

Our low energy signal search, a.k.a. LES search, by measuring both the false alarm probability and the sensitivity to echoes, as described in chapters 6 and 7, can estimate the probability of having an echo candidate in the post-merger phase of a BBH gravitational wave signal. We demonstrate its detection capability in chapter 7, sections 7.2 and 7.3. The LES search found no evidence for echoes in the analysed set of BBH signals detected during O1, O2, and O3 observing runs (see table 5.1, and chapter 7), resulting in general agreement with the literature [108, 103, 104]. Two events, out of the 34 studied, provide an on-source null hypothesis p-value that makes them worthy to be investigated (see section 7.5), but not enough to be considered as certain detection with a 5σ confidence level. Thus, a deep morphological investigation was carried on in chapters 7 and 8, which demonstrates there is no evidence to consider the reconstructed energy excess in the PMW as echo candidates.

10.1 Lessons learned for further improvements

It is obvious that any interpretation of burst candidates in the post-merger phase needs to be based on their morphological characteristics. Our follow-up of the outliers (section 7.5) demonstrates that morphological studies are able to reject the hypothesis that these candidates be related to the BBH coalescences GW190701 and GW200224. In the following, we briefly recap the lessons learned and indicate a path for improving the method.

GW190701. Figure 7.7a clearly shows noise feature of repeated loud glitches for frequencies around 32 Hz. Once the data are conditioned (section 7.5), by using the so-called 32 Hz mitigation plugin, the on-source null hypothesis p-value increases by more than one order of magnitude from ~ 0.0015 up to ~ 0.024, equation 7.5. The 32 Hz mitigation plugin is a filter that normalizes the PSD to reduce the noise around the frequency band $[16 - 40]$Hz. Moreover, the independent reconstruction of the post-merger phase of the BBH event (figure 7.10), shows that the most energetic candidate pulses at time ~ 168.65 s is barely detectable and possess lower energy with respect to the candidate second pulse at ~ 168.85 s. This scenario, toghether with the time duration of the candidates ~ 100 ms, is not plausible within any echo theories in literature so far.

GW200224. Figure 7.13a, as for the case of GW190701, shows an energy outlier in its PM phase at time duration ≥ 400 ms. This is way too wide to match theoretical echoes predictions [96, 53]. Also its $t_{echo} \sim 0.96$ s is far bigger if compared to the prediction of equation (3.4) and table 5.2. Moreover, we have seen in section 7.5 that cWB LES analysis cannot detect the PM signal in the absence of the primary signal.

This follows from the poor coherence of the PM signal in the detectors' network. The frequency of the PM energy excess ~ 30 Hz matches with the $[16-40]$Hz noisy frequency band, and even performing the 32 Hz-LES search which reduces the on-source snr_{rec}^{ON} by the $\sim$ 20%, the null hypothesis p-value is low enough to label the event as an outlier. In this study (see 7.5), the 4096s-LES search analysis shows an incompatibility between the BGK distribution obtained using all the calendar month of data (standard LES search) and the limited set of 4096 s (4096s-LES search) around the GW event. Such occurrence points to systematic error in the p-value evaluation in case of very peculiar noise features inside the on-source data. This does not invalidate the method: we need to be conscious that, until such systematic underestimation of the p-value won't be fixed, there could be times when the search will label an event as interesting and worth to be further investigated while its PMW energy content is due to an isolated and very energetic single interferometer glitch. The near future goal is of course to address such a problem and came out with a solution in order to further reduce the false positives.

In that regard, since the morphological study of the post-merger plays a fundamental role in discriminating between a PM energy excess due to noise fluctuations or genuine astrophysical signals a further development to cWB LES search can be the integration of the comparison between on-source and off-source results in the proceeding of the search.

The detection procedure implemented so far computes the on-source p-value of the *snr* inside the post-merger window relying on the *snr* statistics of the BGK. No information about the morphology is exploited in the detection step since I have been aiming to deploy the most general burst search for post-merger signals. However, without loss of generality, the detection stage of the LES search could be informed about the morphological characteristics of the more common false alarm events measured by the BKG simulation. This calls for a development of a detection ranking based on a multivariate analysis, exploiting e.g. the morphological estimates already provided by the LES search (see chapter 8).

A second impactful development will be the integration in the detection search of the on-source data analysis after the subtraction of the best BBH coalescence estimate, e.g. the maximum likelihood waveform posterior sample from the template-based parameter estimation. The subtraction can be implemented in more ways. The first one is mostly in place and is the one already used and tested. The other possibility will act during the clustering phase, leaving cWB to reconstruct the event, then the "primary" signal is subtracted, and the analysis is carried on over the likelihood of the residuals. These two methods can appear similar but in the first proposal if the signal-subtracted data does not pass all the cWB LES search thresholds then nothing is reconstructed. On the contrary, in the second proposal, the clustering phase is already passed, and so the likelihood is estimated over the leftovers even if they alone won't have been able to pass all the cWB LES search thresholds, so it can allow having deep investigations over the residual data after the removal of the triggering gravitational wave event.

10.2 Remarks on the LIGO-Virgo detector network

Up to now, the cWB LES search was used in the two detectors' network configuration even though the operating detectors were three since the last part of O2 and for

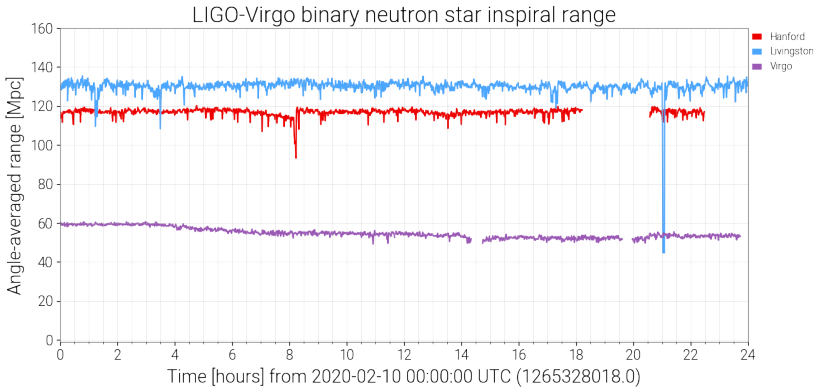

Figure 10.1: Sensitivity for the best BNS range [120] for the three detectors' network: L1, H1, and V1. The data are taken from [121] and relative to the observing day: 2020, February 10th.

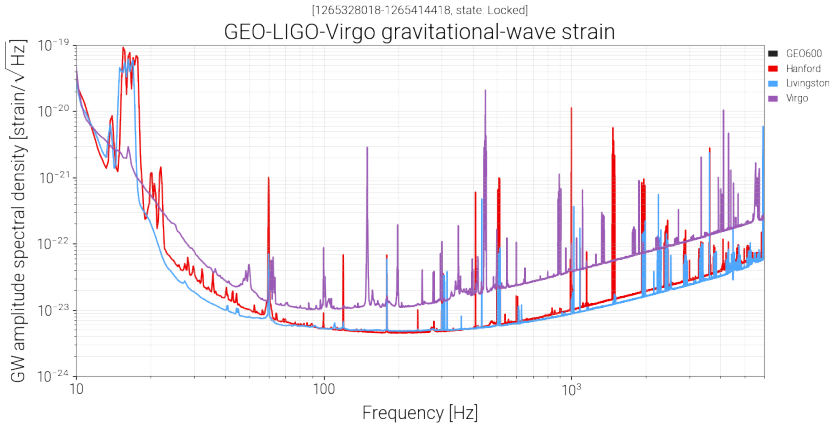

Figure 10.2: Amplitude spectral density for the three detectors' network: L1, H1, and V1. The data are taken from [121] and relative to the observing day: 2020, February 10th.

the entire O3 observing run. The two detectors used in this study are the LIGO interferometers. This choice follows from the analysis of the Virgo detector performances compared to the two LIGOs and for homogeneity with the study of O1. Speaking of the Virgo detector performances, during O3 its sensitivity was around half the LIGOs one. This can be seen from figure 10.1, where is reported the sensitivity for the best BNS range [120] (202, February 10th). Moreover, our search aims to detect poorly energetic signals, with an $hrss_{inj} \geq 1.85 \cdot 10^{-23}/\sqrt{\text{Hz}}$, and as it is possible to see from the amplitude spectral density in figure 10.2, the noise flor of Virgo detector is around half the 50% DE $hrss_{inj}$ value with FAP of 5% (around frequencies of ~ 100 Hz - ~ 200 Hz. Then, having that Virgo detector during O2 and O3 was not as performant as LIGOs, we decided to carry on the cWB LES search over O1, O2, and O3 GW event of table 5.1, in a two detectors' network configuration.

Such a choice has a drawback: the poorly cWB sky localisation of a GW source. This uncertainty leads, among other things, to the bimodal distributions in estimating the arrival time of the injected echo mimickers, treated in section 8.3. Then, in the near future, if the Virgo detector will increase its sensitivity and reduce the gap in performance with respect to LIGOs detectors it is mandatory to implement a triple detector network cWB LES search. The code for the analysis depicted till chapter 8

(included) is already in place but, for now, a complete automation of the code is not ready.

10.3 Beyond echoes

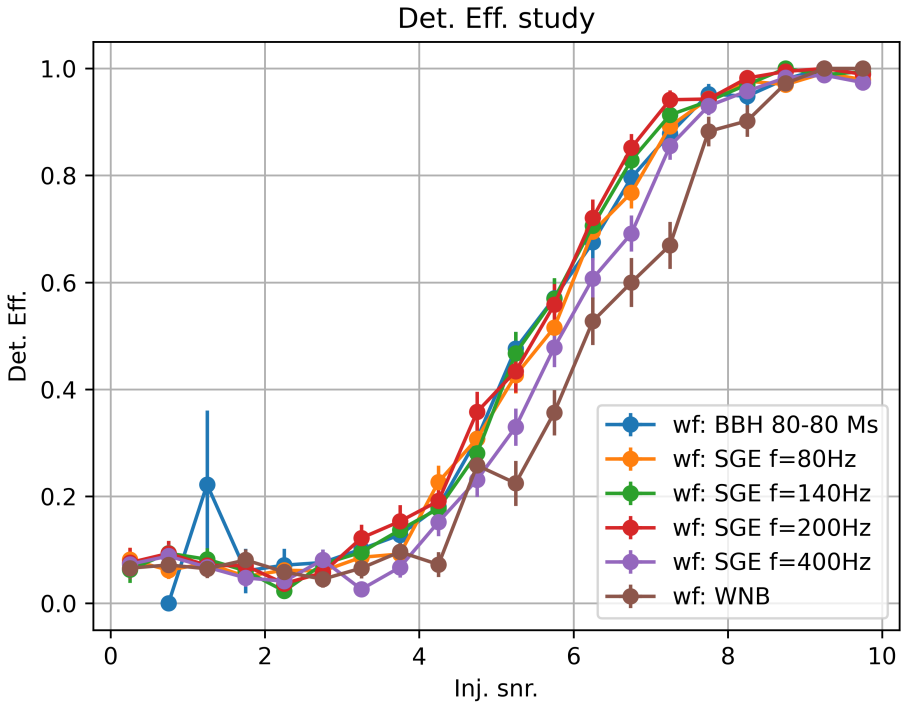

Figure 10.3: Detection efficiency as function of snr_{inj}^{PMW}. The study is carried on for different morphologies of echo's signals: a high mass BBH coalescence (blue), elliptically polarised sine-Gaussian trains of two pulses with different central frequencies $f_0 = 80, 140, 200, 400$Hz (orange, green, red, and violet respectively).

I want to conclude by highlighting that this search was thought and developed aiming to have a general procedure to probe both the inspiral phase and post-merger phase of a BBH coalescence, searching for the presence of possible low energy signals in the data.

Even if here I have only addressed the echoes scenario, the same procedures can be applied to other scientific cases of current interests such as pre-merger pulses or higher harmonic content in highly eccentric BBH signals (3.2) or memory effects (3.3). The procedure will be mostly the same either if one needs to probe the inspiral phase of a BBH event or its PM phase: it is just a matter of changing the PMW starting and ending times, to center it over the interesting time region one wants to analyse and, if desirable, adding a frequency band selection. Moreover, it is true that for the inspiral phase there are no tests of performances so far but, for the other events which are expected to take place in the PM phase, such as memory effects or micro-lensing (3.4), the performances will not suffer relevant degradation.

Regarding memory effects, the main unknown comes from their low-frequency content. Memory effects are ensured signals, but the low-frequency excess noise

of the detectors is expected to pose critical issues. On the contrary, for possible microlensing effects, the frequency band should not be of any harm: they should possess similar frequencies to the one of their companion signal, so within the most favorable band of spectral sensitivity of current detectors, see figure 4.4. As a further proof, here in figure 10.3, the detection efficiency of cWB LES search as function of the PMW injected *snr* (snr_{inj}^{PMW}) is compared for different morphologies of echo-like signals such as *white noise burst* (WNB), and for similar echo-like signals but with different central frequencies $f_0 \in \{80, 140, 200, 400\}$. It is possible to see that the search performances are not affected by the frequency of the low energy signal, inside the frequency band $[80 - 400]$. Moreover, also the morphology of the low energy signal does not affect the detection efficiency significantly, as already seen in section 7.1, and 7.2.

Nevertheless, it could be good to switch the cWB LES search configuration from a single-pixel selection rule (WP10) to a chirping-up one (WP5): micro-lensed signals should retain the well-known chirping morphology when represented in a TF plane. Moreover, new challenges could possibly come from the interference between different occurrences of the same microlensed transient. So, as it is possible to understand for sure there could be some minor adjustments to be done from one analysis to the other, but the main structure and its implementation does not change.

Appendix A

ECO's models

This appendix reports a very brief and schematic summary of the main ECO's models mentioned in chapter 3, section 3.1.

Gravastar model [43] It is an extension of Bose-Einstein condensation's concept to a gravitational system. It is a cold and dark compact object with an arbitrary mass M and it is described by a de Sitter geometry on the inside and a Schwarzschild geometry on the outside, for a static solution of the Einstein field equations. The two space-time regions are separated by a shell with a small but finite proper thickness l of ultrarelativistic fluid, such a shell has an equation of state $P = +\rho$ and replaces both the Schwarzschild and the de Sitter classical horizons. Such a shell is theorised to be a low-temperature condensate of weakly interacting massive bosons trapped inside a self-consistently generated cavity. The idea of a self-consistent generated cavity is motivated if the space-time can undergo a quantum vacuum rearrangement phase transition in the proximity to the would-be r_{sh} for the related BH.

Boson star model [44] This model assumes that fundamental scalar fields exist in nature. In the early stage of the Universe, such fundamental scalar fields would have formed absolutely stable soliton-type configurations kept together by their self-generated gravitational field. In the theory, one refers to such a configuration as boson stars (BSs). Inside the literature were proposed different theoretical models of BSs, and each of those could lead to different observational consequences. The first distinction between BSs is that the matter part of a BS can be described by either a complex or a real scalar field. Then, digging more deeply inside the theory, one can find out that distinctions between BSs can arise also from the different interactions of the scalar fields constituting the BS.

Fuzzball model [46] This BH alternative attempts to resolve two intractable problems that classic black holes pose for modern physics: *the central singularity of a black hole*, and *the information paradox*. The fuzzball theory replaces the singularity at the center of a black hole by filling the entire region within the black hole's event horizon with strings. Then, the strings should be the ultimate building blocks of matter and energy. They are thought to be bundles of energy vibrating in complex ways in both the three physical dimensions of space as well as in compact directions—extra dimensions interwoven in the quantum foam (also known as spacetime foam). Moreover, recent computations suggest that the solution to the information paradox lies in the fact that quantum gravity effects do not stay confined to microscopic distances, and the black hole interior result to be quite different from the naive picture suggested by classical gravity.

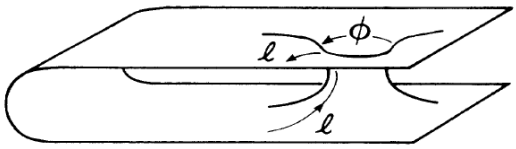

Figure A.1: Illustrative example of a wormhole. Reference: [45].

Wormholes model [45, 122] This models, as expected since we are dealing with ECO proposals, predicts the possibility to have as an alternative to BHs these COs called wormholes. They do not have an event horizon as a BH has, and differs, in principle, in several other important ways from a BH. To understand the essence of a wormhole, we can look at its space-time metric [122]

$$ds^2 = -\left(1 - \frac{2GM}{c^2 r} + \lambda^2\right) c^2 dt^2 + \left(1 - \frac{2GM}{c^2 r}\right)^{-1} dr^2 + r^2 \left(d\theta^2 + \sin^2\theta \, d\psi^2\right) . \tag{A.1}$$

This metric differs from the standard Schwarzschild metric because of the presence of the dimensionless parameter λ. When $\lambda = 0$, the metric describes the space-time geometry outside a Schwarzschild BH with mass M. Opposite, when $\lambda \neq 0$ the structure of the spacetime change completely: there is no event horizon, and instead, there is a throat at $r = r_{sh}$ that joins two isometrics, asymptotically flat space-time regions. An example can be found in figure A.1 (figure 1 of [45]).

Such a wormhole is called Schwarzshild wormhole but it is unstable and it would collapse too quickly for anything to cross from one end to the other. Wormholes that could be crossed in both directions, were thought to only be possible if exotic matter with negative energy density could be used to stabilize them [45]. In this picture, the event horizon of the original black hole metric is replaced, in the wormhole metric, by this exotic matter distribution localized in a thin shell around the center of the throat at $r = r_{sh}$.

Appendix B

CWB LES search parameters

Here, in this appendix, the table B.1 lists all the cWB parameters discussed (see sec. 5.2.4) and studied (see ch. 6) in this dissertation as well as their threshold values. Specifically, the first column of the table reports the name of the cWB parameters, the second column their threshold value for the cWB LES search, and the third column a very brief description of the quantity.

cWB LES search parameters and thresholds

Name	Threshold value	Description
bpp	0.001	**Black pixels probability**. It defines the number of core pixels among all the selected that have to be analysed once a trigger is selected.
cc	0.5	**Network coherent coefficient**. It provides information on a the signal's coherence inside the detectors' network.
ρ	3.5	**Effective network coherent** *snr*. It represents the coherent *snr* per detector of a trigger.
subnet	0.5	**Subnetwork energy asymmetry statistics**. It provides information about the energy distribution of a trigger inside the detectors' network.
Acore	1.7	**Average amplitude**. It estimates the average *snr* of each data pixel per detector.
Tgap	2.0	**Maximum time gap** between two pixels' clusters in order to be considered as a single event.
Fgap	128.0	**Maximum frequency gap** between two pixels' clusters in order to be considered as a single event.
SUBRHO	3.5	Hard-coded threshold over the ρ parameter.
SUBNET	0.1	Hard-coded threshold over the *subnet* parameter.

TABLE B.1: In this table are listed the names (first column), the threshold values (second column) of the cWB production parameters as well as their physical meaning (third column). This table is meant as an operative summary of the parameters introduced and defined in chapter ch. 5, section sec. 5.2.4.

Bibliography

[1] Michele Maggiore. *Gravitational Waves. Vol. 1: Theory and Experiments*. Oxford University Press, 2007. ISBN: 9780198570745.

[2] Charles W. Misner, K. S. Thorne, and J. A. Wheeler. *Gravitation*. W. H. Freeman, 1973. ISBN: 0716703343.

[3] LIGO-Virgo-KAGRA Scientific Collaboration. URL: https://www.ligo.caltech.edu/system/avm_image_sqls/binaries/58/jpg_original/Gravity_Waves_StillImage.jpg?1465865066.

[4] Steven Weinberg. *Gravitation and Cosmology: Principles and Applications of the General Theory of Relativity*. Wiley-VCH, 1972. ISBN: 9780198570745.

[5] Ray d'Inverno. *Introducing Einstein's Relativity*. Oxford University Press, 1992.

[6] S. W. Hawking and W. Israel. *Three hundred years of gravitation*. Cambridge University Press, 1987. ISBN: 0521343127.

[7] Bruce Allen. "The stochastic gravity-wave background: sources and detection". In: (1996). DOI: arXiv:gr-qc/9604033v3. URL: https://arxiv.org/abs/gr-qc/9604033.

[8] J. Cronin et al. "Particle and Nuclear Astrophysics and Cosmology in the Next Millennium - Snowmass 1994". In: *Fermilab Library* (1995).

[9] Kip S. Thorne. "Nobel Lecture: LIGO and gravitational waves III". In: *Rev. Mod. Phys.* 90 (4 2018), p. 040503. DOI: 10.1103/RevModPhys.90.040503. URL: https://link.aps.org/doi/10.1103/RevModPhys.90.040503.

[10] B.S. Sathyaprakash and B.F. Schutz. "Physics, Astrophysics and Cosmology with Gravitational Waves". In: *Living Rev. Relativ.* 12.2 (2019). DOI: https://doi.org/10.12942/lrr-2009-2.

[11] Greg Ushomirsky, Curt Cutler, and Lars Bildsten. "Deformations of accreting neutron star crusts and gravitational wave emission". In: *Monthly Notices of the Royal Astronomical Society* 319.3 (Dec. 2000), pp. 902–932. DOI: 10.1046/j.1365-8711.2000.03938.x. URL: https://doi.org/10.1046/j.1365-8711.2000.03938.x.

[12] Krzysztof Belczynski, Vassiliki Kalogera, and Tomasz Bulik. "A Comprehensive Study of Binary Compact Objects as Gravitational Wave Sources: Evolutionary Channels, Rates, and Physical Properties". In: *The Astrophysical Journal* 572.1 (2002), pp. 407–431. DOI: 10.1086/340304. URL: https://doi.org/10.1086/340304.

[13] LIGO-Virgo-KAGRA Scientific Collaboration. *Gravitational Wave Open Science Center*. URL: https://www.gw-openscience.org/.

[14] LIGO Scientific Collaboration and Virgo Collaboration. "GWTC-1: A Gravitational-Wave Transient Catalog of Compact Binary Mergers Observed by LIGO and Virgo during the First and Second Observing Runs". In: *Phys. Rev. X* 9 (3 2019). DOI: 10.1103/PhysRevX.9.031040. URL: https://link.aps.org/doi/10.1103/PhysRevX.9.031040.

[15] LIGO Scientific Collaboration and Virgo Collaboration. "GWTC-2: Compact Binary Coalescences Observed by LIGO and Virgo during the First Half of the Third Observing Run". In: *Phys. Rev. X* 11 (2 2021). DOI: 10.1103/PhysRevX.11.021053. URL: https://link.aps.org/doi/10.1103/PhysRevX.11.021053.

[16] LIGO Scientific Collaboration and Virgo Collaboration. "GWTC-2.1: Deep Extended Catalog of Compact Binary Coalescences Observed by LIGO and Virgo During the First Half of the Third Observing Run". In: (2022). DOI: arXiv:2108.01045. URL: https://arxiv.org/abs/2108.01045.

[17] LIGO Scientific Collaboration, Virgo Collaboration and KAGRA Collaboration. "GWTC-3: Compact Binary Coalescences Observed by LIGO and Virgo During the Second Part of the Third Observing Run". In: (2022). DOI: arXiv:2111.03606. URL: https://doi.org/10.48550/arXiv.2111.03606.

[18] LIGO Scientific Collaboration and Virgo Collaboration. "An upper limit on the stochastic gravitational-wave background of cosmological origin". In: *Nature* 460 (2009). DOI: 10.1038/nature08278. URL: https://doi.org/10.1038/nature08278.

[19] Chiara Caprini. "Stochastic background of gravitational waves from cosmological sources". In: *Journal of Physics: Conference Series* 610 (2015), p. 012004. DOI: 10.1088/1742-6596/610/1/012004. URL: https://doi.org/10.1088/1742-6596/610/1/012004.

[20] The Event Horizon Telescope Collaboration. URL: https://eventhorizontelescope.org/press-release-april-10-2019-astronomers-capture-first-image-black-hole.

[21] Malcom S. Longair. *High Energy Astrophysics*. Cambridge University Press, 2011. ISBN: 0521756189.

[22] Saul A. Teukolsky Stuart L. Saphiro. *Black Holes, White Dwarfs, and Neutron Stars, the physics of compact object*. WILEY-VCH Verlag GmbH & Co. KGaA, Weinheim, 2004. ISBN: 0716703343.

[23] Pani P. Cardoso V. "Testing the nature of dark compact objects: a status report". In: *Living Rev Relativ* 22.4 (2019). DOI: https://doi.org/10.1007/s41114-019-0020-4.

[24] The LIGO Scientific Collaboration and the Virgo Scientific Collaboration. "Observation of Gravitational Waves from a Binary Black Hole Merger". In: *Phys. Rev. Lett.* 116 (6 2016). DOI: 10.1103/PhysRevLett.116.061102. URL: https://link.aps.org/doi/10.1103/PhysRevLett.116.061102.

[25] Antoni Ramos-Buades et al. "Effective-one-body multipolar waveforms for eccentric binary black holes with nonprecessing spins". In: *Phys. Rev. D* 105 (4 2022). DOI: 10.1103/PhysRevD.105.044035. URL: https://link.aps.org/doi/10.1103/PhysRevD.105.044035.

[26] Koustav Chandra et al. "Numerical relativity injection analysis of signals from generically spinning intermediate mass black hole binaries in Advanced LIGO data". In: *Phys. Rev. D* 102 (4 2020). DOI: 10.1103/PhysRevD.102.044035. URL: https://link.aps.org/doi/10.1103/PhysRevD.102.044035.

[27] Luc Blanchet et al. "Gravitational waveforms from inspiralling compact binaries to second-post-Newtonian order". In: *Classical and Quantum Gravity* 13.4 (1996). DOI: 10.1088/0264-9381/13/4/002. URL: https://doi.org/10.1088/0264-9381/13/4/002.

[28] Konstantin A. Postnov and Lev R. Yungelson. "Physics, Astrophysics and Cosmology with Gravitational Waves". In: *Living Rev. Relativ.* 17.3 (2014). DOI: https://doi.org/10.12942/lrr-2014-3.

[29] Éanna É. Flanagan and Scott A. Hughes. "Measuring gravitational waves from binary black hole coalescences. I. Signal to noise for inspiral, merger, and ringdown". In: *Phys. Rev. D* 57 (8 1998). DOI: 10.1103/PhysRevD.57.4535. URL: https://link.aps.org/doi/10.1103/PhysRevD.57.4535.

[30] LIGO Scientific Collaboration and Virgo Collaboration. "Search for gravitational wave ringdowns from perturbed black holes in LIGO S4 data". In: *Phys. Rev. D* 80 (6 2009), p. 062001. DOI: 10.1103/PhysRevD.80.062001. URL: https://link.aps.org/doi/10.1103/PhysRevD.80.062001.

[31] Matthew Giesler et al. "Black Hole Ringdown: The Importance of Overtones". In: *Phys. Rev. X* 9 (4 2019), p. 041060. DOI: 10.1103/PhysRevX.9.041060. URL: https://link.aps.org/doi/10.1103/PhysRevX.9.041060.

[32] Emanuele Berti, Vitor Cardoso, and Andrei O Starinets. "Quasinormal modes of black holes and black branes". In: *Classical and Quantum Gravity* 26.16 (2009), p. 163001. DOI: 10.1088/0264-9381/26/16/163001. URL: https://doi.org/10.1088/0264-9381/26/16/163001.

[33] Richard Brito, Alessandra Buonanno, and Vivien Raymond. "Black-hole spectroscopy by making full use of gravitational-wave modeling". In: *Phys. Rev. D* 98 (8 2018), p. 084038. DOI: 10.1103/PhysRevD.98.084038. URL: https://link.aps.org/doi/10.1103/PhysRevD.98.084038.

[34] Mark Kac. "Can One Hear the Shape of a Drum?" In: *The American Mathematical Monthly* 73.4 (1966). URL: http://www.jstor.org/stable/2313748.

[35] Emanuele Berti, Vitor Cardoso, and Andrei O Starinets. "Quasinormal modes of black holes and black branes". In: *Classical and Quantum Gravity* 26.16 (2009), p. 163001. DOI: 10.1088/0264-9381/26/16/163001. URL: https://doi.org/10.1088/0264-9381/26/16/163001.

[36] William H. Press. "Long Wave Trains of Gravitational Waves from a Vibrating Black Hole". In: 170 (1971). Provided by the SAO/NASA Astrophysics Data System, p. L105. DOI: 10.1086/180849. URL: https://ui.adsabs.harvard.edu/abs/1971ApJ...170L.105P.

[37] Hans-Peter Nollert. "Quasinormal modes: the characteristic sound of black holes and neutron stars". In: *Classical and Quantum Gravity* 16.12 (1999), R159–R216. DOI: 10.1088/0264-9381/16/12/201. URL: https://doi.org/10.1088/0264-9381/16/12/201.

[38] Kip S. Thorne. "Multipole expansions of gravitational radiation". In: *Rev. Mod. Phys.* 52 (2 1980). DOI: 10.1103/RevModPhys.52.299. URL: https://link.aps.org/doi/10.1103/RevModPhys.52.299.

[39] The LIGO Scientific Collaboration and the Virgo Scientific Collaboration. "Properties of the Binary Black Hole Merger GW150914". In: *Phys. Rev. Lett.* 116 (24 2016). DOI: 10.1103/PhysRevLett.116.241102. URL: https://link.aps.org/doi/10.1103/PhysRevLett.116.241102.

[40] M. Campanelli, C. O. Lousto, and Y. Zlochower. "Spinning-black-hole binaries: The orbital hang-up". In: *Phys. Rev. D* 74 (4 2006), p. 041501. DOI: 10.1103/PhysRevD.74.041501. URL: https://link.aps.org/doi/10.1103/PhysRevD.74.041501.

[41] V. Ferrari and K. D. Kokkotas. "Scattering of particles by neutron stars: Time evolutions for axial perturbations". In: *Phys. Rev. D* 62 (10 2000), p. 107504. DOI: 10.1103/PhysRevD.62.107504. URL: https://link.aps.org/doi/10.1103/PhysRevD.62.107504.

[42] Vitor Cardoso, Edgardo Franzin, and Paolo Pani. "Is the Gravitational-Wave Ringdown a Probe of the Event Horizon?" In: *Phys. Rev. Lett.* 116 (17 2016), p. 171101. DOI: 10.1103/PhysRevLett.116.171101. URL: https://link.aps.org/doi/10.1103/PhysRevLett.116.171101.

[43] Pawel O. Mazur and Emil Mottola. "Gravitational vacuum condensate stars". In: *PNAS* 101 (2004). URL: https://doi.org/10.1073/pnas.0402717101.

[44] Franz E Schunck and Eckehard W Mielke. "General relativistic boson stars". In: *Classical and Quantum Gravity* 20.20 (2003). DOI: 10.1088/0264-9381/20/20/201. URL: https://doi.org/10.1088/0264-9381/20/20/201.

[45] Michael S. Morris, Kip S. Thorne, and Ulvi Yurtsever. "Wormholes, Time Machines, and the Weak Energy Condition". In: *Phys. Rev. Lett.* 61 (13 1988). DOI: 10.1103/PhysRevLett.61.1446. URL: https://link.aps.org/doi/10.1103/PhysRevLett.61.1446.

[46] S. Mathur. "The fuzzball proposal for black holes: an elementary review." In: *Fortschr. Phys.* 53 (2005). URL: https://doi.org/10.1002/prop.200410203.

[47] Qingwen Wang and Niayesh Afshordi. "Black hole echology: The observer's manual". In: *Phys. Rev. D* 97 (12 2018), p. 124044. DOI: 10.1103/PhysRevD.97.124044. URL: https://link.aps.org/doi/10.1103/PhysRevD.97.124044.

[48] Zachary Mark et al. "A recipe for echoes from exotic compact objects". In: *Phys. Rev. D* 96 (8 2017), p. 084002. DOI: 10.1103/PhysRevD.96.084002. URL: https://link.aps.org/doi/10.1103/PhysRevD.96.084002.

[49] Adriano Testa and Paolo Pani. "Analytical template for gravitational-wave echoes: Signal characterization and prospects of detection with current and future interferometers". In: *Phys. Rev. D* 98 (4 2018), p. 044018. DOI: 10.1103/PhysRevD.98.044018. URL: https://link.aps.org/doi/10.1103/PhysRevD.98.044018.

[50] Vitor Cardoso et al. "Light rings as observational evidence for event horizons: Long-lived modes, ergoregions and nonlinear instabilities of ultracompact objects". In: *Phys. Rev. D* 90 (4 2014), p. 044069. DOI: 10.1103/PhysRevD.90.044069. URL: https://link.aps.org/doi/10.1103/PhysRevD.90.044069.

[51] Vitor Cardoso et al. "Geodesic stability, Lyapunov exponents, and quasinormal modes". In: *Phys. Rev. D* 79 (6 2009), p. 064016. DOI: 10.1103/PhysRevD.79.064016. URL: https://link.aps.org/doi/10.1103/PhysRevD.79.064016.

[52] Vitor Cardoso et al. "Gravitational-wave signatures of exotic compact objects and of quantum corrections at the horizon scale". In: *Phys. Rev. D* 94 (8 2016), p. 084031. DOI: 10.1103/PhysRevD.94.084031. URL: https://link.aps.org/doi/10.1103/PhysRevD.94.084031.

[53] Andrea Maselli, Sebastian H. Völkel, and Kostas D. Kokkotas. "Parameter estimation of gravitational wave echoes from exotic compact objects". In: *Phys. Rev. D* 96 (6 2017). DOI: 10.1103/PhysRevD.96.064045. URL: https://link.aps.org/doi/10.1103/PhysRevD.96.064045.

[54] Julian Westerweck et al. "Low significance of evidence for black hole echoes in gravitational wave data". In: *Phys. Rev. D* 97 (12 2018), p. 124037. DOI: 10.1103/PhysRevD.97.124037. URL: https://link.aps.org/doi/10.1103/PhysRevD.97.124037.

[55] Alex B. Nielsen et al. "Parameter estimation and statistical significance of echoes following black hole signals in the first Advanced LIGO observing run". In: *Phys. Rev. D* 99 (10 2019), p. 104012. DOI: 10.1103/PhysRevD.99.104012. URL: https://link.aps.org/doi/10.1103/PhysRevD.99.104012.

[56] Rico K. L. Lo, Tjonnie G. F. Li, and Alan J. Weinstein. "Template-based gravitational-wave echoes search using Bayesian model selection". In: *Phys. Rev. D* 99 (8 2019). DOI: 10.1103/PhysRevD.99.084052. URL: https://link.aps.org/doi/10.1103/PhysRevD.99.084052.

[57] Yoshinta Setyawati and Frank Ohme. "Adding eccentricity to quasicircular binary-black-hole waveform models". In: *Phys. Rev. D* 103 (12 2021). DOI: 10.1103/PhysRevD.103.124011. URL: https://link.aps.org/doi/10.1103/PhysRevD.103.124011.

[58] Michael Ebersold and Shubhanshu Tiwari. "Search for nonlinear memory from subsolar mass compact binary mergers". In: *Phys. Rev. D* 101 (10 2020), p. 104041. DOI: 10.1103/PhysRevD.101.104041. URL: https://link.aps.org/doi/10.1103/PhysRevD.101.104041.

[59] William E. East et al. "Observing complete gravitational wave signals from dynamical capture binaries". In: *Phys. Rev. D* 87 (4 2013), p. 043004. DOI: 10.1103/PhysRevD.87.043004. URL: https://link.aps.org/doi/10.1103/PhysRevD.87.043004.

[60] LIGO Scientific Collaboration and Virgo Collaboration. "Search for Eccentric Binary Black Hole Mergers with Advanced LIGO and Advanced Virgo during Their First and Second Observing Runs". In: *The Astrophysical Journal* 883.2 (2019), p. 149. DOI: 10.3847/1538-4357/ab3c2d. URL: https://doi.org/10.3847/1538-4357/ab3c2d.

[61] Alan J. Weinstein Simona Miller Jonah B. Kanner and Thomas Callister. "Observing complete gravitational wave signals from dynamical capture binaries". In: (2018). URL: https://dcc.ligo.org/LIGO-T1800231.

[62] Linqing Wen. "On the Eccentricity Distribution of Coalescing Black Hole Binaries Driven by the Kozai Mechanism in Globular Clusters". In: *The Astrophysical Journal* 598 (1 2003), pp. 419–430. DOI: 10.1086/378794. URL: https://doi.org/10.1086/378794.

[63] Marc Favata. "The gravitational-wave memory effect". In: *Classical and Quantum Gravity* 27 (8 2010), p. 084036. DOI: 10.1088/0264-9381/27/8/084036. URL: https://doi.org/10.1088/0264-9381/27/8/084036.

[64] Kip S. Thorne. "Gravitational-wave bursts with memory: The Christodoulou effect". In: *Phys. Rev. D* 45 (2 1992), pp. 520–524. DOI: 10.1103/PhysRevD.45.520. URL: https://link.aps.org/doi/10.1103/PhysRevD.45.520.

[65] Demetrios Christodoulou. "Nonlinear nature of gravitation and gravitational-wave experiments". In: *Phys. Rev. Lett.* 67 (12 1991), pp. 1486–1489. DOI: 10.1103/PhysRevLett.67.1486. URL: https://link.aps.org/doi/10.1103/PhysRevLett.67.1486.

[66] Moritz Hubner et al. "Measuring gravitational-wave memory in the first LIGO/Virgo gravitational-wave transient catalog". In: *Phys. Rev. D* 101 (2 2020), p. 023011. DOI: 10.1103/PhysRevD.101.023011. URL: https://link.aps.org/doi/10.1103/PhysRevD.101.023011.

[67] Jose Marí a Ezquiaga and Miguel Zumalacárregui. "Gravitational wave lensing beyond general relativity: Birefringence, echoes, and shadows". In: *Phys. Rev. D* 102 (12 2020). DOI: 10.1103/PhysRevD.102.124048. URL: https://link.aps.org/doi/10.1103/PhysRevD.102.124048.

[68] Jose María Ezquiaga et al. "Phase effects from strong gravitational lensing of gravitational waves". In: *Phys. Rev. D* 103 (6 2021). DOI: 10.1103/PhysRevD.103.064047. URL: https://link.aps.org/doi/10.1103/PhysRevD.103.064047.

[69] Ashish Kumar Meena and Jasjeet Singh Bagla. "Gravitational lensing of gravitational waves: wave nature and prospects for detection". In: *Monthly Notices of the Royal Astronomical Society* 492 (1 2019). ISSN: 0035-8711. DOI: 10.1093/mnras/stz3509. URL: https://doi.org/10.1093/mnras/stz3509.

[70] Masamune Oguri. "Strong gravitational lensing of explosive transients". In: *Reports on Progress in Physics* 82 (12 2019). DOI: 10.1088/1361-6633/ab4fc5. URL: https://doi.org/10.1088/1361-6633/ab4fc5.

[71] Elia Pizzati et al. "Toward inference of overlapping gravitational-wave signals". In: *Phys. Rev. D* 105 (10 2022). DOI: 10.1103/PhysRevD.105.104016. URL: https://link.aps.org/doi/10.1103/PhysRevD.105.104016.

[72] Philip Relton and Vivien Raymond. "Parameter estimation bias from overlapping binary black hole events in second generation interferometers". In: *Phys. Rev. D* 104 (8 2021). DOI: 10.1103/PhysRevD.104.084039. URL: https://link.aps.org/doi/10.1103/PhysRevD.104.084039.

[73] Anuradha Samajdar et al. "Biases in parameter estimation from overlapping gravitational-wave signals in the third-generation detector era". In: *Phys. Rev. D* 104 (4 2021). DOI: 10.1103/PhysRevD.104.044003. URL: https://link.aps.org/doi/10.1103/PhysRevD.104.044003.

[74] Virgo Collaboration. *Virgo Detector Characterization and Data Quality during the O3 run*. 2022. DOI: 10.48550/ARXIV.2205.01555. URL: https://arxiv.org/abs/2205.01555.

[75] LIGO Caltech website. In: (). URL: https://www.ligo.caltech.edu/page/facilities.

[76] Michele Maggiore. "Gravitational wave experiments and early universe cosmology". In: *Physics Reports* 331 (6 2000), pp. 283–367. DOI: https://doi.org/10.1016/S0370-1573(99)00102-7. URL: https://www.sciencedirect.com/science/article/pii/S0370157399001027.

[77] Sanjeev V. Dhurandhar and Massimo Tinto. "Astronomical observations with a network of detectors of gravitational waves – I. Mathematical framework and solution of the five detector problem". In: *Monthly Notices of the Royal Astronomical Society* 234 (3 1988), pp. 663–676. DOI: 10.1093/mnras/234.3.663. URL: https://doi.org/10.1093/mnras/234.3.663.

[78] Bernard F Schutz. "Networks of gravitational wave detectors and three figures of merit". In: *Classical and Quantum Gravity* 28 (12 2011), p. 125023. DOI: 10.1088/0264-9381/28/12/125023. URL: https://doi.org/10.1088/0264-9381/28/12/125023.

[79] S. Klimenko et al. "Method for detection and reconstruction of gravitational wave transients with networks of advanced detectors". In: *Phys. Rev. D* 93 (4 2016). DOI: 10.1103/PhysRevD.93.042004. URL: https://link.aps.org/doi/10.1103/PhysRevD.93.042004.

[80] LIGO Scientific Collaboration and Virgo Collaboration. "All-sky search for short gravitational-wave bursts in the third Advanced LIGO and Advanced Virgo run". In: (2021). arXiv: 2107.03701 [gr-qc].

[81] Marco Drago. "Search for transient gravitational wave signals with unknown waveform in the LIGO Virgo network of interferometric detectors using a fully coherent algorithm". In: (2010). URL: https://gwburst.gitlab.io/documentation/latest/html/documents.html.

[82] "Advanced Virgo: a second-generation interferometric gravitational wave detector". In: *Classical and Quantum Gravity* 32 (2 2014), p. 024001. DOI: 10.1088/0264-9381/32/2/024001. URL: https://doi.org/10.1088/0264-9381/32/2/024001.

[83] et al. Alex Abramovici. "LIGO: The Laser Interferometer Gravitational-Wave Observatory". In: *Science* 256 (1992).

[84] LIGO Scientific Collaboration and Virgo Collaboration. "All-sky search for short gravitational-wave bursts in the first Advanced LIGO run". In: *Phys. Rev. D* 95 (4 2017). DOI: 10.1103/PhysRevD.95.042003. URL: https://link.aps.org/doi/10.1103/PhysRevD.95.042003.

[85] LIGO Scientific Collaboration and Virgo Collaboration. "All-sky search for short gravitational-wave bursts in the second Advanced LIGO and Advanced Virgo run". In: *Phys. Rev. D* 100 (2 2019). DOI: 10.1103/PhysRevD.100.024017. URL: https://link.aps.org/doi/10.1103/PhysRevD.100.024017.

[86] LIGO Scientific Collaboration, Virgo Collaboration and KAGRA Collaboration. "All-sky search for short gravitational-wave bursts in the third Advanced LIGO and Advanced Virgo run". In: *Phys. Rev. D* 104 (12 2021). DOI: 10.1103/PhysRevD.104.122004. URL: https://link.aps.org/doi/10.1103/PhysRevD.104.122004.

[87] S Babak et al. "A template bank to search for gravitational waves from inspiralling compact binaries: I. Physical models". In: *Classical and Quantum Gravity* 23.18 (Aug. 2006), pp. 5477–5504. DOI: 10.1088/0264-9381/23/18/002. URL: https://doi.org/10.1088/0264-9381/23/18/002.

[88] Tagoshi H. Dhurandhar S. Mukhopadhyay M. and Kanda N. "Coherent versus coincidence detection of gravitational wave signals from compact inspiraling binaries". In: (2010). DOI: arXiv:1003.5490. URL: https://doi.org/10.48550/arXiv.1003.5490.

[89] S Klimenko et al. "A coherent method for detection of gravitational wave bursts". In: *Classical and Quantum Gravity* 25.11 (May 2008), p. 114029. DOI: 10.1088/0264-9381/25/11/114029. URL: https://doi.org/10.1088/0264-9381/25/11/114029.

[90] Coherent WaveBurst team. "Coherent WaveBurst site". In: (). URL: https://gwburst.gitlab.io/documentation/latest/html/index.html#.

[91] Éanna É. Flanagan and Scott A. Hughes. "Measuring gravitational waves from binary black hole coalescences. II. The waves' information and its extraction, with and without templates". In: *Phys. Rev. D* 57 (8 1998). DOI: 10.1103/PhysRevD.57.4566. URL: https://link.aps.org/doi/10.1103/PhysRevD.57.4566.

[92] S. Klimenko et al. "Constraint likelihood analysis for a network of gravitational wave detectors". In: *Phys. Rev. D* 72 (12 Dec. 2005), p. 122002. DOI: 10.1103/PhysRevD.72.122002. URL: https://link.aps.org/doi/10.1103/PhysRevD.72.122002.

[93] V Necula, S Klimenko, and G Mitselmakher. "Transient analysis with fast Wilson-Daubechies time-frequency transform". In: *Journal of Physics: Conference Series* 363 (June 2012), p. 012032. DOI: 10.1088/1742-6596/363/1/012032. URL: https://doi.org/10.1088/1742-6596/363/1/012032.

[94] M. P. Maples et al. "Robust Chauvenet Outlier Rejection". In: *The Astrophysical Journal Supplement Series* 238.1 (Aug. 2018), p. 2. DOI: 10.3847/1538-4365/aad23d. URL: https://doi.org/10.3847/1538-4365/aad23d.

[95] Jahed Abedi, Hannah Dykaar, and Niayesh Afshordi. "Echoes from the abyss: Tentative evidence for Planck-scale structure at black hole horizons". In: *Phys. Rev. D* 96 (8 2017). DOI: 10.1103/PhysRevD.96.082004. URL: https://link.aps.org/doi/10.1103/PhysRevD.96.082004.

[96] Ka Wa Tsang et al. "A morphology-independent data analysis method for detecting and characterizing gravitational wave echoes". In: *Phys. Rev. D* 98 (2 2018). DOI: 10.1103/PhysRevD.98.024023. URL: https://link.aps.org/doi/10.1103/PhysRevD.98.024023.

[97] Sascha Husa et al. "Frequency-domain gravitational waves from nonprecessing black-hole binaries. I. New numerical waveforms and anatomy of the signal". In: *Phys. Rev. D* 93 (4 2016). DOI: 10.1103/PhysRevD.93.044006. URL: https://link.aps.org/doi/10.1103/PhysRevD.93.044006.

[98] Sebastian Khan et al. "Frequency-domain gravitational waves from nonprecessing black-hole binaries. II. A phenomenological model for the advanced detector era". In: *Phys. Rev. D* 93 (4 2016). DOI: 10.1103/PhysRevD.93.044007. URL: https://link.aps.org/doi/10.1103/PhysRevD.93.044007.

[99] Mark Hannam et al. "Simple Model of Complete Precessing Black-Hole-Binary Gravitational Waveforms". In: *Phys. Rev. Lett.* 113 (15 2014). DOI: 10.1103/PhysRevLett.113.151101. URL: https://link.aps.org/doi/10.1103/PhysRevLett.113.151101.

[100] Serguei Ossokine et al. "Multipolar effective-one-body waveforms for precessing binary black holes: Construction and validation". In: *Phys. Rev. D* 102 (4 2020). DOI: 10.1103/PhysRevD.102.044055. URL: https://link.aps.org/doi/10.1103/PhysRevD.102.044055.

[101] Vijay Varma et al. "Surrogate models for precessing binary black hole simulations with unequal masses". In: *Phys. Rev. Research* 1 (3 2019). DOI: 10.1103/PhysRevResearch.1.033015. URL: https://link.aps.org/doi/10.1103/PhysRevResearch.1.033015.

[102] LIGO Scientific Collaboration and Virgo Collaboration. "All-sky search for gravitational-wave bursts in the second joint LIGO-Virgo run". In: *Phys. Rev. D* 85 (12 2012), p. 122007. DOI: 10.1103/PhysRevD.85.122007. URL: https://link.aps.org/doi/10.1103/PhysRevD.85.122007.

[103] LIGO Scientific Collaboration and Virgo Collaboration. "Tests of general relativity with binary black holes from the second LIGO-Virgo gravitational-wave transient catalog". In: *Phys. Rev. D* 103 (12 2021). DOI: 10.1103/PhysRevD.103.122002. URL: https://link.aps.org/doi/10.1103/PhysRevD.103.122002.

[104] The LIGO Scientific Collaboration and the Virgo Collaboration, and the KAGRA Collaboration. "Tests of General Relativity with GWTC-3". In: (2021). DOI: arXiv:2112.06861. URL: https://doi.org/10.48550/arXiv.2112.06861.

[105] Tom Fawcett. "An introduction to ROC analysis". In: *Pattern Recognition Letters* 27.8 (2006). ROC Analysis in Pattern Recognition. ISSN: 0167-8655. DOI: https://doi.org/10.1016/j.patrec.2005.10.010. URL: https://www.sciencedirect.com/science/article/pii/S016786550500303X.

[106] Patrick J. Sutton. "A Rule of Thumb for the Detectability of Gravitational-Wave Bursts". In: (2013). DOI: arXiv:1304.0210. URL: https://doi.org/10.48550/arXiv.1304.0210.

[107] Christopher J. Miller et al. "Controlling the False-Discovery Rate in Astrophysical Data Analysis". In: *The Astronomical Journal* 122.6 (2001). DOI: 10.1086/324109. URL: https://doi.org/10.1086/324109.

[108] LIGO Scientific Collaboration and Virgo Collaboration. "Tests of general relativity with the binary black hole signals from the LIGO-Virgo catalog GWTC-1". In: *Phys. Rev. D* 100 (10 2019). DOI: 10.1103/PhysRevD.100.104036. URL: https://link.aps.org/doi/10.1103/PhysRevD.100.104036.

[109] Neyman J. "Outline of a Theory of Statistical Estimation Based on the Classical Theory of Probability". In: *Mathematical and Physical Sciences* 236 (767 1937). DOI: https://doi.org/10.1098/rsta.1937.0005.

[110] M Cabero et al. "Blip glitches in Advanced LIGO data". In: *Classical and Quantum Gravity* 36.15 (2019). DOI: 10.1088/1361-6382/ab2e14. URL: https://doi.org/10.1088/1361-6382/ab2e14.

[111] the Virgo Collaboration The LIGO Scientific Collaboration and the KAGRA Collaboration. "Effects of Data Quality Vetoes on a Search for Compact Binary Coalescences in Advanced LIGO's First Observing Run". In: (). URL: https://dcc.ligo.org/LIGO-P1600110.

[112] Marek Szczepa ńczyk et al. "Observing an intermediate-mass black hole GW190521 with minimal assumptions". In: *Phys. Rev. D* 103 (8 2021). DOI: 10.1103/PhysRevD.103.082002. URL: https://link.aps.org/doi/10.1103/PhysRevD.103.082002.

[113] V Tiwari et al. "Regression of environmental noise in LIGO data". In: *Classical and Quantum Gravity* 32.16 (2015), p. 165014. DOI: 10.1088/0264-9381/32/16/165014. URL: https://doi.org/10.1088/0264-9381/32/16/165014.

[114] The LIGO Scientific Collaboration and the Virgo Scientific Collaboration. "GW190521: A Binary Black Hole Merger with a Total Mass of 150 $M_{\odot}$". In: *Phys. Rev. Lett.* 125 (10 2020). DOI: 10.1103/PhysRevLett.125.101102. URL: https://link.aps.org/doi/10.1103/PhysRevLett.125.101102.

[115] K. M. M. Prabhu. *Window Functions and Their Hpplications in Signal Processing*. CRC Press - Taylor & Francis Group, 2014. ISBN: 9781466515833.

[116] T. Sidery et al. "Reconstructing the sky location of gravitational-wave detected compact binary systems: Methodology for testing and comparison". In: *Phys. Rev. D* 89 (8 2014). DOI: 10.1103/PhysRevD.89.084060. URL: https://link.aps.org/doi/10.1103/PhysRevD.89.084060.

[117] Marek Szczepa ńczyk et al. "Observing an intermediate-mass black hole GW190521 with minimal assumptions". In: *Phys. Rev. D* 103 (8 2021). DOI: 10.1103/PhysRevD.103.082002. URL: https://link.aps.org/doi/10.1103/PhysRevD.103.082002.

[118] Katerina Chatziioannou et al. "Inferring the post-merger gravitational wave emission from binary neutron star coalescences". In: *Phys. Rev. D* 96 (12 2017). DOI: 10.1103/PhysRevD.96.124035. URL: https://link.aps.org/doi/10.1103/PhysRevD.96.124035.

[119] Elisa Maggio et al. "Analytical model for gravitational-wave echoes from spinning remnants". In: *Phys. Rev. D* 100 (6 2019). DOI: 10.1103/PhysRevD.100.064056. URL: https://link.aps.org/doi/10.1103/PhysRevD.100.064056.

[120] Virgo Collaboration. "Virgo Detector Characterization and Data Quality during the O3 run". In: (2022). DOI: 10.48550/ARXIV.2205.01555. URL: https://arxiv.org/abs/2205.01555.

[121] the Virgo Collaboration The LIGO Scientific Collaboration and the KAGRA Collaboration. URL: https://ldas-jobs.ligo.caltech.edu/~detchar/summary/day/20200210/.

[122] Thibault Damour and Sergey N. Solodukhin. "Wormholes as black hole foils". In: *Phys. Rev. D* 76 (2 2007). DOI: 10.1103/PhysRevD.76.024016. URL: https://link.aps.org/doi/10.1103/PhysRevD.76.024016.